

**UCLA**

**UCLA Electronic Theses and Dissertations**

**Title**

Atomic Layer Deposition Enabled Synthesis of Multiferroic Nanostructures

**Permalink**

<https://escholarship.org/uc/item/4qk4w945>

**Author**

Pham, Calvin Dinh-Tu

**Publication Date**

2015

Peer reviewed|Thesis/dissertation

UNIVERSITY OF CALIFORNIA

Los Angeles

Atomic Layer Deposition Enabled Synthesis of Multiferroic Nanostructures

A dissertation submitted in partial satisfaction of the  
requirements for the degree Doctor of Philosophy  
in Chemical Engineering

by

Calvin Dinh-Tu Pham

2015



## ABSTRACT OF THE DISSERTATION

Atomic Layer Deposition Enabled Synthesis of Multiferroic Nanostructures

by

Calvin Dinh-Tu Pham

Doctor of Philosophy in Chemical Engineering

University of California, Los Angeles, 2015

Professor Jane P. Chang, Chair

Complex metal oxides exhibit remarkable tunability in their ferromagnetic, ferroelectric, and multiferroic properties that enable future applications such as non-volatile memory, miniaturized antenna, sensors and actuators. Motivated by the promise of high magnetoelectric coupling from nanostructured multiferroics, atomic layer deposition (ALD) processes were developed to synthesize single-phase ferroics that would be further integrated to form composite multiferroics. The highly conformal ALD coatings promised intimate interfaces of the various ferroic phases to realize tunable magnetoelectric coupling.

In this work, a radical enhanced ALD process was used to synthesize the complex oxide nanostructures, using metalorganic precursors  $Y(\text{tmhd})_3$  ( $\text{tmhd} = 2,2,6,6\text{-tetramethylheptane-3,5 dione}$ ),  $\text{Mn}(\text{tmhd})_3$ ,  $\text{Bi}(\text{tmhd})_3$ ,  $\text{Co}(\text{tmhd})_2$ , and  $\text{Fe}(\text{tmhd})_3$  as well as oxygen atoms produced from a microwave powered atomic beam source. The processing-structure-property relations were systematically studied for three material systems:  $\text{YMnO}_3$  (YMO),  $\text{BiFeO}_3$  (BFO), and  $\text{CoFe}_2\text{O}_4$  (CFO). For YMO, it was found that the crystal structure forming between orthorhombic or hexagonal configurations was due to the substrate and that Si(111) and Y:ZrO<sub>2</sub> (111) substrates preferentially formed the orthorhombic and hexagonal phases respectively. The magnetic susceptibility versus temperature of YMO was characterized and it was determined that

the magnetic anomalies at ~48 K and ~80 K corresponded to orthorhombic and hexagonal phases respectively which matched the reports given from literature. The ALD BFO films were grown on SrTiO<sub>3</sub> (STO) (001) substrates and were found to crystallize epitaxially in the (001) pseudocubic orientation when annealed at 650 °C. The ferroelectric properties were confirmed via PFM while the weak ferromagnetic coupling showed a magnetic saturation ( $M_s$ ) of approximately 27 emu/cm<sup>3</sup>. The ALD CFO films were grown on STO (001) substrates and were mostly polycrystalline with a textured (001) orientation. The magnetic properties were studied and the  $M_s$  ranged from 260 to 550 emu/cm<sup>3</sup> and the magnetic coercivity ( $H_c$ ) ranged from 200 to 2180 Oe depending on the direction of the magnetic field, annealing condition, and thickness which matched values of those found in bulk and other thin film studies.

Synthesis of multiferroic composites with nanostructure was enabled by ALD. 2-2 multiferroic composite configurations using BiFeO<sub>3</sub> and CoFe<sub>2</sub>O<sub>4</sub> were synthesized by ALD and it was determined that for 40 nm thick films, a change in the easy axis of magnetization could be controlled by changing the size and number of repeating BFO/CFO bilayers. 0-3 multiferroic composite configurations using both BFO/CFO and CFO/PZT were synthesized by a hybrid approach first using evaporation induced self-assembly to deposit a porous metal oxide thin film followed by the ALD film. It was confirmed by SEM that the ALD coating was conformal and the magnetic properties were studied. The CFO template film with ALD BFO was found to have an  $M_s$  of 151.1 emu/cm<sup>3</sup> out-of-plane and 89.4 emu/cm<sup>3</sup> in-plane while  $H_c$  was about 2.0 kOe for both orientations. For the PZT template film with CFO overlayer, it was found that the  $M_s$  began to saturate at about 40-45 emu/cm<sup>3</sup> once the CFO thickness exceeded 4 nm due to the restricted pore necks. These volumetric values exceeded thin films found in literature with 0-3 configurations that were synthesized using wet techniques.

The dissertation of Calvin Dinh-Tu Pham is approved.

Gregory Carman

Robert Hicks

Harold Monbouquette

Jane P. Chang, Committee Chair

University of California, Los Angeles

2015

## TABLE OF CONTENTS

CHAPTER 1: INTRODUCTION .....	1
1.1 Motivation.....	1
1.2 Multiferroic Materials.....	17
1.3 Atomic Layer Deposition.....	54
1.4 Scope and Organization .....	62
CHAPTER 2: EXPERIMENTAL SETUP .....	64
2.1 Multi-Beam (MB) chamber .....	65
2.2 Precursor choice and processing conditions .....	71
2.3 Materials characterization.....	74
CHAPTER 3: GROWTH AND CHARACTERIZATION OF YTTRIUM MANGANESE OXIDE USING RADICAL ENHANCED ATOMIC LAYER DEPOSITION .....	98
3.1 Synthesis of $\text{YMnO}_3$ by Radical Enhanced ALD.....	99
3.2 Structure and Morphology of ALD grown $\text{YMnO}_3$ thin films .....	101
3.3 Magnetic properties of ALD grown $\text{YMnO}_3$ thin films.....	105
3.4 Conclusions.....	111
CHAPTER 4: GROWTH AND CHARACTERIZATION OF BISMUTH IRON OXIDE USING RADICAL ENHANCED ATOMIC LAYER DEPOSITION .....	112
4.1 Synthesis of $\text{BiFeO}_3$ by Radical Enhanced ALD.....	113
4.2 Structure and Morphology of $\text{BiFeO}_3$ Thin Films Grown by Radical Enhanced ALD...121	
4.3 Multiferroic Properties of ALD Grown $\text{BiFeO}_3$ Thin Films .....	126
4.4 Conclusions.....	128
CHAPTER 5: GROWTH AND CHARACTERIZATION OF COBALT IRON OXIDE USING RADICAL ENHANCED ATOMIC LAYER DEPOSITION .....	129
5.1 Synthesis of $\text{CoFe}_2\text{O}_4$ by radical enhanced ALD .....	130
5.2 Structure and morphology for ALD grown $\text{CoFe}_2\text{O}_4$ thin films.....	136
5.3 Magnetic properties of ALD grown $\text{CoFe}_2\text{O}_4$ thin films .....	140
5.4 Conclusions.....	146
CHAPTER 6: SYNTHESIS AND CHARACTERIZATION OF MULTIFERROIC COMPOSITE THIN FILMS ENABLED BY ATOMIC LAYER DEPOSITION.....	147
6.1 $\text{CoFe}_2\text{O}_4$ and $\text{BiFeO}_3$ 2-2 configuration composite thin films synthesized by RE-ALD 148	
6.2 $\text{BiFeO}_3$ and $\text{CoFe}_2\text{O}_4$ 0-3 configuration composite thin films enabled by RE-ALD .....	151
6.3 $\text{CoFe}_2\text{O}_4$ and $\text{Pb}(\text{Zr,Ti})\text{O}_3$ 0-3 configuration composite thin films by RE-ALD.....	153
6.4 Conclusions.....	157
CHAPTER 7: SUMMARY.....	158
APPENDIX A. SCHEMATICS OF THE HIGH VACUUM MULTI-BEAM CHAMBER.....	161
APPENDIX B. OPERATING PROCEDURES .....	176
APPENDIX C. LIST OF EQUIPMENT USED .....	185
APPENDIX D. MAINTENANCE .....	187
APPENDIX E. TROUBLESHOOTING .....	193
APPENDIX F. MULTIFERROIC MEASUREMENTS .....	196
APPENDIX G. LABVIEW AND AUTOMATED DEPOSITION .....	198
BIBLIOGRAPHY.....	201

## LIST OF FIGURES

Figure 1.1. Comparison of scenarios illustrating the potential for technological and policy developments to reduce total energy consumption in the United States. (Laitner 2010) .....	1
Figure 1.2 The growth of the solid-state memory market alongside total semiconductor market growth (Bez, Camerlenghi et al. 2003) .....	2
Figure 1.3. Heckmann Diagram illustrating external forces (electric field $E$ , magnetic field $H$ , and stress $\sigma$ ) and material properties (electric polarization $P$ , magnetization $M$ , and strain $\epsilon$ ) and the corresponding coupling between them. Adapted from Reference (Newnham 2004). .....	4
Figure 1.4 Performance of data storage and memory technologies. (a) Capacity versus Write/Program cycle time (b) Endurance cycles versus Write/Program cycle time (Tehrani 2010) .....	7
Figure 1.5. (a) NOR flash memory; each cell is individually controlled (b) NAND flash memory; memory is stored in blocks (Lai 2008) .....	9
Figure 1.6. (a) Perovskite unit cell of PZT showing shift of Ti or Zr with the application of an electric field. (b) hysteresis loop for a ferroelectric material showing polarization vs. applied voltage (Takashima 2010).....	11
Figure 1.7. a.) Schematic for magnetic tunnel junction (MTJ); antiparallel spins (top) have a higher resistance than parallel spins (bottom) b.) Typical materials used in MTJ stack (Slaughter 2009) .....	14
Figure 1.8. Schematic diagram of potential multiferroic memory which resembles MRAM for the storage layer but is controlled by a ferroelectric layer (Bibes and Barthelemy 2008) .....	16
Figure 1.9. Schematic diagram for symmetry considerations in (a) ferromagnets where time reversal symmetry switches the charge orbit, i.e. magnetic momentum $m$ , (b) ferroelectric where spatial inversion reverses the dipole moment $p$ , and (c) multiferroic that are both ferromagnetic and ferroelectric with time reversal and spatial inversion symmetry broken. (Eerenstein, Mathur et al. 2006). .....	20
Figure 1.10. Ferroelectric hysteresis loop showing Polarization vs. Electric field.....	22
Figure 1.11 (a) Perovskite structure of ferroelectric $\text{Pb}(\text{Zr,Ti})\text{O}_3$ showing $\text{ABO}_3$ with Pb at the corners and Zr or Ti in the center surrounded by O octahedron. In the polarized state, the Zr or Ti ion is moved relative to the O atoms (b) Double potential well showing two preferred states that are off-center (Hill 2000) .....	23
Figure 1.12 Schematic diagrams for types of magnetic ordering (a) Paramagnetic, (b) ferromagnetic, (c) antiferromagnetic, (d) ferrimagnetic materials .....	25
Figure 1.13. $M$ vs. $H$ hysteresis loop for a ferromagnetic or ferrimagnetic material .....	26



Figure 1.14. 3d and 4s up-and down-spin densities of states for first row transition metals; the right side includes exchange interactions for antiparallel spin configurations. Fermi levels are shown for Ni, Cu, and Zn (Hill 2000).....	27
Figure 1.15. Schematic representation of hysteresis loop shift caused by exchange bias effect (Nogués, Sort et al. 2005) .....	29
Figure 1.16. Schematic of the prototypical (a) rhombohedral and (b) tetragonal BiFeO <sub>3</sub> unit cell. (c) Ferroelectric hysteresis loop, which shows a saturation polarization of 55 $\mu\text{C}/\text{cm}^2$ in a 200 nm BiFeO <sub>3</sub> thin film. (d) A magnetic hysteresis loop shows the saturation magnetization of $\sim 150 \text{ emu}/\text{cm}^3$ and a coercive field of $\sim 200 \text{ Oe}$ in a 70 nm BiFeO <sub>3</sub> thin film. (Wang, Neaton et al. 2003). .....	32
Figure 1.17. BiFeO <sub>3</sub> : (a) Schematic of the planes of spin rotations and cycloids $k_1$ vector for the two polarization domains separated by a domain wall (b) Schematics of the antiferromagnetic circular cycloid. (Lebeugle, Colson et al. 2008).....	33
Figure 1.18. (a) Three-dimensional schematic view of YMnO <sub>3</sub> in the two polarized states. Arrows indicate the directions of the atomic displacements moving from the centrosymmetric to the ferroelectric structure. (b) Ferroelectric hysteresis loop of YMnO <sub>3</sub> measured in 100 nm YMnO <sub>3</sub> film. (c) Magnetic hysteresis loops at 5 K for the YMnO <sub>3</sub> pellets with different grain sizes. (Van Aken, Palstra et al. 2004), (Posadas, Yau et al. 2005), and (Han, Hsu et al. 2011) respectively. ....	35
Figure 1.19. Schematic illustration of the heterostructures of ME composite nanostructures with the three different connectivity schemes. The time progression of the material synthesis highlights the importance of a uniform and conformal coating to realize the intimately coupled interfaces in these complex structures. (a): 0-3 particulate composite (b): 2-2 laminate composite (c): 1-3 vertical fiber/rod composite. (Marchack and Chang 2012). ....	40
Figure 1.20.(a) Schematic diagram of a 2-2 nanolaminate structure, (b) the magnetoelectric voltage as a function of magnetic field in a 110nm Pb(Zr <sub>0.3</sub> , Ti <sub>0.7</sub> )O <sub>3</sub> / La <sub>1.2</sub> Sr <sub>1.8</sub> Mn <sub>2</sub> O <sub>7</sub> film stack at three different temperatures, and (c) the comparison of temperature dependence of the magnetization measured on the manganite crystal and the peak-to-peak magnetoelectric voltage. (Wu, Zurbuchen et al. 2006) .....	42
Figure 1.21. (a) Schematic diagram of a 2-2 nanolaminate structure, (b) the magnetoelectric hysteresis loop as a function of the applied electric field measured in 250nm Pb(Zr <sub>0.2</sub> , Ti <sub>0.8</sub> )O <sub>3</sub> /4nm La <sub>0.8</sub> Sr <sub>0.2</sub> MnO <sub>3</sub> composite 1 at T = 100K. The insets indicate the magnetic and electric states of the composite. (Molegraaf, Hoffman et al. 2009).....	43
Figure 1.22. (a) Schematic diagram of 1-3 nanorod structure based on ferromagnetic rods (100nm wide CoFe <sub>2</sub> O <sub>4</sub> ) and ferroelectric matrix (300nm thick BiFeO <sub>3</sub> ), (b) the magnetic hysteresis loop for in-plane and out-of-plane measured in self-assembled BiFeO <sub>3</sub> /CoFe <sub>2</sub> O <sub>4</sub> , (c) the current density (J) and polarization (P) as a function of electric fields, (d) the transverse ( $\alpha_{31}$ ) and (e) longitudinal ( $\alpha_{33}$ ) ME susceptibility of the nanostructure composites at 300K. (Oh, Crane et al. 2010). ....	44

Figure 1.23. (a) Schematic diagrams of 2-2 30nm CoFe <sub>2</sub> O <sub>4</sub> /30nm BaTiO <sub>3</sub> and 1-3 400nm thick BaTiO <sub>3</sub> matrix/30nm wide CoFe <sub>2</sub> O <sub>4</sub> rod structures used in Green function's calculations. (b) Magnetic field induced electric polarization $DP3 = P3 - P3(H = 0)$ for both systems and (c) the effect of the magnetostriction of the ferromagnetic phase on $DP3$ for the 1-3 system. (Nan, Liu et al. 2005).....	45
Figure 1.24. (a) Schematic diagram of 0-3 nanoparticulate structure with ferromagnetic particulates (140nm diameter CoF <sub>2</sub> O <sub>4</sub> ) in a ferroelectric matrix (1 $\mu$ m thick Pb(Zr <sub>0.52</sub> , Ti <sub>0.48</sub> )O <sub>3</sub> ). (b) Polarization (magnetization) vs. electric (magnetic) field hysteresis loop measured in the composite and (c) the variation of $\alpha_E$ with $H_{bias}$ at a magnetic frequency $f = 10$ kHz. (Wan, Zhang et al. 2006).....	46
Figure 1.25. (a) Schematic diagram of 0-3 nanoparticulate structure of magnetostrictive particulates (NFO) in a ferroelectric matrix (PZT). The transverse ( $\alpha_{31}$ ) (b) and longitudinal ( $\alpha_{33}$ ) (c) components of the magnetoelectric coefficient measured on the Pb(Zr <sub>0.52</sub> Ti <sub>0.48</sub> )O <sub>3</sub> /NiFe <sub>2</sub> O <sub>4</sub> particulate composite film after poling at 0.8 and -0.8 MV/cm. (Ryu, Murugavel et al. 2006)...	47
Figure 1.26. (a) ALD growth rate of Pb(Zr, Ti)O <sub>3</sub> in comparison with that of its constituent oxides. (b, c) SEM images of mesoporous CoFe <sub>2</sub> O <sub>4</sub> thin films (b) and a Pb(Zr, Ti)O <sub>3</sub> /CoFe <sub>2</sub> O <sub>4</sub> composite multiferroic (c). (d) X-ray diffraction patterns of the composite, confirming the crystal structures of both ferroic phases. (Marchack and Chang 2012). ....	48
Figure 1.27. Schematic showing the steps for atomic layer deposition. (1) The metal precursor is flowed (2) a self-limiting reaction forms a monolayer of metal precursor on the surface (3) the oxidant is flowed (4) the metal precursor is oxidized.....	56
Figure 2.1 Top-down schematic of multi-beam chamber (Hoang 2011).....	65
Figure 2.2 (a) Schematic of coaxial microwave cavity radical beam source (b) Schematic showing magnified view of quartz ampoule and radical source cross-section (c) Example of quartz ampoule with aspect ratio of 3 ( $D \times l = 1 \times 3$ mm) .....	66
Figure 2.3 Schematic drawings showing (a) vacuum side and (b) air side for six doser array designed in-house.....	70
Figure 2.4 Molecular structure of Tris(2,2,6,6-tetramethyl-3,6-heptanedionato)M(III) precursor where M = Co, Bi, Fe, etc.....	72
Figure 2.5. Precursor pulsing sequence for BiFeO <sub>3</sub> and CoFe <sub>2</sub> O <sub>4</sub> using ALD.....	74
Figure 2.6 XPS spectra of BiFeO <sub>3</sub> sample showing major elemental peaks .....	75
Figure 2.7 Photon scattering on parallel crystal planes; Bragg diffraction is a result of constructive interference of scattered photons.....	78
Figure 2.8. Sample X-ray diffraction pattern for SrTiO <sub>3</sub> (001) substrate and ALD BiFeO <sub>3</sub> film grown on SrTiO <sub>3</sub> (001) annealed at 650 °C.....	78

Figure 2.9 (a) Four-circle diffractometer XRD experimental schematic (Scintag 1999), (b) Multiple planes of sample probed using technique.....	79
Figure 2.10. An XAS spectrum collected in the fluorescence mode below and above the Mn K absorption edge of an YMnO <sub>3</sub> thin film. ....	80
Figure 2.11. (a) The EXAFS data and (b) the corresponding FT spectrum of the YMnO <sub>3</sub> film. 83	
Figure 2.12 Schematic diagram of the Stanford Synchrotron Radiation Laboratory (SSRL), showing the electron storage ring, or SPEAR (top), and an experimental station, or hutch (bottom) (Van and Peterson 1998).....	84
Figure 2.13 (a) Schematic drawing of SQUID Magnetometer used in MPMS system (b) Schematic of superconducting coil (c) Schematic of sample space and detector assembly .....	85
Figure 2.14 Magnetic Hysteresis M vs. H of CoFe <sub>2</sub> O <sub>4</sub> thin film showing ferromagnetic ordering. ....	87
Figure 2.15 PFM image of polarized PZT film on Al <sub>2</sub> O <sub>3</sub> /SiC substrate (b.) Surface cross-section of polarization contrast between oppositely poled sections (c.) Hysteresis loop of piezoelectric phase when voltage is scanned (Zhang, Perng et al. 2011) .....	90
Figure 2.16 Angular momentum conservation in photoelectric excitation of magnetic materials with circularly polarized light.....	91
Figure 2.17. M vs. H hysteresis loop measured using MOKE for CoFeB as grown (dashed line) and annealed at 300 °C in vacuum for 30 minutes (solid line). (Courtesy Diana Chien) .....	92
Figure 2.18. (a) Cross-section of ALD Bi <sub>2</sub> O <sub>3</sub> film imaged by SEM. (b) Sample EDX spectra for BiFeO <sub>3</sub> sample on Silicon indicating elemental X-ray emissions. ....	94
Figure 2.19. (a) TEM image of BiFeO <sub>3</sub> film on SrTiO <sub>3</sub> substrate indicating epitaxial microstructure,(b) selected area diffraction pattern (SADP) of SrTiO <sub>3</sub> substrate, and (c) SADP of BiFeO <sub>3</sub> film.....	97
Figure 3.1. (a) Survey XPS spectra for YMO thin film on Si (111) with Mn/Y=0.95, (b) Survey XPS spectra for YMO thin film on YSZ (111) with Mn/Y=1.07. Detailed XPS spectrum of Mn 2p for YMO thin film on Si (111) after RTA under (c) N <sub>2</sub> and (d) Air. C1s spectra was used for peaks alignment and all the FWHM of deconvoluted peaks are fixed as 3.6. ....	99
Figure 3.2. (a) Composition ratio of ~6 nm YMO ultra thin films on Si (111) with different Mn:Y precursor pulsing ratio. (b) Composition ratio of ~6 nm YMO ultra thin films on YSZ (111) with different Mn:Y precursor pulsing cycles.....	100
Figure 3.3. (a) The XRD of YMO thin films on Si (111) as function of RTA condition. (b) The XRD of YMO thin films on YSZ (111) as function of Mn/Y ratio after RTA 900 °C. ....	101

Figure 3.4. Bright field TEM images of ~6 nm YMO ultra thin films on (a) Si (111) and (b) YSZ (111) (c) SEM image of cross section of 80 nm YSZ films on Si (111) and (b) YSZ (111)..... 103

Figure 3.5. Schematic structure of (a) h-YMO with  $\text{MnO}_5$  polyhedron ( $d(\text{Mn}-\text{O}_1)=1.687\text{\AA}$ ,  $d(\text{Mn}-\text{O}_2)=2.043\text{\AA}$ ,  $d(\text{Mn}-\text{O}_3)=1.830\text{\AA}$ ,  $d(\text{Mn}-\text{O}_4)=2.090\text{\AA}$ ) (Katsufuji, Masaki et al. 2002) and (b) o-YMO with  $\text{MnO}_6$  polyhedron ( $d(\text{Mn}-\text{O}_1)=2.209\text{\AA}$ ,  $d(\text{Mn}-\text{O}_2)=1.916\text{\AA}$ ,  $d(\text{Mn}-\text{O}_3)=1.947\text{\AA}$ ) (Iliev, Abrashev et al. 1998). (c) The EXAFS of collected  $k^3$  spectra and (d) respective Fourier Transformation (FT) for 80 nm YMO thin films on Si (111) and 80 nm YMO thin films YSZ (111). The spheres represent the O atoms, the and represent the Y and Mn atoms, respectively. .... 104

Figure 3.6. (a) dc magnetic susceptibility ( $\chi$ ) for the ~6 nm and 80 nm YMO thin films on Si (111) under 100 Oe. Solid symbols represent ZFC condition and open symbols represent FC condition (b) dc magnetic susceptibility ( $\chi$ ) for ~6 nm YMO thin films on YSZ (111) with different Mn/Y atomic ratios under 100 Oe. (c) The temperature dependence of  $d\chi/dT$  for ~6 nm and 80 nm YMO thin film on Si (111) between the range  $0 < T < 95$  K (c) The temperature dependence of  $d\chi/dT$  for ~6 nm ultra thin films on YSZ (111) in range  $0 < T < 95$  K ..... 106

Figure 3.7.  $1/\chi$  as a function of temperature for ~6 nm YMO ultra thin films on YSZ (111) with different Mn/Y atomic ratios. .... 108

Figure 3.8. Magnetic hysteresis loop (M vs. H) measured at (a) 20 K and (b) 298 K for ~6 nm YMO ultra thin films on Si (111) before and after 20 V electric polling. (c) and (d) Closer look at the coercive fields. .... 110

Figure 4.1. High resolution XPS spectra for (a) Fe 2p peak from  $\text{Fe}_2\text{O}_3$  film and (b) Bi 4f peak from  $\text{Bi}_2\text{O}_3$  film grown by ALD ..... 113

Figure 4.2. Calibration of spectroscopic ellipsometry model (solid lines) fitted to experimental data (dashed lines) for (a)  $\text{Bi}_2\text{O}_3$  and (b)  $\text{Fe}_2\text{O}_3$  films grown on Si (001) substrates using cross-section SEM images for (c)  $\text{Bi}_2\text{O}_3$  and (d)  $\text{Fe}_2\text{O}_3$ . .... 115

Figure 4.3. Temperature dependence of ALD growth rate for  $\text{Bi}_2\text{O}_3$  and  $\text{Fe}_2\text{O}_3$  films grown on Si (001) substrates in  $\text{\AA}/\text{cycle}$  measured using ellipsometry..... 116

Figure 4.4. Composition of (a)  $\text{Bi}_2\text{O}_3$  and (b)  $\text{Fe}_2\text{O}_3$  films as a function of growth temperature as calculated using X-ray photoelectron spectra. .... 116

Figure 4.5. Effect of precursor pulse time on ALD growth rate for (a)  $\text{Bi}_2\text{O}_3$  and (b)  $\text{Fe}_2\text{O}_3$  grown on Si (001) substrates in  $\text{\AA}/\text{cycle}$  measured using ellipsometry. .... 119

Figure 4.6. ALD film thickness (nm) as a function of number of cycles of  $\text{Bi}_2\text{O}_3$  and  $\text{Fe}_2\text{O}_3$  consisting of a 90 s metalorganic pulse, 5 s pump-down, 20 s radical pulse, 5 s pump-down cycle sequence. .... 119

Figure 4.7. (a) XPS survey scan for  $\text{BiFeO}_3$  thin film grown by ALD. (b) Composition ratio of bismuth-iron oxide films grown by ALD as a function of pulse sequence ratio between  $\text{Bi}_2\text{O}_3$  and

Fe <sub>2</sub> O <sub>3</sub> . Solid line is a guide for the eye indicating desired stoichiometric 1:1 ratio for BiFeO <sub>3</sub> . Detailed XP spectra for (c) Fe 2p and (d) Bi 4f photoelectron peaks.....	121
Figure 4.8. (a) Diffraction patterns for 35 nm thick BiFeO <sub>3</sub> films grown on SrTiO <sub>3</sub> (001) substrates as prepared and as a function of annealing temperature indicating crystallization. (b) Detailed look at BFO (001) <sub>pc</sub> reflection for samples annealed at 550 °C and 650 °C.....	122
Figure 4.9. (a) TEM micrograph of BiFeO <sub>3</sub> film on SrTiO <sub>3</sub> (001) substrate indicating epitaxial nature of film crystallized at 650 °C. (b) Electron diffraction pattern of BiFeO <sub>3</sub> film.....	123
Figure 4.10. Surface morphology measured by AFM of (a) SrTiO <sub>3</sub> substrate as received and 35 nm thick BiFeO <sub>3</sub> films grown on SrTiO <sub>3</sub> (001) substrates (b) as deposited at 210 °C and annealed at (c) 450 °C, (d) 550 °C, (e) 650 °C, and (f) 750 °C. RMS surface roughness, indicated by R <sub>rms</sub> is increased as annealing temperature increases. ....	125
Figure 4.11. Piezoresponse force microscopy images of BFO film on Nb:STO substrate (a) before and (b) after ±12 V applied using PFM tip in square pattern. ....	126
Figure 4.12. Magnetic hysteresis of BFO film annealed at 650 °C on STO substrate with applied magnetic field oriented in-plane (black squares) and out-of-plane (red circles) relative to the sample plane.....	127
Figure 5.1. Detailed XPS spectra for (a) Co 2p from a cobalt oxide thin film and (b) Fe 2p from an iron oxide thin film.....	130
Figure 5.2. (a) Growth rate versus temperature for Fe <sub>2</sub> O <sub>3</sub> and Co <sub>3</sub> O <sub>4</sub> measured by ellipsometry. Thin film composition as a function of growth temperature for (b) iron oxide and (c) cobalt oxide grown by ALD .....	132
Figure 5.3. Growth rate versus precursor pulse time for (a) Co <sub>3</sub> O <sub>4</sub> and (b) Fe <sub>2</sub> O <sub>3</sub> . Fitted curves provided as guide for the eye. ....	133
Figure 5.4 Film thickness as a function of ALD cycles for Co <sub>3</sub> O <sub>4</sub> (green circles) and Fe <sub>2</sub> O <sub>3</sub> (red squares). ....	134
Figure 5.5. (a) XPS survey scan for CFO film (b) Iron content in CFO film as a function of ALD dosing sequence. Horizontal line is a guide for the eye indicating stoichiometric ratio Co:Fe = 1:2 for CoFe <sub>2</sub> O <sub>4</sub> . Detailed XP spectra for (c) Co 2p and (d) Fe 2p. ....	135
Figure 5.6. Thickness as a function of global ALD cycles using the sequence 1 Co <sub>3</sub> O <sub>4</sub> :5 Fe <sub>2</sub> O <sub>3</sub> . ....	136
Figure 5.7. (a) X-ray diffraction pattern for CoFe <sub>2</sub> O <sub>4</sub> films grown on SrTiO <sub>3</sub> (001) as prepared and annealed between 450 °C and 750 °C. CoFe <sub>2</sub> O <sub>4</sub> (004) peak is found for annealed films. (b) d-spacing of (004) planes as a function of annealing temperature; horizontal line indicates reference value from bulk samples (JCPDS card 022-1086).....	137

Figure 5.8. (a) High-resolution image of CFO film on STO. SAED pattern (b) near the interface and (c) in the bulk film indicating epitaxial transition to polycrystalline film. ....	138
Figure 5.9. Topography of (a) bare SrTiO <sub>3</sub> substrate, CoFe <sub>2</sub> O <sub>4</sub> thin films (b) as-prepared and annealed at (c) 450 °C, (d) 550 °C, (e) 650 °C, and (f) 750 °C. ....	139
Figure 5.10. AFM image of CFO sample annealed at 750 °C indicating domain patterns. ....	140
Figure 5.11. Magnetization versus magnetic field for CoFe <sub>2</sub> O <sub>4</sub> films annealed at 650 °C with thicknesses of (a) 90 nm, (b) 50 nm, (c) 20 nm, and (d) 7 nm. ....	141
Figure 5.12. Coercivity (blue squares) and saturation magnetization (red circles) vs. film thickness for out-of-plane (dashed line) and in-plane orientation (solid line) of applied magnetic field .....	142
Figure 5.13. Magnetization versus magnetic field for 20 nm thick CoFe <sub>2</sub> O <sub>4</sub> films annealed at (a) 450 °C, (b) 550 °C, (c) 650 °C, and (d) 750 °C. ....	143
Figure 5.14. Coercivity (blue squares) and saturation magnetization (red circles) vs. annealing temperature for out-of-plane (dashed line) and in-plane orientation (solid line) of applied magnetic field. ....	144
Figure 6.1. Diffraction patterns for 85 nm BFO /85 nm CFO heterostructure grown on SrTiO <sub>3</sub> (001) substrates as prepared and as a function and annealed at 550 °C indicating crystallization. ....	148
Figure 6.2. M vs. H hysteresis loop for 85 nm BFO/85 nm CFO heterostructure on STO (001) substrate annealed at 550 °C. ....	149
Figure 6.3. M vs. H hysteresis loops for 40 nm thick BFO/CFO heterostructures with (a) 1 bilayer, (b) 2 bilayers, (c) 3 bilayers, and (d) 4 bilayers. ....	150
Figure 6.4. XPS survey scan of mesoporous CFO film before and after ALD BFO film was deposited. ....	152
Figure 6.5. (a) Mesoporous CFO film before ALD BFO deposited (b) Film after ALD BFO deposited .....	152
Figure 6.6. Magnetic hysteresis of ~7nm BFO/~100 nm CFO 0-3 configuration composite. ...	153
Figure 6.7. XPS survey scan of porous PZT/ALD CFO 0-3 multiferroic composite. ....	154
Figure 6.8. Top-down SEM images for (a) bare mesoporous PZT, (b) 1.5, (c) 3, (d) 4.5, (e) 6, and (f) 7.5 nm thick ALD CFO films deposited on mesoporous PZT. ....	155
Figure 6.9. (a) Magnetic hysteresis for CFO/PZT 0-3 composite multiferroics with different CFO thicknesses. (b) Saturation magnetization for 0-3 composites with different CFO thicknesses. ....	156

## LIST OF TABLES

Table 1.1. Target values for various performance aspects of non-volatile memory (Burr, Kurdi et al. 2008) .....	6
Table 1.2 Summary of memory devices and performance parameters (Kryder and Chang Soo 2009; ITRS 2011; Wang, Alzate et al. 2013).....	17
Table 1.3. The classification of single-phase multiferroics and their material properties.....	21
Table 1.4. Ferroelectric and ferromagnetic materials and their respective ferroic properties. ....	39
Table 1.5. Comparison of various multiferroic composites with different configurations and material selections.....	49
Table 1.6. The various deposition techniques that can be used to deposit multiferroic materials	52
Table 2.1. Physical properties of metalorganic precursors used in this work: Co(TMHD) <sub>2</sub> , Bi(TMHD) <sub>3</sub> , Fe(TMHD) <sub>3</sub> , Mn(TMHD) <sub>3</sub> , and Y(TMHD) <sub>3</sub> .....	72
Table 2.2 Process conditions for the respective precursors .....	73
Table 2.3. List of characteristic X-ray energies for elemental emissions .....	94
Table 2.4. Calculated R values, calculated d-spacing, and comparison to d-spacing from JCPDS reference for SrTiO <sub>3</sub> substrate and BiFeO <sub>3</sub> film. ....	97
Table 4.1 Fitted parameters for Lorentz oscillator model used in ellipsometry measurement...	114
Table 4.2 Calculated R values, calculated d-spacing, and comparison to d-spacing from JCPDS reference for SrTiO <sub>3</sub> substrate and BiFeO <sub>3</sub> film. ....	123
Table 5.1 Calculated R values, calculated d-spacing, and comparison to d-spacing from JCPDS reference for SrTiO <sub>3</sub> substrate and CoFe <sub>2</sub> O <sub>4</sub> film.....	138
Table 5.2. Comparison of properties for CoFe <sub>2</sub> O <sub>4</sub> synthesized by different methods. ( $H_c$ : magnetic coercivity, $M_s$ : saturation magnetization, $t$ : film thickness).....	145

## ACKNOWLEDGMENTS

This work and my last five years in this program would not have been possible without the input, support, and caring from countless numbers of people. Unfortunately, although I have tried to include as many people as I could, I will have inevitably left out some people who also deserve to be thanked for which I apologize for not mentioning.

I would first like to thank my doctorate advisor, Professor Jane P. Chang for the guidance and lessons she has given me through the course of this journey. Her ability to combine critical analysis with meticulous and effective presentation has encouraged me to model myself after her. The high attention to detail doing research in the lab, writing manuscripts or proposals, and speaking in oral presentations are things that she has taught me and will last with me throughout my professional career. I hope that I will be able to live up to her high expectations once I leave the university setting and will endeavor to uphold them for myself. I would also like to thank my dissertation committee, Professors Robert Hicks, Harold Monbouquette, and Greg Carman for their time and input as well as the funding support from the FENA and FAME centers which were both funded by SRC and DARPA as well as their respective associated members.

The members of the Chang Lab group, both past and present must also be thanked here, for their collaboration, input, and companionship have been invaluable, without which, both work and life may not have been nearly as pleasant. Of course I must thank my mentor, Dr. John Hoang for teaching me not only how to operate the ALD tool and research analysis skills, but how to be a better researcher and scientist both experimentally and computationally not to mention other life skills outside of the lab. I would also like to thank my successor Jeffrey Chang for being incredibly helpful through his experimental contributions and extreme willingness to learn and dedication to research which helped motivate me to be a suitable mentor. I should also



thank Nathan Marchack for being a great coworker and friend as our discussions about things other than research definitely kept things interesting and helped to broaden my worldview. In addition, the other members of the lab which I have had the privilege of working with and knowing: the former and current grad students Wilson Lin, Ryan Martin, James Dorman, Sandy Perng, Vladan Jankovic, Leo Li, Jay Cho, Stephanie Gachot, Jack Chen, Diana Chien, Colin Rementer, Cyrus Cheung, Trevor Seegmiller, Nicholas Altieri, Luke Minardi, and Kevin Fitzell; the post-doctorate researchers Doctors Jerry Hsu, Ju Hyeon Choi, Taeseung Kim, and Younghee Kim, and the undergraduate or high school researchers Kristen Fernhoff and Carissa Eisler have been instrumental in teaching me through numerous lab presentations and discussions, improving my own teaching skills, and helping me to run experiments or processes when I could not.

My fellow chemical engineering graduate school companions also deserve mention for their camaraderie over the past five plus years but I should give special thanks to Allison Yorita, Jennifer Takasumi, Paul Lin, Larry Gao, Michael Nayhouse, Erica Cahyadi, and countless others for their continued friendship despite the vast chasm between Engineering V and Boelter Hall. Of course outside of the department, I have had the pleasure of meeting, collaborating, and having invaluable discussions with Abraham Buditama, Laura Schelhas, Paul Nordeen, and other fellow grad students. And helping to do or teach me how to do the various analytical techniques: Doctors Ignacio Martini, Adam Stieg, Mark Zurbuchen, Tom Mates, and others.

Finally but most importantly, I would like to thank my family – my mom, dad, brother, grandparents, aunts, uncles, and cousins – the love and support that I got while staying at UCLA the past nearly ten (!) years has been truly wonderful and plentiful and it would not have been possible for me to come this far without their encouragement.

## VITA

- 2009 B.S., Chemical and Biomolecular Engineering  
University of California, Los Angeles  
Los Angeles, CA
- 2010-2015 Graduate Student Researcher  
Department of Chemical and Biomolecular Engineering  
University of California, Los Angeles
- 2010, 2012 Teaching Assistant  
Department of Chemical and Biomolecular Engineering  
University of California, Los Angeles

## PUBLICATIONS AND PRESENTATIONS

Kim, Y.H., Pham, C.D., Chang, J.P., “Potentials and Challenges of Integration for Complex Metal Oxides in CMOS Devices and Beyond”, Journal of Physics: D Applied Physics, 48, 063001 (2015)

Hsu, C.C., Marchack, N.P., Martin, R.M., Pham, C.D., Hoang, J., and Chang, J.P., “Feature profile evolution during shallow trench isolation etching in chlorine-based plasmas. III. The effect of oxygen addition” J. Vac. Sci. Technol. B 31, 042201 (2013)

Pham, C.D., Kim, Y.H., and Chang, J.P., Presentation: “ALD enabled synthesis of nanostructured multiferroics”, 61<sup>st</sup> AVS Symposium, Baltimore MD, November 2014.

Pham, C.D., Kim, Y.H., and Chang, J.P., Presentation: “ALD enabled synthesis of nanostructured multiferroics”, SRC TECHCON 2014, Austin, TX, September 2014.

Pham, C.D., Kim, Y.H., and Chang, J.P., Poster: “ALD enabled synthesis of nanostructured multiferroics”, The 10<sup>th</sup> International Nanotechnology Conference on Communication and Cooperation (INC10), Gaithersburg, MD, May 2014.

Pham, C.D., Kim, Y.H., and Chang, J.P., Presentation: “ALD enabled synthesis of nanostructured BiFeO<sub>3</sub>/CoFe<sub>2</sub>O<sub>4</sub> composites for multiferroic applications” 60<sup>th</sup> AVS Symposium, Long Beach, CA, November 2013

Pham, C.D., Kim, Y.H., and Chang, J.P., Presentation: “ALD enabled synthesis of nanostructured BiFeO<sub>3</sub>/CoFe<sub>2</sub>O<sub>4</sub> composites for multiferroic applications” 2013 AIChE Annual Meeting, San Francisco, CA, November 2013

Pham, C.D. and Chang, J.P., Presentation: “ALD enabled synthesis of nanostructured BiFeO<sub>3</sub>/CoFe<sub>2</sub>O<sub>4</sub> composites for multiferroic applications”, 13<sup>th</sup> International Conference on Atomic Layer Deposition, San Diego, CA, July 2013.

Pham, C.D. and Chang, J.P., Presentation: “ALD enabled synthesis of nanostructured BiFeO<sub>3</sub>/CoFe<sub>2</sub>O<sub>4</sub> composites for multiferroic applications”, 59<sup>th</sup> AVS Symposium, Tampa Bay, FL, November 2012.

Choi, J.H., Pham, C.D., Schelhas, L., Buditama, A., Tolbert S., Chang, J.P., Presentation: “Engineered Multiferroic Composite PZT-CFO by Atomic Layer Deposition”, 59<sup>th</sup> AVS Symposium, Tampa Bay, FL, November 2012.

Pham, C.D. and Chang, J.P., Presentation: “ALD enabled synthesis of nanostructured BiFeO<sub>3</sub>/CoFe<sub>2</sub>O<sub>4</sub> composites for multiferroic applications”, 2012 AIChE Annual Meeting, Pittsburgh, PA, November 2012.

Pham, C.D., Choi, J.H., Dorman, J.A., and Chang, J.P., Presentation: “Synthesis and Characterization of Multiferroic Oxides YMnO<sub>3</sub> and BiFeO<sub>3</sub> by Radical Enhanced Atomic Layer Deposition”, 58<sup>th</sup> AVS Symposium, Nashville, TN, November 2011.

## CHAPTER 1: INTRODUCTION

### 1.1 Motivation

Improvements in microelectronic devices have been driven by Gordon Moore's famous prediction that the number of individual transistors on a fixed area should double every 12 months (which was later amended to 18-24 months). (Moore 1965) Motivated by this continued scaling of integrated circuit (IC) manufacturing, chemical processing of predominantly silicon-based metal-oxide-semiconductor transistors have developed to a highly advanced level for persistently smaller yet higher performance devices. However, in the past decade, the industry has shifted from focusing on higher clock speeds towards more power-efficient designs due to the changing requirements of the semiconductor market which has seen rising demand for mobile devices, internet-of-things, and enterprise-scale server clusters. This motivation led to the highly successful integration of high-k gate dielectrics (Mistry, Allen et al. 2007) and tri-gate FinFETs with 3D geometry. (Auth, Allen et al. 2012) In addition, it has been proposed that highly efficient semiconductor-enabled designs can lower energy consumption despite an increase in the number of devices, as shown in Figure 1.1. (Laitner 2010)

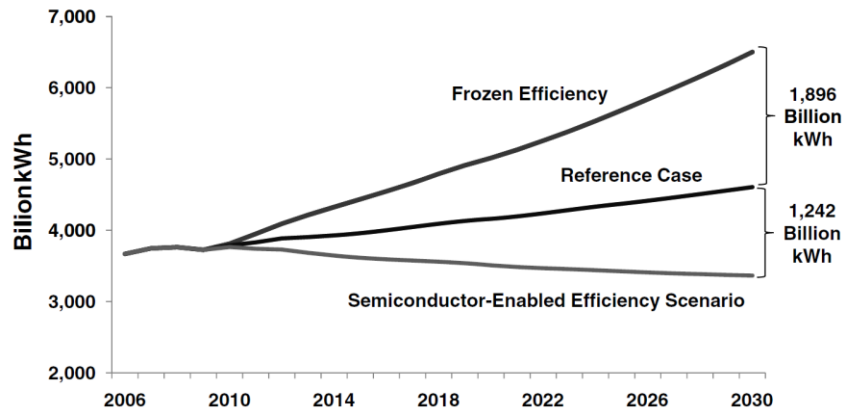


Figure 1.1. Comparison of scenarios illustrating the potential for technological and policy developments to reduce total energy consumption in the United States. (Laitner 2010)

In order to meet the demand for future ultra-low power electronics, new device structures for non-volatile memory have been proposed for novel material systems utilizing new control parameters such as magnetization. (Nikonov and Young 2012) NAND flash, which is currently the most ubiquitous solid-state non-volatile memory, has been able to scale with increasing density and therefore a greater data capacity per cost ratio, which is currently at under 40 cents per GB (Iliev, Abrashev et al. 1998). As shown in Figure 1.2, the growth of solid state memory has matched the overall semiconductor market. However, due to physical limitations with respect to the required electric fields for read-write operation and subsequent size limits, NAND flash memory is approaching its physical boundary at approximately 20 nm per cell. (Lai 2008) In addition, flash memory suffers from a slow write speed meaning that it cannot replace SRAM or DRAM. As a result, new types of devices are being proposed and tested which can simultaneously meet the future performance needs for storage and working memory, which has been termed as “universal memory”.(Wang, Alzate et al. 2013) One such possible route is the use of magnetoelectric multiferroic materials for memory applications. (Thomas 2010)

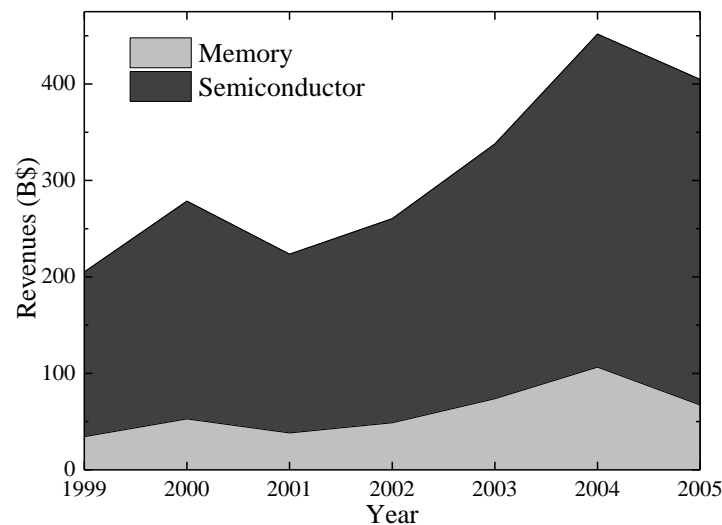


Figure 1.2 The growth of the solid-state memory market alongside total semiconductor market growth (Bez, Camerlenghi et al. 2003)

Multiferroic materials exhibit two or more forms of ferroic order such as (anti)ferroelectricity, (anti)ferromagnetism, or ferroelasticity. (Eerenstein, Mathur et al. 2006)

The relationships between ferroic materials can be seen in Figure 1.3. Due to the efforts of scientific luminaries such as Oersted, Faraday, and Maxwell, the link between magnetism and electricity had been established by the laws of electromagnetism. However, the notion of an intrinsic magnetoelectric material originated with Pierre Curie in 1894 through the basis of symmetry. (Curie 1894) In 1926, Peter Debye authored the first usage of the word ‘magnetoelectric’ during experiments to find such a material, however, they were unsuccessful. (Debye 1926) It was not until the 1960’s when, through the combined work of Shubnikov, Dzyaloshinskii, and Landau with Lifshitz, that the magnetoelectric  $\text{Cr}_2\text{O}_3$  was identified through theoretical predictions based on symmetry. (Dzyaloshinskii 1957; Dzyaloshinskii 1960; Landau 1960; Alekseevskii 1992) Unfortunately, research was limited for several decades afterwards due to the small number of compounds and the relatively small magnetoelectric coupling coefficient for intrinsic multiferroics. Eventually however, it has been revived in the last two decades as a result of improved theoretical calculations and massive improvements in material processing capability, beginning with Schmid who created the word ‘Multiferroic’ and notably by Spaldin (née Hill) who elucidated the requisites for the presence of multiferroic properties for single-phase materials. (Schmid 1994; Hill 2000) As a result, the search for viable multiferroic materials for magnetoelectric devices in which magnetism can be controlled via electric field has since been ongoing. A more detailed review of multiferroic materials is covered in section 1.2.

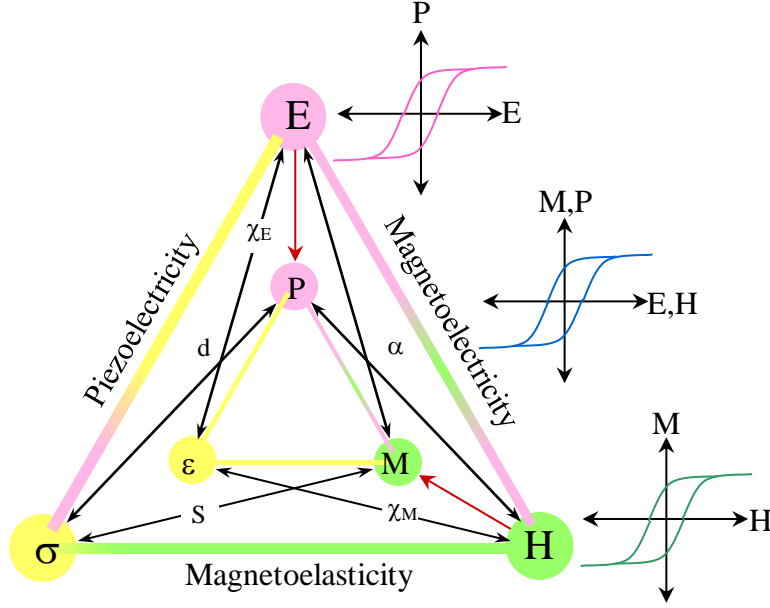


Figure 1.3. Heckmann Diagram illustrating external forces (electric field  $E$ , magnetic field  $H$ , and stress  $\sigma$ ) and material properties (electric polarization  $P$ , magnetization  $M$ , and strain  $\epsilon$ ) and the corresponding coupling between them. Adapted from Reference (Newnham 2004).

Magnetoelectrically coupled materials can potentially be used for devices that would induce the change in magnetization via an electric field or vice versa, as well as fulfill the prospect of four-state memory devices. (Thomas 2010; Wang, Alzate et al. 2013) Research regarding the synthesis and physics for magnetoelectric thin films has occurred over the past decade and most efforts have focused on the characterization of high quality epitaxial samples. (Martin, Chu et al. 2010) Typically the samples have been synthesized by methods like pulsed laser deposition (PLD) which is inherently not scalable to the larger area wafers ( $> 300$  mm) needed for modern IC manufacturing. On the other hand, atomic layer deposition (ALD) is a relatively unexplored method for synthesis (or enabling the synthesis) of multiferroics, especially multiferroic composites, which is attractive because it permits the integration of both single-phase and nano-structured composite multiferroics into current fabrication schemes.

ALD is a thin-film processing technique which involves alternatively flowing self-limiting precursor vapors or gases onto a substrate.(Leskelä and Ritala 2002; Leskelä and Ritala 2003). Ideally, because of the self-limiting reactions, the precursors only form a single sub-monolayer per cycle. The sequential and self-limiting nature of the deposition is used to deposit thin films with good compositional control, high conformity, high uniformity, and excellent thickness control, all factors which make ALD an appealing technique especially for depositing on 3-D structures or creating layered film structures. ALD has been used very successfully in the switch to high-k gate dielectrics and now remains an integral part to the fabrication of modern integrated circuits. (Choi, Mao et al. 2011; Marchack and Chang 2012; Wilk, Verghese et al. 2013)

Therefore, as shown in this dissertation, a scalable method for synthesizing intrinsic multiferroics as well as nanostructured composite multiferroics by ALD can be realized. The complex metal oxides which multiferroics comprise of are a challenge to synthesize using ALD due to the need to control the film composition and subsequent thermal processing; therefore, the importance of controlling the nanostructure and composition of the as-deposited film is demonstrated with respect to the resulting annealed film. To further expand the work on ALD-enabled materials synthesis, novel composite multiferroics are pursued which utilize the ability for ALD to deposit on 3D high aspect ratio structures and thus create 3D nanostructured multiferroic composites which are anticipated to enhance the magnetoelectric effect. In addition to 3D structures, ALD is also well suited for the synthesis of nanolaminate 2D-2D multiferroic films that maximize the surface area of the interface between the ferroelectric and ferromagnetic layers. Therefore, with these considerations, the study of ALD synthesis for single phase ferroics was conducted using ALD to enable nanostructured composite multiferroic thin films.



### 1.1.1 Current and Future Data Storage Trends

The purpose of this section is to address the various types of state-of-the-art or future non-volatile memories and compare the relevant advantages and disadvantages between one another, first beginning with magnetic hard disk drives (HDD), flash memory, ferroelectric random access memory (FeRAM), magnetic random access memory (MRAM), spin-torque transfer random access memory (STT-RAM), and lastly multiferroic or magnetoelectric memory. This is not a comprehensive list as an in-depth review is not the focus of this work; nonetheless, by comparing these devices, performance benchmarks can help facilitate engineering high-quality devices. Important factors to keep in mind when comparing these devices are: access time, data read/write rate, endurance, data retention, and power consumption as well as the potential for scaling up the storage capacity to cost ratio.(Burr, Kurdi et al. 2008) Burr, et al. has compiled a list of targets for various performance aspects shown below in Table 1.1. Additionally, graphs showing the relative performance ability of memory technologies are shown in Figure 1.4. (Tehrani 2010)

Table 1.1. Target values for various performance aspects of non-volatile memory (Burr, Kurdi et al. 2008)

Access time	50-1,000 ns
Data rate	100 MB/s
Endurance (cycles)	10 <sup>9</sup> -10 <sup>12</sup>
Hard error rate (bits/terabyte)	10 <sup>-4</sup>
Mean time between failures	2 million hours
Data retention	10 years
On power	100 mW
Standby power	1 mW
Cost	< \$5/GB
Annual compound growth rate	35%

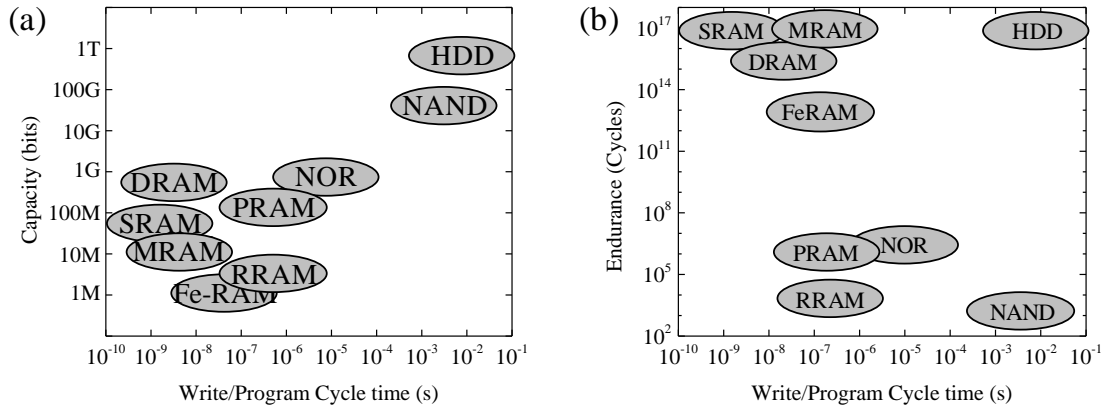


Figure 1.4 Performance of data storage and memory technologies. (a) Capacity versus Write/Program cycle time (b) Endurance cycles versus Write/Program cycle time (Tehrani 2010)

### 1.1.2 Hard Disk Drives

Hard disk drives (HDD) have been ubiquitous with data storage since the introduction of the first HDD by IBM in 1956. (Spaldin 2003) In terms of performance, HDDs have clear advantages and disadvantages. While users must contend with relatively slow access times (3-5 ms), low resistance to shock, high power consumption, noise, and many other negative performance factors stemming from moving parts, HDD remains the best option for data storage in terms of capacity per cost (normally two orders of magnitude higher than solid state drives), complete non-volatility (in the absence of external magnetic fields), and substantially greater endurance with regard to number of read/write cycles and data retention. (Thompson and Best 2000; Burr, Kurdi et al. 2008). Since the strength of HDDs has been primarily the areal density, commonly stated in gigabytes per square inch, most HDD manufacturers have focused on it, leading to a rate of 44% improvement per year. (Wood 2009) Despite the huge gains over time, there is a fundamental boundary for the scaling of HDDs, which is a result of the thermal, or 'superparamagnetic' limit, defined as a minimum magnetic grain size, below which the magnetization is no longer stable. (Richter 2009) Despite this, however, it was estimated that

HDDs could reach 1 terabyte per square inch. (Wood 2000) Nonetheless, the data access time for HDDs is in the order of milliseconds and is a huge bottleneck for data operations which require feeding the processor a substantially higher rate of data. Access times on the order of 1-10 nanoseconds would be more desirable and is feasible for solid-state technologies. (Burr, Kurdi et al. 2008; Freitas and Wilcke 2008) Due to the immense storage density of HDD, it is highly probable that they are not to be replaced until the distant future. However, for very high performance computing needs, the access times of newer solid-state technologies make their development and proliferation a highly attractive goal.

### *1.1.3 Flash Memory*

First introduced in 1984 (Masuoka, Asano et al. 1984), flash memory has become the non-volatile memory of choice for most consumer applications. Originally created to store Basic Input/Output System (BIOS) data, flash has evolved over time into a storage-class memory that is commercially available in solid-state drives offering substantial performance improvements over hard-disk drives at the tradeoff of capacity and cost. Currently there are two major classifications of flash memory depending on their configuration: NOR flash, shown in Figure 1.5 (a), and NAND flash, shown in (b). (Lai 2008) NOR flash technology typically uses a single transistor (1-T) consisting of a highly doped polysilicon floating gate that is sandwiched between the tunneling oxide at the bottom and a charge-blocking oxide at the top.(Hidaka 2009) The architecture of NOR flash allows a fast access rate at up to 100 MB/s making it desirable for embedded systems which favor fast startup time. (Burr, Kurdi et al. 2008) NOR uses channel hot electron injection (CHEI) to program the bit and Fowler-Nordheim tunneling (FNT) to erase leaving NOR flash with a relatively slow write speed of 0.18-0.47 MB/s and erase time of 750-900 ms. (Burr, Kurdi et al. 2008)

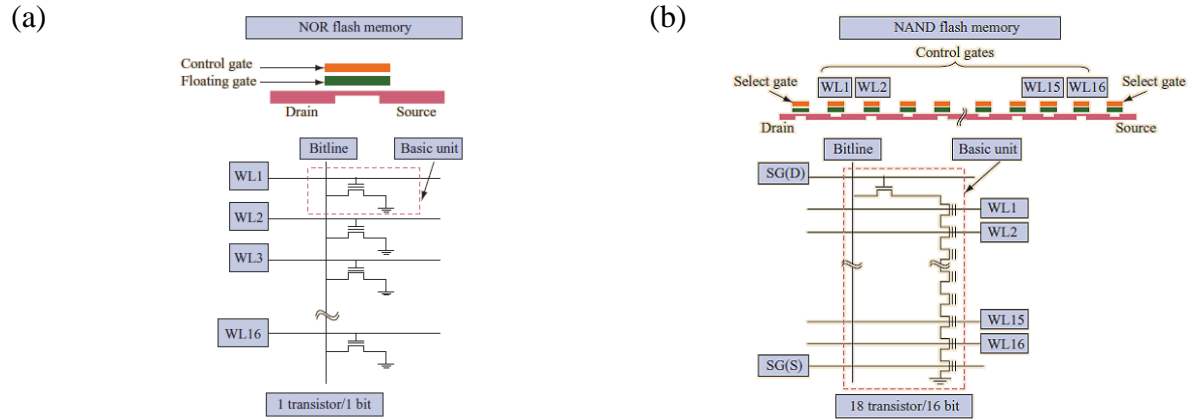


Figure 1.5. (a) NOR flash memory; each cell is individually controlled (b) NAND flash memory; memory is stored in blocks (Lai 2008)

Because of the CHEI write process, the tunneling oxide also faces damage over time with repeated write operations, with an endurance of  $10^4$  cycles. In contrast, NAND architecture flash technology has a slower access rate which ranges from 18-25 MB/s but can be packed more densely allowing higher capacity per square inch. (Burr, Kurdi et al. 2008) The mechanism for data storage utilizes a charge-trapping mechanism such as a silicon-oxide-nitride-oxide-semiconductor (SONOS) structure which uses FNT to both write and erase the cell. Programming a NAND cell has a relatively slow rate; however, unlike NOR, NAND is arranged in blocks of serial bit cells and is able to program several of these cells in parallel giving an overall faster write bandwidth of 8 MB/s while the erase time is still slow at 2 ms. (Burr, Kurdi et al. 2008) Also, NAND technology has better write endurance than NOR with up to  $10^6$  cycles. (Lai 2008) Additionally, charge-storing nano dot floating gates and high- $k$  dielectrics are being implemented to improve endurance. (Kohlstedt, Mustafa et al. 2005)

Typically, data retention for both NAND and NOR flash memory is up to 10 years, though error checking data controllers, originally created for HDD applications, are being now utilized allowing much greater reliability. (Lai 2008) As a result of the aggressive down-scaling of semiconductors, the cost per GB of flash memory has decreased steadily over time with

\$80,000 per GB in 1987 compared to \$10 per GB in 2007. (Lai 2008; Ryu, Kim et al. 2011) Further downscaling of flash memory requires a solution for charge loss in smaller cells, however, efforts are being made to integrate 3D stacking schemes and multilevel cell technology to continue the advancement of flash technology. (Burr, Kurdi et al. 2008; Lai 2008)

#### *1.1.4 Ferroelectric RAM*

Devices which utilize ferroelectric materials to store data are becoming more popular as research continues to solve the underlying processing issues which had previously been problematic. (Sheikholeslami and Gulak 2000; Kohlstedt, Mustafa et al. 2005) Examples of ferroelectric materials include  $\text{Pb}(\text{Zr,Ti})\text{O}_3$  (PZT),  $\text{Pb}(\text{Mg,Nb})\text{O}_3\text{-PbTiO}_3$  (PMN-PT),  $\text{Pb}(\text{Zn,Nb})\text{O}_3\text{-PbTiO}_3$  (PZN-PT),  $\text{BaTiO}_3$  (BTO),  $\text{BiFeO}_3$  (BFO),  $\text{ZnO}$ , and  $\text{SrBi}_2\text{Ta}_2\text{O}_9$  (SBT). (Takashima 2010) Essentially, a ferroelectric memory functions by storing the “ON” and “OFF” states in the two opposing polarizations where the remnant polarization is created by applying a write voltage greater than the coercive electric field in the desired direction. This is explained physically by observing a ferroelectric PZT unit cell with a perovskite structure (shown in Figure 1.6(a)). When a voltage is applied, a Zr or Ti atom is shifted to match the field and it remains in that position after the electric field is turned off. This remnant polarization can be seen in Figure 1.6(b) illustrating a hysteresis loop for a ferroelectric material.

Compared to flash memory, ferroelectric memory has a number of performance tradeoffs which makes the specific application a deciding factor for determining which memory to use. In general, ferroelectric memory has a similar read/write time as flash memory (~10-100 ns), however the energy requirement to write is much lower (~3 orders of magnitude) whereas the read operation takes more energy (~1 order of magnitude). (Sheikholeslami and Gulak 2000).

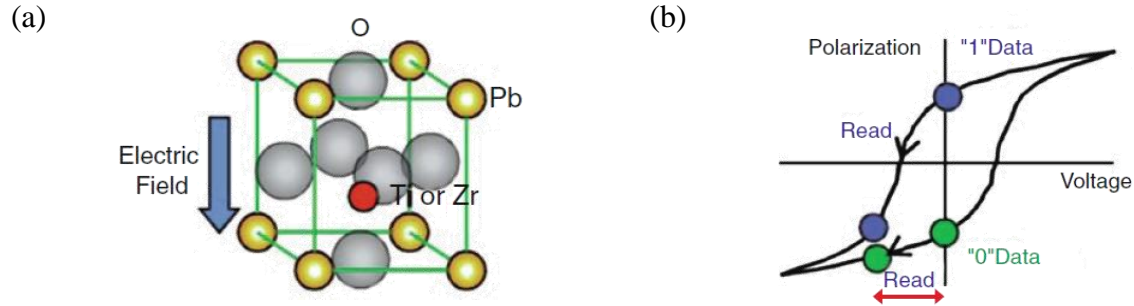


Figure 1.6. (a) Perovskite unit cell of PZT showing shift of Ti or Zr with the application of an electric field. (b) hysteresis loop for a ferroelectric material showing polarization vs. applied voltage (Takashima 2010)

For FeRAM, the read operation is destructive meaning that the data must be rewritten when read. This is due to the fact that after being read, a cell has a certain polarization regardless of the previous data state (with the one exception being 1T FeFET memory). Despite this, ferroelectric memory has better write endurance compared to flash memory with a  $\sim 10^{13}$  cycle lifetime. (Burr, Kurdi et al. 2008; Takashima 2010) These factors together make ferroelectric memory more favorable to applications in which the program operation needs to be faster and more efficient, such as in digital cameras, whereas flash memory is more suited to applications in which data is programmed a single time and read a very large number of times such as in application files. (Sheikholeslami and Gulak 2000)

With regards to storage density, the amount of data in a fixed area is dependent on the architecture of the ferroelectric memory, with each type having their own respective tradeoffs. (Kohlstedt, Mustafa et al. 2005) 2T-2C configurations are more reliable since the data is stored in the two capacitors which are always opposing one another and has a similar access time, the disadvantage obviously lies in the cell area which is twice that of 1T-1C and limits the storage capacity. 1T-1C is the most common and strikes a balance between reliability, speed, and density. Another cell architecture is known as chain FeRAM in which a cell is comprised of a

transistor in parallel with a capacitor and cells are connected in series. The chaining allows for a higher storage density at the cost of access time. Lastly, the 1T or FeFET configuration is easily the best in terms of storage density as a cell is comprised only of a single ferroelectric FET and readout is accomplished non-destructively which is very important in increasing the read/write endurance. However, the drawback is that the data retention time is much shorter compared to the other types and has been reported to be approximately only 3 days. (Hoffman, Pan et al. 2010) For this reason, 1T FeFET memory is recommended for DRAM-like applications as opposed to bulk data storage.

Future efforts to increase the storage density must overcome challenges of decreasing the coercive polarization voltage and thus the power consumption; unfortunately, most research points to the fact that as ferroelectric film thickness decreases, the coercive voltage usually increases. (Kohlstedt, Mustafa et al. 2005) Also, 3-D capacitors have been proposed in order to continue downscaling while retaining enough capacitance to ensure a cell that can be read without error. A geometry that can increase total capacitor surface area while limiting the top-down cross-section is most desired, however, engineering the nanostructure is difficult because it requires highly conformal deposition and high uniformity to maintain a homogenous ferroelectric polarization. (Cross 2004)

#### *1.1.5 Magnetoresistive RAM and Spin-Torque Transfer RAM*

In addition to hard disk drives, magnetic materials have also been used for data storage in the form of magnetoresistive random access memory (MRAM), which is a part of the spintronics field. (Slaughter 2009) The mechanism for MRAM exploits the fact that certain magnetic materials have different resistances depending on the state of the magnetization; therefore the

resistance can be measured at high and low states which correspond to the 1 and 0 digital states. Performance of the MRAM is typically measured as a percentage in change between the high and low states known as the magnetoresistive ratio (MR):

$$MR = \frac{R_{high} - R_{low}}{R_{low}} \quad \text{Eq. (1.1)}$$

Initial attempts at creating MRAM used anisotropic magnetoresistance (AMR) which was the difference in resistance between states that had different relative magnetization orientations.(Baugh, Cullom et al. 1982; Schwee, Hunter et al. 1982; Pohm, Huang et al. 1988) AMR yielded MR values at about 2.0-2.5%. Later, the giant magnetoresistance (GMR) effect was discovered for structured thin metal films (Baibich, Broto et al. 1988) and MRAM utilizing these properties demonstrated improved MR values of approximately 4-8%.(Daughton 1992; Tehrani, Chen et al. 1996; Tehrani, Chen et al. 1999) Nonetheless, the metallic films inherently had a low resistance and therefore the signal ratios were more difficult to detect. More recently, room temperature magnetic tunnel junctions (Moodera, Kinder et al. 1995) were developed into MRAM. Magnetic tunnel junctions (MTJ) utilize two parallel ferromagnetic layers sandwiching a tunneling barrier as shown in Figure 1.7.(Slaughter 2009) One layer is designed to have a fixed direction while the second layer is where the data is written to, which is typically switched via a current using inductive magnetization or by spin torque transfer. The resistance of the device depends on whether the parallel ferromagnetic layers have a parallel magnetization or an antiparallel one; parallel magnetizations have a lower resistance because the majority band tunneling electrons can enter the majority band on the opposite layer while antiparallel magnetizations force majority band electrons to enter the minority band. Typical materials used for the MTJ stacks are shown in Figure 1.7(b).



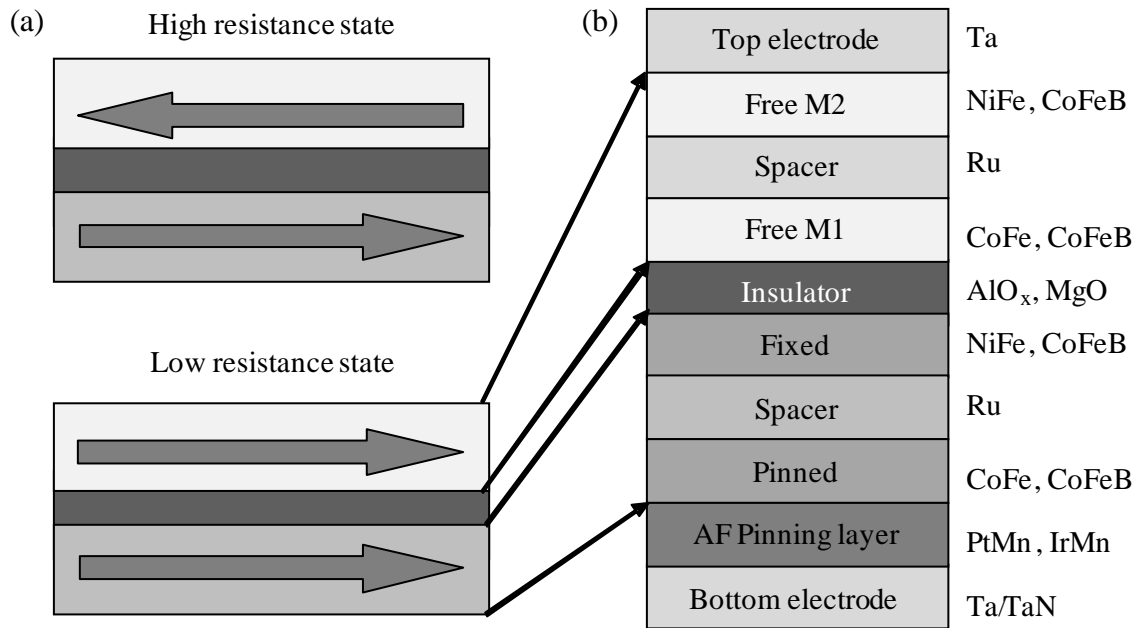


Figure 1.7. a.) Schematic for magnetic tunnel junction (MTJ); antiparallel spins (top) have a higher resistance than parallel spins (bottom) b.) Typical materials used in MTJ stack (Slaughter 2009)

The fixed layers are pinned by using exchange-bias coupling with an antiferromagnetic material and prevent magnetic spin reversal within the magnetic fields generated during device operation. MTJ devices have over time allowed a substantial increase in room temperature MR values beginning with 11.8% (Moodera, Kinder et al. 1995) up to 472%. (Lee, Hayakawa et al. 2007) MRAM is able to be integrated into a semiconductor platform but the overlying principle of its operation offers different advantages and disadvantages when compared to other types of solid-state media. (Slaughter 2009) Magnetoresistive memory is considered in theory to be perfectly non-volatile because the data is magnetically stored, and thus charge leakage is a non-issue. Additionally, read operations are non-destructive because they do not require an application of a magnetic field. Lastly, write operations do not perturb atoms and simply flips electronic spins, therefore the endurance for the magnetic material is not a concern. Disadvantages include the high currents (~1 mA) required to generate the magnetic fields to

write data and the “cross-talk” between cells, where the magnetization of cells can alter or reverse the magnetizations of neighboring cells if they are too close, thereby limiting the memory density. (Burr, Kurdi et al. 2008)

In recent developments, new modifications have been proposed and/or demonstrated to further the scalability of MRAM including the use of the spin-torque transfer (STT) effect to directly switch the writing layer as opposed to using induction (Miura, Kawahara et al. 2007), thermally assisted switching (Prejbeanu, Kula et al. 2004), and more recently a 3-D racetrack memory which stores bits in a series of magnetic domain walls along a loop that is controlled using the STT effect. (Parkin, Hayashi et al. 2008). So far, STT-RAM has been extremely promising since it uses spin-polarized current which is more easily scalable to smaller devices compared to conventional MRAM devices. (Zhu and Kang 2014) In the future, electric field controlled MTJ devices, or magnetoelectric RAM, can even further reduce the switching energy needed. (Khalili and Wang 2014)

#### *1.1.6 Magnetoelectric RAM*

As of now, multiferroic material has not been integrated into memory technology on a mass scale. However, as a result of the simultaneous ferroelectric and ferromagnetic properties, multiferroic material has a promising future as the magnetoelectric coupling effects are quite attractive. In one example, it is proposed that a magnetoelectric RAM (MERAM) utilizing a structure similar to MRAM, however, the data storing "free" ferromagnetic layer is programmed using interfacial exchange coupling with a multiferroic layer as shown in Figure 1.8. (Bibes and Barthelemy 2008)

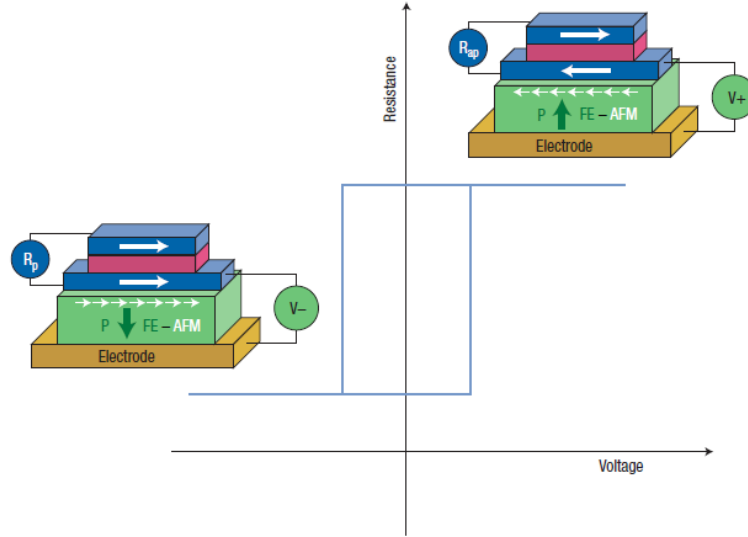


Figure 1.8. Schematic diagram of potential multiferroic memory which resembles MRAM for the storage layer but is controlled by a ferroelectric layer (Bibes and Barthelemy 2008)

The multiferroic layer would be switched using a voltage causing the interfacial exchange coupling to switch the adjacent ferromagnetic layer, thus avoiding the high current necessary to switch MRAM devices, and uses less power when compared to STT-RAM. So far, a few examples of electric field assisted writing have been demonstrated. (Alzate, Amiri et al. 2012; Wang, Zhang et al. 2014) These devices are characterized by a reversible switching of the magnetic easy-axis for the free layer of an MTJ by applying an electric field. When the magnetic anisotropy of the free layer is switched with respect to the fixed layer, a change in the magnetoresistance can be realized.

Another possibility lies in the multiple states that a multiferroic material can carry considering that the electronic states and the magnetic states can each be poled separately. As a result, four-state devices (Gajek, Bibes et al. 2007) have been demonstrated and eight-state devices have been proposed. (Yang, Tang et al. 2007) Using multiple-state logic could potentially increase the storage density by encoding data using quaternary information.

Nonetheless, despite the array of promising features for multiferroic materials, there are several challenges that must first be overcome, namely the fact that there are few materials which exhibit multiferroic properties and only one discovered material ( $\text{BiFeO}_3$ ) which displays these properties at room temperature. (Bibes and Barthelemy 2008) Alternatively, the combination of ferromagnetic and ferroelectric materials to form composite multiferroics could potentially meet the requirements of multiferroic memory with greater performance at room-temperature than that of single-phase multiferroics. (Nan, Bichurin et al. 2008) In the next sections, multiferroic materials and the growth of multiferroic materials is reviewed. Table 1.2 summarizes the types of non-volatile memory devices that were discussed in the previous section.

Table 1.2 Summary of memory devices and performance parameters (Kryder and Chang Soo 2009; ITRS 2011; Wang, Alzate et al. 2013)

	HDD	DRAM	NAND Flash	FeRAM	MRAM	STT- RAM	ME-RAM
Maturity	Product	Product	Product	Product	Product	Product	Research
Density	400 Gb/in	8 Gb/chip	64 Gb/chip	128 Mb/chip	32 Mb/chip	2 Mb/chip	NA
Cell Size	$(2/3)\text{F}^2$	$6\text{F}^2$	$4\text{F}^2$	$6\text{F}^2$	$20\text{F}^2$	$4\text{F}^2$	NA
Program Energy/bit	NA	5 fJ	0.2 pJ	30 fJ	2.5 pJ	0.02 pJ	$\approx$ Fe-RAM
Access Time (W/R)	9.5/8.5ms	10/10ns	1/0.1ms	50/75ns	65/40ns	35/35ns	$\approx$ MRAM
Endurance/ Retention	NA	$10^{16}/64\text{ms}$	$10^4/10\text{yr}$	$10^{14}/10\text{yr}$	$10^{16}/10\text{yr}$	$10^{16}/10\text{yr}$	$\approx$ MRAM

## 1.2 Multiferroic Materials

Using an electrical field to induce a change in a state variable underlines the operation of complementary metal oxide semiconductor (CMOS) field effect transistor, which has been pushed to near its physical limit with the upcoming production of 14nm devices. While there remains some room to further extend the charge-based CMOS, alternative state variables that can be controlled via electrical field hold great potential to enable new devices and architectures

beyond CMOS. One such alternative state variable is the electron spin, which manifests itself as magnetism when it is ordered. To access this variable state via electric field, the Heckmann diagram shown in Figure 1.3 provides a guide to understand the interplay between the external forces (Newnham 2004), such as stress ( $\sigma$ ), electric (E) and magnetic (H) fields with the associated material properties, namely, strain ( $\epsilon$ ), electric polarization (P), and magnetization (M). There are coupling coefficients between the material properties and corresponding external forces, e.g. electric susceptibility ( $\chi_E$ ), magnetic susceptibility ( $\chi_M$ ), and compliance tensor (S). Since the spontaneous polarization may be switched by external fields as shown by the hysteresis curves in Figure 1.3, they can be used as state variables in future devices.

In a quantitative manner, the Landau theory expresses the free energy  $F$  of the system as a function of applied electric field  $E$  and applied magnetic field  $H$ :

$$F(E, H) = F_0 - P_i^S E_i - M_i^S H_i - \frac{1}{2} \epsilon_0 \epsilon_{ij} E_i E_j - \frac{1}{2} \mu_0 \mu_{ij} H_i H_j - \alpha_{ij} E_i H_j - \frac{1}{2} \beta_{ijk} E_i H_j H_k - \frac{1}{2} \gamma_{ijk} H_i E_j E_k \dots \quad \text{Eq. (1.2)}$$

The partial derivatives of Eq. (1.2) with respect to electric field and magnetic field leads to the polarization:

$$P_i(E, H) = -\frac{\partial F}{\partial E_i} = P_i^S + \epsilon_0 \epsilon_{ij} E_j + \alpha_{ij} H_j + \frac{1}{2} \beta_{ijk} H_i H_j + \gamma_{ijk} H_i E_j \dots \quad \text{Eq. (1.3)}$$

and the magnetization:

$$M_i(E, H) = -\frac{\partial F}{\partial H_i} = M_i^S + \mu_0 \mu_{ij} H_j + \alpha_{ij} E_j + \beta_{ijk} E_i H_j + \frac{1}{2} \gamma_{ijk} E_j E_k \dots \quad \text{Eq. (1.4)}$$

where  $P_i^S$  and  $M_i^S$  denote the spontaneous polarization and magnetization for the  $i$ th component;  $\epsilon_{ij}$  and  $\mu_{ij}$  are the electric and magnetic susceptibilities,  $\beta_{ijk}$  and  $\gamma_{ijk}$  denote the higher-order magnetoelectric effects while  $\alpha_{ij}$  is the  $ij^{th}$  component of tensor  $\alpha$  that represents the linear

magnetoelectric effect. These equations explain how ferroelastic, ferroelectric, or ferromagnetic materials exhibit spontaneous strain, polarization, or magnetization, which can be switched by applied stress, electric field, or magnetic field, respectively. In addition, electric polarization can be induced by an external magnetic field, or vice versa when interactions between two ferroic orders take place thorough magnetoelectric coupling as denoted by  $\alpha$ .

For the vast majority of solid-state memory technologies currently being produced such as SRAM, DRAM, and Flash, capacitive charge is used as the control parameter to differentiate between the on and off states. In order to meet the demand for future ultra-low power electronics, new device structures for non-volatile memory have been proposed for novel material systems utilizing different control parameters such as magnetization (Nikonov and Young 2012). Amongst the possible coupling interactions shown in the Heckmann diagram in Figure 1.3, the magnetoelectric effect is the most interesting one as far as electrical field control of state variables is concerned. The magnetoelectric effect was first predicted by Curie in 1894 (Curie 1894), while the term magnetoelectric was coined by Debye in 1926 (Debye 1926). Later in 1994, Schmid defined the term multiferroics to highlight the various ferroic coupling parameters present in these materials (Schmid 1994). So far, more than 100 compounds that exhibit the magnetoelectric effect have been discovered and reported (Fiebig 2005; Spaldin and Fiebig 2005; Eerenstein, Mathur et al. 2006; Tokura 2006; Cheong and Mostovoy 2007; Ramesh and Spaldin 2007), yet their application has been limited because such coupling are typically weak especially at or above room temperature.

The lack of practical application of multiferroic materials originated from the physical contradiction of magnetism and conventional ferroelectricity, as explained in by Spaldin (née Hill) (Hill 2000). For example, in ferroelectric insulators, polarization is represented by a polar

vector and the metal ions usually have an empty  $d$ -shell. In a ferromagnetic conductor, magnetization represented by an axial vector and the metal ions has occupancy in the  $d$ -shell. In terms of symmetry consideration as shown in Figure 1.9, ferroelectricity can occur by the broken spatial inversion symmetry while the time reversal symmetry is invariant.

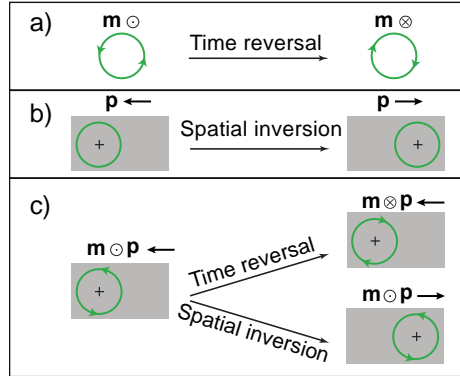


Figure 1.9. Schematic diagram for symmetry considerations in (a) ferromagnets where time reversal symmetry switches the charge orbit, i.e. magnetic momentum  $m$ , (b) ferroelectric where spatial inversion reverses the dipole moment  $p$ , and (c) multiferroic that are both ferromagnetic and ferroelectric with time reversal and spatial inversion symmetry broken. (Eerenstein, Mathur et al. 2006).

In contrast, the time reversal symmetry is broken for magnetism and spin order, while the spatial inversion symmetry is invariant. In magnetoelectric multiferroics, time reversal symmetry and spatial inversion symmetry are simultaneously broken. For these reasons, there are very few ferroelectrics that exhibit magnetic order or significant coupling and vice versa. In fact, only 13-point groups allow the simultaneous appearance of spontaneous polarization and magnetization among the 233 magnetic point groups (Wang, Liu et al. 2009) and some compounds belonging to these 13-point groups do not show any multiferroicity.

From Figure 1.9, it is clear that ferroelectricity and ferromagnetism have incompatible origins. Ferroelectric perovskite oxides need B-site transition metal ions with an empty  $d$ -shell to hybridize with the surrounding anions, while mostly partially filled  $d$ - or  $f$ - shells of transition metal or rare-earth ions have a corresponding localized spin or magnetic moment (Cohen 1992;

Hill 2000; Khomskii 2001; Khomskii 2006). This point is what makes intrinsic and single-phase multiferroic materials so rare. Table 1.3 classifies these materials based on their saturation polarizations and coercive electric fields corresponding to their origin of ferroelectricity: induced by lone pairs, geometric distortion, or spiral spin-order structures. The magnetic properties of these materials are also presented when possible. First, ferroelectricity and ferromagnetism are reviewed separately in 1.2.1 and 1.2.2 respectively, then materials which simultaneously contain both aspects are discussed both using single phase in 1.2.4 and composite configurations in 1.2.5.

Table 1.3. The classification of single-phase multiferroics and their material properties.

Types	Origins	Materials	$P_s$ ( $\mu\text{C}/\text{cm}^2$ )	$E_c$ (kV/cm)	$M_s$ (emu/cm <sup>3</sup> )	$H_c$ (Oe)	Reference
Single-phase Type I	Lone pair electrons	BiFeO <sub>3</sub>	55	20	150	200	(Wang, Neaton et al. 2003)
	Geometric ferroelectricity	BiMnO <sub>3</sub>					(Maeda, Yshimura et al. 2006)
Single-phase Type II	Spiral spin-order-induced	YMnO <sub>3</sub>	2.5	60	-	-	(Lee, Murugavel et al. 2006)
		TbMnO <sub>3</sub>	7	500	-	-	(Lee, Murugavel et al. 2006)
		DyMnO <sub>3</sub>					

### 1.2.1 Ferroelectric Materials

Electronic ordering in materials, known as ferroelectricity, was first discovered and studied in Rochelle salt ( $\text{KNa}(\text{C}_4\text{H}_4\text{O}_6) \cdot 4\text{H}_2\text{O}$ ). (Pockels 1894) For all ferroelectric materials, there exists a transition temperature known as the Curie temperature  $T_C$ . (Hill 2000) Above  $T_C$ , the material acts like a dielectric material in which the polarization is sustained only by the field. Below  $T_C$ , the polarization is stable enough to leave a remnant polarization  $P_r$  when the field is turned off. As a result, ferroelectric materials below  $T_C$  exhibit a hysteretic response to applied electric fields as shown in Figure 1.10. The electric field required to return a ferroelectric from the remnant polarization to zero polarization is known as the coercive field  $E_C$  also shown in Figure 1.10.



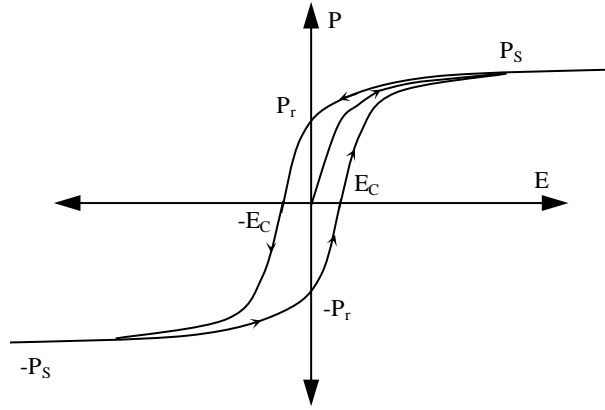


Figure 1.10. Ferroelectric hysteresis loop showing Polarization vs. Electric field

As discussed earlier in this work,  $P_r$  is a property that has been exploited in solid-state memory applications in ferroelectric RAM. Commonly studied ferroelectric materials for ferroelectric RAM applications include  $\text{Pb}(\text{Zr,Ti})\text{O}_3$  (PZT),  $\text{SrBi}_2\text{Ta}_2\text{O}_9$  (SBT),  $(\text{BiLa})_4\text{Ti}_3\text{O}_{12}$ ,  $\text{BaMgF}_4$ ,  $\text{Bi}_4\text{Ti}_3\text{O}_{12}$ , and  $\text{Pb}_5\text{Ge}_3\text{O}_{11}$ . (Setter, Damjanovic et al. 2006) Due to symmetry considerations, ferroelectric materials are also necessarily piezoelectric as well as pyroelectric, but not necessarily the reverse. Nonetheless, the piezoelectric properties of ferroelectrics are exploited in the creation of composite multiferroics as explained in section 1.2.5. Microscopic mechanisms controlling ferroelectricity have been studied much more recently with the advent of density functional theory calculations. (Cohen and Krakauer 1992; Hill 2000) Thus, the majority of theoretical research on ferroelectrics has been focused on  $\text{ABO}_3$  perovskite structure shown in Figure 1.11(a).

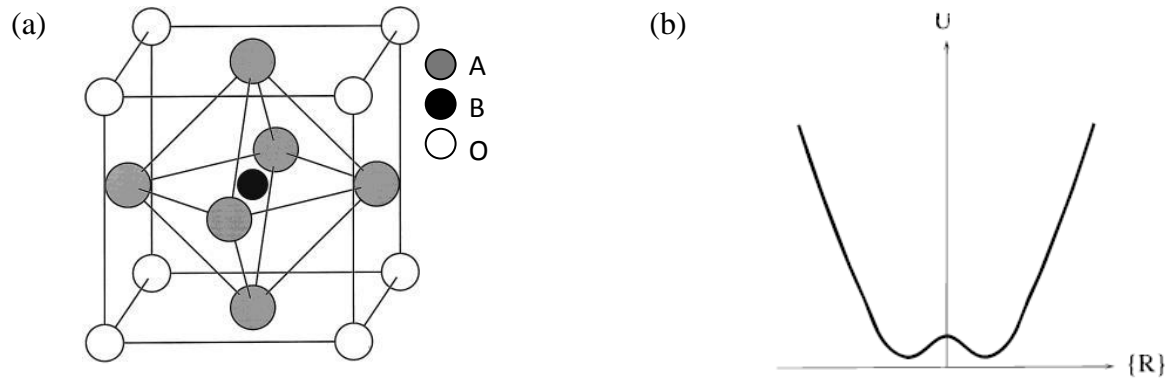


Figure 1.11 (a) Perovskite structure of ferroelectric  $\text{Pb}(\text{Zr,Ti})\text{O}_3$  showing  $\text{ABO}_3$  with Pb at the corners and Zr or Ti in the center surrounded by O octahedron. In the polarized state, the Zr or Ti ion is moved relative to the O atoms (b) Double potential well showing two preferred states that are off-center (Hill 2000)

Below  $T_C$ , the smaller B ion, which is surrounded by six oxygen atoms forming an octahedron, has a more energetically stable asymmetric position that is created from the double-well potential based on density functional theory as shown in Figure 1.11 (b). (Cohen and Krakauer 1992; Hill 2000) This asymmetry is what enables ferroelectric polarization, as the B ion is now offset relative to the center position within the octahedron.

Cohen and Krakauer's study compared the ferroelectric properties between  $\text{PbTiO}_3$  and  $\text{BaTiO}_3$ . Both materials have Ti as the center B ion and as a result Ti 3d-O 2p hybridization is required to stabilize the ferroelectric distortion. However, the A-O interactions are quite different, with Ba-O bonding being mostly ionic whereas Pb-O bonding has Pb 6s - O 2p hybridization from the lone-pair of Pb which dominates the polarizability. According to Spaldin (née Hill), the  $\text{Ti}^{4+}$  ion has a  $d^0$  configuration which makes it more prone to hybridization with O 2p ions. This  $d^0$  B cation is also commonly found in other ferroelectric materials with  $\text{Zr}^{4+}$  and  $\text{Nb}^{5+}$ . By comparison, the presence of  $d^n$ -electrons with  $n > 0$  is a necessity for magnetic moments. It was later shown that, although  $d^0$  cations are common for ferroelectrics, it does not preclude magnetic order due to other mechanisms such as spiral spin order (Mostovoy 2006; Sergienko, Scedilen et al. 2006), magnetic exchange striction (Cheong and Mostovoy 2007), or

charge order (Efremov, van den Brink et al. 2004) which allow multiferroic materials to be feasible.

### 1.2.2 Ferromagnetic Materials

The origin for magnetic moment is quantum mechanical in nature. Electrons with angular momentum and electron spin contribute to the overall magnetic moment. (Spaldin 2003) For non-magnetic materials, either the electrons in the individual atoms cancel out the magnetic moment due to a symmetric angular momentum e.g. diamagnetic materials or magnetic moments are randomized and cancel each other out e.g. paramagnetic materials. However, for magnetic materials, a Curie transition temperature  $T_C$  for ferromagnetic materials or Néel transition temperature  $T_N$  for antiferromagnetic materials exist where above  $T_C$  ( $T_N$ ), the material acts like a paramagnet, but below  $T_C$  ( $T_N$ ), the material's spins align parallel (antiparallel) to one another. All materials exhibit some form of magnetization  $\mathbf{M}$  (units emu/cm<sup>3</sup> in cgs, A/m in SI) with or without an applied magnetic field  $\mathbf{H}$  (units Oe in cgs, A/m in SI). The magnetic induction  $\mathbf{B}$  (units gauss = 10<sup>-4</sup> Tesla) is shown in equation 1.5 and is the material's response to an applied magnetic field.  $\mu_0$  (units Weber/ A m = Henry/m) is the permeability of free space.

$$\begin{aligned} B &= H + 4\pi M \text{ in cgs units} \\ B &= \mu_0 H + M \text{ in mks units} \end{aligned} \tag{Eq. (1.5)}$$

Depending on the type of material (paramagnetic, diamagnetic, ferromagnetic, or antiferromagnetic) the magnitude and sign of the induced magnetic flux differs greatly corresponding to the magnetic susceptibility  $\chi$  as defined by Eq. (1.6).

$$\chi = \frac{M}{H} \tag{Eq. (1.6)}$$

In magnetically ordered materials, the moments are sometimes aligned completely parallel with one another forming ferromagnets, while other spin orientations are antiparallel and depending on the relative strengths of the antiparallel moments can either be antiferromagnets or ferrimagnets. Figure 1.12 shows schematic diagrams for paramagnetic, ferromagnetic, antiferromagnetic, and ferrimagnetic materials. Much like ferroelectric materials, ferromagnetic and ferrimagnetic materials exhibit a hysteresis loop when a field is applied as shown in Figure 1.13. Starting from a paramagnetic state with zero field applied, the material approaches a saturated magnetization  $M_s$  once the field is large enough. When the field is reversed, the magnetization does not follow along the same path reversibly due to the remaining magnetization, and at  $H = 0$ , a remnant magnetization  $M_r$  remains. The amount of field required to reduce the magnetization back to zero is known as the coercive field  $H_c$ .

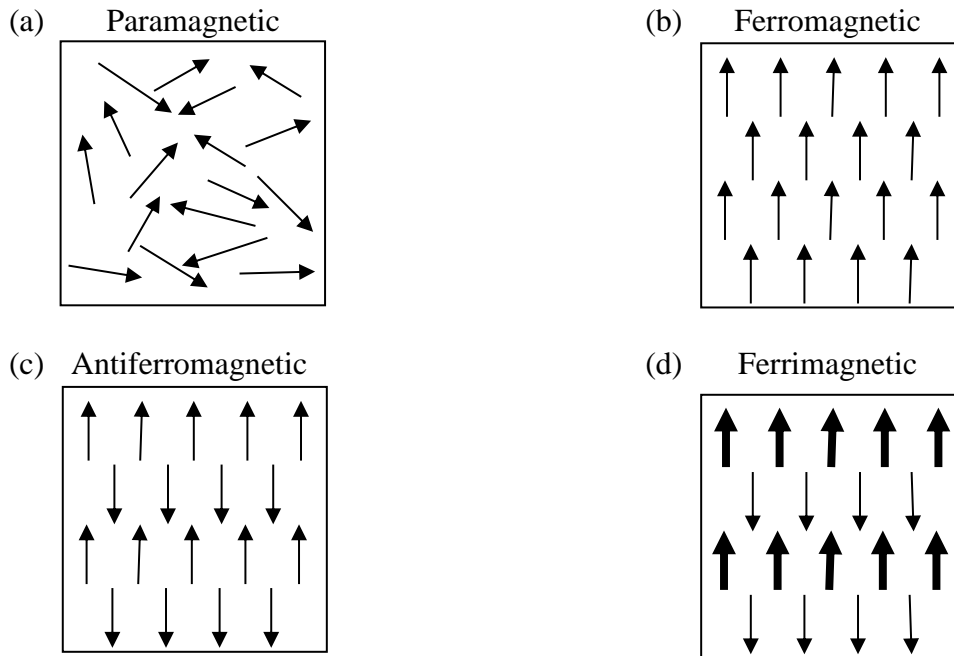


Figure 1.12 Schematic diagrams for types of magnetic ordering (a) Paramagnetic, (b) ferromagnetic, (c) antiferromagnetic, (d) ferrimagnetic materials

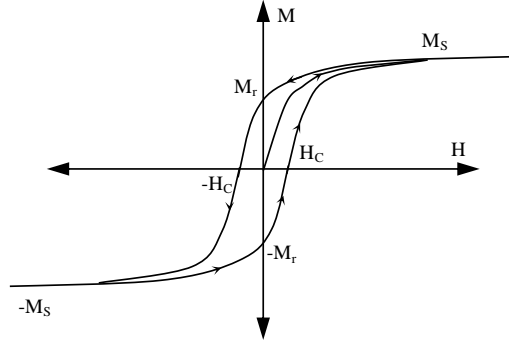


Figure 1.13. M vs. H hysteresis loop for a ferromagnetic or ferrimagnetic material

Two phenomenological theories exist to explain the magnetization responses that ferromagnetic materials have with external fields; the first is called the Curie-Weiss localized moment theory and the second is the Stoner band theory of ferromagnetism. Weiss (Weiss 1907) theorized that a "molecular field" exists in which magnetic moments align parallel with one another as a result of this field. Due to quantum mechanics, it can now be explained that exchange energy causes states in which electrons with the same spin (i.e. same magnetic moment) are more energetically favorable than those having antiparallel spins, thus propagating the magnetic ordering. (Hill 2000) At temperatures below  $T_C$ , the molecular field is able to counteract the thermal energy  $\kappa T$  of electrons and retain a magnetization without an external magnetic field. When the thermal energy is high enough to overcome the molecular field, the material becomes paramagnetic and the magnetic moments are randomized in the absence of a magnetic field. Additionally, the Curie-Weiss law for the temperature dependence for the magnetic susceptibility  $\chi$ , shown in Eq. (1.7), is also explained by this theory.

$$\chi(T) = \frac{C}{T - T_c} \quad \text{Eq. (1.7)}$$

The Curie-Weiss theory, however, fails to predict the quantitative magnetic moment per atom in some cases but mostly ferromagnetic metals. (Hill 2000) Reasons for this are two-fold:

the first is that the Weiss localized-moment theory assumes that the magnetic dipole moment in ferromagnetic and paramagnetic states are the same, which is not experimentally observed; the second is the theory predicts that the bulk magnetic dipole moment per atom should be proportional to the integer number of electrons which also is not observed.

The Stoner band theory was developed in order to explain the discrepancies between the Curie-Weiss theory and experimentally observed results. (Stoner 1933) Similar to the Weiss theory, the exchange energy can be considered to be the driving force of Stoner band theory in which electrons with parallel spins have the lower energy configuration. (Hill 2000) Instead of discretely picking the more favorable energy levels, however, the Stoner band theory also takes into consideration quantum mechanical concepts such as the density of states and the Fermi level that did not exist when Weiss created his theory. The exchange energy can be visualized in Figure 1.14 showing the density of states for the 3d and 4s bands with the downward spins being shifted to higher energy.

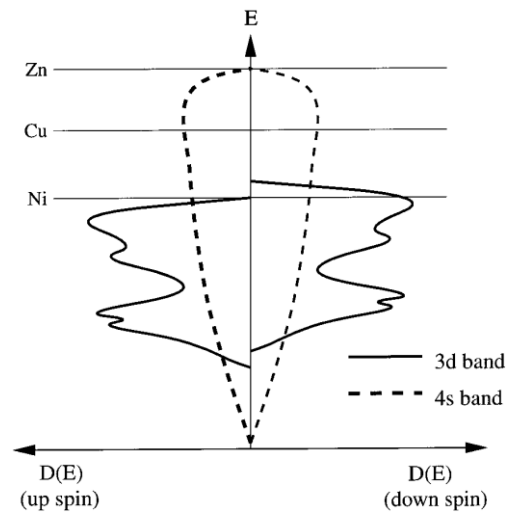


Figure 1.14. 3d and 4s up-and down-spin densities of states for first row transition metals; the right side includes exchange interactions for antiparallel spin configurations. Fermi levels are shown for Ni, Cu, and Zn (Hill 2000)

It is then shown that, for ions whose Fermi energy lies within the overlapping area between the 3d and 4s bands such as Ni, the downward spin 3d band is energetically favorable and only enters the 4s band if there is sufficient thermal energy to widen the Fermi distribution function. Thus, a magnetic dipole is formed due to the asymmetry in electron spin. On the other hand, for ions in which the Fermi level lies above the overlapping region such as Cu and Zr, the 3d band is completely occupied and thus there is no ferromagnetism because the 4s band lacks exchange interactions.

### *1.2.3 Exchange Coupling*

Exchange bias is a phenomenon which originates from the exchange interaction at the interface between a ferro/ferrimagnetic (FM) material and an antiferromagnetic (AFM) material and is characterized by a shift  $H_E$ , or bias, of the  $M$  vs.  $H$  hysteresis loop along the magnetic field axis ( $H$ ) as depicted in Figure 1.15. Currently the most common applications for nanostructured exchange biased systems is in the area of spintronics for which pinned FM layers in spin valves and magnetic tunnel junctions require exchange coupling to AFM materials in order to prevent undesired spin reversal as was previously shown in Figure 1.7. However, if the state of the FM material can be switched via electric field by coupling to it a multiferroic ferroelectric (FE)-AFM material, it may lead to the development of spintronic devices with substantially lower power consumption. In this case, the exchange coupled system is controlled using the magnetoelectric coupling effect of the AFM-FE material where applying an electric field changes the direction of the AFM spins and by extension the FM material through exchange coupling, thus permitting electric field control of magnetism.(Binek, Hochstrat et al. 2005) One such AFM/FE + FM system is  $\text{BiFeO}_3$  and  $\text{CoFe}_2\text{O}_4$ , materials which were the focus of this work, which therefore merited a brief discussion of the exchange bias effect.

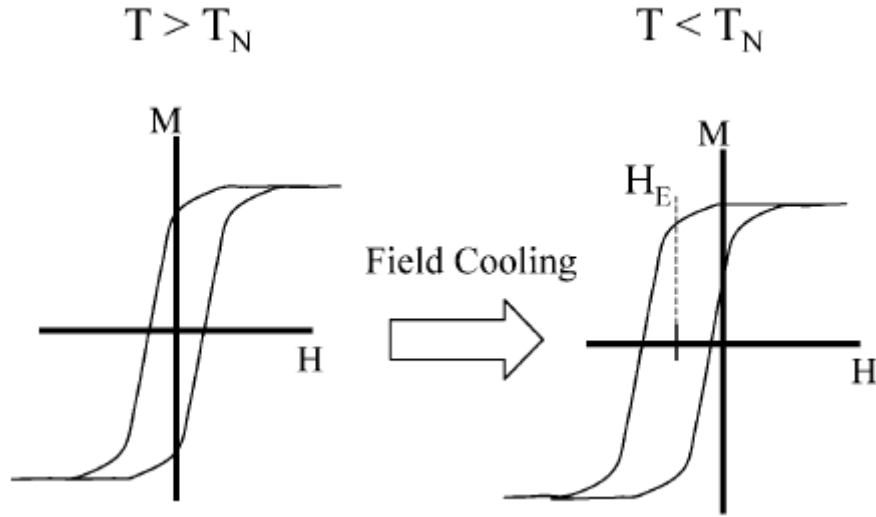


Figure 1.15. Schematic representation of hysteresis loop shift caused by exchange bias effect (Nogués, Sort et al. 2005)

Demonstrating the exchange bias effect is typically done by field cooling a composite AFM-FM system starting from a temperature  $T_S$  such that  $T_N < T_S < T_C$ , where  $T_N$  is the AFM Néel temperature and  $T_C$  is the FM Curie temperature, to a point below  $T_N$ . Above  $T_N$ , the AFM spins are isotropic but after it reaches the ordering temperature they align parallel to the field. A simple intuitive description for the phenomenon, as introduced by Meiklejohn and Bean, is explained by the pinning of the AFM spins at the interface towards the direction of the applied field to match the spins of the FM during the field cooling process. (Meiklejohn and Bean 1956; Meiklejohn and Bean 1957; Meiklejohn 1962) When measuring the hysteresis of the sample following the field cooling, the pinned spins of the AFM impose a torque upon the spins of the FM, causing spin reversal to require more energy in the direction antiparallel to the AFM spins and less energy to return to the parallel direction; the overall result is that the hysteresis loop is shifted, or biased, along the field axis in the opposite sign as the field that was applied during the cooling. This shift of the hysteresis loop is denoted as  $H_E$ . The resulting derived phenomenological model by Meiklejohn and Bean is shown in Eq. (1.8):



$$\mu_0 H_E = -\frac{JS_{AFM}S_{FM}}{M_{FM}t_{FM}} \quad \text{Eq. (1.8)}$$

where  $\mu_0$  is the magnetic permeability of vacuum,  $H_E$  is the magnitude of the exchange bias,  $J$  is the phenomenological coupling coefficient between the FM and AFM layers,  $S_{AFM}$  and  $S_{FM}$  are the interface magnetic moments for the AFM and FM layers respectively,  $M_{FM}$  is the magnetization of the FM layer and  $t_{FM}$  is the thickness of the FM layer. The physical basis of the interaction, however, between the AFM and FM layers and the subsequent exchange bias effect can be much more complex and can depend on a variety of factors including but not limited to the choice of FM-AFM combination, the extent of AFM spin compensation at the interface, and the size and structure of the AFM domains among other microscopic effects which can lead to major challenges in attempting to model the magnitude of the exchange bias effect.

Within the context of exploiting magnetoelectric multiferroic materials in exchange bias, recent research progress has demonstrated the ability to alter the exchange bias effect using an electric field when using a multiferroic FE-AFM material in combination with a FM material. (Borisov, Hochstrat et al. 2005; Laukhin, Skumryev et al. 2006; Wu, Cybart et al. 2010) In the work of Wu, et al., the direction of exchange bias was switched reversibly by applying voltage to the FE using a combination of FE-AFM  $\text{BiFeO}_3$  and FM  $\text{La}_{0.7}\text{Sr}_{0.3}\text{MnO}_3$ .

#### 1.2.4 Single-phase Multiferroics

The existence of  $(ns)^2$  (lone pair) ions in  $\text{ABO}_3$  metal oxides favors breaking the spatial inversion symmetry, thus induce the ferroelectric order. In  $\text{BiFeO}_3$ , and probably in  $\text{BiMnO}_3$  and  $\text{PbVO}_3$ ,  $\text{Bi}^{3+}$  and  $\text{Pb}^{2+}$  lone pairs locating at A-sites play an important role in the origin of ferroelectricity (Trinquier and Hoffmann 1984; Watson, Parker et al. 1999; Seshadri and Hill 2001), while magnetic transition metal ions located at B-sites of the perovskite structure. Thus,

the combination of these ions in the perovskite structure induces ferroelectricity and magnetism simultaneously. Recent experiments of BiFeO<sub>3</sub> and BiMnO<sub>3</sub> show a magnetoelectric coupling of mutual control of ferroelectric domains and magnetic domains (Kimura, Kawamoto et al. 2003; Wang, Neaton et al. 2003). Therefore, it is meaningful to address these two materials.

The ferroelectricity of BiMnO<sub>3</sub> and BiFeO<sub>3</sub> comes from the structural instability toward the polarization state associated with electronic pairing. They were coined as ‘proper’ ferroelectrics (Cheong and Mostovoy 2007). BiFeO<sub>3</sub>, which receives notable attention due to its potential applications in spintronics and memory, is commonly considered to be a model system for multiferroics (Kadomtseva, Popov et al. 2006), especially for ABO<sub>3</sub> perovskite where the ferroelectricity is driven by 6s<sup>2</sup> lone pair electrons. BiFeO<sub>3</sub> is one of the very few robust multiferroics with ferroelectric and antiferromagnetic order well above room temperature – the antiferromagnetic Néel temperature T<sub>N</sub> is ~ 380 °C and a ferroelectric Curie temperature T<sub>C</sub> is ~ 830 °C (Smolenskii, Isupov et al. 1961; Kiselev, Ozerov et al. 1963). The room temperature structure of BiFeO<sub>3</sub> is a rhombohedrally distorted perovskite with the space group of *R3c* as seen in Figure 1.16(a) (Fischer and et al. 1980; Kubel and Schmid 1990). With respect to the cubic *Pm3m* structure, the rhombohedral structure is obtained by an antiphase tilt of the adjacent FeO<sub>6</sub> octahedra and a displacement of the Fe<sup>3+</sup> and Bi<sup>3+</sup> cations from their centro-symmetric positions along (111) as shown by the arrow in Figure 1.16(a) (Wang, Neaton et al. 2003). For bulk BiFeO<sub>3</sub>, the measured polarization along the [111] direction was reported to be 6.1 μC/cm<sup>2</sup> and the Berry-phase calculation confirms the spontaneous polarization of 6.61 μC/cm<sup>2</sup> using local spin density approximation (Kiselev, Ozerov et al. 1963; Wang, Neaton et al. 2003). The reason for this small polarization is possibly due to the high leakage current, a result of defects and the non-stoichiometry of the materials.

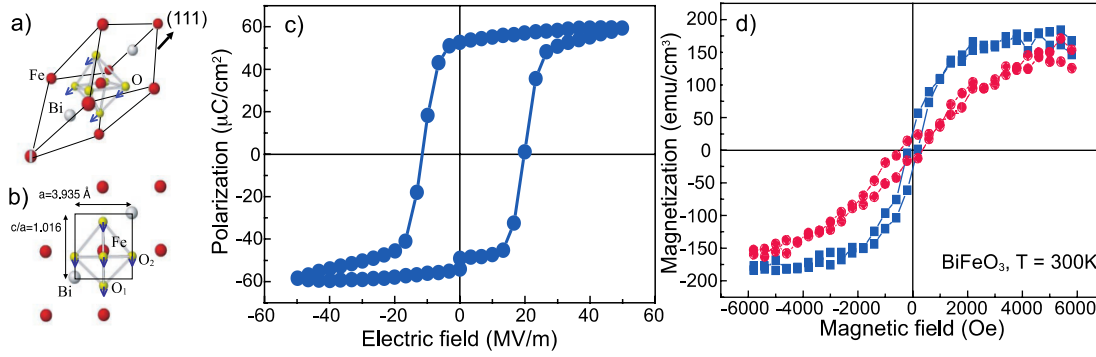


Figure 1.16. Schematic of the prototypical (a) rhombohedral and (b) tetragonal  $\text{BiFeO}_3$  unit cell. (c) Ferroelectric hysteresis loop, which shows a saturation polarization of  $55 \mu\text{C}/\text{cm}^2$  in a 200 nm  $\text{BiFeO}_3$  thin film. (d) A magnetic hysteresis loop shows the saturation magnetization of  $\sim 150 \text{ emu}/\text{cm}^3$  and a coercive field of  $\sim 200 \text{ Oe}$  in a 70 nm  $\text{BiFeO}_3$  thin film. (Wang, Neaton et al. 2003).

For epitaxial  $\text{BiFeO}_3$  thin film of 200 nm, an enhanced ferroelectric polarization of 50 - 60  $\mu\text{C}/\text{cm}^2$  has been reported (Wang, Neaton et al. 2003). Structural analysis with local spin density approximation indicates that the crystal structure of this thin film is monoclinic (Figure 1.16 (b)) in contrast to the bulk  $\text{BiFeO}_3$ , which has rhombohedral structure as seen in Figure 1.16 (a). It was found that the magnitudes of ionic displacement relative to the Bi, Fe, and apical O ions are much larger than what was observed in bulk  $\text{BiFeO}_3$ . Correspondingly, the Berry phase calculation yields a spontaneous polarization of  $63.2 \mu\text{C}/\text{cm}^2$ , agreeing well with experimental result shown in Figure 1.16 (c) (Wang, Neaton et al. 2003). Furthermore, research has revealed that the in-plane strain in the thin films could drive a rotation of the spontaneous polarization on the (110) plane, while the polarization magnitude itself remains almost constant, which is responsible for the strong strain tunability of the out-of-plane remnant polarization in (001)-oriented  $\text{BiFeO}_3$  films (Jang, Baek et al. 2008).  $\text{BiFeO}_3$ , which has a complicated magnetic configuration, was reported to have antiferromagnetic spin order that is not spatially

homogenous but rather a spatially modulated structure, as shown in Figure 1.17 (Cazayous, Gallais et al. 2008; Lebeugle, Colson et al. 2008).

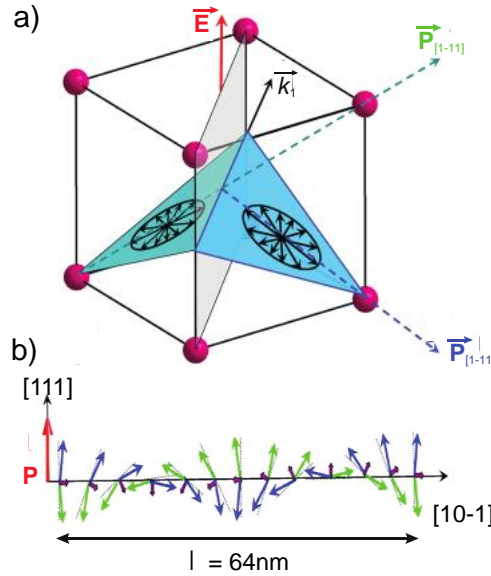


Figure 1.17. BiFeO<sub>3</sub>: (a) Schematic of the planes of spin rotations and cycloids  $k_1$  vector for the two polarization domains separated by a domain wall (b) Schematics of the antiferromagnetic circular cycloid. (Lebeugle, Colson et al. 2008)

The spiral spin propagation wave vector  $k_1$  is along the  $(10\bar{1})$  direction and the polarization is along the  $(111)$  direction. These two directions define the  $(\bar{1}2\bar{1})$  cycloid plane as a cross product where the spin rotation occurs, as shown in Figure 1.17 (b). Thus, the antiferromagnetic vector is averaged to zero in a scale of approximately  $\lambda = 64$  nm and is responsible for the very weak magnetization of bulk BiFeO<sub>3</sub>. Therefore, if the sample is smaller than the wavelength, the cycloid structure may be destroyed and enhanced magnetization and even weak ferromagnetism. This mechanism results in the enhanced magnetization in 70 nm BiFeO<sub>3</sub> thin films as shown in Figure 1.16(d), and was also observed in BiFeO<sub>3</sub> nanoparticles (Mazumder, Devi et al. 2007) and nanowire (Gao, Chen et al. 2007).

When polarization is only a part of a more complex lattice distortion, or when it appears as an accidental by-product of some other ordering, the ferroelectricity is deemed ‘improper’ and

constitutes an entirely different class of ferroelectrics (Levanyuk and Sannikov 1974). Of those ‘improper’ single-phase multiferroics, rare-earth manganites ( $\text{RMnO}_3$ ,  $\text{R}$  = Rare earth ions) have shown promise on theoretical basis as multiferroic materials and have thus been studied experimentally using advanced film growth techniques. Of the  $\text{RMnO}_3$  family, there are two possible routes to functional properties that are manifested through either hexagonal or orthorhombic structures. The first is a geometrically driven effect due to a noncentrosymmetric hexagonal structure ( $P6_3cm$ ) where  $\text{R} = \text{Sc, Y, and Ho-Lu}$  (Yakel, Koehler et al. 1963) which leads to long-range dipole-dipole interactions and anion rotations to drive the system towards a stable ferroelectric state as well as antiferromagnetic behavior as shown in Figure 1.18(a) (Van Aken, Palstra et al. 2004). For hexagonal  $\text{YMnO}_3$  (h-YMO), the ferroelectricity is caused along the c-axis due to the tilting of  $\text{MnO}_5$  bipyramids and the resulting change in distance between  $\text{O}^{2-}$  and  $\text{Y}^{3+}$  ions and exhibits canted antiferromagnetic behavior below the Néel temperature ( $T_N = 65\text{-}80\text{ K}$ ). The second is an orthorhombically distorted perovskite structure ( $P_{bnm}$ ) observed in larger rare earth ions where  $\text{R} = \text{La-Dy}$  (Gilleo 1957; Lorenz, Wang et al. 2004; Yamauchi, Freimuth et al. 2008) which also show ferroelectric Curie temperatures ( $T_C \leq 40\text{K}$ ) and antiferromagnetic Néel temperatures ( $T_N = 40\text{-}50\text{ K}$ ) (Li, Yan et al. 2009). For orthogonal  $\text{YMnO}_3$  (o-YMO), the ferroelectric properties are believed to be a result of the spin-current between noncollinear neighboring spins or the inverse Dzyaloshinskii-Moriya interaction (Cheong and Mostovoy 2007; Nakamura, Tokunaga et al. 2011). Although h-YMO is stable in bulk and thin film form, o-YMO can be obtained either by high pressure synthesis (Iliev, Lorenz et al. 2005) or by epitaxial stabilization when an appropriate substrate such as  $\text{YAlO}_3$  (Nakamura, Tokunaga et al. 2011) and Nb-doped  $\text{SrTiO}_3$  (Li, Yan et al. 2009) with low lattice mismatch is chosen.

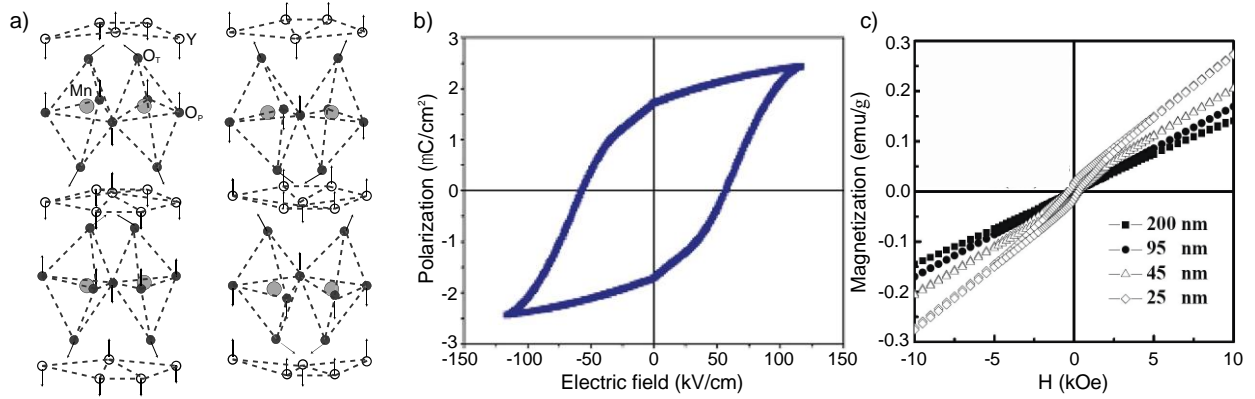


Figure 1.18. (a) Three-dimensional schematic view of  $\text{YMnO}_3$  in the two polarized states. Arrows indicate the directions of the atomic displacements moving from the centrosymmetric to the ferroelectric structure. (b) Ferroelectric hysteresis loop of  $\text{YMnO}_3$  measured in 100 nm  $\text{YMnO}_3$  film. (c) Magnetic hysteresis loops at 5 K for the  $\text{YMnO}_3$  pellets with different grain sizes. (Van Aken, Palstra et al. 2004), (Posadas, Yau et al. 2005), and (Han, Hsu et al. 2011) respectively.

Thus, rehybridization and covalency play a minor role (or no role at all) in the ferroelectric transition. Instead, the huge  $\text{Y-O}_\text{P}$  off-center displacements by tilting cause the oxygen ions to move closer to the rather small Y ions, which are quite distinct from the small displacements driven by chemical activity found in conventional ferroelectric perovskites (Fennie and Rabe 2005; Kang, Han et al. 2005). The polarization is a consequence of the unusual Y-site coordination and the triangular and layered  $\text{MnO}_5$  network. As a consequence, the spin configuration of hexagonal  $\text{YMnO}_3$  is frustrated. The ferroelectric properties in  $\text{YMnO}_3$  is shown in Figure 1.18(b), with a remnant polarization and a coercive field of  $\sim 2 \mu\text{C}/\text{cm}^2$  and  $\sim 50$  kV/cm, respectively (Posadas, Yau et al. 2005). The antiferromagnetic easy plane anisotropy of Mn spins restrict the moments strictly on the  $ab$  plane, which are dominated by the strong in-plane antiferromagnetic interaction. The inter-plane exchange between the Mn spins is two orders of magnitude lower. Therefore,  $\text{YMnO}_3$  is an excellent example of a quasi-two dimensional Heisenberg magnet on a triangular lattice with a spin frustration generated by geometric constraint (Fiebig, Fröhlich et al. 2002; Fiebig, Lottermoser et al. 2002; Park, Park et

al. 2003; Sato, Lee et al. 2003; Tachibana, Yamazaki et al. 2005). In addition,  $\text{YMnO}_3$  shows weak ferromagnetic behavior, as the grain size of the sample is small. The magnetic hysteresis loops for  $\text{YMnO}_3$  samples of different grain sizes are shown in Figure 1.18(c) (Han, Hsu et al. 2011). For the samples with grain size of 25 and 45 nm, weak ferromagnetic behavior is observed with corresponding coercive fields about 395 and 260 Oe, respectively.

In addition to the above mentioned single-phase multiferroics, there are also spiral spin-order-induced multiferroic materials that have stronger magnetoelectric coupling yet with fairly low magnetic and ferroelectric transition temperatures (Khomskii 2009). The physical mechanisms this type of multiferroic can be further divided by the linearity of the spirals, and the cycloidal spiral states, which have been investigated most extensively, is reviewed elsewhere. (Khomskii 2009)

### 1.2.5 Composite Multiferroics

One way around the aforementioned chemical contradiction issue regarding the scarcity of multiferroic materials may be the synthesis of mixed perovskites with  $d^0$  and  $d^n$  ions. For instance, A-sites are facilitated with cations of  $(ns)^2$  valence electron configuration, such as  $\text{Bi}^{3+}$  and  $\text{Pb}^{3+}$ , which favor the stability of ferroelectricity distorted structures. At the same time, the B-sites are occupied with magnetic ions providing magnetism. This simple method allows for ferroelectricity and magnetism in one system. Unfortunately the coupling of magnetic and ferroelectric subsystems in mixed perovskites is rather weak (Wang, Liu et al. 2009; Wu, Burnus et al. 2009). Nonetheless, such simple approaches allow for multiferroics in one system even if the coupling is weak.

Alternatively and with greater design flexibility, investigations have been applied to magnetoelectric composite multiferroics due to enhanced coupling effects with ferroelectric/ferromagnetic materials, which have the larger dielectric/magnetic susceptibility, respectively, through the use of strong internal electromagnetic fields in each component (Nan 1994; Schmid 1994; Vaz, Hoffman et al. 2010). Moreover, composite multiferroics offer distinct advantages as the individual properties of these materials can be adjusted independently, thereby realizing a stronger magnetoelectric coupling (Nan, Bichurin et al. 2008).

Composites can be used to generate magnetoelectric behavior from materials in which magnetoelastic effects are not allowed. Thus, the effect in composite multiferroics is achieved by combining magnetostriction, a change in strain as a quadratic function of applied magnetic field, and piezoelectricity, a change in strain as a linear function of applied electric field, into one compound. As a result, a magnetic field applied to the composite induces strain in the magnetostrictive material, which is coupled to the piezoelectric material, where it induces an electric polarization (Lawes and Srinivasan 2011). In this way, magnetoelectric (ME) effect in composite multiferroics can be written as (Schmid 1994):

$$\text{Direct ME Effect} = \frac{\text{Magnetic}}{\text{Mechanical}} \times \frac{\text{Mechanical}}{\text{Electric}} \quad \text{Eq. (1.9)}$$

$$\text{Converse ME Effect} = \frac{\text{Electric}}{\text{Mechanical}} \times \frac{\text{Mechanical}}{\text{Magnetic}} \quad \text{Eq. (1.10)}$$

Hence, an important condition for the presence of a large coupling in these composite multiferroics is a good elastic coupling between the magnetic and ferroelectric phases. The coupling effect in composite multiferroics has been studied intensively by theoretical work with the intent to better understanding the coupling between the two ferroic phases. The proper description of the coupling effect in magnetoelectric composite multiferroics have taken into



account the magnetic, electrical and mechanical properties, i.e. the stress  $\sigma$ , strain  $\varepsilon$ , electric displacement  $D$ , electric field  $E$ , magnetic induction  $B$ , magnetic field,  $H$  in bulk materials (Schmid 1994; Nan, Li et al. 2001; Wang, Hu et al. 2010), as well as residual stress  $\sigma_s$  or residual strain  $\varepsilon_s$  resulting from misfit between the film and substrate, spontaneous polarization  $P_s$  and magnetization  $M_s$  (Nan, Li et al. 2001):

$$\begin{aligned}\sigma &= c\varepsilon - e^T E - c\varepsilon^{ms} - \sigma_s \\ D &= e\varepsilon + \kappa E + \alpha H + P_s \\ B &= \mu(\varepsilon, E, H)H + E_s\end{aligned}\tag{Eq. (1.11)}$$

In Eq. (1.11),  $c$  and  $\kappa$  are, respectively, the stiffness at constant fields and the dielectric constant at constant strain. The permeability  $\mu$  strongly depends on  $\varepsilon$  and electric and magnetic fields;  $e$  ( $e^T$  being the transpose of  $e$ ) is the piezoelectric coefficient; and  $\varepsilon^{ms}$  is the magnetostrictively induced strain related with the magnetic field and dependent on magnetostriction constants (e.g.,  $\lambda_{001}$  and  $\lambda_{111}$ ) of the ferromagnetic phase (Nan, Liu et al. 2005);  $\alpha$  is the magnetoelectric coefficient. As a result, Eq. (1.11) shows that the effective electric polarization is sensitive to residual strains in thin films, spontaneous polarization, material constants of the two different phases, the coupling of the phases, and applied magnetic field (Nan, Li et al. 2001).

Table 1.4 summarizes major ferroelectric and ferromagnetic materials that can be considered in composite multiferroics, due to their respectively superior ferroic properties such as high polarization and piezoelectricity in ferroelectric materials, and large magnetization and magnetostriction in ferromagnetic materials.

Table 1.4. Ferroelectric and ferromagnetic materials and their respective ferroic properties.

Ferroelectric	$P_r$ ( $\mu\text{C}/\text{cm}^2$ )	$d_{33}$ (pm/V)	References	Ferromagnetic	$M_s$ (emu/cm <sup>3</sup> )	$\lambda_s$ (ppm)	References
BaTiO <sub>3</sub>	10	105	(Park, Xu et al. 2010)	CoFe <sub>2</sub> O <sub>4</sub>	500	-110	(Rigato, Geshev et al. 2009)
PZT*	20.4	65	(Nguyen, Nazeer et al. 2010)	NiFe <sub>2</sub> O <sub>4</sub>	200	-20	(Zeng, Wan et al. 2004)
PMN-PT*	40	260	(Cao, Schmidt et al. 2004)	LaSrMnO <sub>3</sub>	400	30	(Srinivasan, Rasmussen et al. 2002)
BiFeO <sub>3</sub>	55	70	(Wang, Neaton et al. 2003)	FeGaB**	1034	70	(Lou, Insignares et al. 2007)

\* PZT and PMN-PT denote  $\text{Pb}(\text{Zr}, \text{Ti})\text{O}_3$  and  $\text{Pb}(\text{Mg}, \text{Nb})\text{O}_3\text{-PbTiO}_3$ .

\*\*Although FeGaB is not an oxide material, it has very high magnetostriction, magnetization, and a low damping coefficient, ideal for high frequency devices. It is shown here for comparison purposes.

Based on these ferroelectric and ferromagnetic materials, several integration schemes have been considered to attain a strain-induced magnetoelectric coupling in ferroelectric-ferromagnetic nanostructured thin films (Marchack and Chang 2012). For example, in 0-3 particulate multiferroic composite films as shown in (a), one phase fills the pores formed by another. Because of the flexibility of the porous phase, unique strain states can be realized, and very close coupling is expected. Horizontally aligned materials such as nanolaminates with alternating layers of piezoelectric and ferromagnetic materials are the easiest to conceptualize, as shown in (b). This connectivity scheme is classified as a 2-2 configuration and can be realized by thin-film deposition processes. However, the substrate clamping effect limits the amount of piezoelectric strain, thereby limiting the attainable magnetoelectric effect. As a result, vertically aligned structures such as nanorods embedded in the matrix of another phase have also been explored as seen in (c).

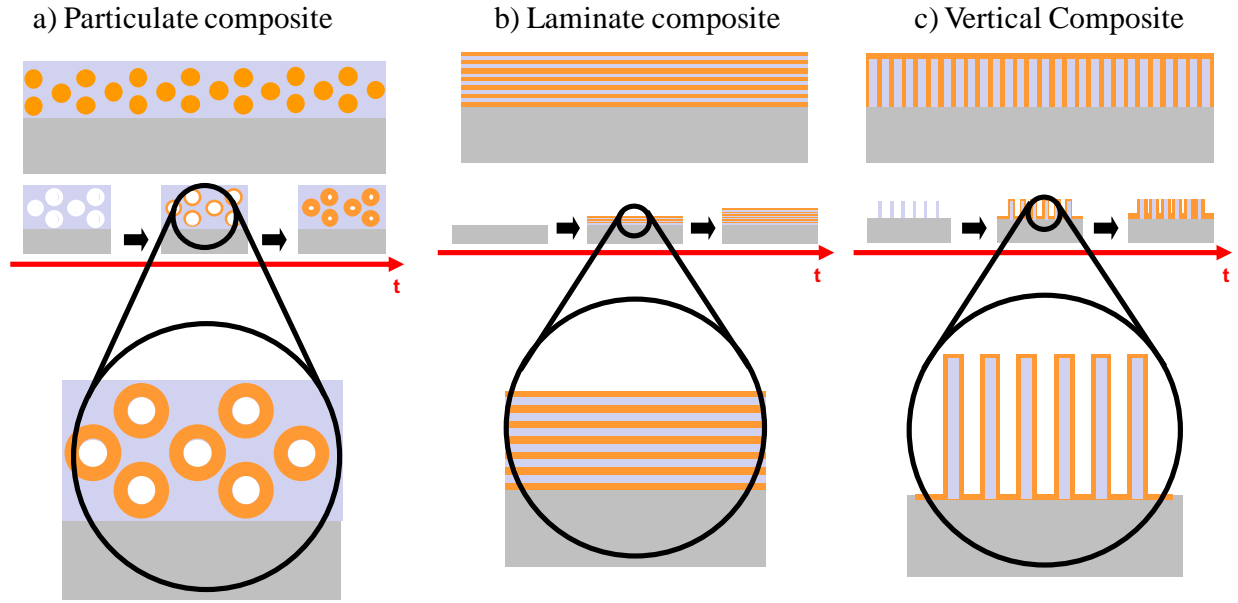


Figure 1.19. Schematic illustration of the heterostructures of ME composite nanostructures with the three different connectivity schemes. The time progression of the material synthesis highlights the importance of a uniform and conformal coating to realize the intimately coupled interfaces in these complex structures. (a): 0-3 particulate composite (b): 2-2 laminate composite (c): 1-3 vertical fiber/rod composite. (Marchack and Chang 2012).

Figure 1.19 not only illustrates the schematics of the composites from these three strategies but also highlights the time evolution of the structure designs. In the following section, each of these strategies are reviewed in more depth to discuss their respective potentials in realize more effective magnetoelectric materials.

2-2 horizontal nanostructures based on the stacking of ferroelectric perovskite and ferromagnetic spinel states usually exhibit weak magnetoelectric effects due to large in-plane constraint from substrate according to the Green's function, as shown in Figure 1.20(a). However, the modern growth techniques make 2-2 laminate structures easy to fabricate and avoid the leakage problem as in 0-3 and 1-3 composites because the ferroelectric layers prevent short circuiting through the PZT. This advantage makes 2-2 laminates the most widely investigated composite nanostructures in the study of magnetoelectric effect (Murugavel, Padhan

et al. 2004; Wu, Zurbuchen et al. 2006; Ziese, Bollero et al. 2006; Eerenstein, Wiora et al. 2007; Ryu, Park et al. 2007; Thiele, Dörr et al. 2007; Zhang, Deng et al. 2008; Li, Wang et al. 2009; Heron, Trassin et al. 2011). For example, a 2-2 heterostructure of  $\text{CoFe}_2\text{O}_4/\text{BaTiO}_3$  grown on a (001)  $\text{SrTiO}_3$  substrate prepared by PLD was shown to exhibit an enhanced magnetoelectric response of  $\sim 66 \text{ mV/cm}\cdot\text{Oe}$  and possessed equivalent saturation polarization and magnetization when compared to values obtained from bulk ceramic of each phase (Zhang, Deng et al. 2008). More interestingly, a special and simple horizontal heterostructure has been constructed by growing epitaxial ferroelectric  $\text{Pb}(\text{Zr}_{0.3}, \text{Ti}_{0.7})\text{O}_3$  film on a manganite single crystal of  $\text{La}_{1.2}\text{Sr}_{1.8}\text{Mn}_2\text{O}_7$  (Wu, Zurbuchen et al. 2006). The efficient mechanical coupling at the interface results in a remarkable magnetoelectric coefficient of  $\sim 600 \text{ mV/cm}\cdot\text{Oe}$ , likely the highest values reported in the laminate composites. A strong temperature-dependent magnetoelectric effect was observed in this composite as a result of the magnetostrictive properties of the manganite crystal. The magnetoelectric voltage was approximately 87% of the theoretical value predicted using a phenomenological thermodynamic model as shown in Figure 1.20 (b). In addition to the direct magnetoelectric effect measurement, the electric field control of magnetism in magnetoelectric thin films can be applied to probe the ferromagnetic states controlled by an applied voltage. In 2-2 type laminate structures containing ultrathin ferromagnetic films, magnetism has been controlled at the interfaces using electric field effects. Magnetoelectric effects at the interfaces have been predicted to arise from spin density accumulation in metallic ferromagnetic/ferroelectric structures, induced by charge screening of the electric field (Rondinelli, Stengel et al. 2007).

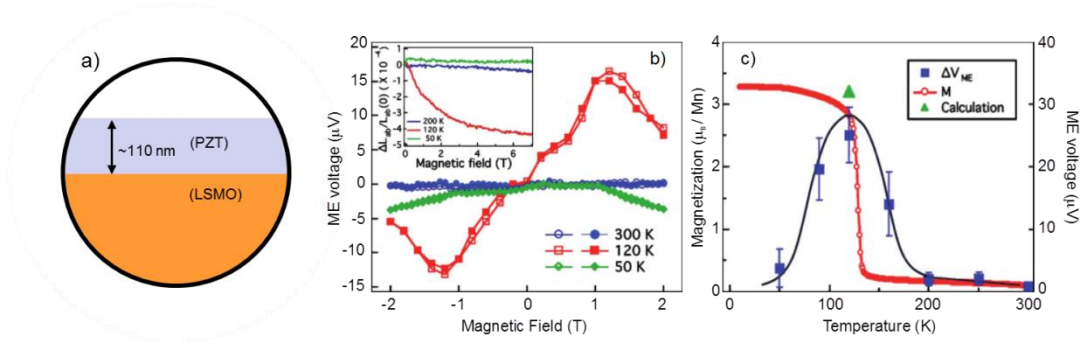


Figure 1.20.(a) Schematic diagram of a 2-2 nanolaminate structure, (b) the magnetoelectric voltage as a function of magnetic field in a 110nm  $\text{Pb}(\text{Zr}_{0.3}, \text{Ti}_{0.7})\text{O}_3/\text{La}_{1.2}\text{Sr}_{1.8}\text{Mn}_2\text{O}_7$  film stack at three different temperatures, and (c) the comparison of temperature dependence of the magnetization measured on the manganite crystal and the peak-to-peak magnetoelectric voltage. (Wu, Zurbuchen et al. 2006)

More recently, such a charge-driven magnetoelectric effect has been observed in the multiferroic magnetoelectric heterostructures containing a 250 nm ferroelectric  $\text{Pb}(\text{Zr}_{0.2}, \text{Ti}_{0.8})\text{O}_3$  film on a ultrathin (4 nm) ferromagnetic  $\text{La}_{0.8}\text{Sr}_{0.2}\text{MnO}_3$  film (Molegraaf, Hoffman et al. 2009). A large change in the magnetic moment of the ferromagnetic layer is found as a function of the ferroelectric polarization state induced by an electric field as shown in Figure 1.21. The abrupt switching between high and low magnetic states according to the ferroelectric polarization states can be understood as the depletion and accumulation of hole carriers from the ferromagnetic layer to the ferroelectric layer, i.e. direct control of magnetism due to the charge carrier density. The effect reported is large, a magnetoelectric coupling coefficient of  $0.8 \times 10^{-3} \text{ cm} \cdot \text{Oe}/\text{V}$  at 100K, which is larger in magnitude than the magnetoelectric coupling coefficients of intrinsic multiferroics. The magnetoelectric response in the composite multiferroic has a temperature dependence and reaches a larger value of  $13.5 \times 10^{-3} \text{ cm} \cdot \text{Oe}/\text{V}$  at about 180 K, which also indicates the change of magnetism with charge carrier doping (Vaz, Segal et al. 2010).

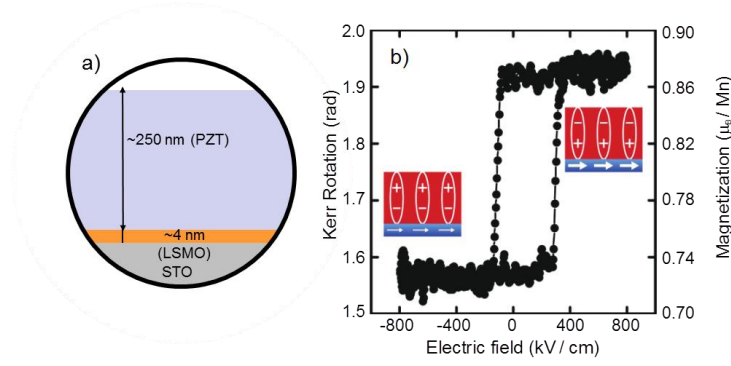


Figure 1.21. (a) Schematic diagram of a 2-2 nanolaminate structure, (b) the magnetoelectric hysteresis loop as a function of the applied electric field measured in 250nm  $\text{Pb}(\text{Zr}_{0.2}, \text{Ti}_{0.8})\text{O}_3/4\text{nm}$   $\text{La}_{0.8}\text{Sr}_{0.2}\text{MnO}_3$  composite 1 at  $T = 100\text{K}$ . The insets indicate the magnetic and electric states of the composite. (Molegraaf, Hoffman et al. 2009).

The 1-3 type vertical heterostructure consisting of magnetic spinel nanopillars epitaxially embedded in the ferroelectric film matrix could exhibit large direct magnetoelectric response due to a reduced clamping effect by the substrate in the vertical structure and more strain coupling from a larger interfacial area (Yan, Xing et al. 2009; Gao, Rodriguez et al. 2010; Oh, Crane et al. 2010; Aimon, Kim et al. 2012). In these three dimensional heteroepitaxial structures, an electric field applied to the piezoelectric matrix induced a change in its shape through the converse piezoelectric effect, thereby altering the magnetic anisotropy of the ferromagnetic pillars via magnetostriction. The converse magnetoelectric coupling coefficient,  $\alpha_{33}$ , was estimated to be  $0.126 \text{ Oe}\cdot\text{cm}/\text{V}$  ( $\sim 1.0 \times 10^{-3} \text{ G}\cdot\text{cm}/\text{V}$ ) from the resulting saturation to remnant magnetization curve obtained from a magnetometer at room temperature after electrical poling (Zavaliche, Zheng et al. 2005). However, the direct magnetoelectric response was not easy to measure in the 1-3 type because of leakage current resulting from the low resistance of the magnetic pillars in the ferroelectric film matrix. For example, an epitaxial thin film composed of  $\text{CoFe}_2\text{O}_4$  nanopillars embedded in a  $\text{BaTiO}_3$  matrix was grown as an alternative to circumvent the substrate clamping effect and showed a sudden kink in the temperature dependent magnetization, which represented a direct observation of magnetoelectric coupling (Zheng, Wang et al. 2004). Although the direct

magnetoelectric effect was observed, it is still difficult to detect the direct magnetoelectric effect because the magnetoelectric voltage signal is proportional to the film thickness; it typically becomes smaller than  $1\mu\text{V}$  for film thickness less than  $1\mu\text{m}$ .

To overcome this issue, the increased thickness could rule out the leakage issue and obtain the direct magnetoelectric effect in the vertical nanostructures with  $\text{CoFe}_2\text{O}_4$  nanopillars in  $\text{BiFeO}_3$  film matrix grown on  $\text{SrTiO}_3$  single crystal substrate as shown in Figure 1.22 (Yan, Xing et al. 2009; Oh, Crane et al. 2010). The results highlights the effectiveness of heteroepitaxial strain to the  $\text{CoFe}_2\text{O}_4$  nanopillars, enabling a transverse ME susceptibility,  $\alpha_{31}$ , as high as  $\sim 130\text{ ps/m}$  ( $\sim 60\text{ mV/cm}\cdot\text{Oe}$ ) at  $6\text{ kOe}$ , as shown in Figure 1.22 (c).

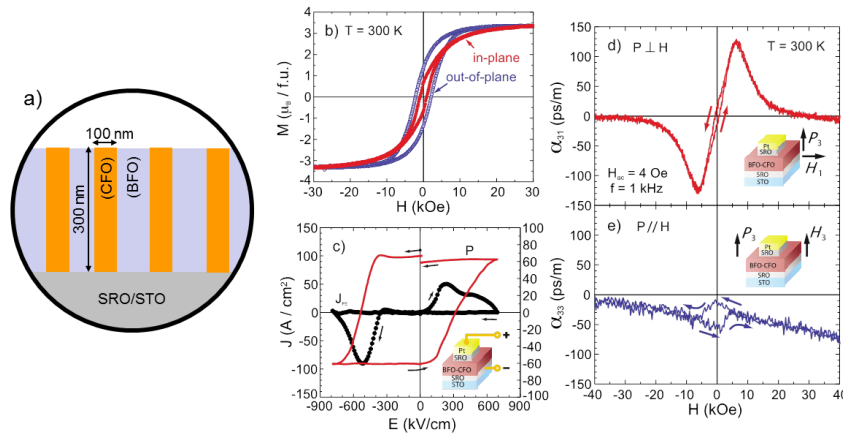


Figure 1.22. (a) Schematic diagram of 1-3 nanorod structure based on ferromagnetic rods (100nm wide  $\text{CoFe}_2\text{O}_4$ ) and ferroelectric matrix (300nm thick  $\text{BiFeO}_3$ ), (b) the magnetic hysteresis loop for in-plane and out-of-plane measured in self-assembled  $\text{BiFeO}_3/\text{CoFe}_2\text{O}_4$ , (c) the current density ( $J$ ) and polarization ( $P$ ) as a function of electric fields, (d) the transverse ( $\alpha_{31}$ ) and (e) longitudinal ( $\alpha_{33}$ ) ME susceptibility of the nanostructure composites at 300K. (Oh, Crane et al. 2010).

The  $\alpha_{31}$  can be further optimized depending on the growth temperatures (Zheng, Kreisel et al. 2007). As predicted by theory (Nan, Liu et al. 2005), thin films with the 1-3 nanostructures have stronger magnetoelectric coupling than other nanostructures, e.g., 0-3 structures  $\text{NiFe}_2\text{O}_4/\text{Pb}(\text{Zr}_{0.52}\text{Ti}_{0.48})\text{O}_3$  with magnetoelectric coupling coefficient of  $\sim 14\text{ ps/m}$  ( $\sim 16\text{ mV/cm}\cdot\text{Oe}$ ) (Ryu, Murugavel et al. 2006). As a point of comparison, Green's function analysis

has been made to compare the ME effect between the 1-3 ferromagnetic nanopillars embedded in the ferroelectric matrix and 2-2 ferroelectric and ferromagnetic nanolaminates, based on  $\text{CoFe}_2\text{O}_4/\text{BaTiO}_3/\text{SrRuO}_3$ , as shown in Figure 1.23 (a) (Nan, Liu et al. 2005; Liu, Obi et al. 2009). The analysis shows that the 1-3 configuration exhibited a large magnetic field induced polarization, while the 2-2 configuration showed a much weaker magnetoelectric effect, owing to the magnetostriction, as shown in Figure 1.23(b). Similar trends were observed in  $\text{NiFe}_2\text{O}_4/\text{Pb}(\text{Zr},\text{Ti})\text{O}_3/\text{MgO}$  based nano-bilayers and nanopillars, where the magnetoelectric interaction is strongly affected by the substrate clamping (Petrov, Srinivasan et al. 2007). Specifically, for increasing volume of MgO substrate in a bilayer, the ME coefficient decreased exponentially and the  $\text{Pb}(\text{Zr}, \text{Ti})\text{O}_3$  volume required for maximum ME effects increases. For nanopillar structures, the substrate clamping effects are negligible only when the length of the pillar is much greater than its radius.

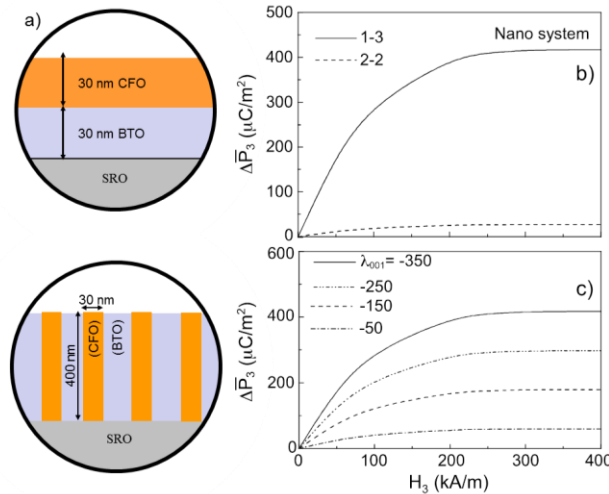


Figure 1.23. (a) Schematic diagrams of 2-2 30nm  $\text{CoFe}_2\text{O}_4$ /30nm  $\text{BaTiO}_3$  and 1-3 400nm thick  $\text{BaTiO}_3$  matrix/30nm wide  $\text{CoFe}_2\text{O}_4$  rod structures used in Green function's calculations. (b) Magnetic field induced electric polarization  $D\bar{P}_3 = \bar{P}_3 - \bar{P}_3(H = 0)$  for both systems and (c) the effect of the magnetostriction of the ferromagnetic phase on  $D\bar{P}_3$  for the 1-3 system. (Nan, Liu et al. 2005)



Two 0-3 composite systems have been shown to be promising multiferroics, e.g.  $\text{CoFe}_2\text{O}_4/\text{Pb}(\text{Zr}, \text{Ti})\text{O}_3$  (Wan, Zhang et al. 2006) and  $x\text{Bi}_{0.35}\text{Nd}_{0.85}\text{Ti}_3\text{O}_{12}/(1-x)\text{CoFe}_2\text{O}_4$  (Zhong, Wang et al. 2007), with reported room temperature ferroelectric and ferromagnetic responses. For  $\text{CoFe}_2\text{O}_4/\text{Pb}(\text{Zr}, \text{Ti})\text{O}_3$ , the magnetoelectric effect was shown to be strongly dependent on the magnetic bias and magnetic field frequency, as shown in Figure 1.24 (Wan, Zhang et al. 2006). For  $x\text{Bi}_{0.35}\text{Nd}_{0.85}\text{Ti}_3\text{O}_{12}/(1-x)\text{CoFe}_2\text{O}_4$ , the magnetoelectric effect was shown to vary with magnetic bias and different compositions of the thin films.

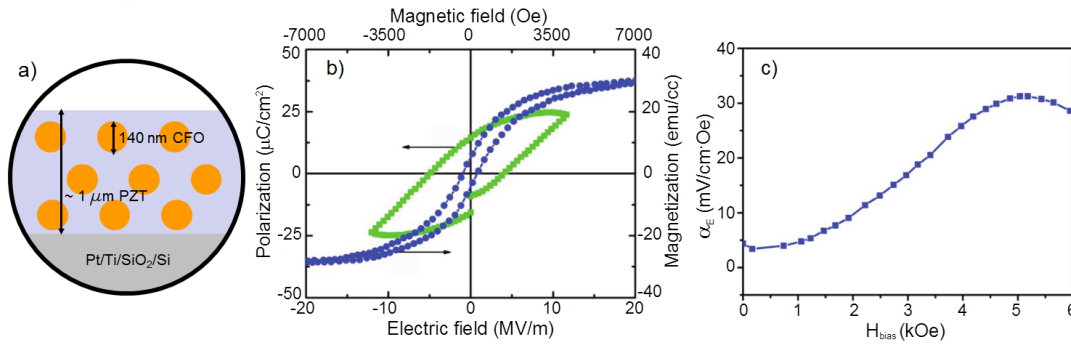


Figure 1.24. (a) Schematic diagram of 0-3 nanoparticulate structure with ferromagnetic particulates (140nm diameter  $\text{CoF}_2\text{O}_4$ ) in a ferroelectric matrix (1  $\mu\text{m}$  thick  $\text{Pb}(\text{Zr}_{0.52}, \text{Ti}_{0.48})\text{O}_3$ ). (b) Polarization (magnetization) vs. electric (magnetic) field hysteresis loop measured in the composite and (c) the variation of  $\alpha_E$  with  $H_{\text{bias}}$  at a magnetic frequency  $f = 10\text{kHz}$ . (Wan, Zhang et al. 2006).

Recently, (100)-oriented  $\text{Pb}(\text{Zr}_{0.52}\text{Ti}_{0.48})\text{O}_3/\text{NiFe}_2\text{O}_4$  composites on (001)  $\text{SrTiO}_3$  substrates were prepared by PLD using a composite target resulting in a film with spinel  $\text{NiFe}_2\text{O}_4$  nanoparticles dispersed within a  $\text{Pb}(\text{Zr}_{0.52}\text{Ti}_{0.48})\text{O}_3$  matrix in a 0.35-0.65 NFO-PZT ratio; subsequently, both the transverse and longitudinal components of the magnetoelectric voltage coefficient were measured (Ryu, Murugavel et al. 2006). The results supported the hypothesis that the magnetoelectric effect comes from direct strain coupling between magnetostrictive  $\text{NiFe}_2\text{O}_4$  and piezoelectric  $\text{Pb}(\text{Zr}_{0.52}\text{Ti}_{0.48})\text{O}_3$  grains. However, the maximum value of magnetoelectric coupling coefficient for these composites, of approximately 16 mV/cm·Oe, are

lower than reported magnetoelectric coefficient of 37 mV/cm·Oe of sol-gel and solid-state reaction synthesized 5  $\mu$ m thick bulk  $\text{Pb}(\text{Zr}_{0.57}\text{Ti}_{0.43})\text{O}_3/\text{NiFe}_2\text{O}_4$  particulate composite (Zhai, Cai et al. 2004). The authors suggested that the smaller values might be due to the lattice clamping effects by the substrate. Figure 1.25 shows sign reversal of transverse ( $\alpha_{31}$ ) and longitudinal ( $\alpha_{33}$ ) components of magnetoelectric voltage coefficients of the composite films between two oppositely poled states. This demonstrated that the magnetoelectric signals originated from ferroelectric domains with an inversion symmetry breaking relationship.

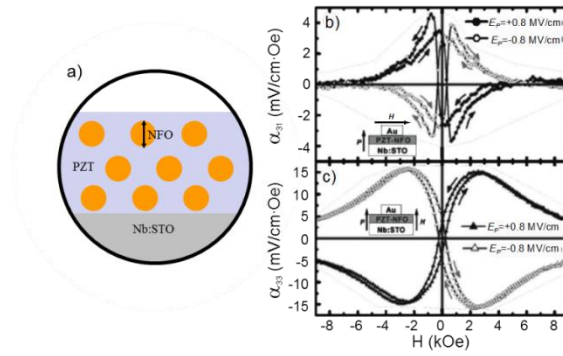


Figure 1.25. (a) Schematic diagram of 0-3 nanoparticulate structure of magnetostrictive particulates (NFO) in a ferroelectric matrix (PZT). The transverse ( $\alpha_{31}$ ) (b) and longitudinal ( $\alpha_{33}$ ) (c) components of the magnetoelectric coefficient measured on the  $\text{Pb}(\text{Zr}_{0.52}\text{Ti}_{0.48})\text{O}_3/\text{NiFe}_2\text{O}_4$  particulate composite film after poling at 0.8 and -0.8 MV/cm. (Ryu, Murugavel et al. 2006)

Based on the above review, ALD is emerging as a viable technique for synthesizing multiferroic composites due to its ability to control the identity, placement, and function of every important element in the engineered composite multiferroics (Marchack and Chang 2012). ALD can deposit highly conformal films with outstanding uniformity and composition control and allow local composition/bonding arrangement to be varied, even if the overall stoichiometry remains constant. By realizing the control of composition and atomic arrangement, the conformality attainable by ALD allows nanostructured composite material systems to be synthesized. An example is the synthesis of the piezoelectric material  $\text{Pb}(\text{Zr}, \text{Ti})\text{O}_3$  via ALD

over a mesoporous  $\text{CoFe}_2\text{O}_4$  material formed by evaporation-induced self-assembly (Marchack and Chang 2012). As shown in Figure 1.26, the growth rate of  $\text{Pb}(\text{Zr}, \text{Ti})\text{O}_3$  was determined to be 0.7 nm/cycle, and film thickness of 6-12 nm was achieved by repeating the ALD cycle sequence. Mesoporous CFO thin films with a pore diameter of approximately 14 nm were used as a template to form a 0-3 nanostructured composite multiferroic. Scanning electron microscopy (SEM) confirmed that the coating was uniform and conformal over the interior surface of the pores, which is an advantage of the ALD process.

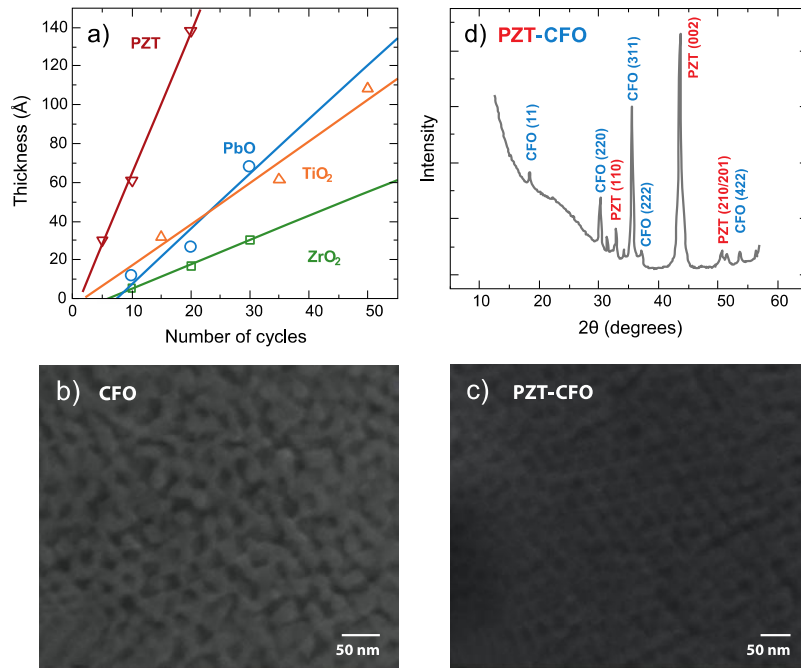


Figure 1.26. (a) ALD growth rate of  $\text{Pb}(\text{Zr}, \text{Ti})\text{O}_3$  in comparison with that of its constituent oxides. (b, c) SEM images of mesoporous  $\text{CoFe}_2\text{O}_4$  thin films (b) and a  $\text{Pb}(\text{Zr}, \text{Ti})\text{O}_3/\text{CoFe}_2\text{O}_4$  composite multiferroic (c). (d) X-ray diffraction patterns of the composite, confirming the crystal structures of both ferroic phases. (Marchack and Chang 2012).

Contained in Table 1.5 is a list of various multiferroic composite materials with different configurations and material choices. As can be seen by the general trend of minimizing the critical dimension, the magnetoelectric coefficient is maximized. This is due to the increase of

the interfacial surface area between the ferroic materials thus increasing the coupling for strain-mediated composite multiferroics.

Table 1.5. Comparison of various multiferroic composites with different configurations and material selections

MF Composites		Type (D-D)	Thickness ( $\mu\text{m}$ )	Critical Dimension ( $\mu\text{m}$ )	ME Coefficient $\alpha_{\text{ME}}$ (mV/cm-Oe)	S/V ( $\text{m}^{-1}$ )
FE	FM					
PZT	CFO	Bulk	2000.00	5.00	30	$10^4$
BNT	CFO	Bulk	2000.00	4.00	34	$10^4$
BaTiO <sub>3</sub>	Co	0-3	0.50	0.07	160	$10^7$
PLT	CFO	0-3	0.35	0.05	250	$10^8$
PZT	CZFO	2-2	20.00	0.65	155	$10^6$
PZT	Terfenol-D	2-2	0.80	0.40	150	$10^6$
PZT	LSMO	2-2	0.27	0.14	300	$10^6$
PZT	CFO	1-3	0.40	0.15	390	$10^7$

### 1.2.6 Synthesis Methods for Multiferroic Materials

Experimental methods to produce multiferroic thin films has benefitted greatly from past research to produce other complex materials such as superconductors.(Martin, Chu et al. 2010) The importance of growing high quality films cannot be understated, as many of the important properties of multiferroics are derived from the structure of the material. Additionally, system cost and ease of integration, among others, are also important factors. In this section, the various methods for producing multiferroic thin films are reviewed, and a subsection is devoted to atomic layer deposition, as it is the focus of this study.

Pulsed laser deposition (PLD) is by far the most commonly used method to produce high-quality epitaxial multiferroic films.(Martin, Chu et al. 2010) Essentially, a pulsed laser is applied to a set of bulk targets that emit a plume of material that is then deposited onto a substrate while

an oxygen source is flowing into the environment to oxidize the metal ions on the substrate.(Greer and Tabat 1995; Greer 2007) The targets can be alternated in order to produce a complex film with multiple types of ions. One advantage of PLD is the overall simplicity of the setup consisting of a vacuum chamber (with all the requisite pumps and pressure gauges), a heated sample holder, a rotating target holder, an oxygen source, and the optics required to focus a laser to the target. Additionally, with PLD, it is possible to produce high quality films, easily replace targets in order to investigate new material systems, and to produce complex stoichiometries.(Willmott and Huber 2000) Challenges in using PLD include the potential to eject large macroscopic particles from the target which end up in the film creating unwanted phases, difficulties in scaling up the process to larger wafer sizes ( > 8 inch diameter), and the importance of controlling the target erosion so that the correct stoichiometry can be maintained.(Greer 2007; Martin, Chu et al. 2010)

Molecular beam epitaxy (MBE) is a technique that was created in 1960 and later helped to produce research in high quality oxide films for high  $T_c$  superconductor applications.(Cho and Arthur 1975; Webb, Weng et al. 1987) MBE typically involves a long tube held at ultra-high vacuum pressures ( $\sim 10^{-13}$  Torr) where, at one end, houses the source materials which are slowly evaporated, and at the other end holds the substrate. Low energy atomic beams are created either by radiative heating of a target via Knudsen effusion cells or by electron beam evaporation.(Martin, Chu et al. 2010) Using this method, researchers are able to produce extremely high quality films with few, if any, defects. Unfortunately, MBE chambers are quite high in cost ( $\sim \$1$  million) and thus the usage is uncommon. Nonetheless, MBE serves a need to produce extremely high quality films that can help verify results from theoretical calculations.

Sputtering is a method that has been used widely in the semiconductor industry to produce both metals and metal oxides and is classified as a physical vapor deposition (PVD) technique.(Kelly and Arnell 2000) Generally, a rf magnetron produces a plasma from which highly energetic ions collide onto a target material which then evaporates and is energized by the plasma it passes through until it reaches the surface and forms a film on the substrate. The advantages of sputtering are that it is very scalable as evidenced by the widespread usage in the semiconductor industry and can deposit complex oxides using multiple targets. Certain parameters must be controlled in order to produce a high quality film, and they are the deposition rate of each target, oxidant gas concentration in the chamber, temperature, and bias voltage.

Metalorganic chemical vapor deposition (MOCVD) is also a highly scalable method in which metalorganic precursor vapors are flowed to a substrate along with some reactive oxidation gas.(Leskelä and et al. 1993; Schwarzkopf and Fornari 2006) At high enough temperatures, the organic ligands on the metalorganic molecules decompose leaving the metallic ion and the oxidant to react together on the substrate forming a metal oxide film. Most of the challenges for MOCVD involve the design of metalorganic molecules that deposit only on the desired location, namely the substrate. MOCVD is capable of producing fairly high quality films but can easily be contaminated due to unreacted organic ligands i.e. carbon compounds which remain in the film.

Solution based techniques used to research multiferroics include sol-gel, chelate, and metalorganic decomposition.(Martin, Chu et al. 2010) The essential steps involve creating a precursor solution which is then used to spin-coat or dip-coat the substrate and then heated at ~300-400 °C to dry and pyrolyze organic compounds, then heated at a higher temperature (~600-1100 °C) to anneal and crystallize the sample. The advantages of these solution based techniques

low-cost and take a small amount of time to produce. The challenges are that higher quality films are dependent on the organic chemistry and the ability to purge unwanted contaminants in the film during the pyrolysis and annealing steps. Table 1.6 compares the various deposition methods and includes atomic layer deposition which is discussed in section 1.3.

Table 1.6. The various deposition techniques that can be used to deposit multiferroic materials

Parameter	PLD	MBE	Sputtering	MOCVD	Solution based	ALD
Deposition rate	High	Low	High	High	High	Low
Thickness control	High	High	High	High	Low	Very high
Uniformity	Medium	High	High	High	Medium	Very high
Conformity	Low	Medium	Low	Medium	Unknown	Very high
Film quality	High	Very high	Medium	Medium	Low	Medium
Integration ability	Medium	Low	Very high	Very high	Medium	Very high
Thickness	$\sim \mu\text{m}$	$\sim \text{nm}$	$\sim \mu\text{m}$	$\sim \mu\text{m}$	$\sim \mu\text{m}$	$\sim \text{nm}$

### 1.2.7 Integration of multiferroic thin films

Whereas much work has been done in materials discovery and characterization for scientific research, additional effort is required to integrate these complex metal oxide materials and realize composite multiferroic thin films for future device purposes. One major issue is the ability to fabricate these devices on large scale substrates. As the capacity to synthesize 300 mm wafers on an industrial scale exists solely on silicon, it becomes necessary to identify a way to deposit high quality complex oxides onto silicon substrates. One such method is to buffer the silicon with a thin layer of epitaxial oxide that can serve as a platform for other materials which, by themselves, may not necessarily have a good lattice match with silicon.

During the search of stable high  $\kappa$  materials on silicon, thermodynamic stability of many binary oxides and nitrides in contact with silicon were comprehensively assessed at temperatures from 300K to 1600K (Schlom and Haeni 2002) and led to the conclusion that very few oxides are indeed thermally stable on silicon. Among those, perovskite-type  $\text{SrTiO}_3$  lends itself as one of the promising materials since it has a reasonably small ( $\sim 1.7\%$ ) lattice mismatch to silicon ( $a_{0_{\text{STO}}} = 3.905\text{\AA}$  and  $a_{0_{\text{Si}}} = 5.431\text{\AA}$ ). Very high quality have been realized by molecular-beam epitaxy (Kim, Khartsev et al. 2003) and the availability of such high-quality (001)  $\text{SrTiO}_3$  perovskite-terminated (100) Si substrate provides a platform for integrating other thin film perovskite oxides onto silicon (McKee, Walker et al. 1998).

Once a suitable template has been identified, such as  $\text{SrTiO}_3$ , it becomes possible to integrate multiferroic thin films on silicon. When large wafer processing compatibility is a requirement, techniques like PLD and MBE can no longer be used, and if 3D geometry is to be taken into consideration, ALD becomes an attractive choice from the standpoint of conformal and uniform deposition that has already been demonstrated for high  $\kappa$  materials. Nonetheless, there are several key challenges that must be addressed if these complex material systems are to be fabricated using ALD. Because the material performance for composite multiferroics have been demonstrated to be more effective than intrinsic materials, the added complexity in depositing multiple oxides by ALD in a single reactor points to a concern in precursor selection. The compatibility of multiple precursors is typically determined by their reactivity to one another on the surface upon oxidation and the ALD temperature windows for each respective precursor. Whereas thermal ALD processes using  $\text{H}_2\text{O}$ ,  $\text{O}_3$ , or other gases may face some difficulties in achieving these challenges, plasma enhanced processes could enable an easier route to utilizing multiple precursors (Profijt, Potts et al. 2011). Using highly reactive oxygen atoms is another



approach to realize a constant temperature for processing multiple precursors. In addition, the reactivity between precursors could be improved using plasma, and therefore any nucleation delay may be alleviated, and the growth rate is usually enhanced. However, there are challenges with using plasma enhanced processes, namely the possibility of plasma induced damage to the film as well as less than ideal step-coverage onto high-aspect ratio features compared what can be achieved with thermal ALD. Typically, these issues can be alleviated with proper process optimization. Last but not the least, the non-epitaxial nature of the ALD growth requires post-deposition annealing to achieve the proper crystal structure of the multiferroic composites, a critical factor in realizing effective multiferroic materials. Balancing the merits and challenges of ALD processing, it becomes possible to envision nanoscale composites enabled by the ALD process, especially the multilayer 2-2 configuration which can easily be controlled by varying the number of ALD cycles of each constituent oxides. On the other hand, 3D composites would require a pre-patterned template over which ALD can form a conformal coating, such as the 1-3 configuration using ferromagnetic nanopillars embedded in an ALD ferroelectric matrix or a 0-3 configuration with porous ferroelectric template coated by an ALD ferromagnetic film.

### 1.3 Atomic Layer Deposition

Atomic layer deposition (ALD) is a technique in which specialized precursor gases are alternatively flowed onto a surface upon which they react in a self-limiting fashion.(Leskelä and Ritala 2002) ALD is similar to CVD, however, the self-limiting steps and alternating gas flow deposition sequence is what sets it apart and thus the advantages and disadvantages stem from these facts. Advantages include the capability to deposit ultra-thin films with excellent uniformity, conformal deposition over high-aspect ratio features or even 3-D structures, and an

ability to control the relative atomic composition between metal ions by manipulating the precursor sequence. On the other hand, the disadvantages are a relatively slow deposition rate, difficulty to control the absolute ion compositions precisely, and the fact that as-deposited films are typically amorphous or polycrystalline in structure. A typical setup for ALD consists of a vacuum chamber with a sample chuck that is heated on its own or by heating the entire chamber (hot wall reactor), various gas inputs that can be opened and closed individually, along with any additional monitoring hardware and electronics that can control the deposition. Important parameters that control ALD deposition are the substrate temperature which controls the growth rate, the precursor type, the oxidant type, and the cycle ratio of multiple types of precursors which can control the composition of the film.

In order to deposit a metal oxide, as shown below in Figure 1.27, ALD begins with (1) the pulsing of a metal precursor, which is typically a metalorganic molecule, that (2) reacts in a self-limiting manner to a hydroxyl  $\text{-OH}$  group on the substrate and forms a monolayer, the system is then purged either by flowing an inert gas or by pumping the chamber out, then (3) the oxidant gas is flowed and (4) removes organic ligands from the metal precursors and prepares the sample for the next metal precursor pulse by creating a newly reactive  $\text{-OH}$  terminated surface, after which the chamber is purged again and the process is repeated. In this way, multiple metal precursors can also be introduced to deposit complex thin films and different types of oxidants can be used to create oxides, sulfides, and nitrides among other compounds such as organic films using molecular layer deposition (MLD).

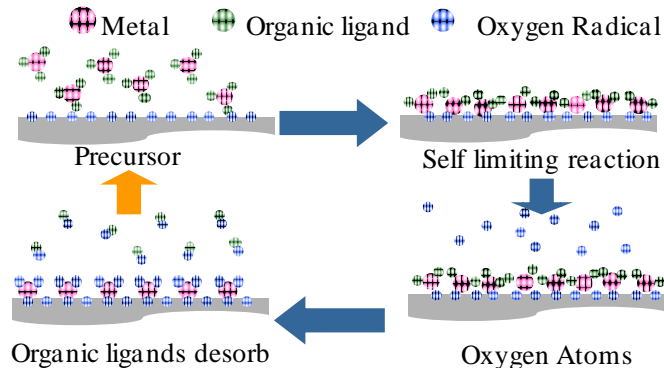


Figure 1.27. Schematic showing the steps for atomic layer deposition. (1) The metal precursor is flowed (2) a self-limiting reaction forms a monolayer of metal precursor on the surface (3) the oxidant is flowed (4) the metal precursor is oxidized

The nature of ALD allows it to have a very controllable deposition rate and highly conformal deposition, making it an attractive choice for depositing ultra-thin films over nanostructured structures. Under ideal conditions, the precursors are chosen to be as small as possible so that a full monolayer can be formed.(Leskelä and Ritala 2002) However at times, when very large precursor are used, the steric hindrances can prevent a full monolayer from forming and thus epitaxial growth may be difficult. Also, it is important that each step completes to saturation so that the growth is consistent throughout the entire deposition sequence. The typical pulse time for each precursor can be between ~0.5 to a few seconds depending on the reactivity.

Much work has been done to study ALD precursors and precursor chemistry.(Leskelä and Ritala 2003) An ALD precursor must be self-limiting meaning that chemisorption does not continue to occur once an initial monolayer has been saturated. Additionally, it is important to select precursors that easily react with the oxidant and thus it is important to pair precursors with compatible oxidants. The ALD processing window is defined as the temperature range within which ALD growth is controlled and relatively constant. Temperatures below the ALD window

result either in minimal growth due to lack of thermal energy for surface reactions or increased growth due to precursor physisorption resulting in higher carbon contamination. On the other hand, temperatures above the ALD window can cause higher deposition rates due to precursor decomposition causing substantially increased carbon contamination or lower deposition rates due to precursor desorption and failure to adsorb on the surface. For most cases, the processing window is wide and permits deposition at temperatures less than 400 °C. This is important for materials which are sensitive to high temperatures and gives flexibility to the ALD process. Typically, the lower limit for the temperature is determined by the reactivity of the precursor while the upper limit is where the precursor becomes decomposed.(Leskelä and Ritala 2002) It is necessary that the temperatures remain low enough such that the precursors are thermally stable and that decomposition does not occur, otherwise the self-limiting aspects could be lost as well as the associated benefits. In general, the precursor families for metals include halides, alkyl compounds, and alkoxides while the oxidation gas can be water, ozone, hydrogen peroxide, or atomic oxygen for oxides; ammonia, hydrazine, and amines for nitrides; and hydrides for group V elements.(Leskelä and Ritala 2002)

While ALD usually has a lower processing temperature than CVD processes, there are times when the thermal ALD temperature window or precursor chemistries are not compatible with the criterion for the specific application. To alleviate these issues, plasma enhanced ALD (PE-ALD) or plasma assisted ALD have been employed to deposit a variety of materials including oxides, nitrides, and metals using O<sub>2</sub>, N<sub>2</sub>, and H<sub>2</sub> plasmas respectively.(Kim and Rossmagel 2002; Lee, Cho et al. 2002; Lao, Martin et al. 2005; Profijt, Potts et al. 2011) In other examples, a microwave powered atomic or radical source have also been used.(Van and Chang 2005; Van and Chang 2005; T. Van, Hoang et al. 2006; Hoang, T. Van et al. 2007; Hoang,

Schwartz et al. 2012; Hoang, Schwartz et al. 2012) A comprehensive overview of plasma enhanced ALD can be found in the review by Profijt, et al. (Profijt, Potts et al. 2011) so only a brief literature review is covered here, where some of the benefits, challenges, and potentials for PE-ALD are discussed. There are several advantages to plasma enhanced or plasma assisted ALD including improved film properties, reduction of substrate temperature, expanded selection of precursors and resultant materials, easier control of film stoichiometry and composition especially for nitrides, enhanced growth rate, and the ability to use plasma as a surface treatment tool. Some challenges arise however due to some unique aspects of the nonequilibrium species contained within plasma including reduced step-coverage or conformality due to sidewall recombination of radical species for high aspect-ratio features as well as the potential for ion-induced damage. These factors can fortunately be mitigated with proper process optimization. Currently, plasma assisted ALD is uniquely capable of providing higher quality nitride and (semi)metal films for use in the semiconductor industry with greater throughput and film quality when compared to the thermal ALD process counterparts. In addition, for complex metal oxide films, which are the focus of this work, plasma assisted methods enable a higher degree of freedom when utilizing certain precursor chemistries due to the improved reactivity of atomic oxygen over other oxidants like water and ozone.

### *1.3.1 ALD of ferroic and multiferroic thin films*

As discussed in 1.2, the synthesis of multiferroic thin-films has been studied in-depth using high quality deposition techniques such as MBE and PLD. Consequently, the desired integration of such a multiferroic material into novel memory devices motivates the study of extending BFO growth into methods which enable large scale manufacturing. Such an approach

is ALD due to its superior step coverage on three-dimensional features, atomic-scale thickness control, and conformal uniformity over large area wafers, and is currently being utilized in the semiconductor industry as the technique of choice for other complex metal oxides like hafnium based high- $\kappa$  gate dielectrics as well as other steps such as FinFET sidewall isolation, gap fill, and interconnect lining which all require atomic scale thickness control and center-to-edge wafer uniformity (Auth, Allen et al. 2012; Marchack and Chang 2012; Clarke, George et al. 2014).

Multiferroic thin films such as  $\text{BiFeO}_3$  (Akbashev, Chen et al. 2013; Liu, Ku et al. 2013; Zhang, Sun et al. 2013; Jalkanen, Tuboltsev et al. 2014),  $\text{YMnO}_3$  (Uusi-Esko, Malm et al. 2009), and other rare-earth manganates (Uusi-Esko and Karppinen 2011) have been demonstrated using thermal ALD processes, indicating the potential application of ALD in synthesizing multiferroic thin films. In addition, ferroelectric oxides such as  $\text{BaTiO}_3$  (Vehkamäki, Hatanpää et al. 1999),  $\text{Pb}(\text{Zr},\text{Ti})\text{O}_3$  (Zhang, Perng et al. 2011; Choi, Zhang et al. 2013), and  $\text{BiTiO}_3$  (Cho, Min et al. 2003; Harjuoja, Väyrynen et al. 2006; Vehkamäki, Hatanpää et al. 2006); as well as magnetic oxides such as  $\text{CoFe}_2\text{O}_4$  (Lie, Barnholt Klepper et al. 2008) and  $\text{NiFe}_2\text{O}_4$  (Chong, Yau et al. 2010) have also been shown. However, at the time of this writing, there had been no reports of using ALD to enable the synthesis of composite multiferroic films. Therefore, the focus of this work was to use radical enhanced ALD to enable nanostructured composite multiferroic thin films by integrating single-phase (multi)ferroic oxides such as yttrium manganese oxide ( $\text{YMnO}_3$ ), bismuth iron oxide ( $\text{BiFeO}_3$ ), and cobalt iron oxide ( $\text{CoFe}_2\text{O}_4$ ) either through purely ALD processing or by some other hybrid methods. Afterwards, materials characterization on those films would be conducted to examine the crystalline and/or nano-structure, which would lead towards understanding the resulting magnetic and/or ferroelectric properties as well as the magnetoelectric coupling exhibited by these compounds.

So far, the synthesis of YMO has been accomplished using a variety of techniques such as pulsed-laser deposition (Fujimura, Shigemitsu et al. 2007; Li, Yan et al. 2009; Singh, Snure et al. 2009), sol-gel deposition (Kitahata, Tadanaga et al. 2000), sputtering (Fujimura, Ishida et al. 1996; Zapata, Narvaez et al. 2008), metal-organic chemical vapor deposition (Bosak, Kamenev et al. 2001; Kim, Killingsmith et al. 2006) and molecular beam epitaxy (Imada, Kuraoka et al. 2001; Chye, Liu et al. 2006). Regarding substrates, depending upon the deposition method used it has been reported that YMO films on Si (111) exhibits both o- and h- phases (Aoki, Fujimura et al. 1997; Imada, Shouriki et al. 1998). On the other hand, when the substrates had similar lattice parameters, such as YSZ (111), only h-YMO was observed due to the reduced lattice misfit (Dho, Leung et al. 2004). ALD, which consists of self-limiting surface reactions has previously been demonstrated to be a viable route to the synthesis of YMO, (Uusi-Esko, Malm et al. 2009) and due to the conformal nature of the films could also enable complex nanostructured composites in 2D-2D, 3D-1D or 3D-0D geometries for nanostructured composite multiferroic systems (Zheng, Straub et al. 2006; Nan, Bichurin et al. 2008). Recently, Uusi-Esko *et al.* demonstrated the growth of h-YMO on Si(100) and o-YMO on  $\text{LaAlO}_3$  and  $\text{SrTiO}_3$  using thermal ALD processes with ozone as an oxygen source (Uusi-Esko, Malm et al. 2009; Uusi-Esko and Karppinen 2011). However, so far the magnetic properties of YMO ultra thin films have not been fully characterized. Thus, as shown in Chapter 3, motivated by the potential applications in magnetoelectric devices, YMO is demonstrated using radical enhanced atomic layer deposition and the magnetic properties are shown while using the structural data to provide context for the observed properties.

$\text{BiFeO}_3$  (BFO) is a single-phase multiferroic material with both ferroelectricity ( $T_C = 1103 \text{ K}$ ) and anti-ferromagnetism ( $T_N \sim 643 \text{ K}$ ), which both exist above room temperature

(Section 1.2.4), which makes the study of BFO an active area of research both scientifically due to its unique properties and technologically due to the potential impact for future memory devices which utilize voltage-switched magnetism (Section 1.1.6) (Wang, Neaton et al. 2003; Chu, Martin et al. 2007; Catalan and Scott 2009). Although BFO growth by thermal ALD using water or ozone as the oxidant have been described elsewhere (Akbashev, Chen et al. 2013; Liu, Ku et al. 2013; Zhang, Sun et al. 2013; Jalkanen, Tuboltsev et al. 2014), there have not been any reports of plasma-enhanced or radical-enhanced ALD processes for BFO so far. Additionally, it is important to note that the ALD growth of individual oxides  $\text{Bi}_2\text{O}_3$  (Hatanpaa, Vehkamaki et al. 2010; Shen, Li et al. 2012) and  $\text{Fe}_2\text{O}_3$  (Lie, Fjellvåg et al. 2005; Rooth, Johansson et al. 2008) have also been reported, again however, there have been no publications for plasma-enhanced or radical-enhanced processes. Therefore, as described in Chapter 4, the study of BFO growth using radical enhanced ALD is motivated by the ability to synthesize the films at a lower deposition temperature and the resulting structural and material properties are demonstrated.

$\text{CoFe}_2\text{O}_4$  (CFO) is a ferrimagnetic ternary oxide with an inverse  $\text{MgAl}_2\text{O}_4$  (spinel)-type structure. Because of its robust magnetic properties and potential use in technological applications, most notably for magnetic data storage for microelectronics, spintronics, sensors, etc., there has been a wealth of scientific literature for CFO in bulk, thin film, and nano-scale form. In the past, CFO had been synthesized in a multitude of manners including bulk synthesis in powder (Gibart, Robbins et al. 1974) and single crystal (Bozorth, Tilden et al. 1955) forms, as well as thin films using pulsed laser deposition (Suzuki, Hu et al. 1999), magnetron sputtering (Rigato, Geshev et al. 2009), sol-gel deposition (Quickel, Le et al. 2010), chemical vapor deposition (Coll, Montero Moreno et al. 2014), and atomic layer deposition (Kato and Takei 1933; Lie, Barnholt Klepper et al. 2008; Chong, Yau et al. 2010). Throughout the literature, CFO



has also been used as the magnetic component for composite multiferroic materials as described in 1.2.5 using 0-3 (Liu, Fu et al. 2005; Wan, Wang et al. 2005), 2-2 (Ortega, Kumar et al. 2008; Sim, Pan et al. 2008; He, Ma et al. 2009; Wu and Wang 2009), and most notably 1-3 configurations (Dho, Leung et al. 2004; Zheng, Straub et al. 2006; Zheng, Kreisel et al. 2007; Zheng, Wang et al. 2008; Dix, Muralidharan et al. 2009; Yan, Xing et al. 2009; Yan, Wang et al. 2010; Aimon, Kim et al. 2012; Aimon, Choi et al. 2014; Kim, Aimon et al. 2014). Thus, motivated by the potential for a large magnetoelectric coupling coefficient using nanostructured multiferroic composites, an RE-ALD process for CFO was developed with the intention to integrate it with the BFO process as described in Chapter 4. In Chapter 5, therefore, the process for CFO growth using RE-ALD and the structural and magnetic film characterization is described.

#### 1.4 Scope and Organization

Motivated by the potential for voltage controlled magnetism as a possible route for new low-power memory devices, the varieties of research on multiferroic materials were abundant and diverse. However, in order to fully realize the integration of these complex metal oxides, it was necessary to develop a method to synthesize the films which was compatible with the large scale manufacturing for the semiconductor industry, such as atomic layer deposition (ALD). As a result, the following chapters contained herein describe ALD processes that were developed to synthesize  $\text{YMnO}_3$ ,  $\text{BiFeO}_3$  and  $\text{CoFe}_2\text{O}_4$  and subsequently used to synthesize nanoscale multiferroic composites with different nanostructure configurations. The ability of the ALD technique to control the thickness of these conformal films resulted in the tunability of the nanostructure, and the resulting effect upon the functional properties was studied.

Chapter 2 consists of the experimental details for synthesizing and characterizing the thin films, beginning with a description of the radical enhanced ALD reactor, including the coaxial microwave cavity atomic beam source and the metalorganic precursor doser arrays; a description of the chemicals used in the experiments; and finally detailed descriptions of the instruments used to study the structural, chemical, and properties such as ferroelectricity and ferromagnetism.

Chapter 3 describes the ALD growth and characterization of the ferroelectric and antiferromagnetic multiferroic  $\text{YMnO}_3$  (YMO). The composition and structure of the YMO films with different crystal structures, substrates, and processing conditions are discussed and the magnetic properties are shown.

Chapter 4 describes the ALD growth and characterization of the ferroelectric and antiferromagnetic multiferroic  $\text{BiFeO}_3$  (BFO). The ALD synthesis of the binary oxides  $\text{Bi}_2\text{O}_3$  and  $\text{Fe}_2\text{O}_3$  are shown followed by the integration of the binary oxides to form the BFO ternary oxide. The structure of the films characterized by XRD and TEM are discussed and its multiferroic properties are examined.

Chapter 5 describes the ALD growth and characterization of the ferromagnetic oxide  $\text{CoFe}_2\text{O}_4$  (CFO). The processing for the binary oxides  $\text{Co}_3\text{O}_4$  and  $\text{Fe}_2\text{O}_3$  are discussed as well as the combination of the two to form high quality CFO thin films. In addition, the magnetic properties as a function of the film thickness and annealing conditions are shown.

Chapter 6 describes the ALD growth and characterization of the multilayer 2-2 configuration nanoscale multiferroic composite  $\text{BiFeO}_3/\text{CoFe}_2\text{O}_4$  as well as the ALD enabled filled mesoporous thin films with a 0-3 configuration for  $\text{BiFeO}_3/\text{CoFe}_2\text{O}_4$  and  $\text{Pb}(\text{Zr,Ti})\text{O}_3/\text{CoFe}_2\text{O}_4$ . The processing details are discussed and the characterization of the material properties is shown.

## CHAPTER 2: EXPERIMENTAL SETUP

This chapter illustrates, in three components, the experimental setup that was utilized in this study. In the first section, the ultra-high vacuum (UHV) multi-beam (MB) chamber used for radical enhanced atomic layer deposition is described, which includes the coaxial microwave cavity radical beam source and the metalorganic precursor dosers. Second, the chemicals and material systems used in the study are detailed. Metalorganic precursors used in this study were metal  $\beta$ -diketonates, specifically, tris (2,2,6,6)-tetramethyl-(3,5)-heptanedione metal(III) compounds, or abbreviated as  $M(\text{TMHD})_3$  ( $M = \text{Bi, Fe, Co}$ ). With the radical beam source, atomic oxygen was used as the oxidant. The films were deposited on Si(100),  $\text{SrTiO}_3$  (001) (STO), and  $\text{Nb:SrTiO}_3$  (001) (Nb:STO). Third, the material characterization methods are explained in detail. Specifically, X-ray photoelectron spectroscopy (XPS) was used to elucidate the film atomic composition, X-ray diffraction spectroscopy (XRD) was used to examine crystal structure, X-ray absorption spectroscopy (XAS) was used to probe atomic environments, superconducting quantum interference device (SQUID) magnetometry was used to measure the magnetic responses, and scanning probe microscopy was used in the form of atomic force microscopy (AFM) for surface topology, and piezoresponse force microscopy (PFM) was used to detect and modify ferroelectric domains.

## 2.1 Multi-Beam (MB) chamber

The multi-beam system used in this study, seen in Figure 2.1, consisted of a 10''-outer diameter stainless steel main chamber along with a load lock assembly that facilitated sample insertion and removal without exposing the entire system to atmosphere. Affixed to the main chamber ports were several components: a coaxial microwave cavity radical beam source used to introduce highly reactive atomic oxygen to the sample, a six precursor doser array used to introduce evaporated metalorganic precursor fluxes to the sample, a temperature-controlled sample stage, and a hot filament ion gauge which was used to measure the chamber pressure. Pressure in the chamber was maintained between  $1 \times 10^{-6}$  Torr at base and  $2 \times 10^{-5}$  Torr during operation using a CTI 4000 L/s cryogenic pump. At the top of the chamber was a 10''-quartz window that was used to facilitate beam alignment to the sample. The load lock base pressure was maintained at approximately  $1.0 \times 10^{-5}$  Torr by a 56 L/s Pfeiffer-Balzers turbomolecular pump backed by a 6.67 L/s Leybold mechanical pump and was measured by an MKS Micropirani gauge. In the following subsections 2.1.1 and 2.1.2, both the radical beam source and the precursor dosers are described in more detail.

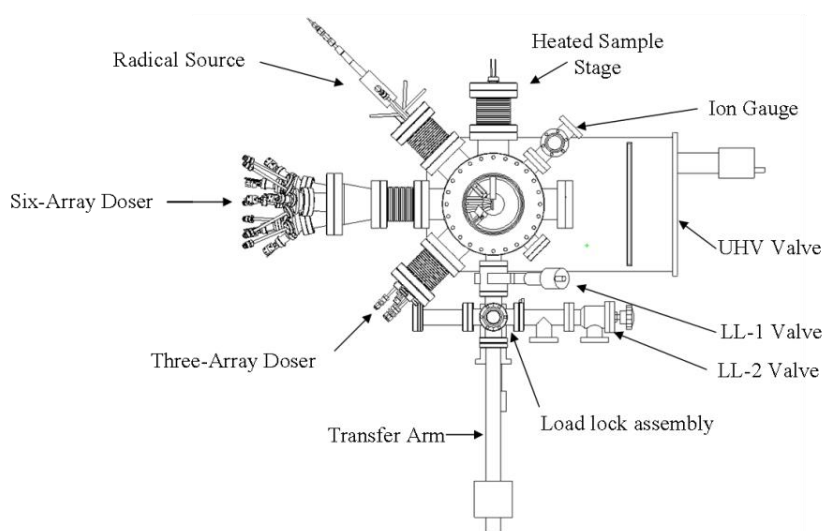


Figure 2.1 Top-down schematic of multi-beam chamber (Hoang 2011)

### 2.1.1 Coaxial microwave cavity radical beam source

Schematic drawings for the coaxial microwave cavity radical beam source used for atomic oxygen generation are shown in Figure 2.2. The radical source was originally developed in order to improve upon the shortcomings of a traditional remote microwave plasma source. (Chang, Arnold et al. 1997) The long distance needed to be traversed before reaching the sample meant that radicals were more likely to recombine with the wall, thereby limiting the available radical flux. Instead, the radical beam source was designed to have the plasma at the vacuum side within close proximity to the sample surface. This in turn substantially reduced the amount of radicals that recombined with the walls of the enclosure and maximized the flux of atoms that were transported to the sample.

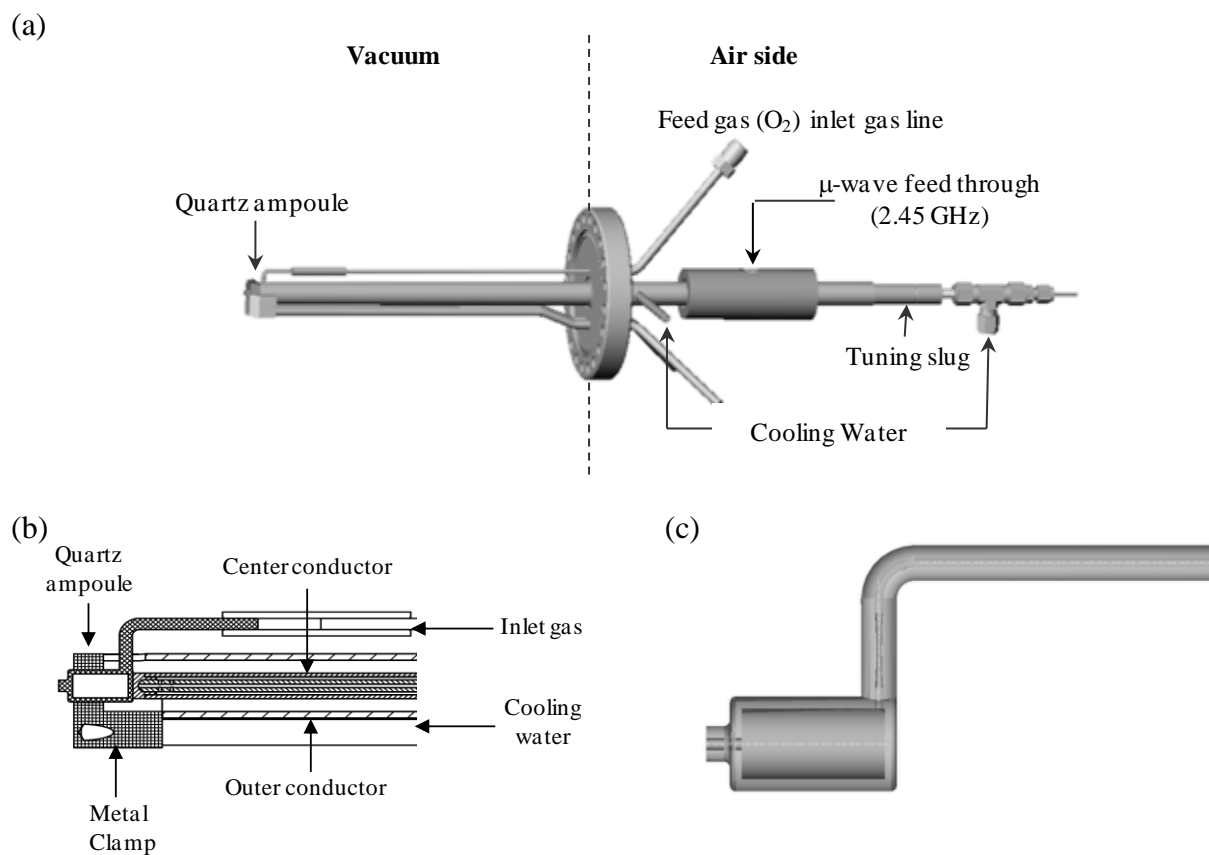


Figure 2.2 (a) Schematic of coaxial microwave cavity radical beam source (b) Schematic showing magnified view of quartz ampoule and radical source cross-section (c) Example of quartz ampoule with aspect ratio of 3 ( $D \times L = 1 \times 3$  mm)

The cavity consisted of two coaxial conductors; one hollow 0.25” center conductor and one 0.625” outer conductor, which were fixed in series by a metal clamp which surrounded a quartz ampoule at the end. Using a coaxial cavity, in contrast to a waveguide, allowed the radical beam source to have a smaller diameter than the ~10 cm microwave wavelength. The cavity was vacuum sealed by two Teflon bushings which sealed up to  $\sim 10^{-8}$  Torr; the two Teflon bushings formed a small volume which was differentially pumped via mechanical pump in order to reduce the leak rate of the radical source. Gas was fed from the air side through a vacuum feed through built onto the radical beam source and then entered the quartz ampoule through a channel. The plasma was generated inside the quartz ampoule when the microwave power dissociated the feed gas. Microwave power was supplied by a 2.45 GHz, 300 W (maximum) Sairem microwave power supply using an N-type connector which was attached in series to the center conductor.

Operation of the radical beam source was dependant on the resonance condition of the microwave cavity, which acted similarly to an “Evenson” cavity. At the resonance condition, reflected power was minimized and the most efficient operation was realized. The resonance condition was determined by:

$$\frac{2\pi L}{\lambda} = \tan^{-1} \left( \frac{1}{Z_0 \omega C_0} \right) \quad \text{Eq. (2.1)}$$

where the impedance of the cavity is given by  $Z_0$ , the microwave frequency (2.45 GHz) is given by  $\omega$ , the capacitance of the end of the cavity is given by  $C_0$ , and the wavelength of the microwave frequency is given by  $\lambda$ . When the gap between the center conductor and the end of the metal clamp was smaller than  $\lambda$  and  $Z_0 \omega C_0 \ll 1$ , the resonance cavity length could be estimated as

$$L_{\text{resonance}} = \left( \frac{n}{2} + \frac{1}{4} \right) \lambda, \text{ where } n = 0, 1, 2, 3... \quad \text{Eq. (2.2)}$$

Therefore, the resonance condition could be achieved by adjusting the cavity length to an integral number of half-wavelengths which was easily accomplished using the tuning slug and the movable collar where the N-type connector was fixed, both located on the air-side. During operation, the radical beam source was operated at 25 W forward power, 1 W reflected power.

Molecular oxygen, at 99.999% purity, was fed to the quartz ampoule at a rate between 0.5 and 0.75 sccm; the rate was controlled by an MKS instruments mass flow controller. The quartz ampoule itself could control the characteristics of the radical beam output depending on the volume, shape, and channel dimensions. Radical flux could be estimated by calculating the conductance  $C$  through the nozzle of the quartz ampoule using the Hagen-Poiseuille equation (O'Hanlon 2003):

$$C = \frac{\pi D^4}{128 \eta l} \frac{P_1 + P_2}{2} \quad \text{Eq. (2.3)}$$

where  $D$  is the diameter of the nozzle,  $l$  is the length,  $P_1$  and  $P_2$  are the pressures at either end of the nozzle, and  $\eta$  is the gas dynamic velocity. Using gas kinetic theory, the gas dynamic velocity  $\eta$  could be estimated:

$$\eta = \frac{0.499 (4mk_B T)^{1/2}}{\pi d^2} \quad \text{Eq. (2.4)}$$

where  $m$  is the mass of the gas molecule,  $k_B$  is the Boltzmann constant ( $1.38 \times 10^{-23}$  J/K),  $T$  is the gas temperature (assumed to be 300 K), and  $d$  is the gas molecule collision diameter. Thus,  $\eta$  for  $\text{O}_2$  could be estimated as  $2 \times 10^{-5}$  Pa·s (Lide 2010). Assuming that the  $\text{O}_2$  flow rate was 1 sccm,  $P_1 + P_2 \approx 733$  Pa and with both  $D$  and  $l$  at 1 mm, the conductance was estimated at  $4.5 \times 10^{-4}$  m<sup>3</sup>/s

which corresponded in a radical flux of  $5.7 \times 10^{19}$  radicals/s exiting the nozzle when 80% oxygen feed gas dissociation was assumed.

Since the plasma emits a large amount of heat during operation, the beam source was designed to utilize water cooling, as heat dissipation is challenging in vacuum environments in the absence of conductive gaseous media. Cooling water was fed through both the metal holder for the quartz ampoule and the center conductor. The quartz ampoule holder consisted of a piece of stainless steel that was clamped to the ampoule at the top and a hollow block of stainless steel that cooling water flowed through at the bottom. To facilitate conductive heat transfer, the quartz ampoule was wrapped with a thin layer (~0.25 mm thick) of 99.9975% purity indium foil. The center conductor was a hollow 0.25” stainless steel tube coated with gold through which an additional 0.125” inner tube sat inside; cooling water was flowed into the inner tube and exited through the annular space between the inner tube and the center conductor.

Additionally, the radical beam source had an ignition wire that was wrapped around the channel of the quartz ampoule and was attached to a high voltage feed through. The plasma could be ignited manually by touching the feed through with a Tesla coil while applying microwave power.

During normal operation, the radical beam source was controlled remotely by LABVIEW software and a National Instruments (NI) DAQ USB-9481 relay module which turned on and off the microwave power. After the resonance condition had been reached by tuning the radical source, applying microwave power while the feed gas was flowing (at ~1 sccm) resulted in spontaneous ignition of the plasma within the quartz ampoule. At a sample temperature of 573 K, it was found previously that molecular oxygen did not react to the TMHD ligands allowing



the flow of precursor and molecular oxygen simultaneously without causing CVD growth. (Van and Chang 2005)

### 2.1.2 Metalorganic precursor doser arrays

In order to deliver the metalorganic precursors to the substrate, precursor dosers were used, each consisting of a precursor housing, pneumatic valve, and heated gas line. Each precursor had an individual doser in order to prevent cross contamination seen in Figure 2.3, using parts from MDC Vacuum, Nor Cal products, Swagelok, and Insulator Seal. The six doser array consisted of three 5-way 1.33" CF to 2.75" CF multiports which were themselves mounted on a single 3-way 2.75" CF to 6" CF multiport. The 6" CF multiport led to a 6" CF to 4.625" CF conical reducer. The doser was then equipped with a 4.625" CF bellow that led to the chamber. The bellow allowed for manual alignment of the doser beams towards the sample surface.

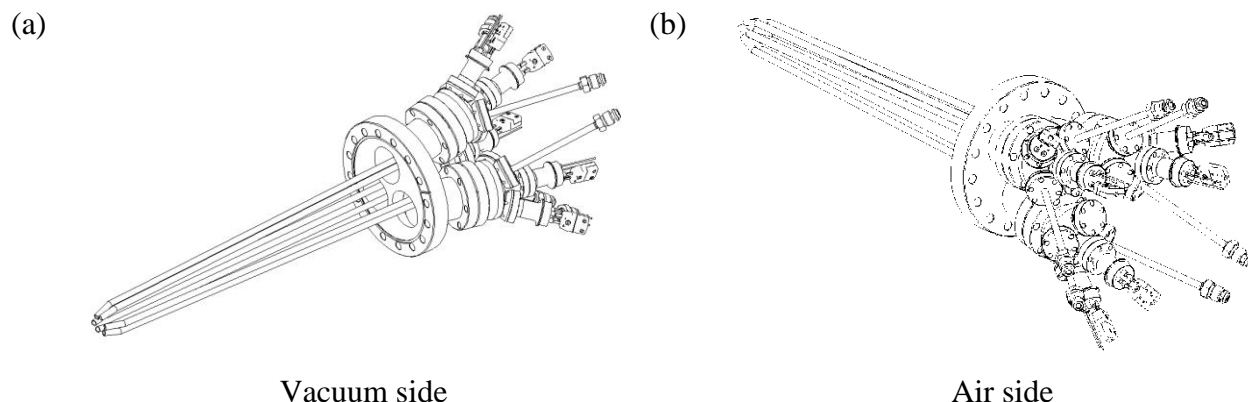


Figure 2.3 Schematic drawings showing (a) vacuum side and (b) air side for six doser array designed in-house

For a single doser line, solid precursor in powder form was held inside the housing which was a 1.33" OD, 3" long stainless steel nipple with a Conflat flange, with a cap on one end, and led to a SS-HB series Swagelok brand pneumatic valve at the other end using VCR fittings. The pneumatic valve controlled the introduction of evaporated precursor gas into the chamber by a

0.25” stainless steel feed through with an air-side VCR fitting. On the vacuum side, the feed through was welded to an additional 0.25” stainless steel line that terminated approximately 2” from the sample surface. Air side gas lines, pneumatic valves, and housings were heated by wrapping heat rope acquired from McMaster-Carr supply company, whereas in-vacuum gas lines were heated by flexible Kapton™ heaters. The temperatures for the gas lines were measured by Omega brand Cr/Al K-type thermocouples and were controlled by several Omega CN1500 series multi-zone ramp and soak controllers which consisted of seven independent PID temperature controllers. For the automated deposition, the pneumatic precursor valves were controlled by LABVIEW software through NI USB-9481 general purpose relay modules.

## 2.2 Precursor choice and processing conditions

The metal  $\beta$ -diketonate precursors used in this study were bis(2,2,6,6-tetramethyl-3,5-heptanedionato) Cobalt (III)  $[\text{Co}(\text{TMHD})_2]$ , Tris(2,2,6,6-tetramethyl-3,5-heptanedionato) bismuth (III)  $[\text{Bi}(\text{TMHD})_3]$ , Tris(2,2,6,6-tetramethyl-3,5-heptanedionato) iron (III)  $[\text{Fe}(\text{TMHD})_3]$ , Tris(2,2,6,6-tetramethyl-3,5-heptanedionato) manganese (III)  $[\text{Mn}(\text{TMHD})_3]$ , and Tris(2,2,6,6-tetramethyl-3,5-heptanedionato) yttrium (III)  $[\text{Y}(\text{TMHD})_3]$  for which the physical properties are shown in Table 2.1.

Table 2.1. Physical properties of metalorganic precursors used in this work: Co(TMHD)<sub>2</sub>, Bi(TMHD)<sub>3</sub>, Fe(TMHD)<sub>3</sub>, Mn(TMHD)<sub>3</sub>, and Y(TMHD)<sub>3</sub>

	Co(TMHD) <sub>2</sub>	Bi(TMHD) <sub>3</sub>	Fe(TMHD) <sub>3</sub>	Mn(TMHD) <sub>3</sub>	Y(TMHD) <sub>3</sub>
CAS Number	13986-53-3	142617-53-6	14876-47-2	14324-99-3	15632-39-0
Melting point (°C)	143°C	114-116°C	164°C	165°C	170-173°C
Boiling point(°C)	Not determined	dec. 295°C	dec. 300°C	dec. 255°C	dec. 290 °C
Vapor pressure (Torr)	Not determined	0.05mm	Not determined	Not determined	Subl. 95°C/0.05 mm
Company	Alfa Aesar	Strem Chemicals, Inc.	Strem Chemicals, Inc.	Strem Chemicals, Inc.	Strem Chemicals, Inc.

For this precursor family, the TMHD ligand was formed by substituting the methyl substituents on acetylacetone with the bulky *tert*-butyl moiety. The molecular structure of the  $M(TMHD)_3$  precursor, with  $M = Co, Bi, \text{ or } Fe$  is shown in Figure 2.4. The Co(TMHD)<sub>2</sub>, Bi(TMHD)<sub>3</sub>, and Fe(TMHD)<sub>3</sub> precursors, of 99.9% purity on a metals basis (Alfa Aesar and Strem Chemicals, Inc.), were solids at room temperature (Strem Chemicals 2005).

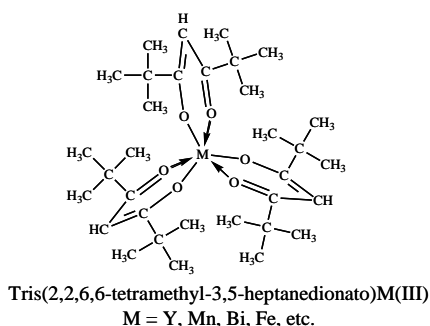


Figure 2.4 Molecular structure of Tris(2,2,6,6-tetramethyl-3,6-heptanedionato)M(III) precursor where  $M = Co, Bi, Fe, \text{ etc.}$

Each precursor was housed in a 1.33''-diameter by 4.93''-long electropolished Conflat tube that was connected directly to the precursor doser through a Swagelok pneumatic valve. In all experiments performed, the precursor vapor was delivered to the reaction chamber without a

carrier gas by heating the precursor housing. The temperatures that the precursors were heated at, as shown in Table 2.2 were chosen to enable high enough vapor pressure for sufficient precursor flux while minimizing decomposition and therefore carbon contamination. Molecular oxygen ( $O_2$ ) of 99.999% purity was used as the feed gas for the radical source.

Table 2.2 Process conditions for the respective precursors

Parameter	Co(TMHD) <sub>2</sub>	Bi(TMHD) <sub>3</sub>	Fe(TMHD) <sub>3</sub>	Mn(TMHD) <sub>3</sub>	Y(TMHD) <sub>3</sub>
Evaporation housing temperature (°C)	120	140-160	120-130	130	110-130
Doser gas-line temperature (°C)	190	210	190	170	170
In-vacuum gas-line temperature (°C)	185	185	185	170	170
Precursor Pulse time (s)	45-90	45-90	45-90	10-30	10-30
Pump down 1 (s)	5	5	5	5-15	5-15
Atomic oxygen pulse time (s)	20	20	20	20-30	20-30
Pump down 2 (s)	5	5	5	5	5

The composition of the thin films were controlled by pulsing the precursors in a sequence as shown in Figure 2.5 which consisted of  $a$  cycles of Bi(TMHD)<sub>3</sub>:O and  $b$  cycles of Fe(TMHD)<sub>3</sub>:O for BiFeO<sub>3</sub> or  $c$  cycles of Co(TMHD)<sub>2</sub>:O and  $d$  cycles of Fe(TMHD)<sub>3</sub>:O for CoFe<sub>2</sub>O<sub>4</sub>. The desired thickness was realized by controlling the number of global cycles  $n$ , consisting of repeated  $x$  cycles for BiFeO<sub>3</sub> or  $y$  cycles of CoFe<sub>2</sub>O<sub>4</sub>. A similar approach was used for YMnO<sub>3</sub> thin films by adjusting the ratio between the Y and Mn precursor pulse sequence. For the experiments that were performed, the process conditions are shown in Table 2.2. For the atomic layer deposition sequences, the process consisted of repeating cycles of a metalorganic precursor dose, followed by a pump-down to prevent gas-phase reactions, followed by the atomic oxygen pulse, and finished with a subsequent pump-down.

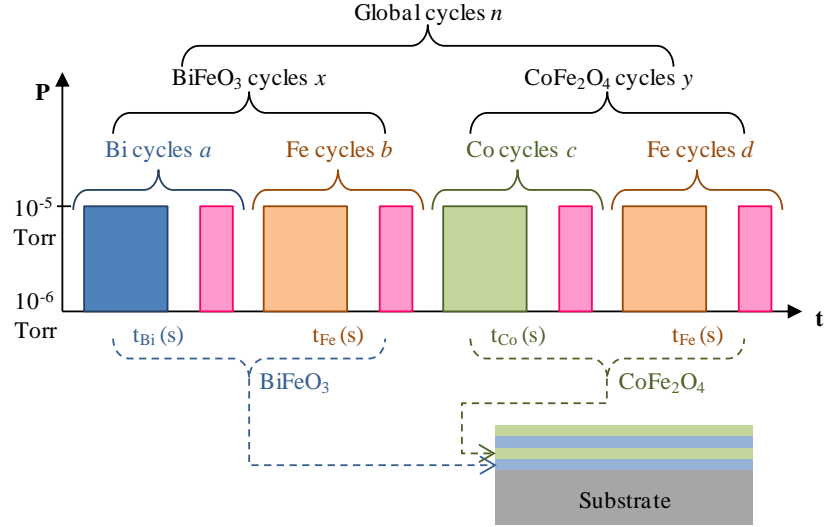


Figure 2.5. Precursor pulsing sequence for BiFeO<sub>3</sub> and CoFe<sub>2</sub>O<sub>4</sub> using ALD

### 2.3 Materials characterization

In this section, the principles for operation of the materials characterization techniques are discussed. Each sub-section describes the physical phenomena that were exploited to extract information about the thin film materials as well as the analysis techniques to interpret the data.

#### 2.3.1 X-ray Photoelectron Spectroscopy (XPS)

Albert Einstein's famous discovery of the photoelectric effect, which garnered him the Nobel Prize in physics, was defined by his observance that a photon with sufficient energy could eject an electron from an atom. (Wagner and Muilenberg 1979; Alford, Feldman et al. 2007) This was quantified by the following energy conservation equation:

$$KE = h\nu - BE - \Phi \quad \text{Eq. (2.5)}$$

where  $KE$  is the kinetic energy of the ejected electron,  $h\nu$  is the energy of the incident photon,  $BE$  is the characteristic binding energy of the electron in the atom, and  $\Phi$  is the spectrometer work function. The photoelectric effect was the basis for several spectroscopy techniques used

for the characterization of materials known as Electron Spectroscopy for Chemical Analysis or ESCA. Since the spectra of binding energies for the electrons were quantized and unique to each element, they could be tabulated and used in order to characterize new samples of unknown composition. Typically, these techniques utilized ultraviolet (Ultraviolet Photoelectron Spectroscopy; UPS) or X-ray (X-ray Photoelectron Spectroscopy; XPS) emission sources, which could be equipped with a monochromator for superior energy line width, and used detectors which counted the intensity, or the number of electrons over time, for a given energy. An example XPS spectra is shown in Figure 2.6. For the purposes of this work, only XPS was used since it could detect the heavier ions in the films that were studied. In the experiments performed for this work, the instrument used was a Kratos DLD Axis Ultra, utilizing an aluminum anode X-ray source at 1486.6 eV that was equipped with a monochromator. For the spectra that were collected, the pass energy was 160 eV for large area survey scans and 20 eV for detailed elemental scans.

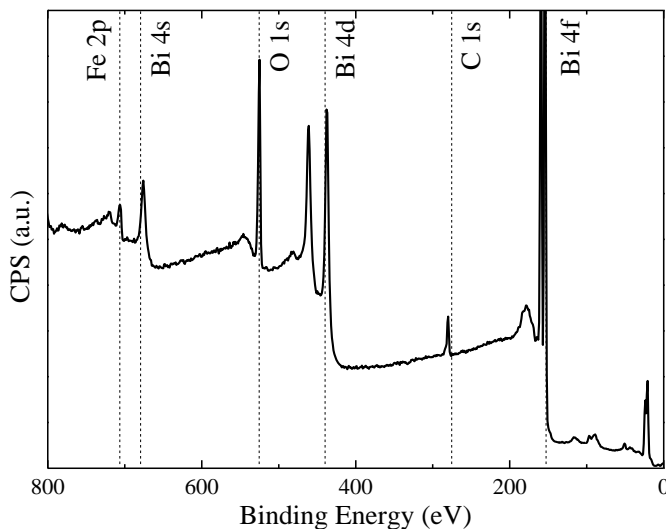


Figure 2.6 XPS spectra of  $\text{BiFeO}_3$  sample showing major elemental peaks

While X-rays could penetrate quite deeply into a sample, the outgoing electrons had an inelastic mean free path (IMFP) of approximately 30-50 Å and it had been shown that XPS could only probe the first 90-100 Å of the film, or three times the IMFP, before the signal was exponentially attenuated by over ~95%. (Powell and Jablonski 2000) Aside from Hydrogen and Helium, of which the binding energies were too low, XPS could detect all of the elements in the periodic table. Additionally, the binding energies for individual ions may have shifted due to the chemical environment and thus qualitative information regarding chemical bonding could be obtained. Once the spectral peaks had been assigned to the corresponding elements, the atomic concentrations for each constituent in the film could be calculated using Eq (2.6):

$$C_i = \frac{I_i / ASF_i}{\sum_{i=1}^n (I_i / ASF_i)} \quad \text{Eq. (2.6)}$$

where  $I_i$  and  $ASF_i$  are the integrated intensity of the photoemission spectral peak and the corresponding atomic sensitivity factor for species  $i$ , respectively. For deposited films that had a thickness below 80 Å, the substrate peak would typically be visible on the XPS spectra. Using this fact, a method developed by Hill et al. could be used to estimate the thickness of the deposited film utilizing Eq. (2.7):

$$t = \lambda \sin \theta \ln \left( 1 + \frac{I_o / ASF_o}{I_s / ASF_s} \right) \quad \text{Eq. (2.7)}$$

where  $\lambda$  is the IMFP of the photoelectron within the material, assumed to be ~30 Å;  $\theta$  is the take-off angle which is 90° with respect to the sample surface,  $I_o$  and  $I_s$  are the integrated photoelectron intensities of the overlayer and the substrate elemental peaks respectively, and  $ASF_o$  and  $ASF_s$  are the corresponding atomic sensitivity factors. When depositing films with

more than one metal cation, the sum of the integrated intensities divided by the corresponding atomic sensitivity factors was used in place of the overlayer term as shown in Eq. (2.8):

$$t = \lambda \sin \theta \ln \left( 1 + \frac{I_A / ASF_A + I_B / ASF_B}{I_s / ASF_s} \right) \quad \text{Eq. (2.8)}$$

where A and B were the two metal species in the deposited film. In this work, *ex-situ* XPS was used to analyze film composition. As a result, contamination from the ambient atmosphere would have to be taken into account. Previous studies in this lab revealed that when a sample that was held in the chamber at 300 °C for one hour that carbon and oxygen had a surface concentration of 13 atomic percent (at. %) and 15 at. % respectively, however, hydrogen was not included in the analysis due to its low atomic number.

### 2.3.2 X-Ray Diffraction spectroscopy (XRD)

In order to characterize the crystalline structure of a sample, a technique called X-ray diffraction (XRD) was used. XRD functions by subjecting a sample to an X-ray beam of which the wavelengths were smaller than the interatomic spacing of the sample. When the photons enter the sample, they are scattered by the atoms and undergo constructive or destructive interference with other scattered photons as shown in Figure 2.7. Constructive interference occurs when the scattered photon path lengths are equal to an integral number of the photon's wavelength, as given by Bragg's diffraction law:

$$n\lambda = 2d \sin \theta_B \quad \text{Eq. (2.9)}$$

where  $n$  is an integer number called the order of reflection,  $\lambda$  is the X-ray wavelength,  $d$  is the atomic plane spacing, and  $\theta_B$  is the Bragg angle of diffraction.



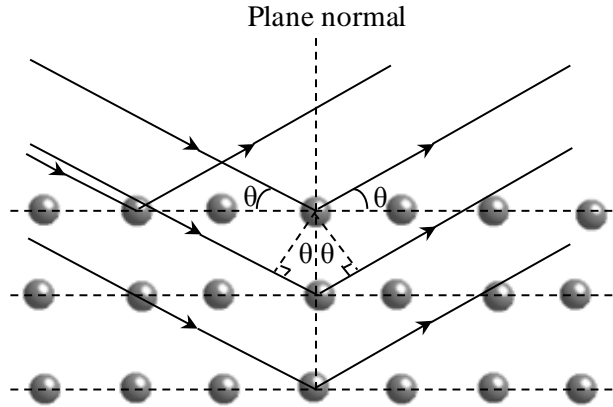


Figure 2.7 Photon scattering on parallel crystal planes; Bragg diffraction is a result of constructive interference of scattered photons

The scattered beams then entered a detector which measure the intensity as a function of  $\theta$ ; the constructively interfering beams have a substantially intensified signal which, when plotted, show the Bragg diffraction peaks at the various values of  $\theta_B$  for a highly crystallized sample. An example XRD pattern is shown in Figure 2.8.

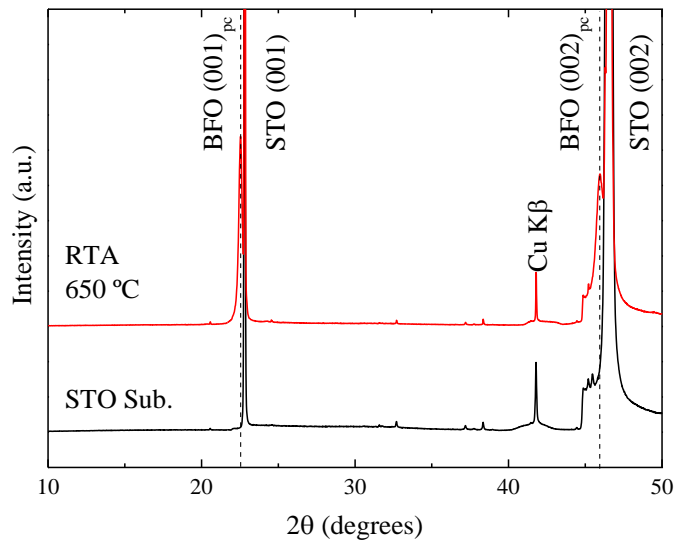


Figure 2.8. Sample X-ray diffraction pattern for  $\text{SrTiO}_3$  (001) substrate and ALD  $\text{BiFeO}_3$  film grown on  $\text{SrTiO}_3$  (001) annealed at 650 °C.

For the purposes of this work's thin film experiments, the Bragg diffraction peaks were used to reveal crystal information of the sample such as lattice parameter and crystal basis through analysis or through comparison to a reference sample. In a more advanced experimental

setup, a four-angle diffractometer could be used that could rotate the sample with respect to the X-ray beam for the  $2\theta$ ,  $\kappa$ ,  $\phi$ , and  $\omega$  angles as seen below in Figure 2.9.(Scintag 1999) This enabled a three dimensional examination of the film's crystal structure, as a conventional  $2\theta$  setup was limited to crystal planes parallel to the sample surface. In addition to identification of crystal phases, X-ray diffraction could also be used to quantify the ratios of the different crystal phases in a material by integrating the peaks corresponding to different phases and comparing them to the sum of the areas.

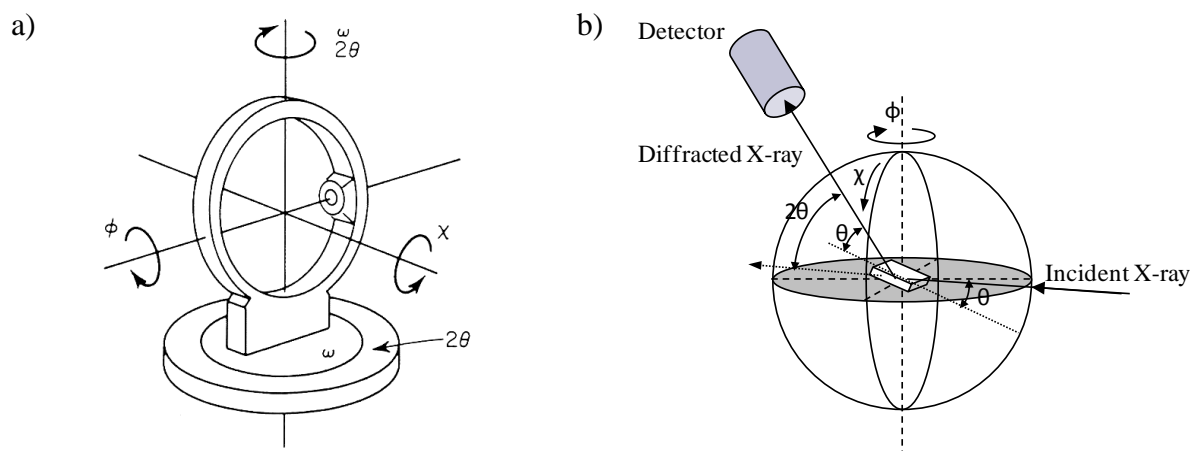


Figure 2.9 (a) Four-circle diffractometer XRD experimental schematic (Scintag 1999), (b) Multiple planes of sample probed using technique

### 2.3.3 X-ray Absorption Spectroscopy (XAS)

X-ray Absorption Spectroscopy (XAS) spectroscopy was used to obtain element-specific information for the cations in the thin films, such as its oxidation state, structural symmetry, average coordination number, and the chemical identity of the surrounding atoms at specific distances. In XAS, the x-ray absorption of a sample is measured as a function of the x-ray energy. As the energy increases, the absorbance usually decreases smoothly. However, when the energy nears the binding energy of a core electron, the absorbance suddenly increases by a factor of 2-10, which is known as the absorption edge of the element. Superimposed over the absorption edge are smaller features that vary sinusoidally as a function of the photon energy.

These features can be classified depending on their relative position from the edge as pre-edge, edge, near-edge (x-ray absorption near edge structure, XANES), and extended x-ray absorption fine structure (EXAFS) as shown in Figure 2.10.

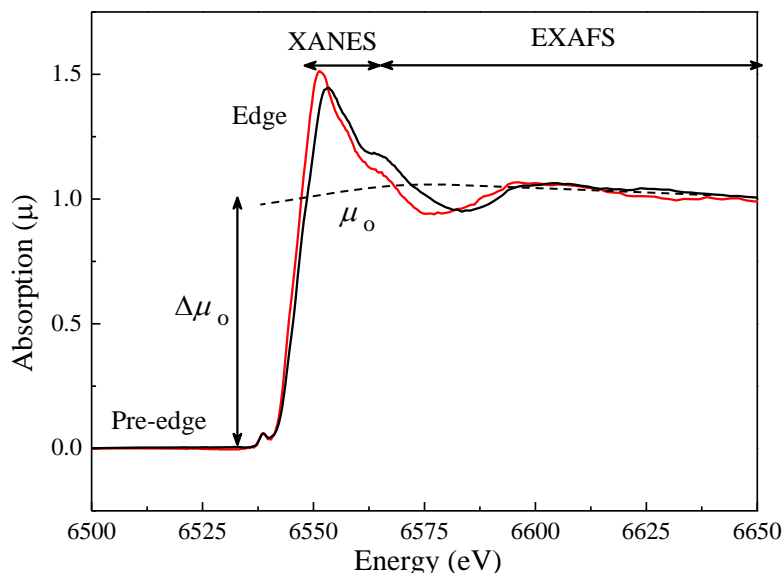


Figure 2.10. An XAS spectrum collected in the fluorescence mode below and above the Mn K absorption edge of an  $\text{YMnO}_3$  thin film.

While both XAS and XPS used the photoelectric effect to influence electrons using X-rays, unlike XPS in which electrons were ejected and the kinetic energies were measured, XAS was concerned primarily with measuring the X-ray absorbance by detecting the outgoing X-ray fluorescence as a function of the incident X-ray energy. According to Fermi's Golden Rule, the probability of absorbance was proportional to the square of the overlap between the initial and final states of the system. Thus, within the EXAFS region, the absorbance was dependent on the interference between the ground state electronic wave function and the component backscattered from the neighboring atoms. This interference was a function of the wavelength of the photoelectron, the interatomic distance, and the atomic potentials. The interference changed the absorption probability of the absorber and was manifested through the fine sinusoidal oscillations

that can be detected as a function of incident X-ray energy. The relation between the absorption coefficient depended on the X-ray energy  $E$ , the density  $\rho$  of the sample, the atomic number  $Z$ , and the atomic mass  $m$  of the absorbing atom (Newville 2004):

$$\mu \propto \frac{\rho Z^4}{mE^3} \quad \text{Eq. (2.10)}$$

According to the  $Z^4$  relation, it could be seen that ions with sufficiently large distance on the periodic table would result in a substantial contrast (Newville 2004). In XAFS spectroscopy, the energy dependence of the absorption coefficient  $\mu(E)$  could be measured either in the transmission mode as:

$$\mu(E) = \log \frac{I_o}{I} \quad \text{Eq. (2.11)}$$

or in the fluorescence mode as:

$$\mu(E) \propto \frac{I_f}{I} \quad \text{Eq. (2.12)}$$

where  $I_o$  is the incident X-ray intensity,  $I$  and  $I_f$  are the intensities of the transmitted and fluorescence X-rays, respectively. Fluorescence mode was more favorable for films on substrates that were not transparent to X-rays, such as Si. X-ray fluorescence occurred when an excited electron dropped down to a ground state releasing an X-ray photon of the characteristic energy difference between the excited and ground states.

XANES contained the energies a few eV before the absorption edge to ~50 eV after the edge and could be used to identify coordination symmetry i.e. octahedral versus tetrahedral as well as bond angles. Additionally, information about the oxidation state could also be extracted when compared to standard powder samples. The EXAFS region consisted of the fine oscillations after the XANES region and could be used to elucidate the local coordination, bond

distances, and chemical identity of the nearby ions. The resulting EXAFS spectrum plotted  $\chi \cdot k^3$  as a function of wave number  $k$ , where  $\chi$  and  $k$  were defined as:

$$\chi = \frac{\mu(E) - \mu_o(E)}{\Delta\mu_o(E)} \quad \text{Eq. (2.13)}$$

$$k = \sqrt{\frac{8\pi^2 m(E - E_o)}{h}} \quad \text{Eq. (2.14)}$$

In the above equations,  $\mu(E)$  is the measured absorption coefficient at  $E$ ,  $\mu_o(E)$  is a smooth background function representing the absorption of an isolated atom (shown as dash line in Figure 2.10),  $\Delta\mu_o(E)$  is the measured increase in the absorption coefficient at the absorption edge (Figure 2.10),  $m$  is the free electron mass,  $h$  is Planck's constant, and  $E_o$  is the absorption edge specific to the element. Since the EXAFS oscillations decayed quickly with  $k$ ,  $\chi$  is multiplied by  $k^3$  ( $k$ -weighted) to amplify these oscillations at higher  $k$ . The EXAFS spectrum was also Fourier transformed (FT) from  $k$  into  $R$  space. In this case, each main peak in the FT spectrum represents a coordination shell from which the bond distance could be deduced.

Shown in Figure 2.11(a) is a  $k^3$ -weighted Mn K EXAFS spectrum of the YMnO<sub>3</sub> thin film, obtained after performing the data reduction using the standard background subtraction procedure. The corresponding Fourier transformed spectrum without phase shift correction was shown in Figure 2.11(b). For this sample, the first coordination shell was oxygen, which manifested itself as the first distinct peak at  $R+\Delta R$  of  $\sim 1.19$  Å for the film grown on YSZ(111) and at  $R+\Delta R$  of  $\sim 1.38$  Å for the film grown on Si(111). In modeling the EXAFS, theoretical backscattering amplitudes and phase shifts up to 5-Å radial distance from the center absorbing atom were first calculated using FEFF6L and the IFEFFIT 1.2.7 program.

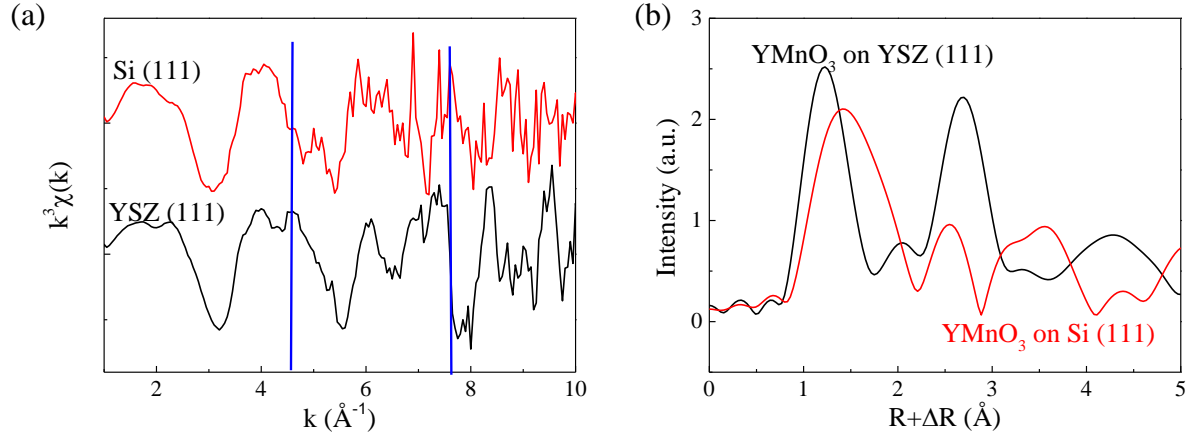


Figure 2.11. (a) The EXAFS data and (b) the corresponding FT spectrum of the  $\text{YMnO}_3$  film.

Results from the calculations were used directly to fit unsmoothed EXAFS spectra obtained after the data reduction by using the following EXAFS fine-structure function  $\chi(k)$  (Stern 1988):

$$\chi(k) = S_o^2 \sum_{i=1}^n \frac{N_i F_i(k, R_i)}{k R_i^2} e^{\left( \frac{-2R_i}{\lambda(k, R_i)} \right)} e^{(-2\sigma_i^2 k_i^2)} \sin[2kR_i + \phi_i(k, R_i) + \phi_o(k)] \quad \text{Eq. (2.15)}$$

with an assumed set of structural parameters, which were then allowed to vary until the best fit was achieved. In the above equation, the absorption coefficient written in terms of wave number  $k$  is a function of the amplitude reduction factor  $S_o^2$  determined empirically from the model compound, the mean free path of elastically-scattered photoelectrons  $\lambda$ , the coordination number  $N_i$  of atoms type  $i$ , each at a distance of  $R_i$  from the center absorbing atom with a Debye-Waller factor  $\sigma_i$  to account for the variations in  $R_i$  due to disorder and thermal motion. The backscattering amplitude and phase shift from atom  $i$  is  $F_i$  and  $\phi_i$ , respectively.

The XAS experiments were conducted at the Stanford Synchrotron Radiation Laboratory (SSRL). A schematic drawing of the experimental setup was shown in Figure 2.12. Synchrotron radiation was capable of emitting X-rays with energies ranging from 5-40 keV, generated by

accelerating electrons in a circular storage ring, or the Stanford Positron Electron Accelerating Ring (SPEAR), at relativistic velocities. The emission was tangential to the acceleration ring which allowed beams to be directed away from the ring to the experimental stations known as hutches. Located at the hutch, an aperture, which was a rectangular opening between two metal plates, could be adjusted to control the amount of radiation entering the hutch. From the aperture, the beam was directed to a double (220) Si crystal monochromator which facilitated the precise control of incoming X-rays to the sample as well as the rejection of harmonic modes of the incoming X-rays when slightly detuned.

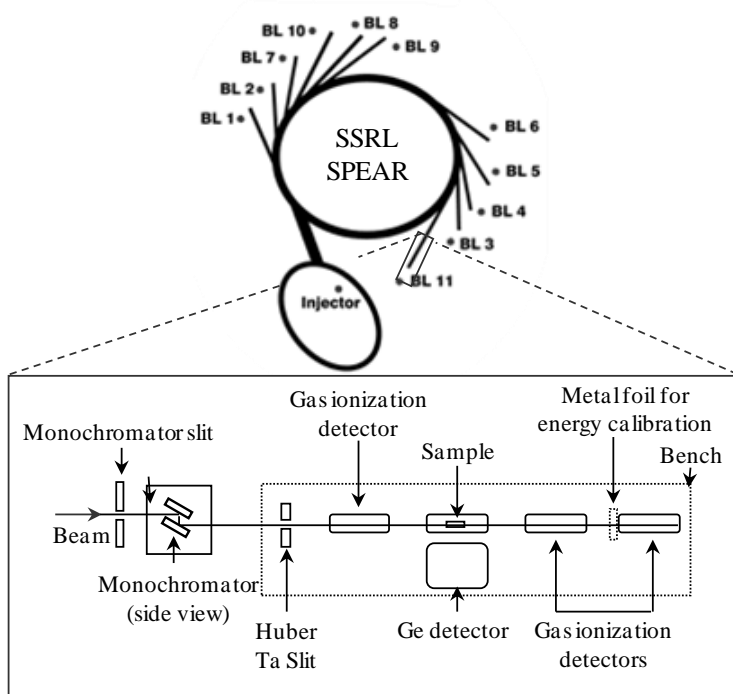


Figure 2.12 Schematic diagram of the Stanford Synchrotron Radiation Laboratory (SSRL), showing the electron storage ring, or SPEAR (top), and an experimental station, or hutch (bottom) (Van and Peterson 1998).

The output monochromatic X-rays were incident on the sample and fluorescence-yield XAS data for the thin films were acquired with a 30-element Ge detector cooled at 77 K. One main problem typically encountered in the data collection was Bragg diffraction from the Si

substrate. Since a multi-channel energy-dispersive detector was used, this was eliminated by simply discarding the data channels in which Bragg diffraction was presented with high enough intensity that caused spikes in the raw spectra. The XAS for oxide powders could also be collected as standard references in the transmission mode.

#### 2.3.4 Superconducting Quantum Interference Device Magnetometer (SQUID)

In order to analyze magnetic thin films, a very sensitive magnetometer was utilized which could also maintain high sensitivity within a large magnetic field environment known as a SQUID (Superconducting Quantum Interference Device) magnetometer. (Quickel, Le et al. 2010) The magnetometer used in this study is a Magnetic Property Measurement System (MPMS) built by Quantum Design, Inc. as shown in Figure 2.13.

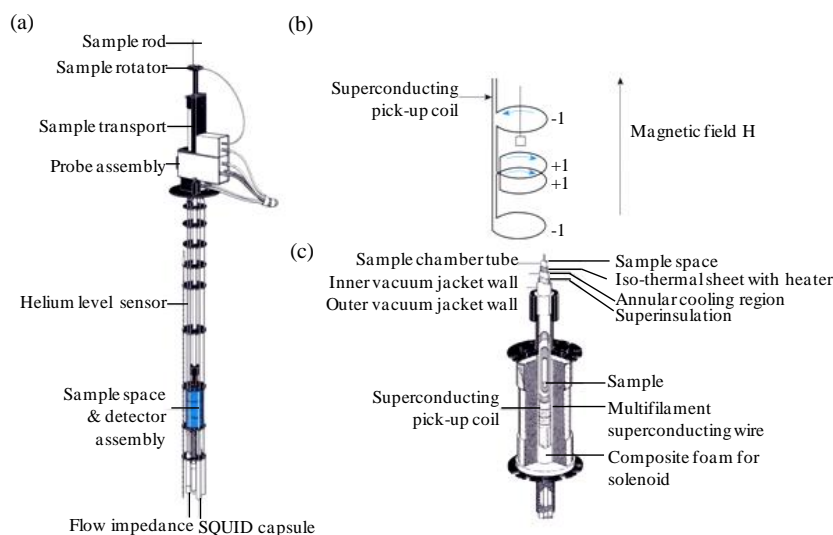


Figure 2.13 (a) Schematic drawing of SQUID Magnetometer used in MPMS system (b) Schematic of superconducting coil (c) Schematic of sample space and detector assembly

Superconductivity is a phenomenon that was first discovered in 1911 by Heike Kamerlingh-Onnes who observed that mercury, when cooled below a critical temperature  $T_C$ , abruptly had its electrical resistance dropped to zero. This meant that a very large amount of



current could be passed through without a substantial energy loss through heat dissipation. Unfortunately, the challenge in the application of superconductors lies in the fact that the  $T_C$  for most superconducting materials is very low; ranging from less than 1 K for Zn to 23 K for  $Nb_3Ge$ . Therefore, it is necessary to utilize cryogenic coolants such as liquid  $H_2$  (boiling point: 20.3 K) and liquid He (boiling point: 4.2 K) which are both expensive and difficult to manage. In the SQUID magnetometer, superconductivity was exploited in two ways. The first was the ability to create a very large inductive magnetic field by passing large amounts of current through superconducting coils. The MPMS had a capability of generating magnetic fields up to 5 Tesla (T) or 50,000 Oersteds (Oe) in strength. The second usage of superconductivity was the Josephson junction. The Josephson junction consisted of a sandwich structure of two superconducting wires separated by an insulating barrier layer that allowed the tunneling of Cooper electron pairs which was used in the SQUID as an extremely sensitive current to voltage converter. When a magnetic sample was moved between the superconducting circuit coils, the magnetic flux within the coil was changed and an inductive current was generated and superimposed upon the biasing current; the induced current was thus proportional to the magnitude of the magnetic moment. The change in biasing current altered the frequency of the AC voltage output at the Josephson junction; the phase difference in the AC voltage was proportional to the current induced by the magnetic sample and could be thus collected as data.

The magnetic moment was measured as a function of dependent variables such as temperature (M vs. T measurement) and magnetic field (M vs. H hysteresis measurements). The sample temperature was controlled by purging the sample area with helium gas and using the reservoir of liquid helium as a coolant. The MPMS had the capability of varying the temperature between 2 K to -400 K (-271 °C to 127 °C). Superconductor magnets were used to control the

magnetic field; the MPMS was capable of generating a magnetic field of 5 T (50,000 Oe) within the sample space. Using  $M$  vs.  $T$  data, one could calculate the magnetic susceptibility as a function of temperature and obtain information regarding magnetic phase changes as seen in Figure 2.14(a). In  $M$  vs.  $H$  data, the remnant magnetization, saturated magnetization, and coercive magnetic field could be found as seen in Figure 2.14(b).

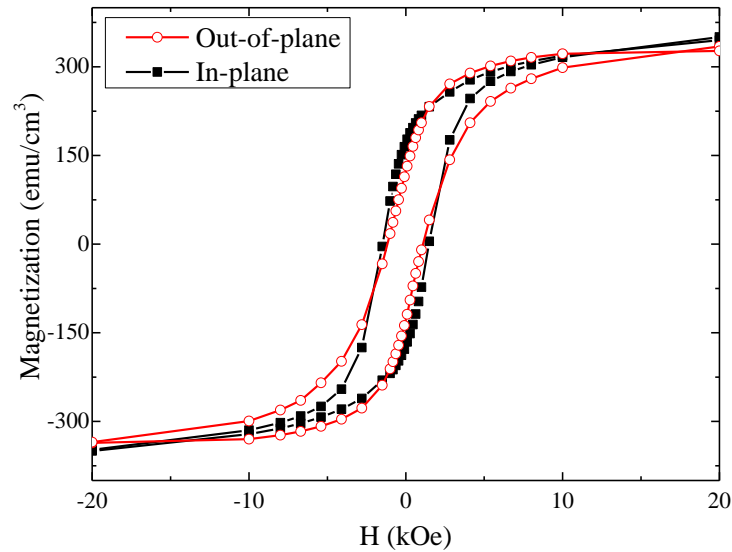


Figure 2.14 Magnetic Hysteresis  $M$  vs.  $H$  of  $\text{CoFe}_2\text{O}_4$  thin film showing ferromagnetic ordering.

### 2.3.5 Scanning Probe Microscopy (SPM)

In general, scanning probe microscopy (SPM) methods are used to characterize the surface of a sample. (Alford, Feldman et al. 2007) While there are several types of SPM methods used for specific applications, there are typically three common aspects. The first aspect is a needle-like probe which is suspended extremely close to the surface, generally in the order of single angstroms, such that the interactions between the probe and the surface can be measured. Next is a detection method that is essentially able to convert the interaction into an electrical signal, for example, a force as in atomic force microscopy, an electron tunneling

current as in scanning tunneling microscopy, or a change in capacitance as in scanning capacitance microscopy, among others. Last is the fact that the measurement is raster-scanned, meaning that the probe is scanned in lines relative to the sample with a resolution on the order of nanometers. In this section, atomic force microscopy (AFM) and piezoresponse force microscopy (PFM) are reviewed.

Atomic force microscopy utilizes a cantilevered beam to which the probe is attached; as the probe scans the sample, the tip of the probe interacts with the atoms on surface and the force applied to the cantilevered beam and its resulting deflection is what is measured in accordance with Hooke's law.(Alford, Feldman et al. 2007) Similar to applying a force upon a spring, the movement of the cantilever correlates to the interatomic forces which are being applied on the probe tip from the sample surface located fractions of a nanometer away. Methods for detecting the force can vary, but one common method is to reflect a laser off of the cantilevered beam. As the beam shifts, the intensity of the reflected laser is detected and recorded so that a 3-dimensional representation of the sample surface can be obtained. Generally, the movement of the probe tip is set in either "constant force" mode or "constant height" mode. In constant force mode, the system uses a feedback loop to apply a counteracting force relative to the sample surface, and keeps the total forces applied on the tip constant. Constant force mode is the typical configuration used in the majority of AFM applications; with the scanning speed dependent on the feedback circuit. In contrast, constant height mode essentially records the movement of the cantilever itself and directly results in the topographical data without using a feedback loop. This mode is usually used for scans of extremely flat surfaces at high resolution since thermal drift is eliminated and also can result in faster scans since the feedback system is turned off, however, rough surfaces can damage probe tips or cantilevers in this mode.

During normal AFM operation, there are a handful of forces which can dominate the interactions between the probe tip and the sample surface, in addition to magnetic and electrostatic forces for materials relevant to those interactions.(Alford, Feldman et al. 2007) The first is van der Waals forces which can cause attractions that dominate up to ~1 nm between the tip and the surface. At short distances that are ~0.1 nm from the surface, quantum-mechanical exchange-correlations repel the tip from the surface which is attributed to the Pauli Exclusion Principle as the wave functions for the tip and the sample begin to overlap. Also, capillary forces in which the thin film of water on a sample left in ambient conditions are attracted to the probe tip and pull the tip closer to the sample. Lastly, the force that the cantilever applies onto the sample surface is also taken into account. In constant force mode, the cantilever force is actually controlled by the feedback loop such that the sum of the repulsive and attractive forces is kept at a constant value. The total magnitude of the force that is applied to the sample can range from  $10^{-8}$  N, when only the capillary force is keeping the tip in pseudo-contact with the sample, to the normal operation mode where the force is between  $10^{-7}$  and  $10^{-6}$  N.

Piezoresponse Force Microscopy (PFM) utilizes AFM in contact mode, however, the difference lies in the application of an AC electric field which causes the material to expand in contract with the same frequency as the applied field and the movement of the tip with the sample is detected using a lock-in amplifier. Thus, PFM is primarily used for the characterization of ferroelectric materials. Additionally, the lock-in amplifier can detect the contrast of the frequency phase shift between oppositely polarized materials which is used to image the ferroelectric phases. When held in one location, the PFM tip can pole a sample by varying the voltage (ergo the electric field) and create a hysteresis loop. As shown in Figure 2.15 (a) and (b), PFM data for a PZT film on  $\text{Al}_2\text{O}_3/\text{SiC}$  substrate is displayed. By poling the PZT in a square

pattern, the ferroelectric domains can be written and thus the piezoelectric phase contrast can be observed with the same pattern.

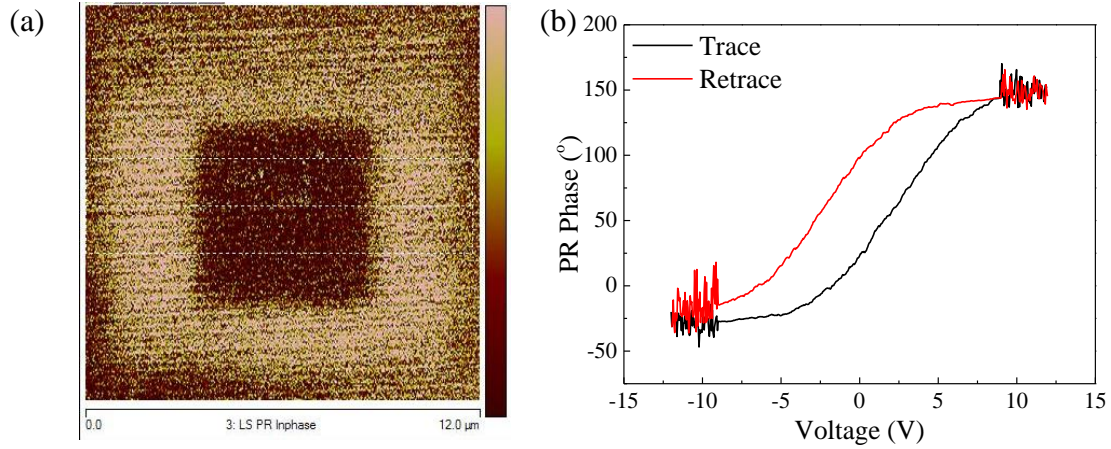


Figure 2.15 PFM image of polarized PZT film on  $\text{Al}_2\text{O}_3/\text{SiC}$  substrate (b.) Surface cross-section of polarization contrast between oppositely poled sections (c.) Hysteresis loop of piezoelectric phase when voltage is scanned (Zhang, Perng et al. 2011)

### 2.3.6 Magneto-Optic Kerr Effect (MOKE) magnetometer

The Magneto-Optic Kerr Effect (MOKE) is known as a magneto-optic interaction in which the plane of polarization for a polarized light beam becomes rotated when it is reflected from a magnetized sample. (Spaldin 2003) The amount of rotation varies between the direction and magnitude of the magnetization and is on the order of  $10^{-1}$  degrees. A typical MOKE experiment consists of a light source which is passed through a polarizer. The polarized light then reflects from the sample into a detector which determines the magnitude of rotation. If the magnetization of the sample becomes altered due to an external magnetic field (or electric field for a magneto-electric material) the change in the rotation of polarization can be detected and indeed a hysteresis loop for the sample can be generated, however, the magnetization is not directly measured. Additionally by utilizing the MOKE, images of the magnetic domains can be generated within a  $1 \mu\text{m}$  resolution.

The principles of the MOKE phenomena can be explained from the Zeeman splitting of the electronic states as well as their interactions with polarized light. (Spaldin 2003) Circularly polarized light can have two oppositely poled directions that have angular momentums that are equal in magnitude (with a value of 1) but opposite in direction (- or +). When a polarized photon excites an electron from one split energy level B to another split energy level A, as shown in Figure 2.16, the angular momentum must be conserved meaning that one direction of photon corresponds to the  $\Delta L = +1$  and the other corresponds to  $\Delta L = -1$ .

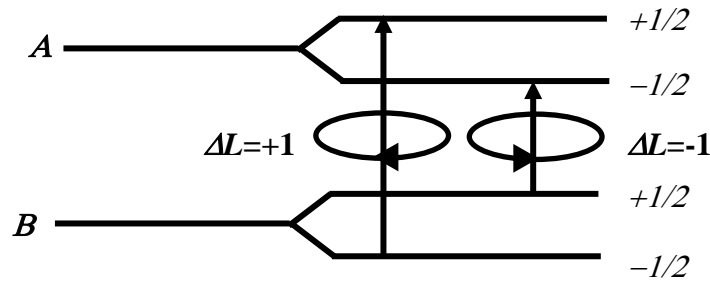


Figure 2.16 Angular momentum conservation in photoelectric excitation of magnetic materials with circularly polarized light

Since the population of electrons in the lower energy level is statistically greater than that of the higher energy level, the photons corresponding to those electrons are absorbed at a higher rate meaning that the amount of *reflected* or *transmitted* light is lower compared to the oppositely polarized photons. This phenomenon is called circular dichroism and when the reflected light is combined to a linearly polarized beam, the rotated polarization, or phase difference, when compared to the incoming beam is known as the circular birefringence. An example M vs. H hysteresis measurement is shown in Figure 2.17.

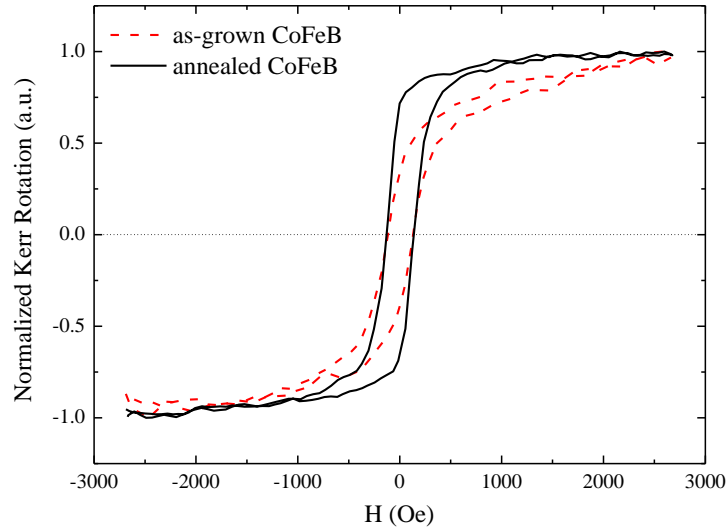


Figure 2.17.  $M$  vs.  $H$  hysteresis loop measured using MOKE for CoFeB as grown (dashed line) and annealed at 300 °C in vacuum for 30 minutes (solid line). (Courtesy Diana Chien)

### 2.3.7 Scanning Electron Microscopy (SEM)

Scanning electron microscopy (SEM) was used to obtain a myriad of information from the thin film specimens including the thicknesses, composition via energy dispersive x-ray spectroscopy, and nanostructuring for composite multiferroic samples. In SEM, the process by which samples are analyzed consists of the following: electrons are accelerated to high energies between 2-40 keV, which correspond to wavelengths between 0.62-0.03 nm; the electrons interact with the specimen in a variety of manners which cause outgoing particles usually consisting of backscattered electrons and emitted photons; finally the particles are collected by detectors and the analyzed data results in the image and various information about the sample such as composition using energy dispersive x-ray spectroscopy (EDX or EDS). (Vernon-Parry 2000). For the purposes of this work, SEM was primarily utilized in the imaging of nanostructures and detection of elemental compositions by EDX, therefore the basic operation for those techniques is described in further detail.

Inside the SEM instrument consists of the following: an electron gun, several electromagnetic focusing lenses, scanning coils, an aperture, sample(s) which are mounted on the sample chuck, the detector(s) for electrons or photons, and a detection monitor which displays the image. The most common electron gun uses thermal emissions of electrons from a tungsten filament which is resistively heated to high temperatures up to 2500 °C. The electrons are focused by two to three electromagnetic condenser lenses into a fine beam which is then scanned in a raster fashion using the scan coils over the desired area. The electrons, when entering the sample, can cause several interactions which result in secondary electrons, backscattered electrons, Auger electrons, or x-rays. The particle intensities are detected in synchronization with the rastered electron beam, and are fed to the monitor which then results in the image. The resolution limit of SEM is thus determined by the interaction volume of the electron beam and the specimen, and is usually on the order of 1-10 nm depending on the instrument.

In typical SEM experiments, the secondary electrons, or electrons which have been knocked free from the surface with energies lower than 50 eV, provide the signal for topographical imaging, as seen in Figure 2.18 (a), since they are emitted from a shallow depth from the specimen. For samples analyzed by SEM, some considerations must be made when preparing the samples especially for highly insulating materials such as the metal oxides synthesized in this work. Since insulating materials collect charge on the surfaces, a blurry image may result from the exaggerated electron density. A solution to this, for cross-section images, is to cover the material with a thin film of conductive material, usually platinum to dissipate the charge. Unfortunately, this is not a viable solution when it is desired to image the top surface, so care must be taken to avoid scanning the same region for too long thereby mitigating the effect of charging in a particular spot.



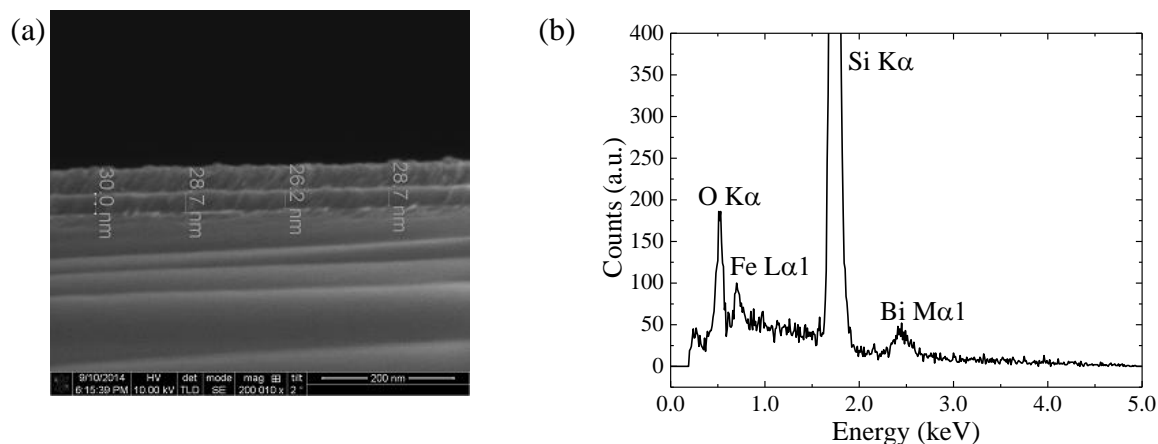


Figure 2.18. (a) Cross-section of ALD  $\text{Bi}_2\text{O}_3$  film imaged by SEM. (b) Sample EDX spectra for  $\text{BiFeO}_3$  sample on Silicon indicating elemental X-ray emissions.

Besides imaging the topographical features for a sample, the SEM can be used in conjunction with an x-ray detector to determine the composition of a sample by measuring the characteristic photoemissions from the energy decay of excited electrons located in the sample. Since these characteristic x-rays have well-defined energies, some of which are listed in Table 2.3, it is possible to determine the identity and approximate quantity of most elements, as seen in Figure 2.18 (b). For more sensitive quantification, a specialized wavelength-dispersive spectrometer with the conjunction of standard samples is necessary. Since the x-ray emissions may come from the entire volume of the sample being excited by the electrons, the probe depth is on the order of 1  $\mu\text{m}$ .

Table 2.3. List of characteristic X-ray energies for elemental emissions

Elemental X-ray emission	Energy (keV)
O $\text{K}\alpha_1$	0.52
Si $\text{K}\alpha_1$	1.74
Fe $\text{L}\alpha_1$	0.71
Co $\text{L}\alpha_1$	0.78
Bi $\text{M}\alpha_1$	2.42

### 2.3.8 *High Resolution Tunneling Electron Microscopy (HRTEM)*

Although SEM is very versatile and relatively easy to use, a major limitation is the lack of atomic resolution for which high resolution tunneling electron microscopy (HRTEM) is necessary. (2000; Cheong and Mostovoy 2007; Nan, Bichurin et al. 2008) For the purposes of this work, the TEM was able to determine a variety of data depending on the mode. Using imaging mode, the nano/microstructure, crystal quality, and defect density could be determined. In diffraction mode, it was possible to characterize the lattice parameters and crystal symmetry. Lastly, the elemental composition was able to be determined using energy dispersive x-ray spectroscopy (EDX), Auger electron spectroscopy (AES), or electron energy loss spectroscopy (EELS).

Compared to SEM, the electron energies used for TEM are greater, between 100-1000 keV allowing a higher resolution. However, the sample must be much thinner, usually less than 100 nm, to allow some of the electrons to pass through to generate the image. In addition, the image is only obtained from a small portion of the sample, which may not necessarily represent the whole of the sample, which is why other bulk techniques such as XRD are usually used in conjunction with TEM. A typical TEM instrument consists of the following: an evacuated tube with an electron gun at one end pointed downwards towards the specimen, several electromagnetic lenses above and below the sample, and an image detector at the bottom. A load-lock assembly is needed to insert the sample into the beam path and remain within vacuum. It is by focusing the electron beam using the electromagnetic lenses that the desired image and magnification can be generated with a resolution limit that is approximately 2 Å for modern TEMs. As mentioned previously, the TEM operates in different modes depending on the desired functionality mainly imaging mode or diffraction mode. For imaging mode, there are three main

interactions which generate contrast: absorption, diffraction, or phase contrast. For absorption, the contrast is due to either variations in sample thickness or the mass of the atoms in the specimen. An example is shown in Figure 2.19 (a). In diffraction contrast, the settings of the lenses are changed such that a certain Bragg diffraction condition is met, resulting in two beams: a direct beam and the diffracted beam. Focusing on one beam over the other results in contrast between the regions of the film in which the diffraction condition is or is not met which are known as dark field and bright field imaging respectively. In diffraction mode, selected area diffraction patterns (SADPs) are generated using the Bragg diffraction condition and contain information regarding the crystal structure of the specimen. An example is shown in Figure 2.19 (b). Highly crystalline samples will generate diffraction patterns in addition to the transmitted beam and can be used to characterize the crystal structure. On the other hand, polycrystalline films generate ring patterns around the transmitted beam. The SADP patterns can be quantified using Eq. (2.16):

$$R \cdot d = \lambda \cdot L \quad \text{Eq. (2.16)}$$

where  $R$  is the separation between the diffraction spots on the screen,  $d$  is the spacing between the lattice planes,  $\lambda$  is the wavelength of the electrons, which for this work was operated at 300 kV which translates to a wavelength of  $\lambda = 4.13 \times 10^{-3}$  nm, and  $L$  is the distance from the film to the detector screen known as the Camera Length. When using a known standard sample, such as a single crystal substrate, the specimen can be indexed.

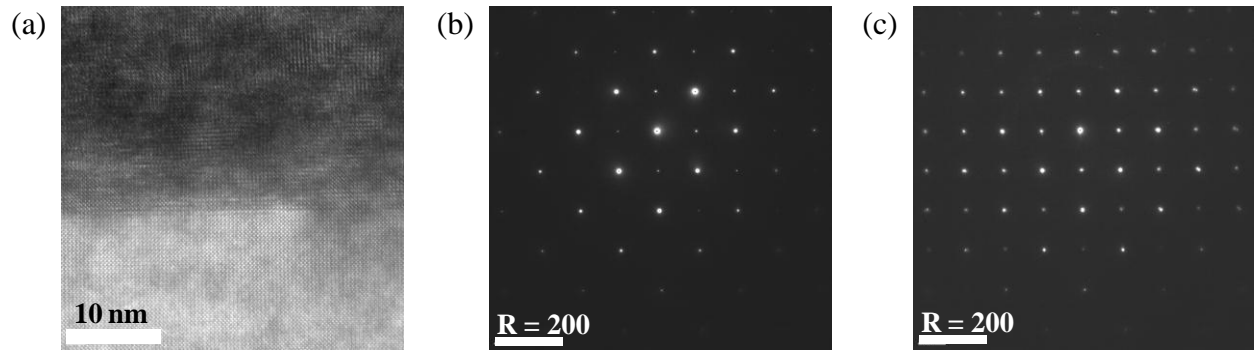


Figure 2.19. (a) TEM image of BiFeO<sub>3</sub> film on SrTiO<sub>3</sub> substrate indicating epitaxial microstructure, (b) selected area diffraction pattern (SADP) of SrTiO<sub>3</sub> substrate, and (c) SADP of BiFeO<sub>3</sub> film.

The SrTiO<sub>3</sub> substrate shown in the figure is a cubic rock salt structure with  $a = 3.9010$ . Using the substrate pattern as a calibration, the product of the wavelength and camera constant  $\lambda \times L$  was calculated, and the BiFeO<sub>3</sub> film d-spacing could also be indexed by calculating  $R$ . The values are shown in and compared to reference data.

Table 2.4. Calculated  $R$  values, calculated d-spacing, and comparison to d-spacing from JCPDS reference for SrTiO<sub>3</sub> substrate and BiFeO<sub>3</sub> film.

Material and Index	$R$ (pixels)	d-spacing (Å)	d-spacing (Å) (JCPDS)
SrTiO <sub>3</sub> (001)	237.427	3.901	3.901
BiFeO <sub>3</sub> (001) <sub>pc</sub>	232.337	3.987	3.968

TEM sample preparation is a non-trivial task, especially for thin films. Generally, the cross-section image for thin films is desired, and thus a combination of mass removal techniques are necessary to obtain desired portion of the specimen and to thin it down to about 100 nm. For this work, the focused ion beam (FIB) technique was utilized in which a SEM instrument equipped with an ion gun prepared a thinned cross-section and adhered it to a TEM sample grid.

### CHAPTER 3: GROWTH AND CHARACTERIZATION OF YTTRIUM MANGANESE OXIDE USING RADICAL ENHANCED ATOMIC LAYER DEPOSITION

$\text{YMnO}_3$  (YMO) thin films were synthesized by radical enhanced atomic layer deposition (RE-ALD) on yttria-stabilized zirconia (YSZ (111)) and silicon (Si (111)) substrates, to investigate the effect of film composition, thickness, and substrates on their intrinsic magnetic properties. The crystalline phase of these ultra thin films depended on the processing conditions and weakly on the substrate lattice parameters. The Mn/Y atomic ratio of the YMO thin films could be deposited near unity by adjusting the Mn:Y precursor pulsing ratio during the RE-ALD processes. ALD YMO thin films on Si (111) were orthorhombic, regardless of the film thickness with a Néel temperature ( $T_N$ ) between 48 ~ 57 K as observed during DC magnetic susceptibility measurements. However, ultra-thin ALD YMO films (~6 nm) on YSZ (111), at a Mn/Y atomic ratio near unity, had both orthorhombic- and hexagonal- phases in co-existence, which was consistent with the two  $T_N$  anomalies measured at ~48.5 K and ~80 K. The induction of magnetization of ultra thin YMO film on Si (111) under an *in-situ* 20 V electric poling indicated magnetoelectric coupling below  $T_N$ , demonstrating that ALD synthesis is a promising technique to deposit ultra-thin magnetoelectric films.

### 3.1 Synthesis of $\text{YMnO}_3$ by Radical Enhanced ALD

Synthesis of YMO was accomplished by using two beam systems, one was discussed in 0, and the other had a similar setup with an identical precursor delivery system and microwave radical source. The substrates used were Silicon (111) and Yttria stabilized Zirconia or YSZ (111). As was discussed in 2.2, the stoichiometry of the YMO films was controlled by adjusting the precursor sequence. The composition was confirmed using XPS as seen in Figure 3.1.

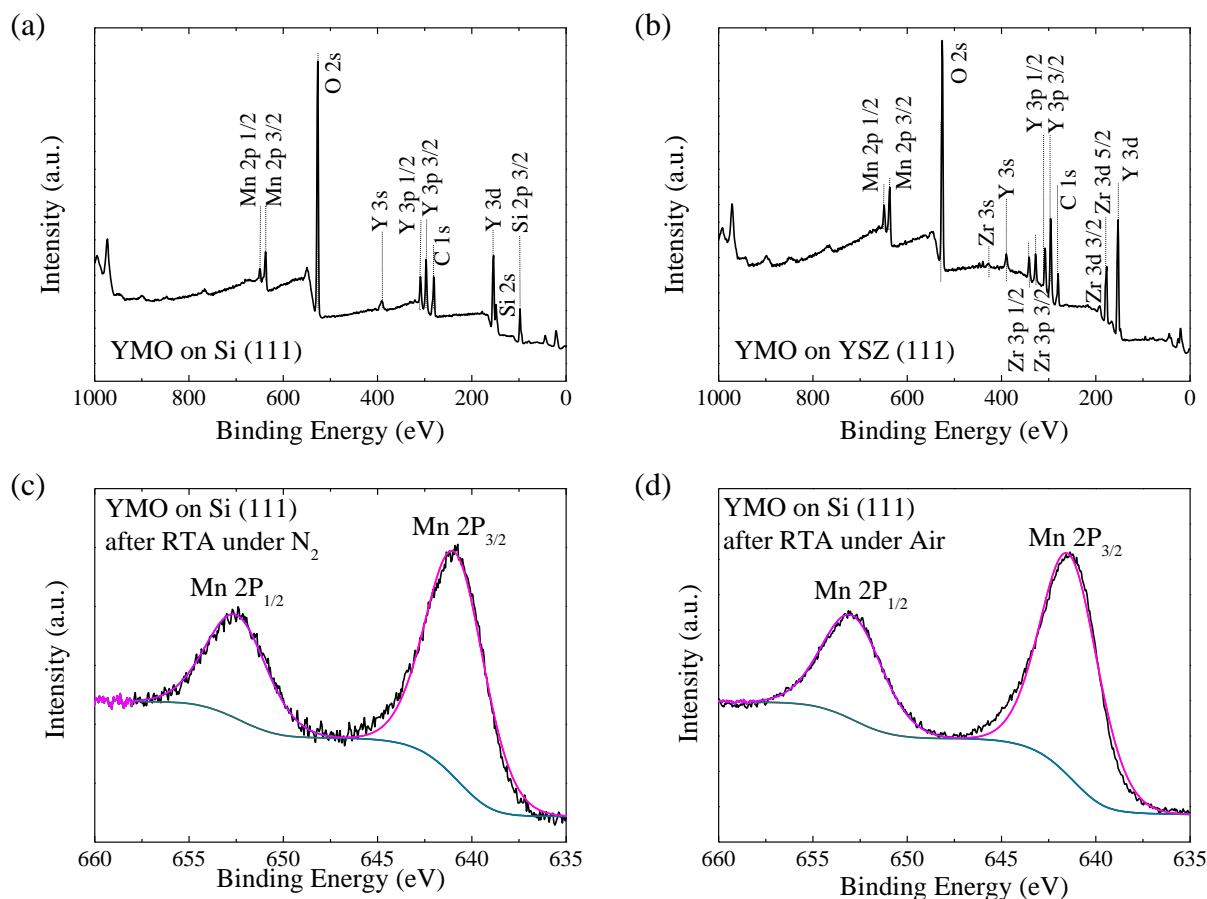


Figure 3.1. (a) Survey XPS spectra for YMO thin film on Si (111) with Mn/Y=0.95, (b) Survey XPS spectra for YMO thin film on YSZ (111) with Mn/Y=1.07. Detailed XPS spectrum of Mn 2p for YMO thin film on Si (111) after RTA under (c) N<sub>2</sub> and (d) Air. C1s spectra was used for peaks alignment and all the FWHM of deconvoluted peaks are fixed as 3.6.

In the XPS survey scans, the peaks detected were Mn 2p, Y 3d and 3p, and O 1s from the film as well as Si 2p and 2s from Si(111) substrates and Zr 3d and 3p from YSZ(111) substrates.

The substrate peaks were still visible because of the ultra-thin nature of the YMO films. From the XPS scans shown in Figure 3.1, the obtained Y  $3d_{5/2}$  and O  $1s$  binding energies for YMO thin film were 153.6 and 527 eV, respectively, while the  $3/2$  and  $1/2$  spin-orbit doublet components of the Mn  $2p$  photoemission were located at 641 and 652 eV, respectively. As seen in (a) and (b), by adjusting the precursor dosing sequence, films with Mn/Y ratio close to 1:1 was attainable. For films grown on Si (111), the ratio was increased from 0.53 to 0.95 as the ALD precursor ratio was adjusted from 1.2 to 1.8; whereas for films grown on YSZ (111), the ratio increased from 0.69 to 1.07 as the precursor ratio was changed over the same range.

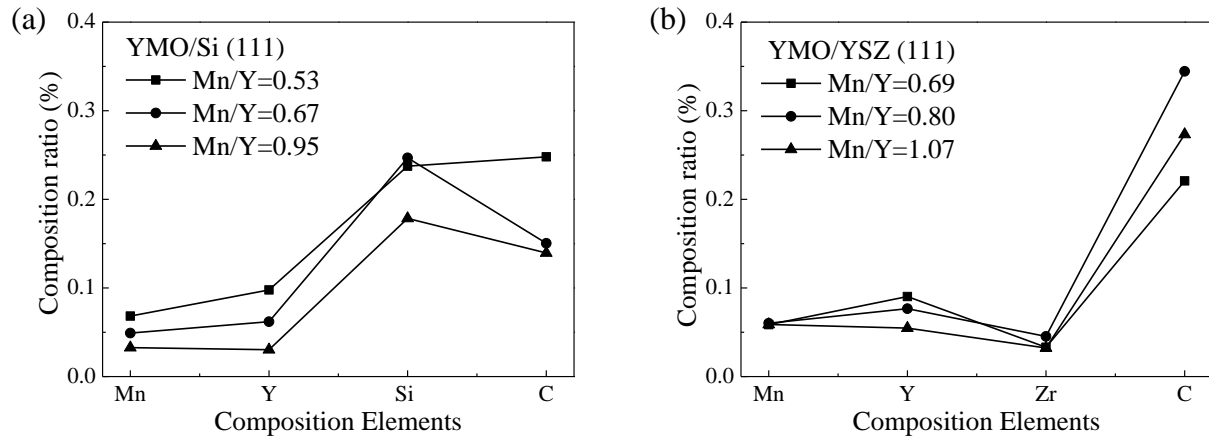


Figure 3.2. (a) Composition ratio of ~6 nm YMO ultra thin films on Si (111) with different Mn:Y precursor pulsing ratio. (b) Composition ratio of ~6 nm YMO ultra thin films on YSZ (111) with different Mn:Y precursor pulsing cycles.

As the films needed to be annealed in order to reach the desired (poly)crystalline state, the effect of the annealing process upon the films' chemical states was studied using XPS. For this work, using the samples that were the closest to a Mn/Y = 1:1 stoichiometry, the films grown on Si(111) were rapid thermal annealed at 900 °C for 2 min under air and N<sub>2</sub> atmospheres. As seen in Figure 3.1 (c) and (d), both the films that were annealed in N<sub>2</sub> and air showed only a doublet which could not be deconvoluted into multiple peaks. Due to the absence of a satellite peak between the Mn  $2p$  doublets, it was assumed that there was no YMn<sub>2</sub>O<sub>5</sub> phase and that the

Mn ions were of only a single oxidation state. On the other hand, using XRD, the films that were grown on YSZ (111) showed the coexistence of o-YMO and h-YMO as seen in Figure 3.3, however the XPS results were not reliable enough to confirm the mixed oxidation states of the Mn ions.

### 3.2 Structure and Morphology of ALD grown $\text{YMnO}_3$ thin films

To elucidate the structure of the YMO films grown by ALD, a combination of XRD, TEM, and EXAFS was utilized. As mentioned previously, films of thicknesses between 6-80 nm on both Si (111) and YSZ (111) were annealed at 900 and 1000 °C for 2 min. As reported in literature, YMO films on Si (111) exhibits both o- and h- phases, depending upon the deposition method used (Aoki, Fujimura et al. 1997; Imada, Shouriki et al. 1998). However, only the h-YMO phase was observed when the substrates had similar lattice parameters, such as YSZ (111), due to the reduced lattice misfit (Dho, Leung et al. 2004). The films that were annealed on Si (111) were identified to correspond to the o-YMO phase with space group  $P_{bnm}$  (JCPDS: 20-0732) as seen in Figure 3.3 (a).

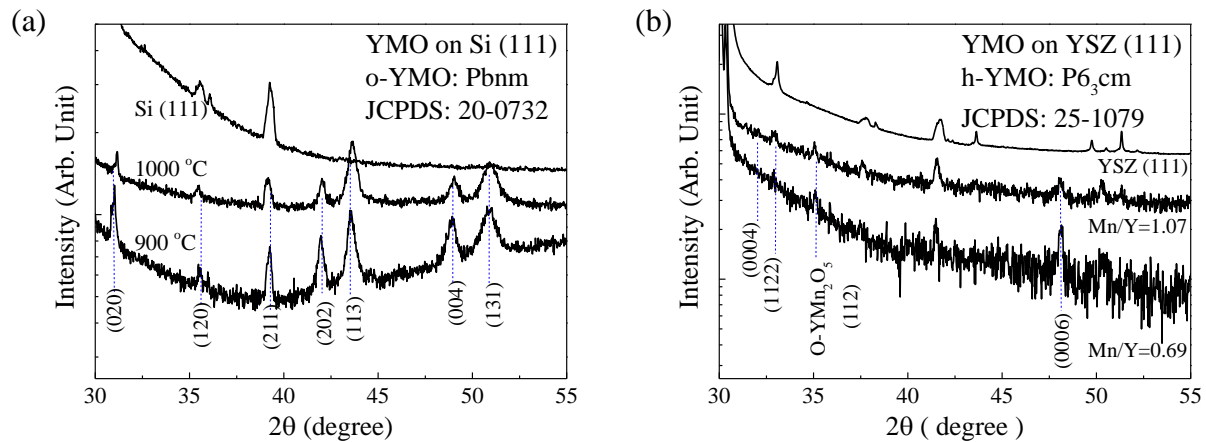


Figure 3.3. (a) The XRD of YMO thin films on Si (111) as function of RTA condition. (b) The XRD of YMO thin films on YSZ (111) as function of Mn/Y ratio after RTA 900 °C.



Based on the diffraction pattern, the crystallinity of the o-YMO films increased as a function of the RTA temperature. On the other hand, films as a function of composition with Mn/Y = 1.07 and 0.69 were annealed on YSZ (111) and the diffraction patterns are shown in Figure 3.3 (b). Due to the ultra-thin nature of these films, however, the XRD patterns were very noisy. The film peaks had an average signal-to-noise ratio (defined as the intensity of the peak divided by the background) at approximately 1.21 when compared to the single crystal substrates which were approximately 41.3.

It has previously been reported that h-YMO preferentially grows on YSZ (111) because the lattice mismatch between the h-YMO and the YSZ (111) is about 2.8% (Dho, Leung et al. 2004). In this work, for the annealed films grown on YSZ were identified as space group  $P6_{3cm}$  (JCPDS: 25-1079) but an additional o- $\text{YMn}_2\text{O}_5$  (112) peak was identified in the film with a composition of Mn/Y=0.69, which indicates the coexistence of h-YMO and o-YMO phases. On the other hand, for the YMO thin film with Mn/Y=1.07, the (0004) and (122) peaks from h-YMO were intensified in comparison to the o-YMO peak. It was then interpreted that h-YMO phase with space group  $P6_{3cm}$  would become more dominant as the Mn/Y atomic ratio approached toward unity and YMO phase on YSZ (111) is more dependent on atomic composition ratio than on substrate lattice parameters in this system.

To obtain more confirmation of the XRD results, TEM was used to image the atomic structure of the thin films. As seen in Figure 3.4 (a) and (b), for both the films grown on Si (111) and YSZ (111), there were two distinctive layers, with a 6 nm of crystalline YMO which transitioned to a nano-polycrystalline region further away from the substrate. Atomically sharp interfaces were not observed but interrupted lattice lines with nano-polycrystalline domains were

observed. As seen in Figure 3.4 (c) and (d), the total thicknesses for the film was measured by SEM to be approximately 80 nm with flat and uniform interfaces between the film and substrate.

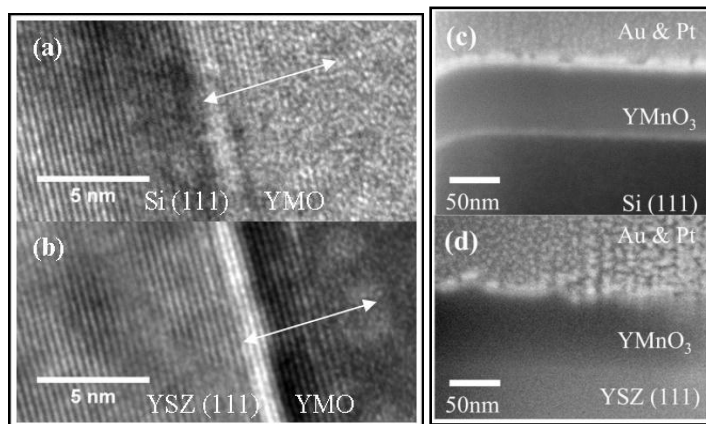


Figure 3.4. Bright field TEM images of ~6 nm YMO ultra thin films on (a) Si (111) and (b) YSZ (111) (c) SEM image of cross section of 80 nm YSZ films on Si (111) and (b) YSZ (111)

To obtain further information from the thin films, EXAFS taken at the Mn K-edge was used to determine the local atomic environment and oxidation states for the  $\text{Mn}^{3+}$  ions in the films grown on both YSZ (111) and Si (111). Based on the XRD data, it was expected to observe  $\text{MnO}_5$  bipyramids in the h-YMO on YSZ (111) and  $\text{MnO}_6$  polyhedron in the o-YMO on Si (111). Shown in Figure 3.5 (a) and (b) are schematic structures for (a) h-YMO with the  $\text{MnO}_5$  polyhedron ( $d(\text{Mn-O1})=1.687\text{\AA}$ ,  $d(\text{Mn-O2})=2.043\text{\AA}$ ,  $d(\text{Mn-O3})=1.830\text{\AA}$ ,  $d(\text{Mn-O4})=2.090\text{\AA}$ ) (Katsufuji, Masaki et al. 2002) and (b) o-YMO with  $\text{MnO}_6$  polyhedron ( $d(\text{Mn-O1})=2.209\text{\AA}$ ,  $d(\text{Mn-O2})=1.916\text{\AA}$ ,  $d(\text{Mn-O3})=1.947\text{\AA}$ ) (Iliev, Abrashev et al. 1998). Based on the structures from literature, the average bond lengths for O-Mn in h-YMO and o-YMO should be  $1.9125\text{\AA}$  and  $2.024\text{\AA}$  respectively. Shown in Figure 3.5 (c) and (d) are the  $k^3$  weighted EXAFS data and Fourier transformed (FT) spectra respectively. Unfortunately, the quality of the data was degraded after a  $k$  of 6, due to the ultra-thin nature of the films, which limited the accuracy for these films. Nonetheless, the FT spectra demonstrated distinct  $R$  spaces for the data collected on

the films grown on Si (111) and YSZ (111). By using the crystal structures as a guide, the FT peaks could be indexed to the respective Mn bonding distances as seen in Figure 3.5 (b). Additionally, as a comparison to this work,  $R$  spaces from literature for the manganate with hexagonal phase (Asokan, Chen et al. 2009) and manganate with orthorhombic phase (Sanchez, Subias et al. 2003) are plotted in Figure 3 (d). Compared to the references, the interaction distances from the ALD films are slightly larger, but are qualitatively similar.

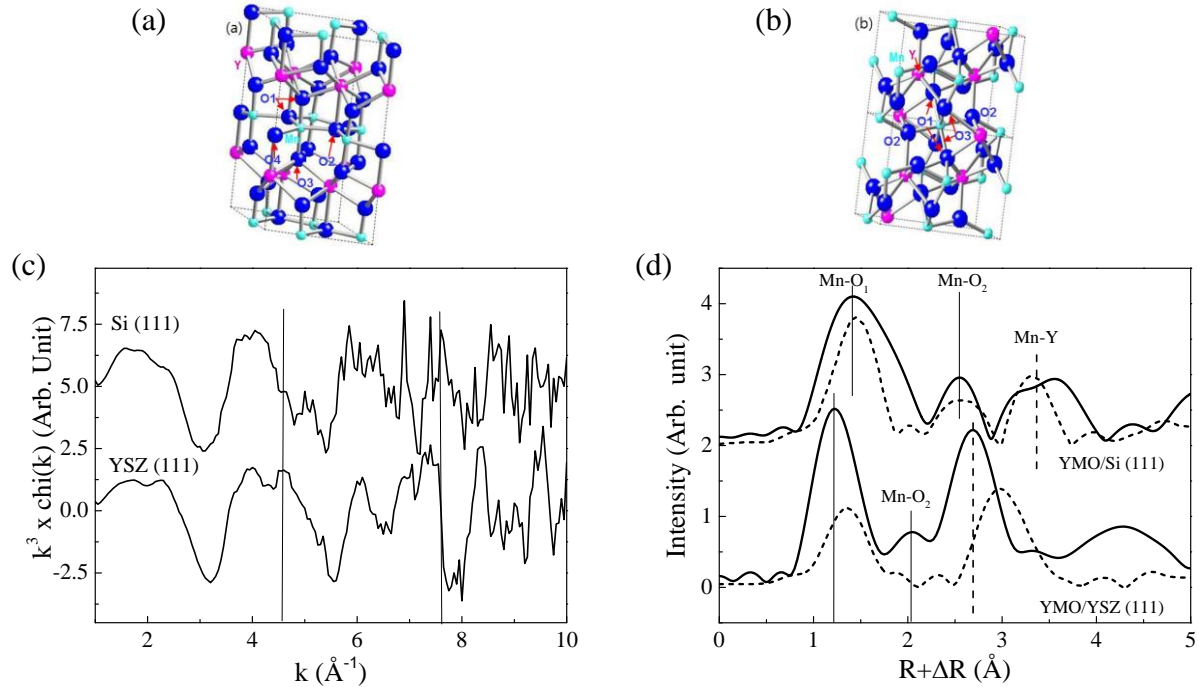


Figure 3.5. Schematic structure of (a) h-YMO with MnO<sub>5</sub> polyhedron ( $d(\text{Mn-O}_1)=1.687\text{\AA}$ ,  $d(\text{Mn-O}_2)=2.043\text{\AA}$ ,  $d(\text{Mn-O}_3)=1.830\text{\AA}$ ,  $d(\text{Mn-O}_4)=2.090\text{\AA}$ ) (Katsufuji, Masaki et al. 2002) and (b) o-YMO with MnO<sub>6</sub> polyhedron ( $d(\text{Mn-O}_1)=2.209\text{\AA}$ ,  $d(\text{Mn-O}_2)=1.916\text{\AA}$ ,  $d(\text{Mn-O}_3)=1.947\text{\AA}$ ) (Iliev, Abrashev et al. 1998). (c) The EXAFS of collected  $k^3$  spectra and (d) respective Fourier Transformation (FT) for 80 nm YMO thin films on Si (111) and 80 nm YMO thin films YSZ (111). The ● spheres represent the O atoms, the ● and ● represent the Y and Mn atoms, respectively.

It was therefore more strongly suggested that the YMO on the Si (111) has the orthorhombic phase and the YMO on YSZ (111) has the hexagonal phase. Additionally, the observed magnetic properties were consistent with the proposed phases for the YMO films on

YSZ (111) and Si (111). Unfortunately, a detailed analysis of the  $\text{Mn}^{3+}$  local environment using either L-edge absorption or grazing-incidence experiments for exact confirmation of the crystal structure was not possible due to the lack of availability for the beamlines. However, the FT performed (up to  $6 \text{ \AA}^{-1}$ ) was used in conjunction with the XRD to give confidence to the interpretation of the data.

### 3.3 Magnetic properties of ALD grown $\text{YMnO}_3$ thin films

As mentioned previously, the reported literature values for the Néel temperatures of h-YMO and o-YMO are  $T_N = 65\text{-}80 \text{ K}$  (Van Aken, Palstra et al. 2004) and  $40\text{-}50 \text{ K}$  (Li, Yan et al. 2009) respectively. Therefore, to characterize the ALD YMO films, the temperature dependence was studied to corroborate the structural data that was discussed in 3.2. Shown in Figure 3.6 (a) and (b) are the magnetic susceptibility dependencies on temperature ( $\chi$  vs.  $T$ ) of YMO grown on Si (111) and YSZ (111) respectively, using zero-field cooled (ZFC, solid symbols) and field cooled (FC, open symbols) at  $100 \text{ Oe}$  conditions. For the films grown on Si (111), two thicknesses of  $6 \text{ nm}$  (triangles) and  $80 \text{ nm}$  (squares) were studied, with the divergence between the ZFC and FC curves being caused by the diamagnetic silicon substrate. To determine the antiferromagnetic Néel transition temperatures,  $d\chi/dT$  was plotted, as seen in Figure 3.6 (c). Pointed out by the vertical lines, the transition points are marked by the sudden variation in the slope of the FC curves. These cusps were at approximately  $49 \text{ K}$  and  $57 \text{ K}$  for the  $6 \text{ nm}$  and  $80 \text{ nm}$  films respectively. These values were consistent with the structural data that determined the films to be primarily o-YMO (Iliev, Abrashev et al. 1998; Hsieh, Lin et al. 2008; Marti, Skumryev et al. 2009; Bergum, Okamoto et al. 2011). In addition to those cusps, another sudden change in the slope of  $\chi$  was observed below  $28 \text{ K}$ . This was interpreted to be a spin-glass behavior as the temperature approached absolute zero (Li, Yan et al. 2009). This spin-glass

phenomenon has been attributed to the spin reorientation of the  $\text{Mn}^{3+}$  ions and is present regardless of the sample thickness. Similar Néel and spin-glass transition temperatures have been observed in o-YMO films grown on  $\text{SrTiO}_3$  (001) at  $T_N = 44$  K and  $T_{SG} = \sim 28$  K respectively (Hsieh, Lin et al. 2008).

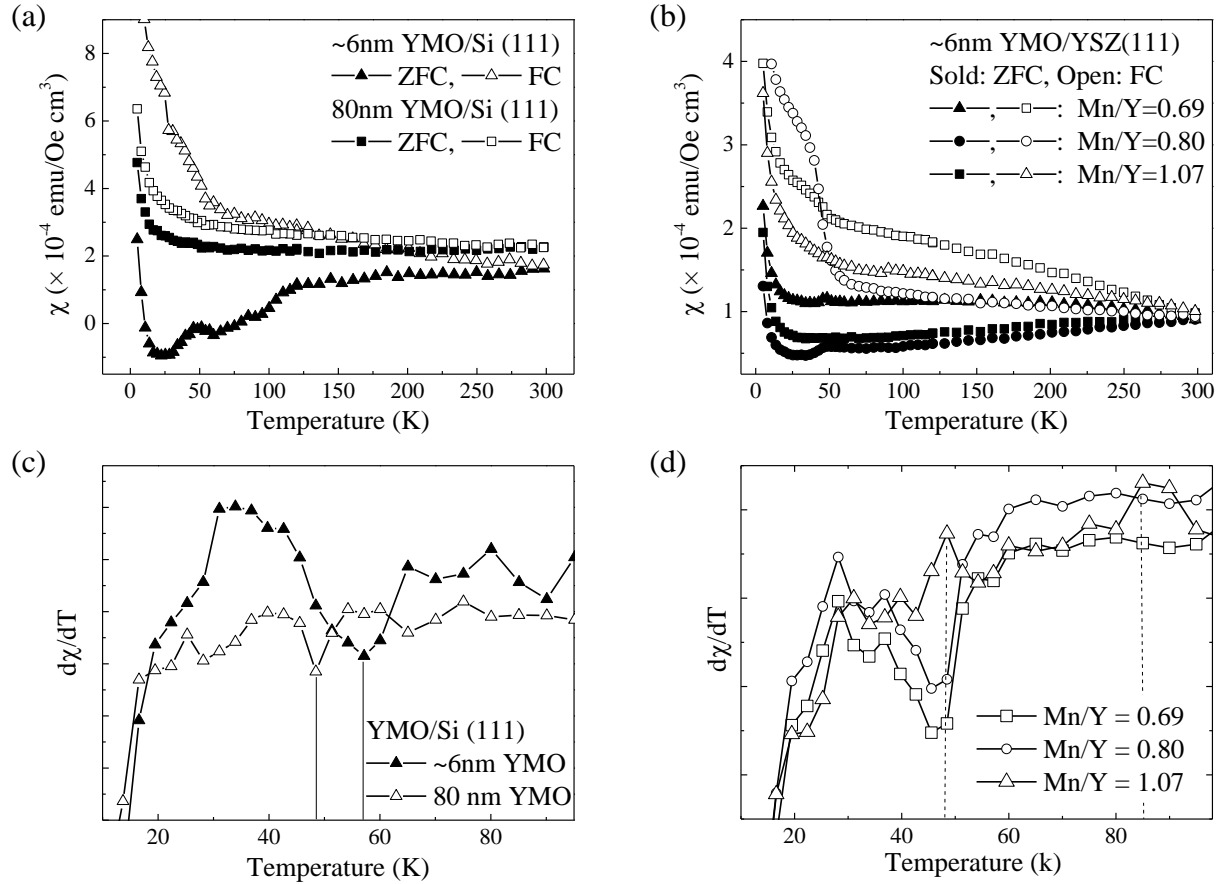


Figure 3.6. (a) dc magnetic susceptibility ( $\chi$ ) for the ~6 nm and 80 nm YMO thin films on Si (111) under 100 Oe. Solid symbols represent ZFC condition and open symbols represent FC condition (b) dc magnetic susceptibility ( $\chi$ ) for ~6 nm YMO thin films on YSZ (111) with different Mn/Y atomic ratios under 100 Oe. (c) The temperature dependence of  $d\chi/dT$  for ~6 nm and 80 nm YMO thin film on Si (111) between the range  $0 < T < 95$  K (c) The temperature dependence of  $d\chi/dT$  for ~6 nm ultra thin films on YSZ (111) in range  $0 < T < 95$  K

The  $\chi$  vs.  $T$  at ZFC (solid symbols) and FC (open symbols) for ~6 nm thick YMO films grown on YSZ (111) are shown in Figure 3.6 (b) for films with varying degrees of Mn:Y ratios of 0.69 (triangles), 0.80 (circles), and 1.07 (squares). The divergences of the ZFC-FC curves are

due to the paramagnetic contributions from the YSZ (111) substrate. Similarly to the films grown on Si (111), the  $d\chi/dT$  was plotted as seen in Figure 3.6 (d). For the films with lower Mn content, Mn/Y = 0.69 and 0.80, cusps could be seen at ~44 K which corresponded to the  $T_N$  for the o-YMO phase that was detected using XRD. On the other hand, for the film with Mn/Y = 1.07, a small cusp was found at ~48 K and a larger one at 85 K which was consistent with the reported  $T_N$  value for h-YMO (Huang, Fjellvag et al. 2006). These results were corroborated by the structural data that showed a structural transition as the composition ratio between Mn/Y approached unity.

To determine the antiferromagnetic coupling strength between Mn ions, the paramagnetic Curie temperature ( $\theta_{cw}$ ) was calculated by plotting  $\chi^{-1}$  vs.  $T$  for the YMO films grown on YSZ (111) at the three varying compositions of Mn/Y = 0.69, 0.80, and 1.07 as seen in Figure 3.7. At temperatures above 150 K,  $\chi^{-1}$  vs.  $T$  was determined to have a linear relationship, indicating the applicability of the Curie-Weiss Law. By fitting  $\chi^{-1} = (T - \theta_{cw})/C$  between 150-320 K,  $\theta_{cw}$  was calculated for the three samples with varying composition. For the films with Mn/Y = 0.69 and 0.80,  $\theta_{cw}$  was -280 K and -440 K respectively, which were similar to the reported value for o-YMO at -330 K by Chen *et al.* (Chen, Zhang et al. 2005). On the other hand, the value of  $\theta_{cw}$  for the film with Mn/Y=1.07 was -580 K, which was similar to -510 K ~ -550 K for h-YMO reported previously (Huang, Fjellvag et al. 2006; Park, Lee et al. 2010).

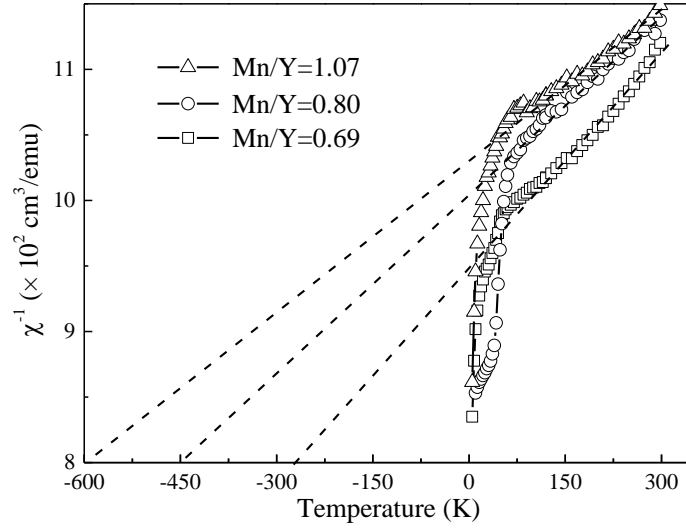


Figure 3.7.  $1/\chi$  as a function of temperature for ~6 nm YMO ultra thin films on YSZ (111) with different Mn/Y atomic ratios.

These values suggested that the antiferromagnetic coupling strength between Mn ions became enhanced as Mn/Y approached unity. The enhanced antiferromagnetic strength may have pushed the systems from a frustrated antiferromagnetic state to a spin glass state at low temperatures as proposed by *Chen et al.* (Chen, Zhang et al. 2005). Using these fitted values, it was then possible to calculate the frustration parameter ( $f$ ) =  $|\theta_{cw}|/T_N$ . Reported literature values for  $f$  for h-YMO range from 5.32 ~ 7.33 (Munoz, Alonso et al. 2000; Tomuta, Ramakrishnan et al. 2001; Singh, Patnaik et al. 2010) whereas  $f$  for o-YMO reported was much lower, from 0.7 ~ 1.3 (Munoz, Alonso et al. 2002; Iliev, Lorenz et al. 2005). On the other hand, for a similar RMnO<sub>3</sub> manganate system, YbMnO<sub>3</sub>, the  $f$  value for h- phase is smaller than that of o- phase (Huang, Fjellvag et al. 2006). In this work, the calculated  $f$  for h-YMO thin films with Mn/Y=1.07 was 6.82 while  $f$  for the o-YMO thin film with Mn/Y=0.69 was 6.36. This indicated that the geometric frustration increased as the Mn/Y ratio approached unity in the YMO thin films grown on YSZ (111) which is consistent with the trend reported previously, despite the fact that the values are not perfectly the same.

The magnetic field dependence upon magnetization ( $M$  vs.  $H$ ) was studied between -3000 Oe and +3000 Oe at temperatures of 20 K and 298 K for the 6 nm thick YMO films grown on Si (111). As shown in Figure 3.8 (a) and (b) in black, the saturation magnetizations ( $M_s$ ) at 20 K and 298 K were found to be  $4.24 \times 10^{-5}$  emu and  $3.34 \times 10^{-5}$  emu, respectively whereas the remnant magnetizations ( $M_r$ ) were approximately  $6.8 \times 10^{-4}$  emu and  $4.8 \times 10^{-4}$  emu, respectively which are shown in greater detail in Figure 3.8 (c) and (d). The coercive fields ( $H_C$ ) at 20 K and 298 K were 114 Oe and 54.5 Oe respectively which indicated the higher energy required to rotate the spins at lower temperatures. While bulk YMO is known to demonstrate antiferromagnetic properties for both o-YMO and h-YMO phases, the data for these ultra-thin YMO films indicated ferromagnetic ordering. It is hypothesized that this is due to uncompensated Mn spins at the surface and interface, which has been previously reported in literature for nanoparticles (Zheng, Straub et al. 2006) or ultra thin film (Bergum, Okamoto et al. 2011) systems. The TEM result shown in Figure 3.4 of the YMO film on Si (111) indicated interrupted lattice lines and nano-polycrystalline domains throughout the film and could have contributed to the weak ferromagnetic ordering at the interfaces and grain boundaries. It has also been reported that weak ferromagnetic ordering in bulk antiferromagnetic systems has been predicted due to the interaction of canted spins known as the Dzyaloshinskii-Moriya interaction (Dzyaloshinsky 1958; Moriya 1960). For YMO thin films, the ferroelectric displacement between noncollinear neighboring spins in o-YMO thin films was shown to create a spin current which caused weak ferromagnetic coupling (Cheong and Mostovoy 2007; Nakamura, Tokunaga et al. 2011).

As YMO is purportedly a magnetoelectric material, the effect of electric field upon the magnetization was studied by applying an *in-situ* 20 V dc voltage across the YMO film grown on



Si (111) inside the SQUID magnetometer during a  $M$  vs.  $H$  experiment. Shown in Figure 3.8 (a) and (b) in red are the hysteresis loops for the samples while the voltage is being applied. The data shows that the hysteresis loops were not significantly changed after the electric field was applied for the measurement at 298 K, however at 20 K the coercivity decreased from 114 Oe to 109 Oe, indicating weak magnetoelectric coupling below TN. For the films grown on YSZ (111), the magnetization was not substantially changed at both 298 K and 20 K which is probably due to the very high dielectric constant (24-29.5) of the YSZ substrate.

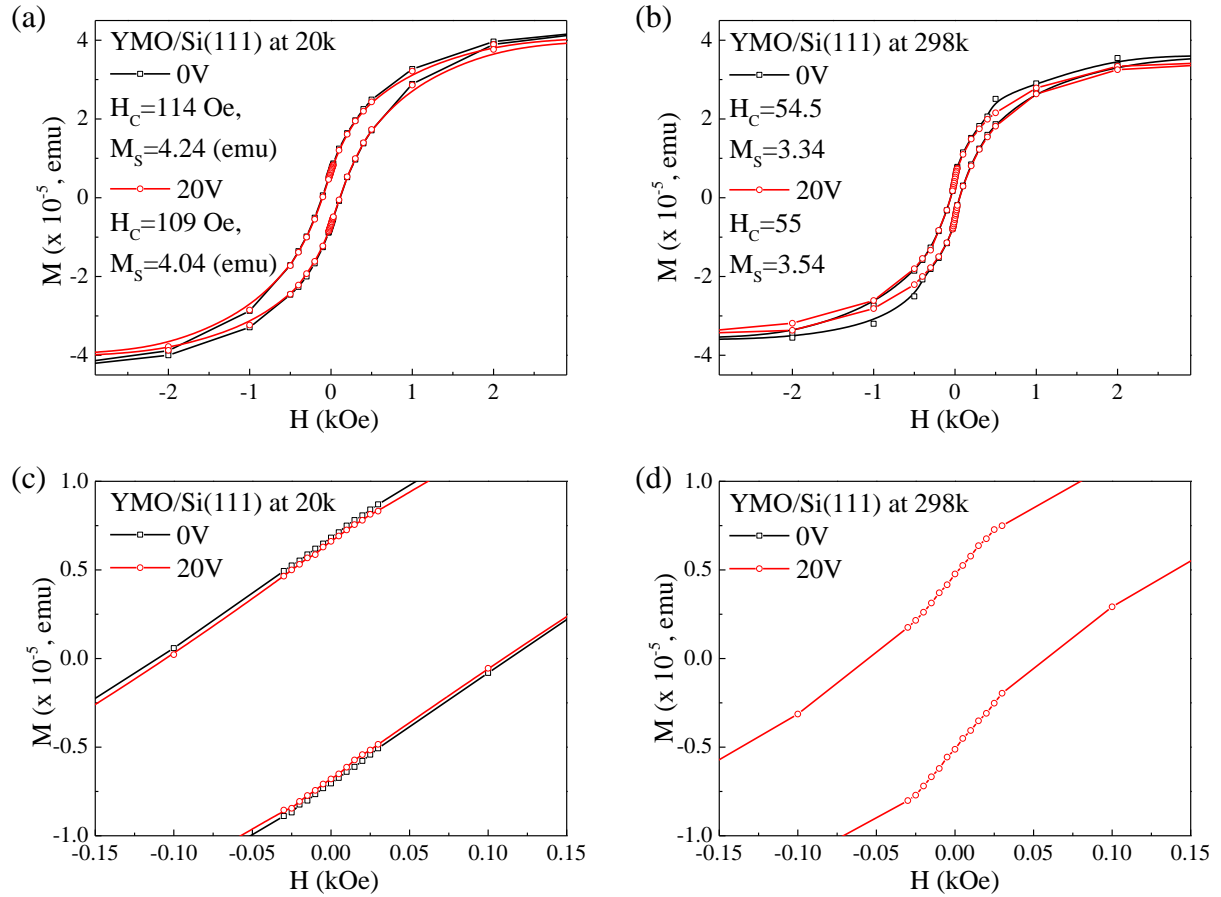


Figure 3.8. Magnetic hysteresis loop ( $M$  vs.  $H$ ) measured at (a) 20 K and (b) 298 K for  $\sim 6$  nm YMO ultra thin films on Si (111) before and after 20 V electric polling. (c) and (d) Closer look at the coercive fields.

### 3.4 Conclusions

$\text{YMnO}_3$  (YMO) was synthesized using radical enhanced atomic layer deposition (RE-ALD) on Si (111) and YSZ (111) between 6-80 nm thick. The film composition was controlled by adjusting the precursor pulsing sequence between  $\text{Mn}(\text{tmhd})_3$  and  $\text{Y}(\text{tmhd})_3$  precursors and was confirmed using XPS. The structure of the film was assessed as a function of the substrate choice, annealing conditions, as well as the composition and was shown to have primarily orthorhombic (o-YMO) phase when grown on Si (111), whereas on YSZ (111) had a mixture of hexagonal (h-YMO) and o-YMO, with the fraction of h-YMO increasing as the ratio between Mn/Y approached unity. In addition, the atomic structure for the films were assessed using HR-TEM and were found to contain a crystalline interfacial layers which then transitioned to nanopolycrystalline films. For additional confirmation of the structure, EXAFS was used to determine the local bonding environment for the  $\text{Mn}^{3+}$  ions. The magnetic properties of the YMO films on both Si (111) and YSZ (111) were studied as a function of the temperature, applied magnetic field, and dc electric field. The dc magnetic susceptibility as a function of temperature showed that the films grown on Si (111) had  $T_N = \sim 48 - 57$  K corresponding to the o-YMO phase, while the films on YSZ (111) had two anomalies at  $\sim 48.5$  K and  $\sim 80$  K indicating the coexistence of o-YMO and h-YMO, but the anomaly at  $\sim 80$  K became more pronounced at compositions which approached unity. The magnetic field dependence showed weak ferromagnetism and was likely due to uncompensated spins at the interface and surface for the ultra-thin films. When an electric field was applied *in-situ* during the  $M$  vs.  $H$  measurement, a change in  $H_C$  was recorded at 20 K indicating magnetoelectric coupling below  $T_N$ . The experiments demonstrated that ALD growth of YMO was a viable method for the integration of magnetoelectric thin films and could be used in conjunction with 3-D geometries for nanoscale multiferroic composites in the future.

## CHAPTER 4: GROWTH AND CHARACTERIZATION OF BISMUTH IRON OXIDE USING RADICAL ENHANCED ATOMIC LAYER DEPOSITION

Multiferroic  $\text{BiFeO}_3$  (BFO) thin films were deposited using radical enhanced atomic layer deposition (RE-ALD) on  $\text{SrTiO}_3$  (STO (001)) and silicon (Si (001)) substrates. As a prerequisite to depositing the mixed oxide BFO films, the growth of binary oxides  $\text{Fe}_2\text{O}_3$  and  $\text{Bi}_2\text{O}_3$  was studied to assess the optimal ALD processing conditions as a function of processing temperature, precursor pulse time, and ALD cycle number and it was determined that an ALD temperature window exists at approximately 200-210 °C. By adjusting the precursor cycle pulsing sequence, stoichiometric BFO thin films were synthesized and the composition was confirmed using X-ray photoelectron spectroscopy (XPS). To study the crystallization of these films, the crystal structure for stoichiometric films deposited on STO (001) was investigated as a function of the annealing temperature and it was found that the films crystallized with a (001) pseudocubic orientation with epitaxial quality when annealed between 550-650 °C as confirmed using x-ray diffraction (XRD) and high-resolution transmission electron microscopy (HR-TEM). The surface roughness was also assessed using atomic force microscopy (AFM) as a function of the annealing temperature and the RMS roughness ranged between 3.8 Å as synthesized to 44.8 Å at the optimal annealing condition of 650 °C. To study the multiferroic properties, the ferroelectric switching and ferromagnetic hysteresis was demonstrated using piezoresponse force microscopy (PFM) and superconducting quantum interference device (SQUID) magnetometry respectively with a measured saturation magnetization of approximately 27 emu/cm<sup>3</sup>. BFO grown by RE-ALD was determined to have comparable properties to films grown by other methods and demonstrated the potential of ALD to synthesize multiferroic complex oxide thin films.

#### 4.1 Synthesis of BiFeO<sub>3</sub> by Radical Enhanced ALD

Synthesis BFO by radical enhanced ALD was accomplished using the multi-beam reactor which was described earlier in section 2.1 using the solid precursors Bi(tmhd)<sub>3</sub> and Fe(tmhd)<sub>3</sub>, as well as oxygen radicals as described in section 2.2. The oxygen radicals were produced from a coaxial microwave cavity radical beam source, which was discussed in section 2.1.1. To confirm the initial growth of the constituent oxides Fe<sub>2</sub>O<sub>3</sub> and Bi<sub>2</sub>O<sub>3</sub> by ALD, X-ray photoelectron spectroscopy (XPS) was utilized as shown in Figure 4.1; the films were grown at 210 °C on Si (001), consisting of 100 cycles of the following sequence: 90 seconds metalorganic precursor, 5 seconds pump down, 20 seconds oxygen radical exposure, and 5 seconds pump down.

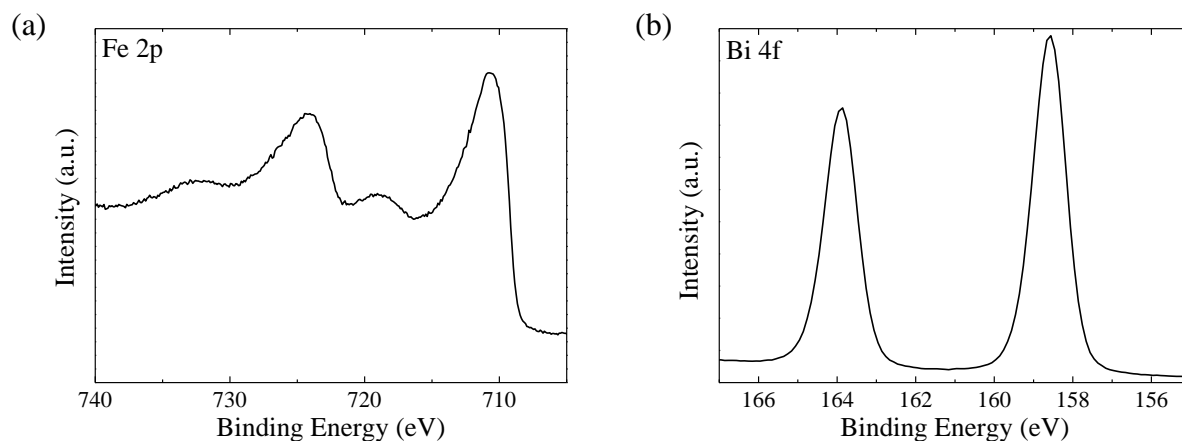


Figure 4.1. High resolution XPS spectra for (a) Fe 2p peak from Fe<sub>2</sub>O<sub>3</sub> film and (b) Bi 4f peak from Bi<sub>2</sub>O<sub>3</sub> film grown by ALD

The XP spectra were corrected to the accepted literature value of 284.8 eV for C 1s. According to the spectra for Fe<sub>2</sub>O<sub>3</sub> seen in Figure 4.1 (a), the peak positions for Fe 2p<sub>3/2</sub> and 2p<sub>1/2</sub> were approximately 710.7 eV and 724.0 eV respectively. For Bi<sub>2</sub>O<sub>3</sub> seen in Figure 4.1 (b), the peak positions for Bi 4f<sub>7/2</sub> and 4f<sub>5/2</sub> were 158.6 eV and 163.9 eV respectively. These values indicated a 3+ oxidation state for both the Fe<sub>2</sub>O<sub>3</sub> (Tan, Klabunde et al. 1990) and Bi<sub>2</sub>O<sub>3</sub> films (Uchida and Ayame 1996), as was expected due to the oxidation state of the precursors as-received. In addition, the detailed spectra for the Fe 2p region also featured shake-up satellite

peaks at 718.9 eV and 732.8 eV which were to be expected for the  $\text{Fe}^{3+}$  oxidation state (Mills and Sullivan 1983).

To determine optimal processing conditions, the ALD growth rate had to be quantized by measuring the film thickness, then to calculate resulting growth rate. Therefore, it was first necessary to develop a spectroscopic ellipsometry model that could quickly and non-destructively determine the film thickness. By depositing sufficiently thick films, it was possible to initially determine the exact film thicknesses using a cross-section SEM micrograph as seen in Figure 4.2 (c) and (d). Then by fitting a Lorentz oscillator model Eq. (4.1) to the experimental ellipsometric data, using the known thickness as seen in Figure 4.2, the model constants could be determined. Therefore, the Lorentz model constants, listed in Table 4.1, were determined and the resulting fitted data showed good agreement to the measurements made using SEM micrographs.

$$\tilde{\epsilon} = \epsilon_{1,offset} + \frac{AE_c}{E_c^2 - E^2 - iBE} \quad \text{Eq. (4.1)}$$

Table 4.1 Fitted parameters for Lorentz oscillator model used in ellipsometry measurement

Material	$\epsilon_1(\text{inf})$	$A_m$	$B_r$	$E_n$
$\text{Bi}_2\text{O}_3$	1.58	107.97	1.0671	4.9328
$\text{Fe}_2\text{O}_3$	1.7588	4.7688	1.263	3.487

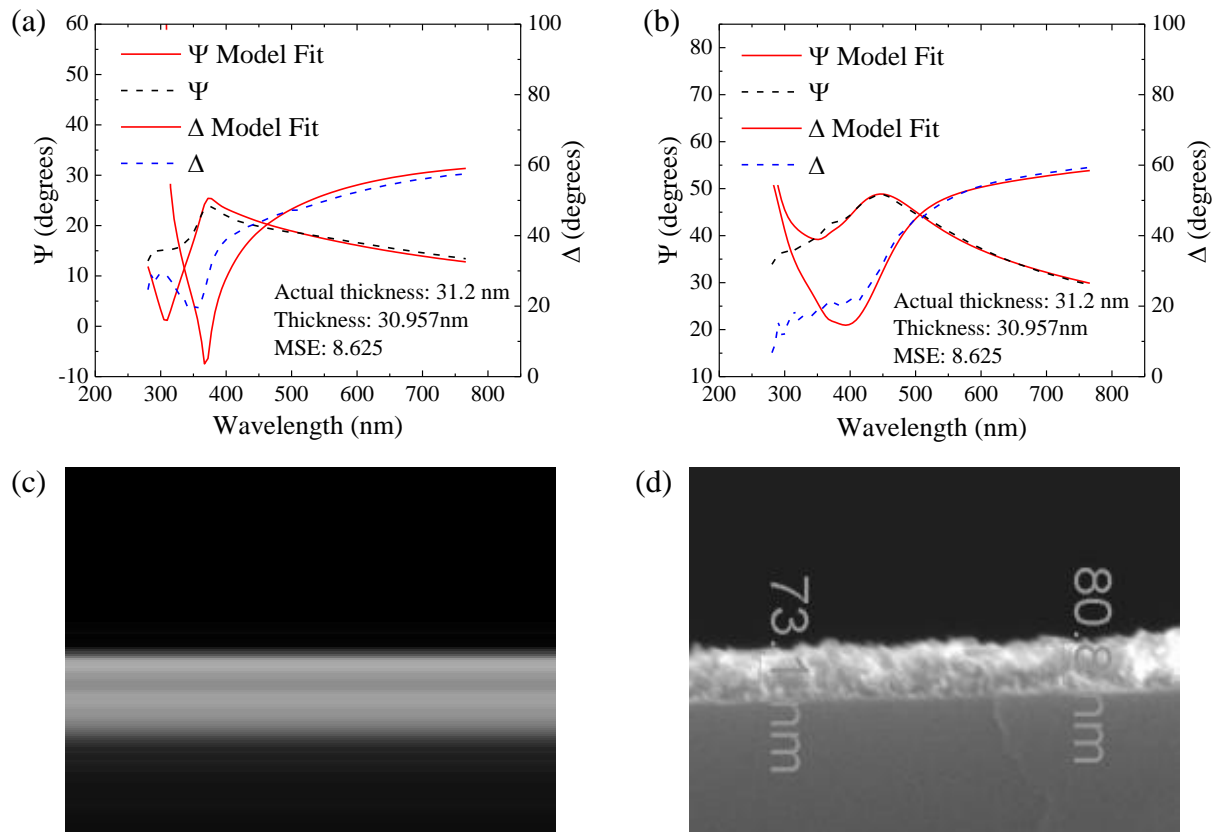


Figure 4.2. Calibration of spectroscopic ellipsometry model (solid lines) fitted to experimental data (dashed lines) for (a)  $\text{Bi}_2\text{O}_3$  and (b)  $\text{Fe}_2\text{O}_3$  films grown on Si (001) substrates using cross-section SEM images for (c)  $\text{Bi}_2\text{O}_3$  and (d)  $\text{Fe}_2\text{O}_3$ .

Subsequently, the characterization for the growth of  $\text{Bi}_2\text{O}_3$  and  $\text{Fe}_2\text{O}_3$  could systematically be studied to determine optimal ALD processing parameters. First the temperature dependence of the growth rate was determined by depositing films of  $\text{Bi}_2\text{O}_3$  and  $\text{Fe}_2\text{O}_3$  on Si (001) substrates at varying temperatures between 190 °C and 230 °C. The ALD sequence for both oxides consisted of 100 cycles each of the following: 90 seconds metalorganic precursor, 5 seconds pump down, 20 seconds oxygen radical exposure, and 5 seconds pump down. By dividing the thickness by the number of cycles, the growth rate could be determined which is shown in Figure 4.3. In addition, the compositions of the films were also measured as a function of the growth temperature as seen in Figure 4.4.

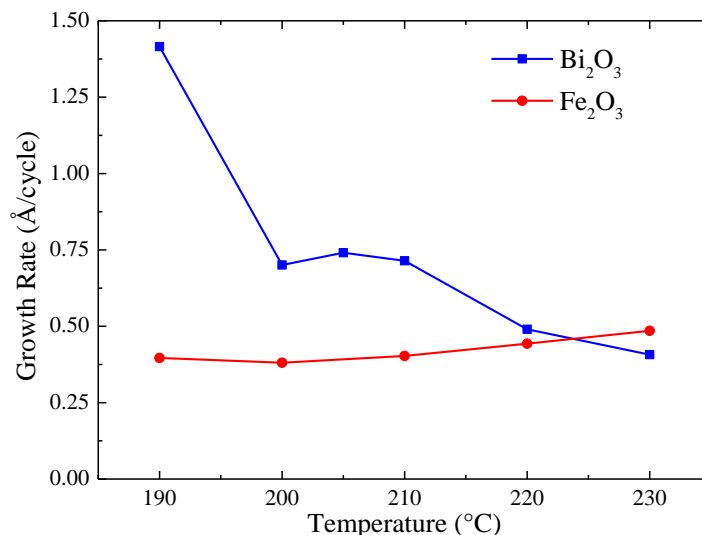


Figure 4.3. Temperature dependence of ALD growth rate for Bi<sub>2</sub>O<sub>3</sub> and Fe<sub>2</sub>O<sub>3</sub> films grown on Si (001) substrates in Å/cycle measured using ellipsometry

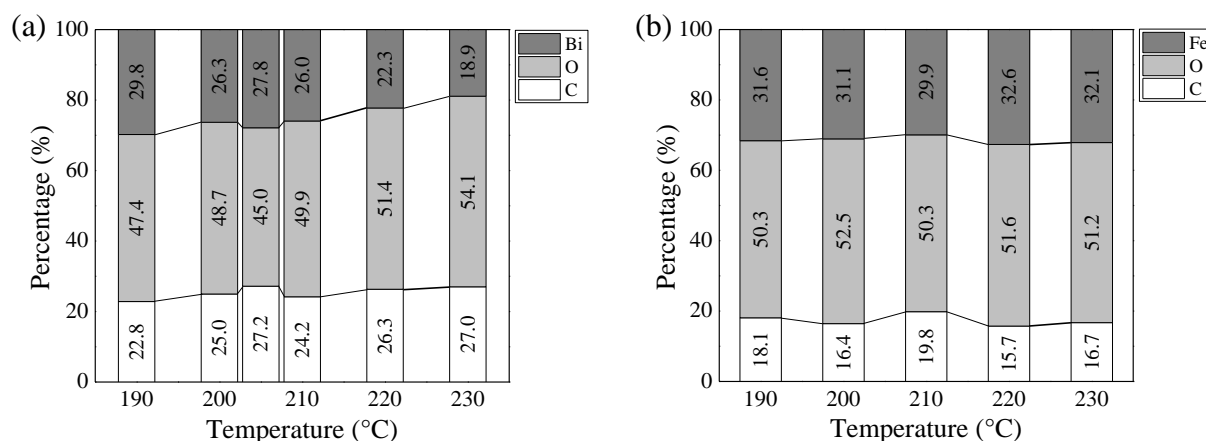


Figure 4.4. Composition of (a) Bi<sub>2</sub>O<sub>3</sub> and (b) Fe<sub>2</sub>O<sub>3</sub> films as a function of growth temperature as calculated using X-ray photoelectron spectra.

Based on the data given by the temperature dependence of the growth rates, it was determined that an ALD growth window existed approximately between 200 °C and 210 °C where the deposition rates for both Bi<sub>2</sub>O<sub>3</sub> and Fe<sub>2</sub>O<sub>3</sub> were relatively constant.

For Bi<sub>2</sub>O<sub>3</sub>, the growth rate was approximately 0.70-0.74 Å/cycle within the growth window as seen in Figure 4.3 (a). At a lower temperature of 190 °C, the growth rate was drastically higher at ~1.4 Å/cycle, indicating a condensation effect in which the Bi(tmhd)<sub>3</sub>

precursor was growing in a CVD manner and did not self-saturate as per ideal ALD growth. This effect was also observed in the work of Shen, et al. for the thermal ALD of  $\text{Bi}_2\text{O}_3$  also using  $\text{Bi}(\text{tmhd})_3$  but using  $\text{H}_2\text{O}$  as the oxidation source (Shen, Li et al. 2012). On the other hand, at increasing temperatures up to 230 °C beyond the growth window of 200-210 °C, the growth rate decreased, meaning that the precursor desorbed from the surface. This result was also mirrored in the work of Shen, et al. By comparison however, for this work, the ALD window is much lower compared to the thermal ALD process which reported a growth window between 270-300 °C. In addition, the growth rate of the RE-ALD process is much higher at 0.70-0.74 Å/cycle compared to ~0.1 Å/cycle for the thermal process. In addition, a report using another bismuth-containing precursor  $\text{Bi}(\text{OCMe}_2\text{iPr})_3$  and water as the co-reactant demonstrated a growth rate of ~0.36 Å/cycle which is still much smaller than the RE-ALD results. Using quantitative XPS, as discussed in 2.3.1 particularly using equation 2.7, the  $\text{Bi}_2\text{O}_3$  film composition was determined within the temperature range of 190-230 °C as shown in Figure 4.4. (a). The relative amount of Bi decreased and the amount of oxygen and carbon increased as the temperature increased. At 190 °C, the Bi content was the highest at ~30% whereas the C content was the lowest at ~23%. This indicated that although the Bi precursor was condensing on the surface, because the oxidation step was taken separately after the pump down period, it was still effective at removing the organic ligands from the precursor and not causing uncontrolled incorporation of carbon into the film. On the other hand, at the higher temperatures, the carbon content was larger while the growth rate became diminished due to desorption of precursor from the surface. Because the deposition rate of  $\text{Bi}_2\text{O}_3$  was lower, the relative fraction of Bi/C decreased. Nonetheless, the amount of carbon contamination was not substantially changed over the temperature range studied, increasing from ~23% at 190 °C to ~27% at 230 °C. According to research previously



done using the same experimental setup, the amount of adventitious oxygen and carbon was estimated to be 15% and 13% respectively (Van and Chang 2005).

The growth of  $\text{Fe}_2\text{O}_3$  by RE-ALD using  $\text{Fe}(\text{tmhd})_3$  was also studied within the same temperature range of 190-230 °C and had a relatively consistent growth rate that slightly increased from  $\sim 0.40$  to  $\sim 0.48$  Å/cycle as the temperature was increased as seen in Figure 4.3 (b), indicating that the temperature window was stable. However, it was observed experimentally that as the temperature increased further beyond 250 °C, the precursor decomposed on the surface and engaged in CVD growth. This observation was relatively consistent with the work of Lie, et al. who used  $\text{Fe}(\text{tmhd})_3$  precursor with ozone as the co-reactant and reported a growth window from 160-310 °C after which the precursor decomposed on the surface. The difference in the maximum allowable temperature is possibly due to the difference in oxidation sources, as the oxygen atoms used in this work are more reactive compared to ozone. When comparing the growth rate within the temperature window, the thermal ALD process had a growth rate of 0.124 Å/cycle which is substantially slower than the RE-ALD process in this work. For the composition of  $\text{Fe}_2\text{O}_3$  as a function of the growth temperature, shown in Figure 4.4. (b), the composition ratio between Fe, O, and C did not vary much within the temperature range studied. The Fe content was fairly consistent between  $\sim 30$ -32% while the C content was between  $\sim 17$ -20% with no obvious trend corresponding to the growth rate. When taking into account the results of the temperature dependence for both  $\text{Bi}_2\text{O}_3$  and  $\text{Fe}_2\text{O}_3$  growth, a sample temperature of 210 °C was chosen for the remainder of the experiments.

As ALD is a self-limiting technique, it was necessary to determine the effect of precursor pulse time upon the growth rate, as it coincides with the ability for the process to conduct conformal deposition over three-dimensional surfaces. The growth rate of  $\text{Bi}_2\text{O}_3$  and  $\text{Fe}_2\text{O}_3$  as a

function of the pulse time are shown in Figure 4.6 (a) and (b) respectively. A precursor pulse time of 90 seconds was then chosen to maximize growth rate as a function of actual time. To demonstrate a linear growth rate, the thicknesses of the  $\text{Bi}_2\text{O}_3$  and  $\text{Fe}_2\text{O}_3$  films were measured as a function of number of cycles as shown in Figure 4.6. According to the fitted linear curves,  $\text{Bi}_2\text{O}_3$  had a growth rate of  $\sim 0.65 \text{ \AA/Cycle}$  and  $\text{Fe}_2\text{O}_3$  had a growth rate of  $\sim 0.49 \text{ \AA/Cycle}$ , with no apparent nucleation delay.

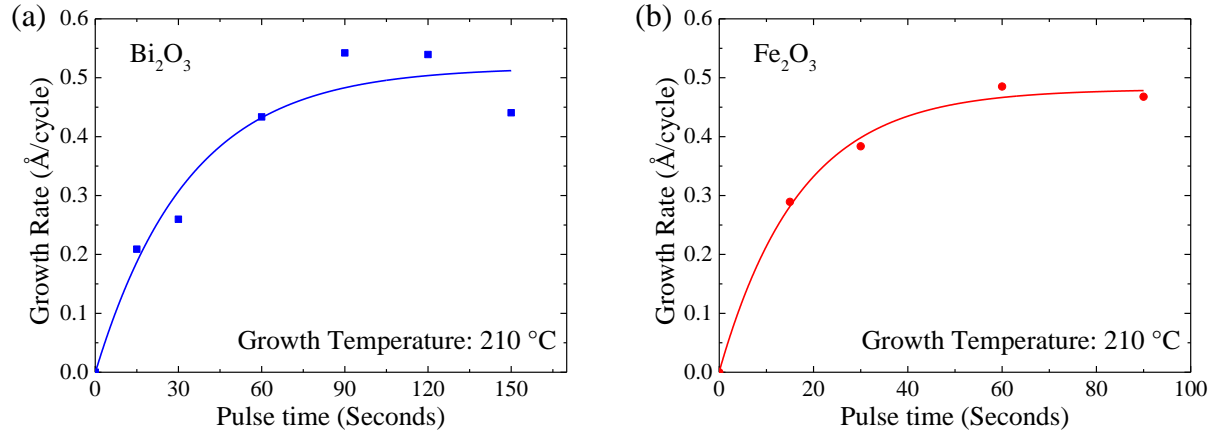


Figure 4.5. Effect of precursor pulse time on ALD growth rate for (a)  $\text{Bi}_2\text{O}_3$  and (b)  $\text{Fe}_2\text{O}_3$  grown on Si (001) substrates in  $\text{\AA/cycle}$  measured using ellipsometry.

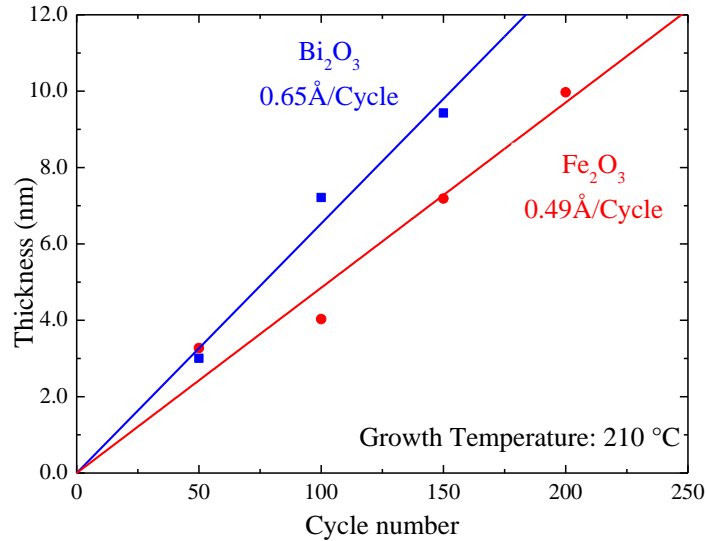


Figure 4.6. ALD film thickness (nm) as a function of number of cycles of  $\text{Bi}_2\text{O}_3$  and  $\text{Fe}_2\text{O}_3$  consisting of a 90 s metalorganic pulse, 5 s pump-down, 20 s radical pulse, 5 s pump-down cycle sequence.

Once the baseline growth of  $\text{Fe}_2\text{O}_3$  and  $\text{Bi}_2\text{O}_3$  was established, it was possible to integrate the processes to produce the BFO ternary oxide. As mentioned previously in 2.2, the precursors were pulsed sequentially in an  $x(\text{Fe}(\text{tmhd})_3\text{:O}) + y(\text{Bi}(\text{tmhd})_3\text{:O})$  manner while controlling the values of  $x$  and  $y$  to achieve the desired stoichiometry. Thus the deposition of the mixed composition films could be confirmed using XPS as seen in the survey scan shown in Figure 4.7 (a) and the stoichiometry could be controlled as shown in Figure 4.7 (b). In addition, the detailed spectra for Fe 2p and Bi 4f are displayed in Figure 4.7 (c) and (d) respectively. The detailed spectra, specifically the peak positions as well as satellite peaks for Fe 2p suggested that the metal ions consisted of the 3+ oxidation state. The carbon content was approximately 25 at. %. Since the multiferroic phase of BFO has a stoichiometry of  $\text{Fe}/\text{Bi} = 1$ , the values of  $x$  and  $y$  were then adjusted to achieve that value.

Once the process for stoichiometric BFO films was finalized, the next step was to anneal the films to induce crystallization. Because the multiferroic phase of BFO consists of a rhombohedrally distorted perovskite structure ( $a = b = c = 5.63 \text{ \AA}$ ,  $\alpha = \beta = \gamma = 59.4^\circ$ ) with space group  $R3c$ , it was also important to deposit the films onto a closely lattice matched substrate. In this case, single crystal simple cubic  $\text{SrTiO}_3$  (001) (STO) ( $a = b = c = 3.9 \text{ \AA}$ ) was used for most experiments and conducting 0.7 wt. % Nb doped  $\text{SrTiO}_3$  (001) (Nb:STO) was utilized for ferroelectric or piezoelectric testing. It has previously been demonstrated that BFO grows epitaxially on these substrates with a (012) orientation, that has also been notated as a (001) pseudocubic orientation (Wang, Neaton et al. 2003). The following section describes the structure and morphology of the ALD BFO samples before and after they had been annealed.

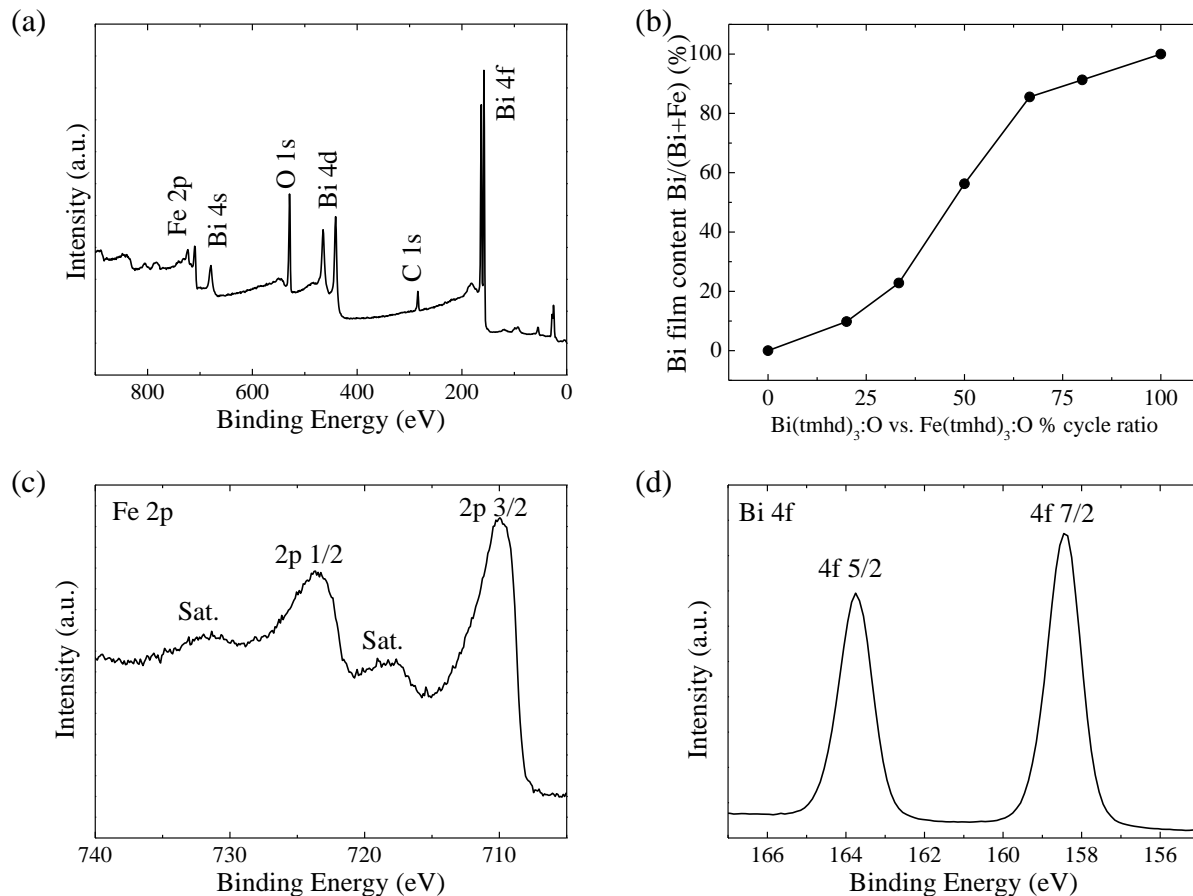


Figure 4.7. (a) XPS survey scan for  $\text{BiFeO}_3$  thin film grown by ALD. (b) Composition ratio of bismuth-iron oxide films grown by ALD as a function of pulse sequence ratio between  $\text{Bi}_2\text{O}_3$  and  $\text{Fe}_2\text{O}_3$ . Solid line is a guide for the eye indicating desired stoichiometric 1:1 ratio for  $\text{BiFeO}_3$ . Detailed XP spectra for (c) Fe 2p and (d) Bi 4f photoelectron peaks.

#### 4.2 Structure and Morphology of $\text{BiFeO}_3$ Thin Films Grown by Radical Enhanced ALD

The BFO films grown on STO (001) were annealed using a rapid thermal annealing process at various temperatures under an oxygen atmosphere for 60 seconds using a 50 °C/s ramp. The films were then analyzed as a function of the annealing temperature using XRD as shown in Figure 4.8. It was observed that the BFO film as deposited at 210 °C consisted of some  $\alpha\text{-Bi}_2\text{O}_3$  phase indicated by the (012) reflection at approximately  $2\theta = 28.01$  (JCPDS card 71-2274) which also persisted as the film was annealed to 450 °C. Low temperature crystallization

of  $\text{Bi}_2\text{O}_3$  had been observed previously in literature (Shen, Li et al. 2012). Once the annealing temperature surpassed  $550^\circ\text{C}$ , the reflection from  $\alpha\text{-Bi}_2\text{O}_3$  became diminished and the reflections from BFO pseudocubic  $(001)_{\text{pc}}$  at  $2\theta = 22.4^\circ$  and  $(002)_{\text{pc}}$  at  $2\theta = 45.8^\circ$  (JCPDS card 74-2016) became prominent with the highest intensity when the sample was annealed at  $650^\circ\text{C}$ . A detailed look at the BFO  $(001)_{\text{pc}}$  reflection is shown in Figure 4.8 (b) for the samples annealed at  $550^\circ\text{C}$  and  $650^\circ\text{C}$ . However, once the annealing temperature surpassed  $750^\circ\text{C}$ , it was determined that the film had begun phase separation as indicated by the appearance of the  $(001)$ ,  $(110)$ ,  $(002)$ , and  $(220)$  reflections originating from  $\text{BiFe}_2\text{O}_9$  (JCPDS card 20-0836).

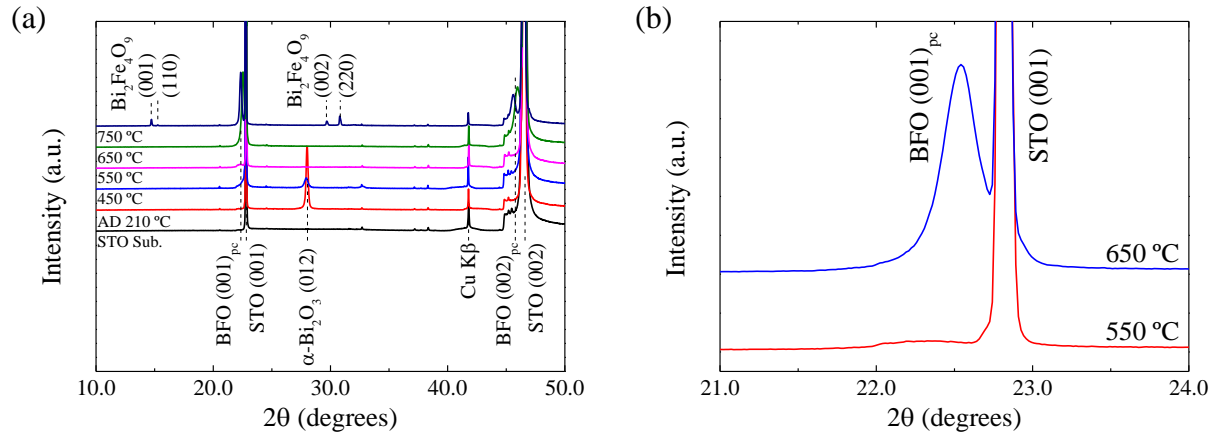


Figure 4.8. (a) Diffraction patterns for 35 nm thick  $\text{BiFeO}_3$  films grown on  $\text{SrTiO}_3$  (001) substrates as prepared and as a function of annealing temperature indicating crystallization. (b) Detailed look at BFO  $(001)_{\text{pc}}$  reflection for samples annealed at  $550^\circ\text{C}$  and  $650^\circ\text{C}$ .

Because the XRD data for the films annealed at  $550^\circ\text{C}$  and  $650^\circ\text{C}$  did not indicate additional BFO reflections, it suggested that the BFO films were oriented towards the STO substrate rather than being polycrystalline, which is typically the case for films synthesized by ALD. In order to confirm the crystal structure of the film, cross-section HR-TEM was utilized to reveal the local structure. As seen in Figure 4.9 (a), the TEM imaging showed that the film annealed at  $650^\circ\text{C}$  was epitaxial with respect to the substrate and had no visible secondary

phases. As expected from the XRD results, the (001)<sub>pc</sub> orientation was observed for the BFO film.

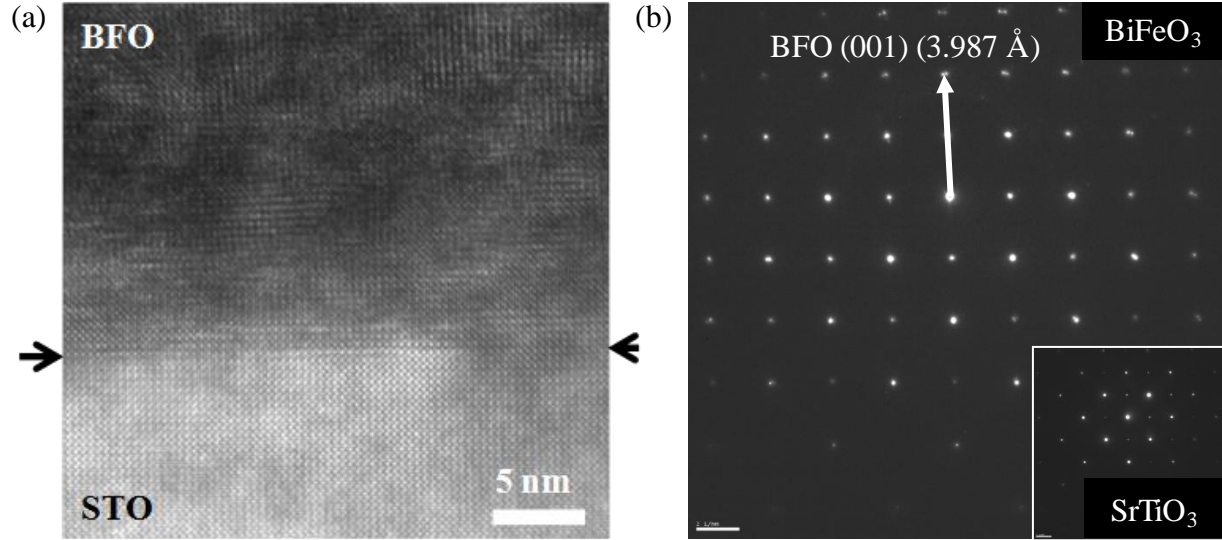


Figure 4.9. (a) TEM micrograph of BiFeO<sub>3</sub> film on SrTiO<sub>3</sub> (001) substrate indicating epitaxial nature of film crystallized at 650 °C. (b) Electron diffraction pattern of BiFeO<sub>3</sub> film.

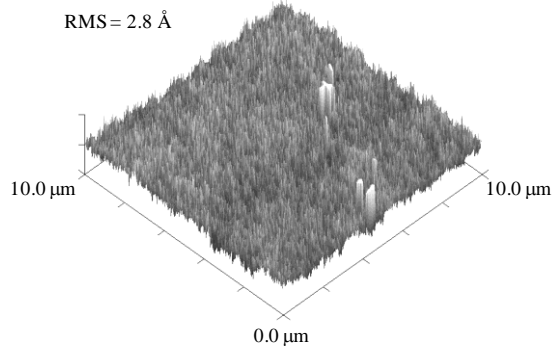
The electron diffraction pattern focused on the BFO film, seen in Figure 4.9 (b), showed that the film was single crystal without polycrystalline phases, which was corroborated by the XRD results. Since BFO consists of a rhombohedrally distorted perovskite structure, twinning of the diffraction spots was also observed. The interface between the STO and BFO was smooth without any visible misfit dislocations, most likely due to the close lattice between the film and substrate. The lattice d-spacing for BiFeO<sub>3</sub> was calculated using the method shown in 2.3.8 and is shown in Table 4.2.

Table 4.2 Calculated R values, calculated d-spacing, and comparison to d-spacing from JCPDS reference for SrTiO<sub>3</sub> substrate and BiFeO<sub>3</sub> film.

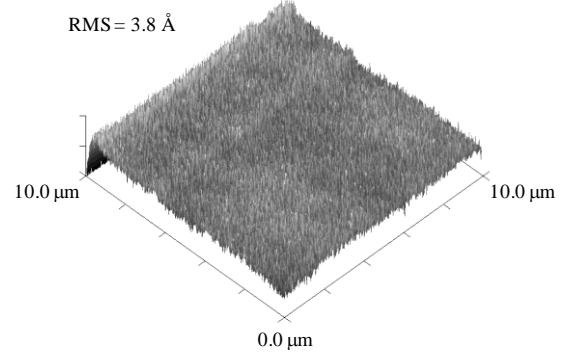
Material and Index	R (pixels)	d-spacing (Å)	d-spacing (Å) (JCPDS)
SrTiO <sub>3</sub> (001)	237.427	3.901	3.901
BiFeO <sub>3</sub> (001) <sub>pc</sub>	232.337	3.987	3.968

In addition to the microstructure, the surface topography of BFO grown on STO was studied using atomic force microscopy (AFM) on the samples as a function of the annealing temperature as seen in Figure 4.10. As a baseline, the bare STO substrate was measured and the surface roughness was atomically smooth at approximately RMS roughness = 2.8 Å. The as-synthesized BFO film had a roughness of RMS roughness = 3.8 Å which was consistent with typical ALD synthesized films. As the annealing temperature increased, however, the surface roughness increased dramatically. At the optimal annealing condition of 650 °C, the RMS roughness was 44.8 Å which was rather significant. Although the diffraction data did not reveal any substantial phase impurities, this surface roughness could have been caused by local regions of non-stoichiometry coalescing together. Lastly, the sample that was annealed at 750 °C showed the presence of phase separation with very large islands appearing on the surface and RMS roughness was 463 Å which was an order of magnitude larger than the 650 °C annealed sample.

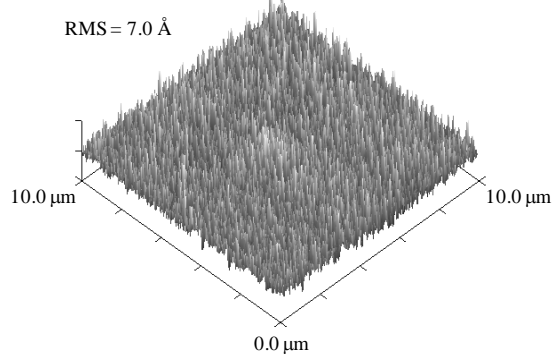
(a)  $\text{SrTiO}_3$  (100) substrate as received



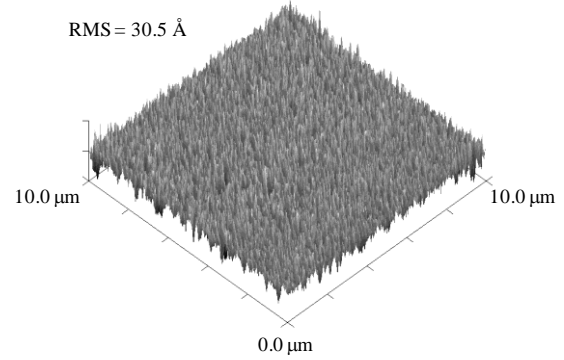
(b)  $\text{BiFeO}_3$  As Deposited at 210 °C



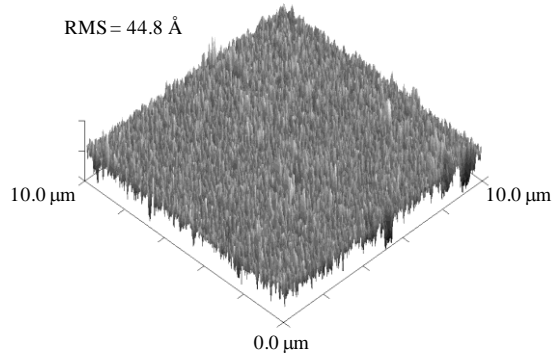
(c)  $\text{BiFeO}_3$  RTA at 450 °C



(d)  $\text{BiFeO}_3$  RTA at 550 °C



(e)  $\text{BiFeO}_3$  RTA at 650 °C



(f)  $\text{BiFeO}_3$  RTA at 750 °C

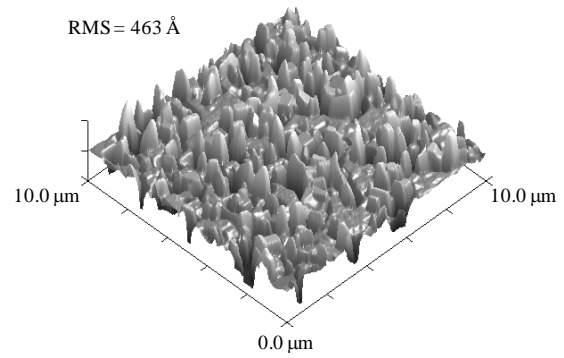


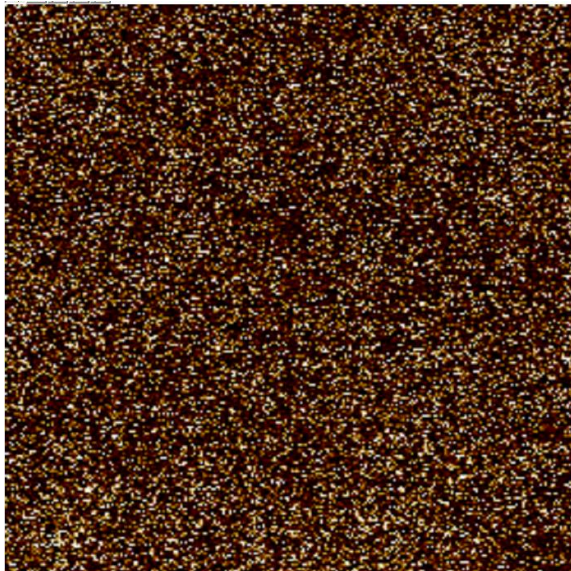
Figure 4.10. Surface morphology measured by AFM of (a)  $\text{SrTiO}_3$  substrate as received and 35 nm thick  $\text{BiFeO}_3$  films grown on  $\text{SrTiO}_3$  (001) substrates (b) as deposited at 210 °C and annealed at (c) 450 °C, (d) 550 °C, (e) 650 °C, and (f) 750 °C. RMS surface roughness, indicated by  $R_{\text{rms}}$  is increased as annealing temperature increases.



### 4.3 Multiferroic Properties of ALD Grown BiFeO<sub>3</sub> Thin Films

Once high quality BFO films could be attained by RE-ALD, it was then possible to characterize the functional properties such as the ferroelectric and magnetic responses. Because of the quality of the XRD and TEM data, the samples annealed at 650 °C were used. Ferroelectric testing was conducted using a piezoresponse force microscope (PFM) as explained previously in 2.3.5. For these experiments, a sample was deposited on conductive 0.7 wt% Nb:SrTiO<sub>3</sub> substrates. As shown in Figure 4.11, the ferroelectric domain switching could be demonstrated by locally applying  $\pm 12$  V using the conductive PFM tip. A square pattern could be reversibly written onto the ferroelectric domains as seen in Figure 4.11 (b). Because the samples were not smooth, however, the PFM measurement could not be conducted in contact-resonance mode, meaning that the collected signal was relatively noisy and ferroelectric domains could not be observed before it was poled with an electric field. Nonetheless, the phase contrast after the film was poled indicated that the film was ferroelectric.

(a) Before Poling



(b) After Poling

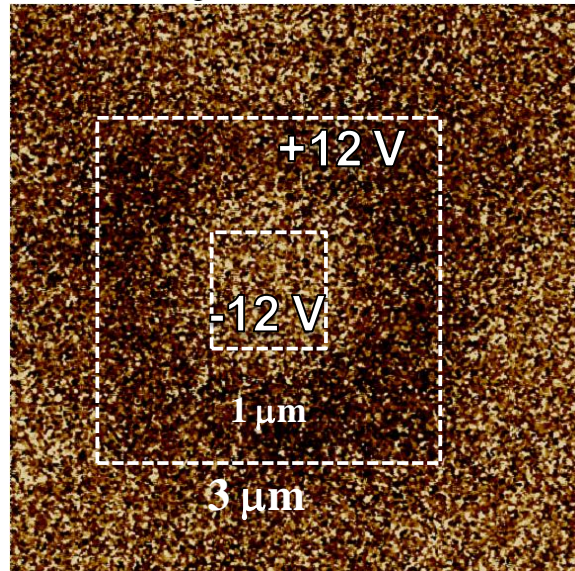


Figure 4.11. Piezoresponse force microscopy images of BFO film on Nb:STO substrate (a) before and (b) after  $\pm 12$  V applied using PFM tip in square pattern.

The magnetic hysteresis of the BFO film was also studied using the SQUID magnetometer. Since BFO is normally antiferromagnetic, the magnetization was not expected to be very high. Nonetheless, it has also been reported that weak ferromagnetic ordering in bulk antiferromagnetic systems has been predicted due to the interaction of canted spins known as the Dzyaloshinskii-Moriya interaction (Dzyaloshinsky 1958; Moriya 1960). Indeed, as shown in Figure 4.12, the BFO sample annealed at 650 °C was observed to be weakly ferromagnetic as demonstrated by the small hysteresis loop. The saturation magnetization  $M_s$  was approximately 27 emu/cm<sup>3</sup>, whereas the magnetic coercivity  $H_C$  was about 63 Oe.

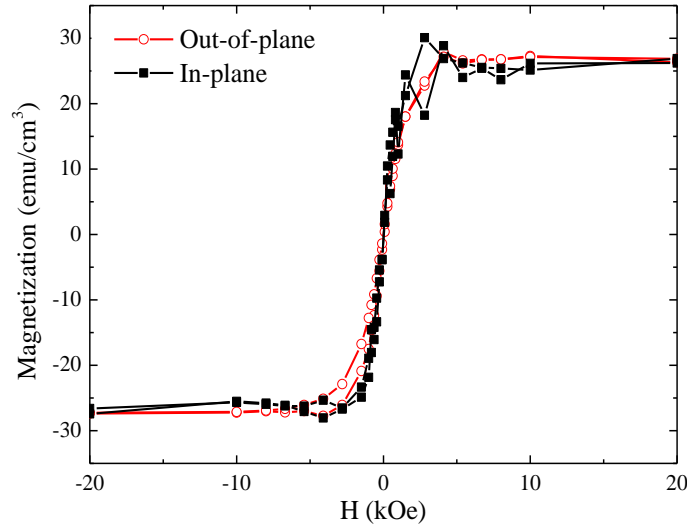


Figure 4.12. Magnetic hysteresis of BFO film annealed at 650 °C on STO substrate with applied magnetic field oriented in-plane (black squares) and out-of-plane (red circles) relative to the sample plane.

#### 4.4 Conclusions

$\text{BiFeO}_3$  (BFO) thin films were synthesized using radical enhanced atomic layer deposition (RE-ALD), and the stoichiometry Bi/Fe could be controlled towards unity by adjusting the precursor cycle sequence as confirmed using XPS. Crystallization of the samples was obtained by rapid thermal processing of the samples between 550-650 °C and epitaxial BFO was formed on  $\text{SrTiO}_3$  (001) substrates as confirmed by XRD and TEM. However, the surface roughness substantially increased after the annealing process. Ferroelectric switching was demonstrated using piezoresponse force microscopy and weak ferromagnetic coupling was shown using the SQUID magnetometer, possibly due to the Dzyaloshinskii-Moriya interaction. Thus, the RE-ALD of high quality BFO thin films was achieved and the potential for large scale integration of BFO in microelectronics was demonstrated.

## CHAPTER 5: GROWTH AND CHARACTERIZATION OF COBALT IRON OXIDE USING RADICAL ENHANCED ATOMIC LAYER DEPOSITION

A radical enhanced atomic layer deposition (RE-ALD) process was developed for the synthesis of  $\text{CoFe}_2\text{O}_4$  (CFO) using  $\text{Co}(\text{tmhd})_2$  and  $\text{Fe}(\text{tmhd})_3$  metalorganic precursors using oxygen atoms produced by a coaxial microwave cavity radical beam source as the oxidation source. Stoichiometric CFO films were synthesized at 200 °C and annealed between 450 °C and 750 °C in order to crystallize the films. The structure of the films deposited on  $\text{SrTiO}_3$  (001) substrates were studied using XRD and TEM and it was found that the films were crystallized with a (001) c-axis texture alongside polycrystalline phases which existed beyond an epitaxial interfacial layer. The surface topography was studied using AFM and it was found that the RMS surface roughness increased as the annealing temperature increased from 38 Å as synthesized to 65 Å at 750 °C. The magnetic properties were studied as a function of the film thickness and annealing temperature, and the saturation magnetization ranged from 260 to 550  $\text{emu}/\text{cm}^3$  and the magnetic coercivity ranged from 200 to 2180 Oe depending on the direction of the magnetic field, annealing condition and thickness. The results demonstrated the viability of atomic layer deposition for the integration of CFO with regards to film quality and material properties.

### 5.1 Synthesis of $\text{CoFe}_2\text{O}_4$ by radical enhanced ALD

The synthesis of CFO by RE-ALD was realized by combining the growth of cobalt and iron oxides. Deposition was accomplished by subliming the solid metalorganic precursors for cobalt and iron,  $\text{Co}(\text{tmhd})_2$  and  $\text{Fe}(\text{tmhd})_3$  respectively, and alternatively pulsing them with oxygen atoms separated by a purge step within the RE-ALD reactor that was discussed in 2.1. The initial growth of  $\text{CoO}/\text{Co}_3\text{O}_4$  and  $\text{Fe}_2\text{O}_3$  on Si (001) substrates, using a substrate temperature of 200 °C, was characterized using *ex-situ* XPS as shown in Figure 5.1. As expected, the high-resolution XP spectra for both Co 2p and Fe 2p displayed the spin orbital doublets  $2p_{3/2}$  and  $2p_{1/2}$ . For Co, it was difficult to determine the ratio between  $\text{Co}^{2+}$  and  $\text{Co}^{3+}$  based on the XPS data alone as there was not sufficient energy resolution to deconvolute separate peaks, however the atomic ratio between the Co and O was approximately 43:57, when removing adventitious O species, and therefore it could be surmised that the film comprised mostly of  $\text{Co}_3\text{O}_4$ . For Fe, the peak positions for Fe  $2p_{3/2}$  and  $2p_{1/2}$  were approximately 710.7 eV and 724.0 eV respectively indicating the  $\text{Fe}^{3+}$  oxidation state for  $\text{Fe}_2\text{O}_3$ , which was further corroborated by the presence of the satellite peaks at 718.9 eV and 732.8 eV which were anticipated for the  $\text{Fe}^{3+}$  oxidation state (Mills and Sullivan 1983).

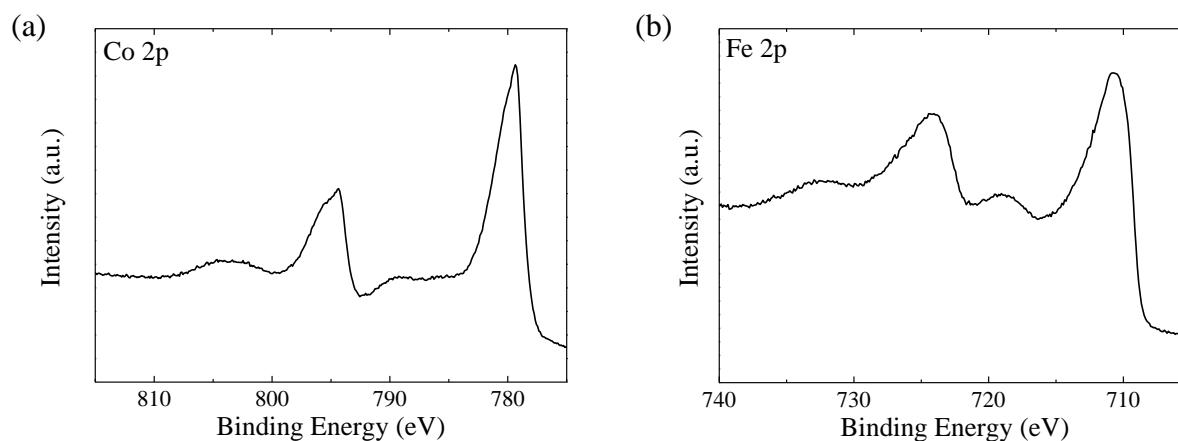


Figure 5.1. Detailed XPS spectra for (a) Co 2p from a cobalt oxide thin film and (b) Fe 2p from an iron oxide thin film

After confirming the initial growth of the films, it was then possible to characterize the growth in order to determine the optimal processing parameters. The growth rate was characterized using a combination of SEM cross-section micrographs and ellipsometry measurements which were fitted using a Lorenz oscillator set to the measured thickness by SEM. The growth rates for  $\text{Co}_3\text{O}_4$  and  $\text{Fe}_2\text{O}_3$  were characterized as a function of the sample temperature between 190-230 °C, shown in Figure 5.2 (a). The films were grown using 100 cycles of the following sequence: 90 seconds metalorganic precursor exposure, 5 seconds pump-down, 20 seconds oxygen atom exposure, and 5 seconds pump-down.

For  $\text{Fe}_2\text{O}_3$ , the growth rate was relatively consistent, increasing slightly from 0.40 to 0.49 Å/cycle within the temperature range. However, it was observed experimentally that as the temperature increased further beyond 250 °C, the precursor decomposed on the surface and engaged in CVD growth. This observation was relatively consistent with the work of Lie, et al. who used  $\text{Fe}(\text{tmhd})_3$  precursor with ozone as the co-reactant and reported a growth window from 160-310 °C after which the precursor decomposed on the surface (Lie, Fjellvåg et al. 2005). The difference in the maximum allowable temperature is possibly due to the difference in oxidation sources, as the oxygen atoms used in this work are more reactive compared to ozone. When comparing the growth rate within the temperature window, the thermal ALD process had a growth rate of 0.124 Å/cycle which is substantially slower than the RE-ALD process in this work. For the composition of  $\text{Fe}_2\text{O}_3$  as a function of the growth temperature, shown in Figure 5.2 (b), the composition ratio between Fe, O, and C did not vary much within the temperature range studied. The Fe content was fairly consistent between ~30-32% while the C content was between ~17-20% with no obvious trend corresponding to the growth rate.

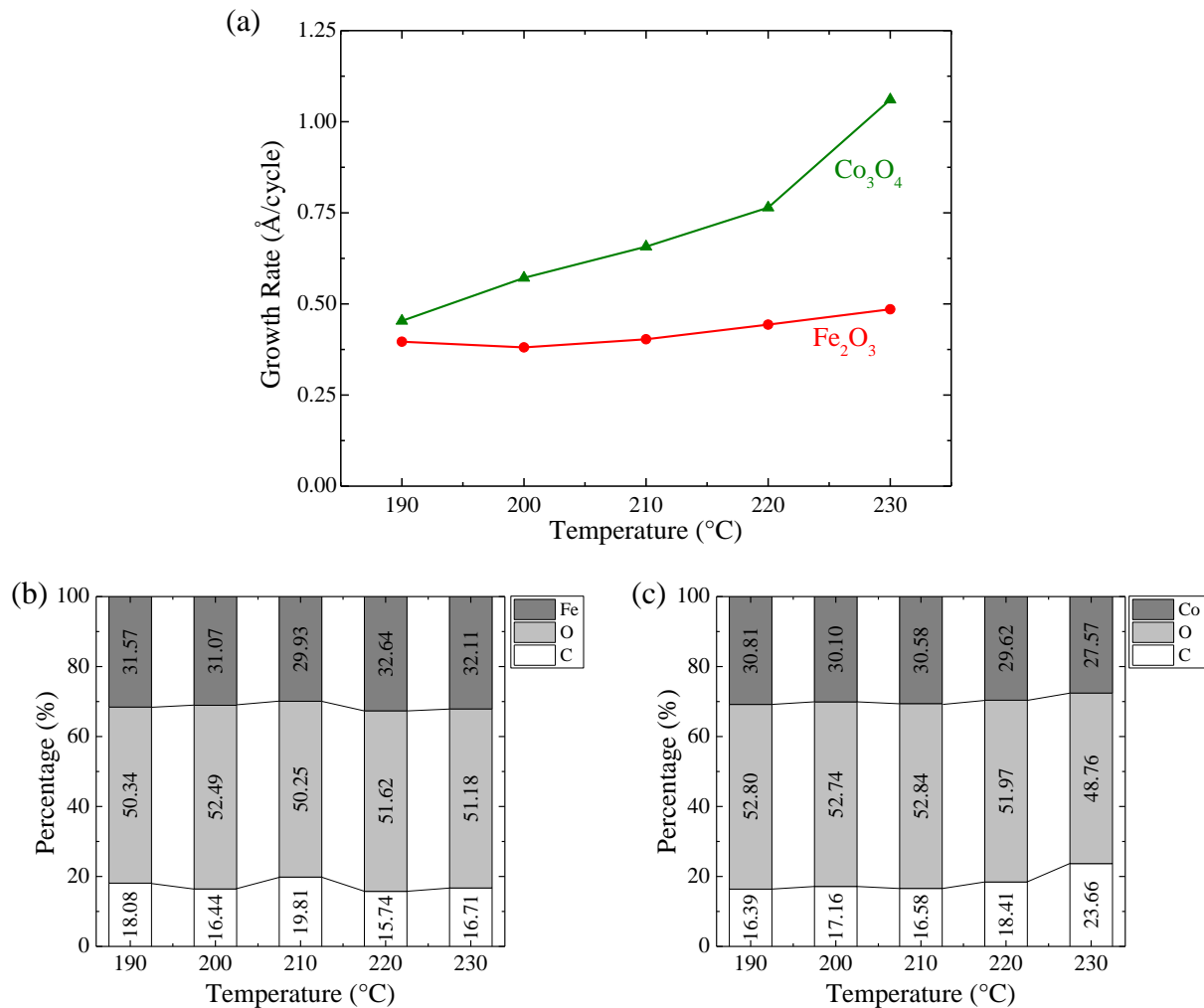


Figure 5.2. (a) Growth rate versus temperature for Fe<sub>2</sub>O<sub>3</sub> and Co<sub>3</sub>O<sub>4</sub> measured by ellipsometry. Thin film composition as a function of growth temperature for (b) iron oxide and (c) cobalt oxide grown by ALD

On the other hand, the Co<sub>3</sub>O<sub>4</sub> growth rate increased from 0.45 to 0.76 Å/cycle between 190 to 220 °C, before suddenly increasing to 1.06 Å/cycle at 230 °C. Although this phenomenon is generally attributed to surface precursor decomposition due to elevated temperature, the analyzed XP spectra, seen in Figure 5.2 (c), showed that the carbon content did not substantially increase until the temperature reached 230 °C. This meant that the gradual growth rate increase from 190-220 °C was possibly caused by a different mechanism such as enhanced ligand removal. In the work of Klepper, et al., using Co(tmhd)<sub>2</sub> and ozone to grow Co<sub>3</sub>O<sub>4</sub> films, the

measured growth rates within a similar temperature range also increased gradually, however their reported growth rate was about 0.2 Å/cycle at 200 °C on Si (001) substrates, which is about 65% lower than the measured growth rate for the radical enhanced process at the same temperature. On the other hand, their reported decomposition temperature for uncontrolled CVD growth was about 310 °C which is much higher than what was measured in this work. Because the growth of Fe<sub>2</sub>O<sub>3</sub> and Co<sub>3</sub>O<sub>4</sub> was relatively stable, the growth was conducted at 200 °C for the remainder of this work.

The effect of precursor pulse time on the growth rate was studied in order to determine the necessary pulse to saturate the precursor upon the substrate surface. This was done using 100 ALD cycles while keeping the pump down times and atomic oxygen pulse time consistent at 5 seconds and 20 seconds respectively. For Co<sub>3</sub>O<sub>4</sub>, the estimated saturation time was approximately 45 seconds, while for Fe<sub>2</sub>O<sub>3</sub>, it is about 60 seconds as shown in Figure 5.3 (a) and (b) respectively. The saturation time was important when coating CFO onto three-dimensional surfaces. However, when compared to the reported literature for these materials, at 1.5 seconds for Co<sub>3</sub>O<sub>4</sub> (Klepper, Nilsen et al. 2007) and 1.0 seconds for Fe<sub>2</sub>O<sub>3</sub> (Lie, Fjellvåg et al. 2005) the saturation time was much greater in this work, which was attributed to the lack of a carrier gas.

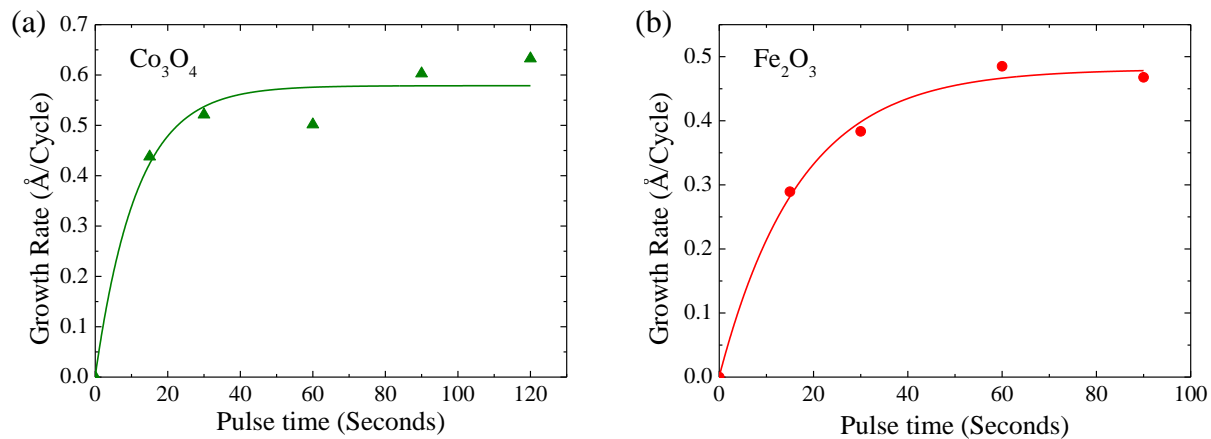


Figure 5.3. Growth rate versus precursor pulse time for (a) Co<sub>3</sub>O<sub>4</sub> and (b) Fe<sub>2</sub>O<sub>3</sub>. Fitted curves provided as guide for the eye.



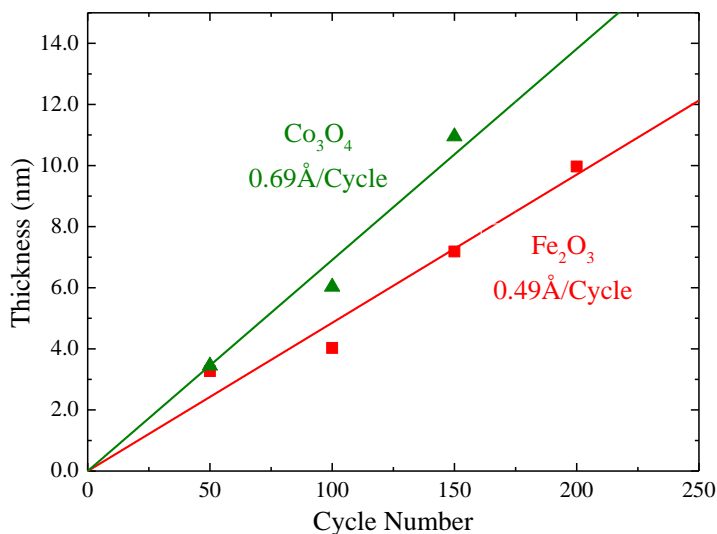


Figure 5.4 Film thickness as a function of ALD cycles for Co<sub>3</sub>O<sub>4</sub> (green circles) and Fe<sub>2</sub>O<sub>3</sub> (red squares).

Subsequently, the pulse time was kept constant at 90 seconds for both Co<sub>3</sub>O<sub>4</sub> and Fe<sub>2</sub>O<sub>3</sub> in order to assure total saturation of the samples. The film thickness as a function of number of ALD cycles was then measured to precisely determine the growth rate at 200 °C as shown in Figure 5.4. For Fe<sub>2</sub>O<sub>3</sub>, the measured growth rate was 0.49 Å/cycle while for Co<sub>3</sub>O<sub>4</sub>, the growth rate was 0.69 Å/cycle. When compared to literature using the same metalorganic precursors and growth temperature but using thermal ALD, the growth rate for Fe<sub>2</sub>O<sub>3</sub> was 0.124 Å/cycle (Lie, Fjellvåg et al. 2005) and was 0.20 Å/cycle for Co<sub>3</sub>O<sub>4</sub> (Klepper, Nilsen et al. 2007) which indicated that the radical enhanced process had a substantially higher growth rate.

Once the growth processes of the binary cobalt and iron oxides were stable and well characterized, the CoFe<sub>2</sub>O<sub>4</sub> (CFO) films could be deposited by using those processes in concert with one another while controlling the precursor pulse sequence to achieve the desired stoichiometry. As seen in Figure 5.5 (a), the co-deposition of Co<sub>3</sub>O<sub>4</sub> and Fe<sub>2</sub>O<sub>3</sub>, resulting in CFO growth, was confirmed using XPS. By adjusting the pulse sequence between cobalt oxide and iron oxide, the composition of the film, as determined by quantitative XPS, could be controlled

such that the desired stoichiometry of  $\text{Co/Fe} = 1/2$  was achieved, shown in Figure 5.5 (b). The detailed XP spectra for Co 2p and Fe 2p is also shown in Figure 5.5 (c) and (d) respectively which, although they could not be deconvoluted into multiple oxidation states, were consistent with the data on the binary oxides.

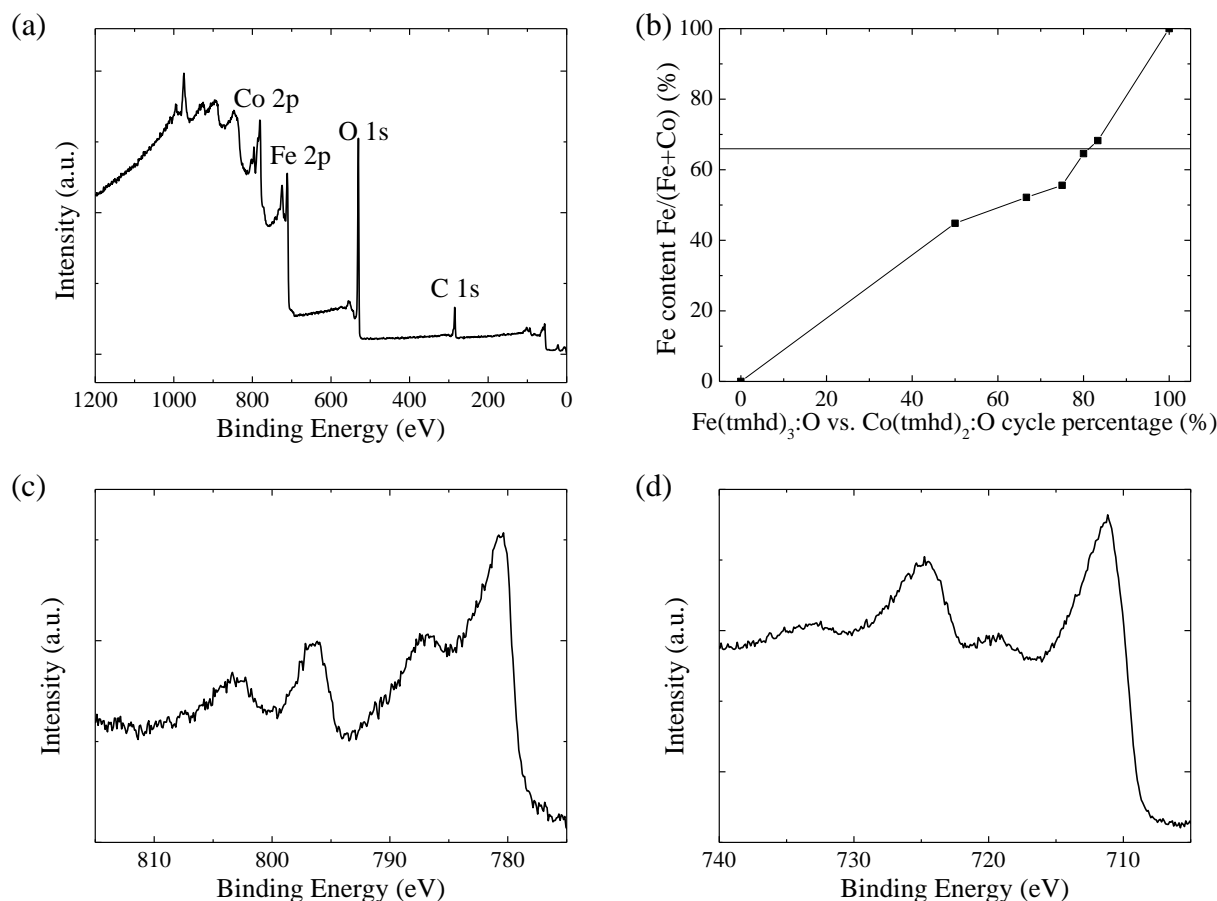


Figure 5.5. (a) XPS survey scan for CFO film (b) Iron content in CFO film as a function of ALD dosing sequence. Horizontal line is a guide for the eye indicating stoichiometric ratio  $\text{Co:Fe} = 1:2$  for  $\text{CoFe}_2\text{O}_4$ . Detailed XP spectra for (c) Co 2p and (d) Fe 2p.

In addition, the thickness as a function of cycles for the CFO films was characterized, first by masking a portion of the substrate during deposition, and by measuring the profiled step height difference between the surface of the film and the substrate using AFM. Using a growth sequence of 1  $\text{Co}_3\text{O}_4$ : 5  $\text{Fe}_2\text{O}_3$  ALD cycles, the growth was relatively linear at  $2.41 \text{ \AA/global}$

cycle, as seen in Figure 5.6, and it corresponded with the measured  $\text{Co}_3\text{O}_4$  and  $\text{Fe}_2\text{O}_3$  growth rates when added together in that ratio.

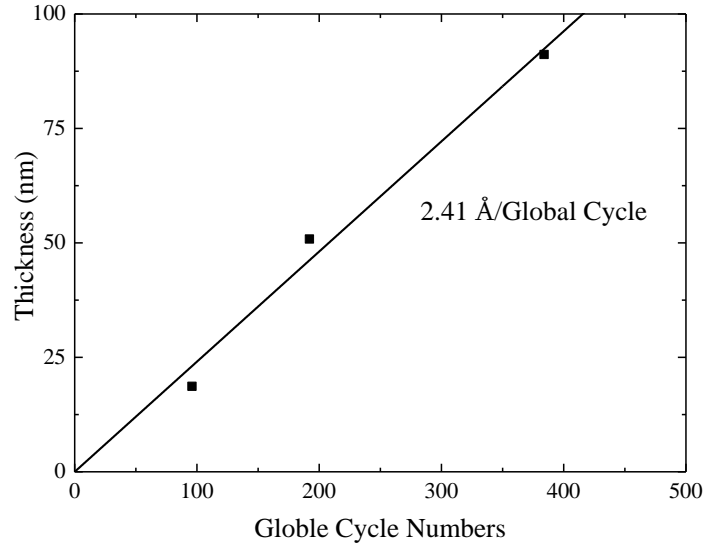


Figure 5.6. Thickness as a function of global ALD cycles using the sequence 1  $\text{Co}_3\text{O}_4$ :5  $\text{Fe}_2\text{O}_3$ .

## 5.2 Structure and morphology for ALD grown $\text{CoFe}_2\text{O}_4$ thin films

In order to crystallize the material, stoichiometric CFO films were deposited onto single crystal  $\text{SrTiO}_3$  substrates and annealed using a rapid thermal process for 1 minute under oxygen gas at various temperatures ranging from 450 to 750 °C. Although  $\text{CoFe}_2\text{O}_4$  (cubic inverse spinel,  $a = 8.396 \text{ Å}$ ) has a large (~7%) lattice mismatch with two unit cells of  $\text{SrTiO}_3$  (simple cubic,  $a = 3.9 \text{ Å}$ ), epitaxial growth of  $\text{CoFe}_2\text{O}_4$  has been demonstrated using STO substrates in the past using both buffered (Suzuki, Hu et al. 1999) and un-buffered substrates (Rigato, Geshev et al. 2009; Aimon, Kim et al. 2015) and the literature reports demonstrated that the growth occurred with a cube on cube c-axis orientation. As shown in Figure 5.7(a), the XRD patterns for 20 nm thick films suggested that they had a c-axis texture because only the CFO (004) reflection was detected (JCPDS card 022-1086), aside from the substrate reflections. As the annealing temperature increased, the peaks became narrower and higher intensity, indicating an increase in

size of the crystal grains from amorphous as synthesized to approximately 40 nm crystallites when annealed at 750 °C, estimated using the Scherrer formula..

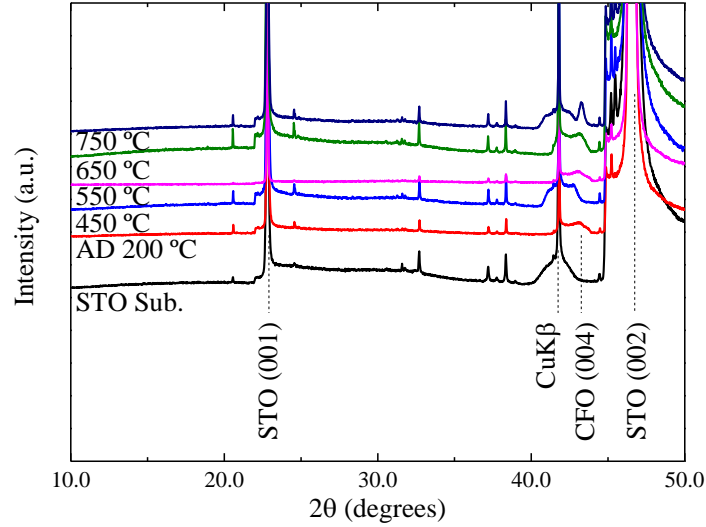


Figure 5.7. (a) X-ray diffraction pattern for CoFe<sub>2</sub>O<sub>4</sub> films grown on SrTiO<sub>3</sub> (001) as prepared and annealed between 450 °C and 750 °C. CoFe<sub>2</sub>O<sub>4</sub> (004) peak is found for annealed films. (b) d-spacing of (004) planes as a function of annealing temperature; horizontal line indicates reference value from bulk samples (JCPDS card 022-1086)

As bulk CFO and STO have a ~7% lattice mismatch, epitaxial growth would normally be characterized by a lattice compression at the interface. Because the XRD data showed that as the annealing temperature increased the d-spacing decreased, it suggested that the CFO film relaxed and released the clamping from the substrate.

For a more detailed view of the local microstructure, high resolution TEM was used to characterize the films. For a film annealed at 650 °C, there was an epitaxial interfacial layer which transitioned into a polycrystalline bulk film as shown in Figure 5.8 (a).

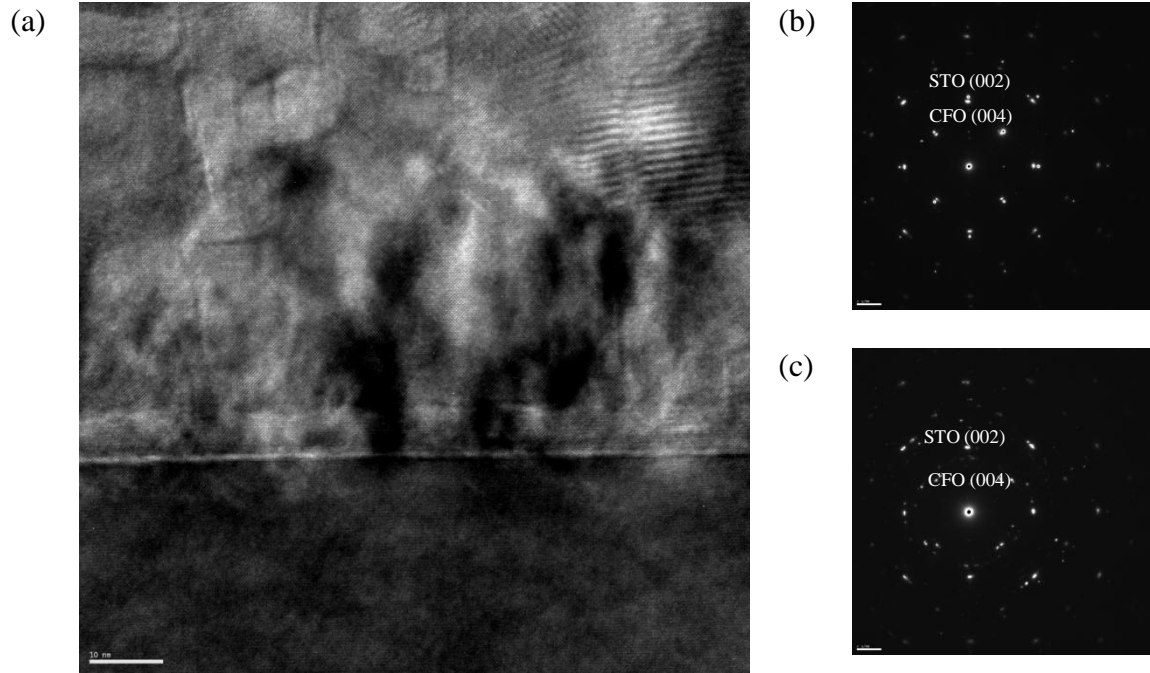


Figure 5.8. (a) High-resolution image of CFO film on STO. SAED pattern (b) near the interface and (c) in the bulk film indicating epitaxial transition to polycrystalline film.

Using selected area electron beam diffraction (SAED), the epitaxial to polycrystalline transition could be verified as shown in Figure 5.8 (b) with the well ordered reciprocal space pattern at the interface including spot splitting in the diffraction pattern of CFO and STO versus (c) the diffraction rings that are indicative of polycrystalline phases. The lattice d-spacing for  $\text{CoFe}_2\text{O}_4$  was calculated using the method shown in 2.3.8 and is shown in Table 5.1.

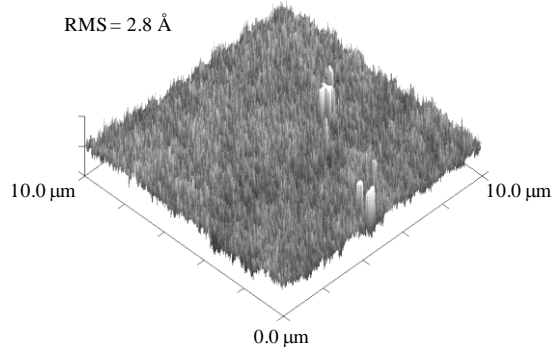
Table 5.1 Calculated R values, calculated d-spacing, and comparison to d-spacing from JCPDS reference for  $\text{SrTiO}_3$  substrate and  $\text{CoFe}_2\text{O}_4$  film.

Material and Index	R (pixels)	d-spacing ( $\text{\AA}$ )	d-spacing ( $\text{\AA}$ ) (JCPDS)
$\text{SrTiO}_3$ (002)	232.015	1.9505	1.9505
$\text{CoFe}_2\text{O}_4$ (004)	216.016	2.095	2.099

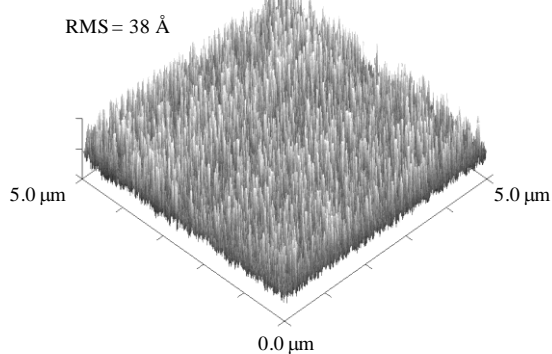
Atomic force microscopy (AFM) was used to study the surface topography for the films before and after annealing at various temperatures. As shown in Figure 5.9 (a) and (b), the

roughness for the as deposited sample was much greater compared to the substrate surface. This is contrary to most results obtained using ALD processes but was within the same order of magnitude as results obtained by Lie, et al. for cobalt iron oxide grown by ALD using the same metalorganic precursors (Lie, Barnholt Klepper et al. 2008).

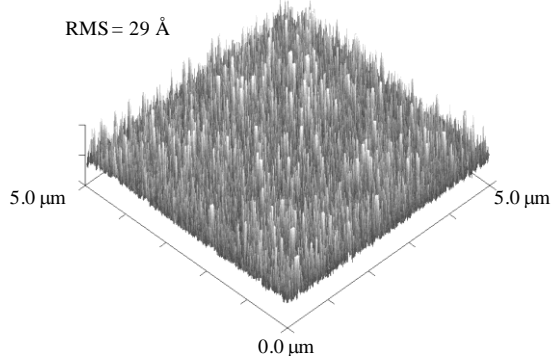
(a) SrTiO<sub>3</sub> (001) Substrate



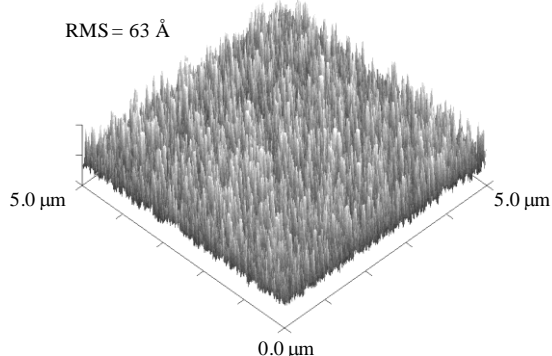
(b) As Deposited 200 °C



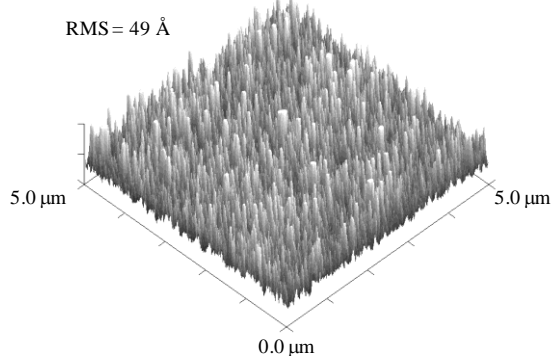
(c) RTA 450 °C



(d) RTA 550 °C



(e) RTA 650 °C



(f) RTA 750 °C

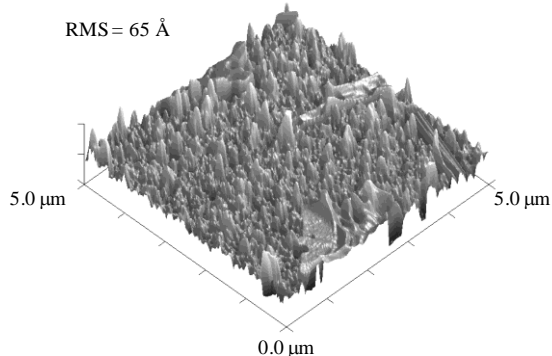


Figure 5.9. Topography of (a) bare SrTiO<sub>3</sub> substrate, CoFe<sub>2</sub>O<sub>4</sub> thin films (b) as-prepared and annealed at (c) 450 °C, (d) 550 °C, (e) 650 °C, and (f) 750 °C.

As expected, when the annealing temperature increased, the roughness also increased dramatically. Finally when the annealing temperature reached 750 °C, visible domain patterns appeared as shown in Figure 5.10

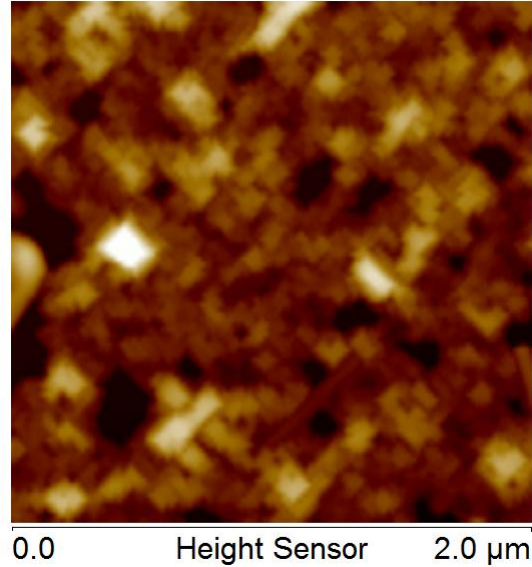


Figure 5.10. AFM image of CFO sample annealed at 750 °C indicating domain patterns.

### 5.3 Magnetic properties of ALD grown $\text{CoFe}_2\text{O}_4$ thin films

To probe the magnetic properties of the CFO thin films grown by ALD, a superconducting quantum interference device (SQUID) magnetometer was used. The effect of the film thickness and annealing condition was studied to determine the correlation between the structure and material properties and to compare it against the reported literature. Four film thicknesses were studied, all of which were annealed at 650 °C for 1 minute under oxygen gas. As shown in Figure 5.11 and summarized in Figure 5.12 it was observed that, as the film thicknesses decreased from 90 to 20 nm, the out-of-plane saturation magnetization ( $M_s$ ) reduced from 465  $\text{emu}/\text{cm}^3$  to 305  $\text{emu}/\text{cm}^3$ , however, the 7 nm thick sample increased to 410  $\text{emu}/\text{cm}^3$ . On the other hand, the in-plane  $M_s$  gradually increased from 355  $\text{emu}/\text{cm}^3$  to 550  $\text{emu}/\text{cm}^3$  as the

film thickness decreased. The out-of-plane magnetic coercivity ( $H_c$ ) decreased from 1.77 kOe to 0.35 kOe as the film thickness decreased while the in-plane  $H_c$  slightly increased from 1.37 kOe to 1.6 kOe.

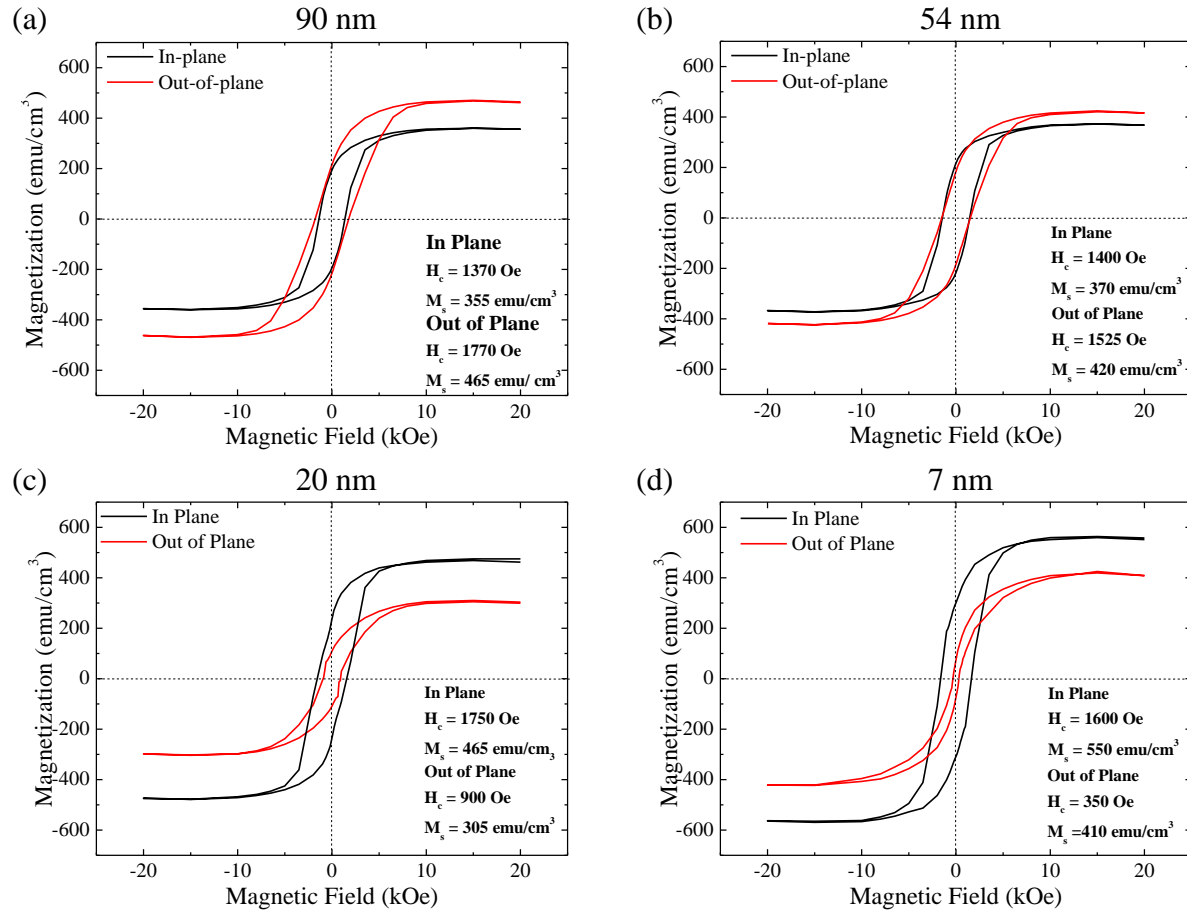


Figure 5.11. Magnetization versus magnetic field for  $\text{CoFe}_2\text{O}_4$  films annealed at  $650^\circ\text{C}$  with thicknesses of (a) 90 nm, (b) 50 nm, (c) 20 nm, and (d) 7 nm.



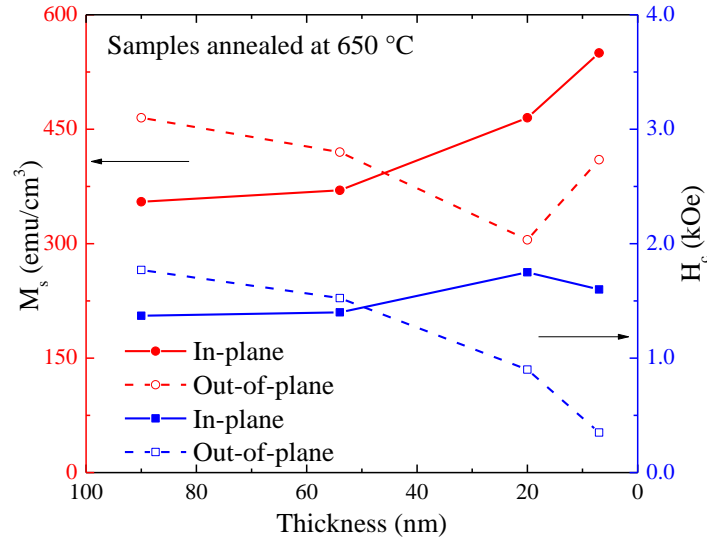


Figure 5.12. Coercivity (blue squares) and saturation magnetization (red circles) vs. film thickness for out-of-plane (dashed line) and in-plane orientation (solid line) of applied magnetic field

The effect of annealing temperature was also studied as shown in Figure 5.13 for a set of 20 nm thick films. In general, as the annealing temperature increased, both the  $M_s$  and the  $H_c$  increased, as summarized in Figure 5.14. For the out-of-plane  $M_s$ , the values for increasing annealing temperatures between 450 °C and 750 °C were 290, 260, 305, and 425 emu/cm<sup>3</sup>, while the in-plane  $M_s$  values were 430, 280, 405, and 550 emu/cm<sup>3</sup>. The out-of-plane  $H_c$  increased with increasing annealing temperatures from 0.2 kOe to 2.18 kOe while the in-plane  $H_c$  values increased between 1.2 kOe at 450 °C and 1.75 at 650 °C before decreasing to 1.1 kOe at 750 °C. It had been shown in literature that due to the large magnetostriction of CFO, induced lattice strain from the underlying substrate would coincide with a change in the properties for epitaxial thin films when compared to bulk (Suzuki, Hu et al. 1999; Rigato, Geshev et al. 2009). Although our ALD films were not fully epitaxial, as indicated by the TEM data, the XRD showed that the films were likely to be textured-polycrystalline and that there could be some possible explanations for the observed magnetic properties obtained by cross-correlating the processing

parameters to the structural data and the magnetic properties. In general, it is expected that magnetic anisotropy has contributions from several factors which are the strain, crystal structure, and shape. It was previously reported in literature that for epitaxial CFO films grown on MgO (100) substrates, increasing the film thickness or the growth temperature causes the magnetic domains to relax and are therefore less affected by the lattice strain (Newville 2004). For our work, we found that the magnetic properties drastically could drastically change as a function of the thickness and annealing temperature.

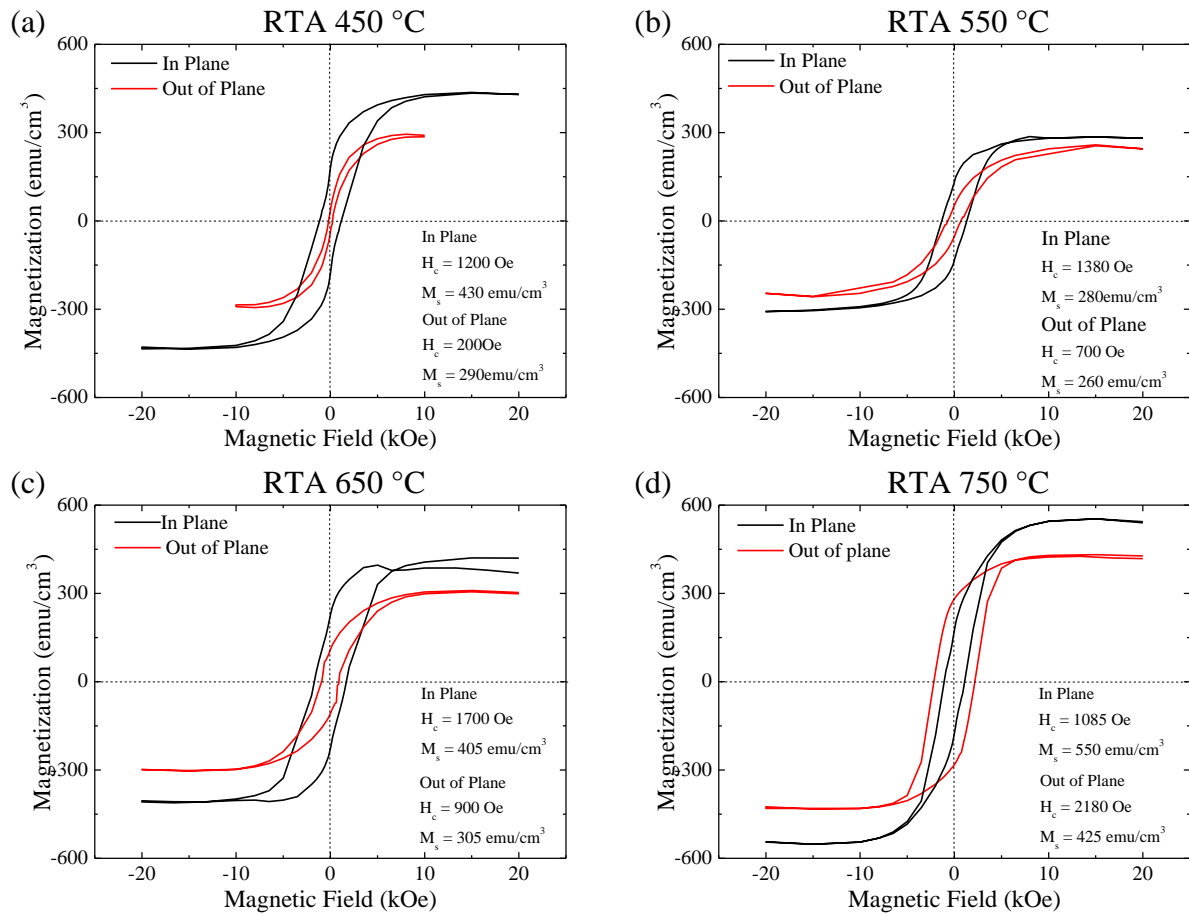


Figure 5.13. Magnetization versus magnetic field for 20 nm thick  $\text{CoFe}_2\text{O}_4$  films annealed at (a) 450 °C, (b) 550 °C, (c) 650 °C, and (d) 750 °C.

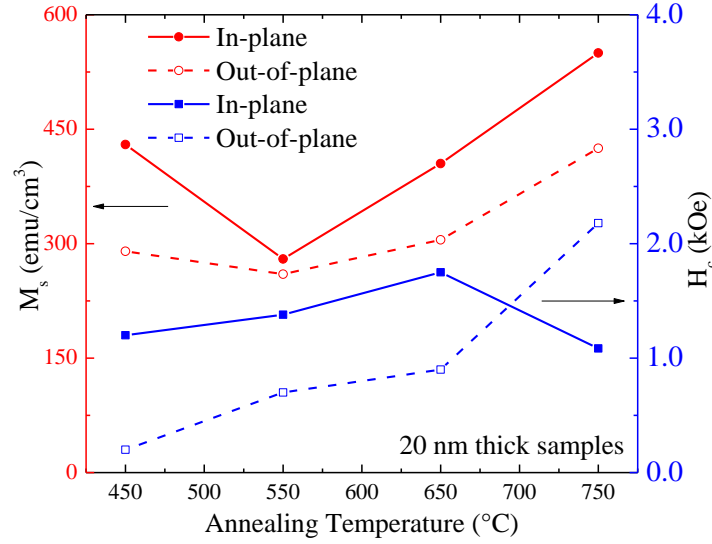


Figure 5.14. Coercivity (blue squares) and saturation magnetization (red circles) vs. annealing temperature for out-of-plane (dashed line) and in-plane orientation (solid line) of applied magnetic field

When compared to the bulk CFO  $M_S$  of about  $\sim 400 \text{ emu/cm}^3$ , the values of the in-plane  $M_S$  for the 7 nm and 20 nm thick samples were enhanced at 550 and  $465 \text{ emu/cm}^3$  respectively. On the other hand, the in-plane  $M_S$  for the 54 and 90 nm thick samples were lower compared to bulk at  $370$  and  $355 \text{ emu/cm}^3$  respectively. This contrast between samples of different thicknesses has been explained by a competition of magnetic property contributions from the substrate lattice-mismatch strain versus the surface microstructure (Rigato, Geshev et al. 2009). The surface morphology in epitaxial CFO films on STO substrates grown by PLD was observed to consist of microscopic pyramidal features that contributed to the surface roughness. When compared to the AFM for the CFO films grown by ALD in this work, there was a similar observation of surface features. It was observed that the thinner films had a drastically smaller  $H_C$  in the out-of-plane direction compared to the in-plane direction whereas the thicker films only had a slightly higher  $H_c$ . This indicated that the magnetic softness was also affected by the film strain states and that the energy required to flip the magnetic spins in the out-of-plane

direction could be reduced for thinner films. By contrast, the thicker films were relatively similar regardless of the direction which was likely due to the lower effect from the substrate strain.

When correlating the magnetic properties with the annealing temperature, the MS and HC generally increased with increasing annealing temperature. Because it was observed that the CFO (004) crystallographic peak increased in intensity and decreased in FWHM, it indicated that the crystal domains increased in size. Because the ALD film is deposited with alternating layers of  $\text{Co}_3\text{O}_4$  and  $\text{Fe}_2\text{O}_3$ , the as-deposited films may consist of discrete phases. As the magnetic properties in CFO arise due to the spin-orbit coupling interaction of the  $\text{Co}^{2+}$  and  $\text{Fe}^{3+}$  ions, it follows that by adding external energy, the crystallites of CFO are formed by mixing the phases. As the diffusion and kinetics are improved by increasing temperature, it results in improved mixing and formation of CFO crystallites. This increase in saturation magnetization as a function of processing temperature was also observed in other reports for growth of CFO thin films (Van and Peterson 1998). The magnetic properties of the ALD grown films are compared against literature values for bulk and thin films in Table 5.2. It was found that ALD grown CFO films had no apparent disadvantage in terms of magnetic performance when compared to more well-established synthetic techniques for high quality thin films of CFO.

Table 5.2. Comparison of properties for  $\text{CoFe}_2\text{O}_4$  synthesized by different methods. ( $H_c$ : magnetic coercivity,  $M_s$ : saturation magnetization,  $t$ : film thickness)

	Bulk	MBE	PLD	Sputter	This work
$H_c$ (kOe)	~0.3	0.5-12	0.5-5.2	~0.5-3.4	~0.2-2.2
$M_s$ (emu/cm <sup>3</sup> )	~400	140	~420-430	~50-523	~290-550
$t$ (nm)	-	~120	~200-500	~100-1000	~7-90
Quality	-	Epitaxial	Epitaxial	Polycrystalline or Epitaxial	Textured Polycrystalline
Reference	-	(Horng, Chern et al. 2004)	(Van and Peterson 1998; Suzuki, Hu et al. 1999; Terzzoli, Duhalde et al. 2004)	(Thomas and Goringe 1979; Rigato, Geshev et al. 2009)	-

## 5.4 Conclusions

In conclusion, stoichiometric  $\text{CoFe}_2\text{O}_4$  thin films were synthesized by RE-ALD which was confirmed using XPS. The crystal structure was determined using XRD and TEM to be c-axis textured consisting of both polycrystalline phases and an epitaxial interfacial transition. The magnetic properties were studied as a function of the annealing temperature and film thickness and the  $M_s$  ranged from 260 to 550 emu/cm<sup>3</sup> and the  $H_c$  ranged from 200 to 2180 Oe. As the thickness increased, the induced lattice strain from the substrate was relaxed which resulted in an increase in the  $M_s$  and  $H_c$ . As the annealing temperature increased, the CFO crystallites became larger, increasing both the  $M_s$  and  $H_c$ . RE-ALD was therefore found to be a viable technique for the synthesis of CFO and it produced magnetic properties which were comparable to those of thin films produced by other techniques such as MBE, PLD, and sputtering.

## CHAPTER 6: SYNTHESIS AND CHARACTERIZATION OF MULTIFERROIC COMPOSITE THIN FILMS ENABLED BY ATOMIC LAYER DEPOSITION

Synthesis of multiferroic composites with nanostructure was enabled by ALD. 2-2 multiferroic composite configurations using  $\text{BiFeO}_3$  and  $\text{CoFe}_2\text{O}_4$  were synthesized purely by ALD. The films were annealed at 550 °C to assess the effect on crystal structure and it was confirmed that BFO continued to grow with a (001) pseudocubic orientation while the CFO was understood to be polycrystalline. 40 nm thick films were synthesized and the magnetic properties were compared as a function of the nanostructure and it was determined that a change in the easy axis of magnetization could be controlled by changing the size and number of repeating BFO/CFO bilayers. 0-3 multiferroic composite configurations using both BFO/CFO and CFO/PZT were synthesized by a hybrid approach first using evaporation induced self-assembly to deposit a porous metal oxide thin film followed by the conformal deposition of the ALD film. It was confirmed by SEM that the ALD coating was conformal and the magnetic properties were studied. The CFO template film with BFO overlayer was found to have comparable magnetic properties to that of the base template, without significant magnetic contributions from the BFO. The PZT template film with CFO overlayer was found to have magnetic coupling which increased as the CFO film thickness increased.

## 6.1 CoFe<sub>2</sub>O<sub>4</sub> and BiFeO<sub>3</sub> 2-2 configuration composite thin films synthesized by RE-ALD

The synthesis of 2-2 configuration thin films consisting of alternating layers of BFO and CFO was accomplished using ALD by depositing the layers in a controlled fashion which was then followed by an anneal step to crystallize the films. To assess the structure of the films, a bilayer film consisting of an 85 nm thick BFO layer and then an 85 nm CFO overlayer was deposited on a STO (001) substrate and annealed at 550 °C for 1 minute under oxygen atmosphere. A lower annealing temperature was chosen to avoid cross-mixing between the ferrite layers. As seen in Figure 6.1, the diffraction pattern after the film was annealed indicated the presence of BFO according to the (001)<sub>pc</sub> reflection but there was only a slight increase in the intensity for the CFO (004) reflection. This was not unexpected as CFO was not intended to have an epitaxial relation with BFO. Nonetheless, the crystal structure of CFO was not critical for the magnetic properties of the film.

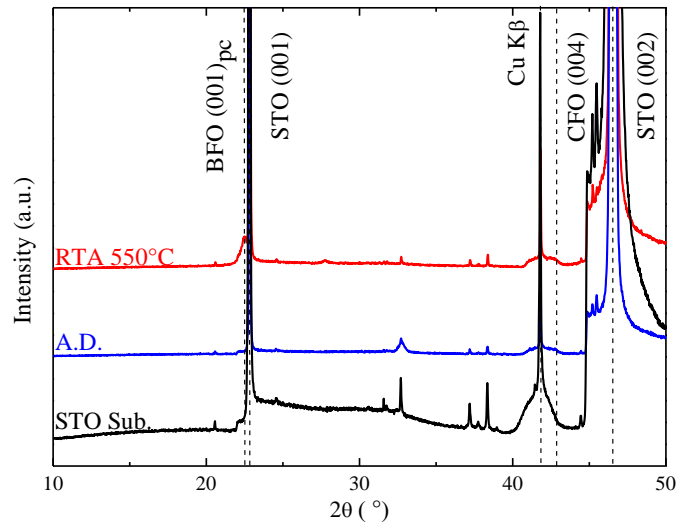


Figure 6.1. Diffraction patterns for 85 nm BFO /85 nm CFO heterostructure grown on SrTiO<sub>3</sub> (001) substrates as prepared and as a function and annealed at 550 °C indicating crystallization.

The magnetic hysteresis of the bilayer film was assessed as shown in Figure 6.2. The magnetic coercivity ( $H_C$ ) was 800 Oe in-plane and 920 Oe out-of-plane while the magnetic saturation ( $M_S$ ) was 280 emu/cm<sup>3</sup> in-plane and 260 emu/cm<sup>3</sup> out-of-plane. Because the magnetization was normalized for the entire film volume, the volumetric magnetization was lower than that of pure CFO films due to the presence of the antiferromagnetic BFO. Nonetheless, the result demonstrated the ability to deposit high quality magnetic oxide film over the BFO underlayer.

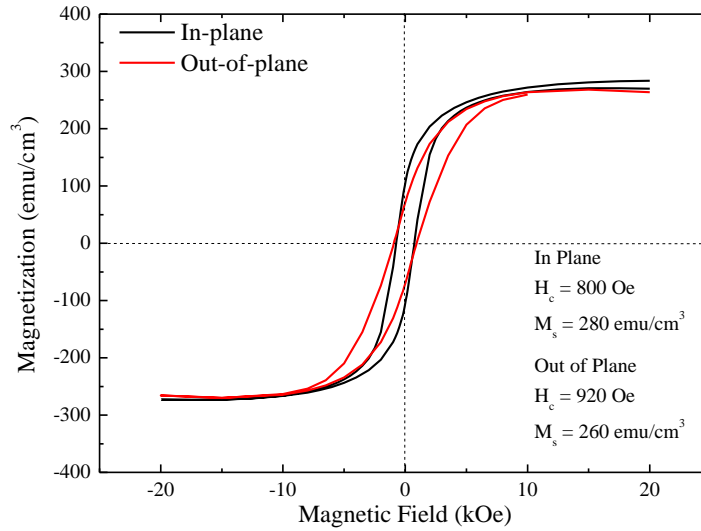


Figure 6.2. M vs. H hysteresis loop for 85 nm BFO/85 nm CFO heterostructure on STO (001) substrate annealed at 550 °C.

To investigate the effect of nanostructuring on the magnetic properties, a set of films was synthesized using a common total thickness of 40 nm and annealing the films at 550 °C, however subdividing the alternating layers into smaller but equal thicknesses. Four structures were assessed one, two, three, and four BFO/CFO bilayers each. The magnetic hysteresis loops were measured and an effect upon the magnetic anisotropy was found shown in . Specifically, for the single bilayer structure, the easy-plane of magnetization was found to exist in-plane relative to the substrate. This is normally expected for thin films due to the shape anisotropy. However



when compared to the single phase CFO films that were 20 nm thick and annealed at 550 °C, the magnetic coercivity was substantially lower. This could possibly have been due to the lack of single crystal underlying layer which would have applied a compressive strain on the CFO film and instead the film more relaxed and/or polycrystalline. This may have resulted in lowering the required switching energy needed to reverse the magnetic polarization. Nonetheless, as the number of bilayers increased, it was observed that the magnetization was isotropic for two and three bilayers. However with four bilayers, it was observed that the easy-plane of magnetization had instead switched to out-of-plane relative to the substrate.

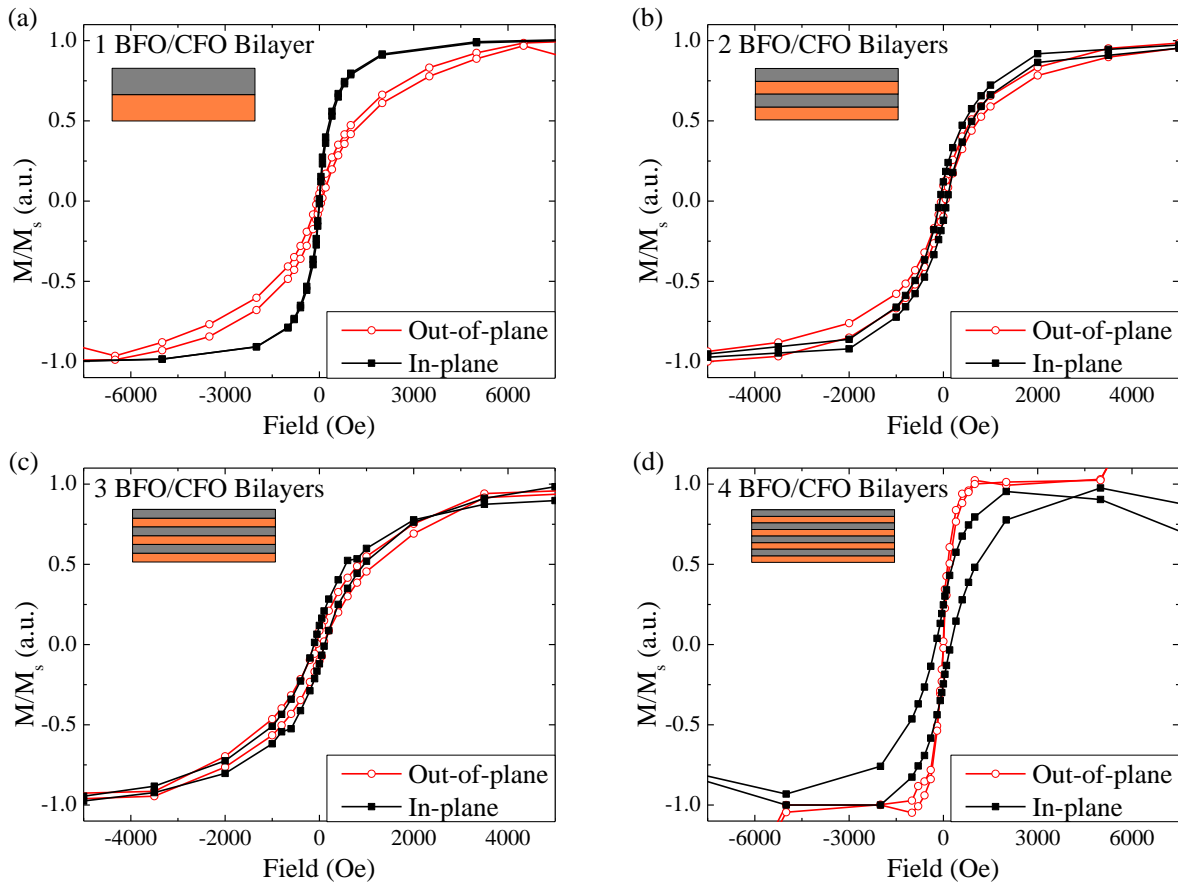


Figure 6.3.  $M$  vs.  $H$  hysteresis loops for 40 nm thick BFO/CFO heterostructures with (a) 1 bilayer, (b) 2 bilayers, (c) 3 bilayers, and (d) 4 bilayers.

It is then proposed that the reason that the magnetic anisotropy switched to out-of-plane was due to the competition between the strain anisotropy against the shape anisotropy. This control of the magnetic anisotropy could be used for the design of future spintronic devices as different configurations will control the performance and characteristics such devices, particularly STT-RAM devices with perpendicular anisotropy have been demonstrated to have lower switching currents (Wang, Alzate et al. 2013).

## 6.2 BiFeO<sub>3</sub> and CoFe<sub>2</sub>O<sub>4</sub> 0-3 configuration composite thin films enabled by RE-ALD

By increasing the surface area of the interfaces between the ferroic phases, thereby increasing the strain-induced magnetoelectric coupling, nanocomposites were synthesized by depositing films onto porous ferroic thin film templates with 10-15 nm diameter pores by leveraging the ability of ALD to deposit conformal thin films over three-dimensional surfaces. The evaporation induced self-assembly of the mesoporous CFO has been discussed elsewhere (Quickel, Le et al. 2010). In this work, ALD BFO was deposited onto mesoporous CFO. To confirm the initial growth of BFO, XPS was used to analyze the surface after a ~7 nm BFO film was deposited and the growth was confirmed as shown in Figure 6.4 indicated by the addition of the Bi 4f peaks as well as the increased intensity of the Fe 2p peaks. Because the BFO film was thin enough, the Co 2p doublet was also present. Because the spectra consisted of both the BFO film as well as the CFO underlayer, it was not possible to calculate the composition of the BFO film due to the contribution to the Fe 2p spectra from both the BFO and the CFO underlayer.

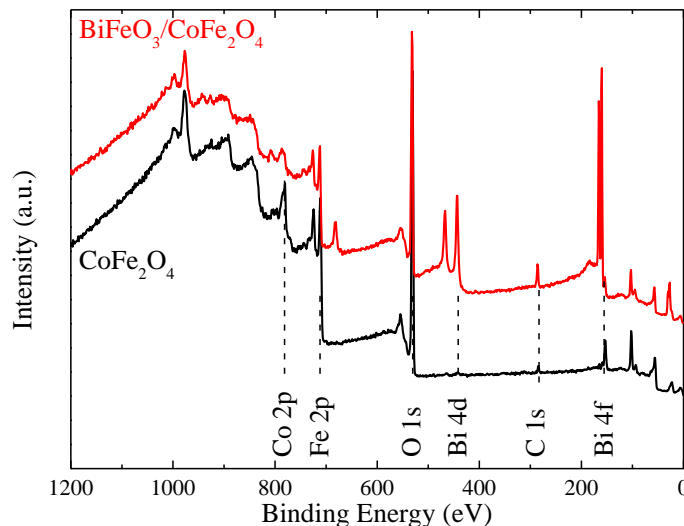


Figure 6.4. XPS survey scan of mesoporous CFO film before and after ALD BFO film was deposited.

To confirm that the nanostructuring was preserved, SEM was used to image the films before and after the ALD BFO deposition. As seen in Figure 6.5, the top down SEM images of the CFO film (a) before and (b) after the ALD BFO was deposited indicate that the nanostructure was indeed maintained due to the conformal nature of the ALD deposition. Future work will confirm whether or not the BFO had fully penetrated the porous film.

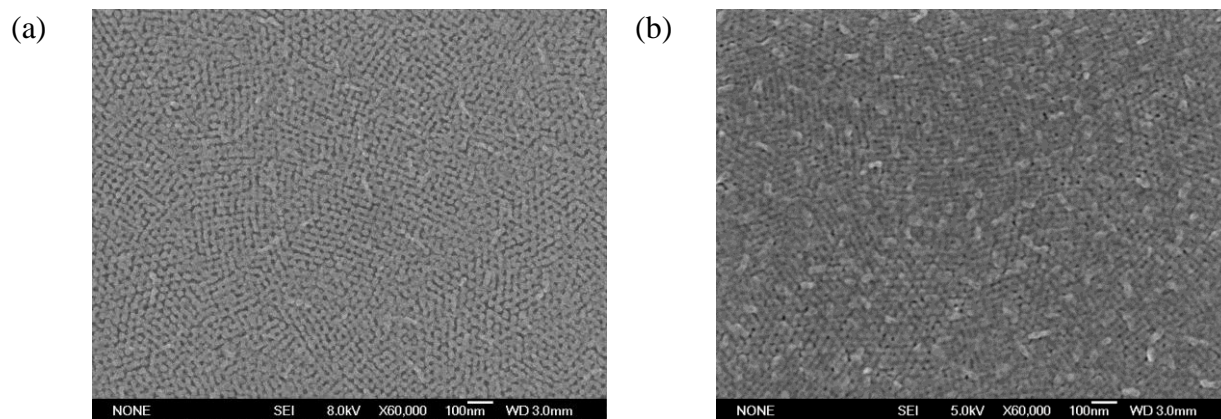


Figure 6.5. (a) Mesoporous CFO film before ALD BFO deposited (b) Film after ALD BFO deposited

Lastly the magnetic hysteresis was investigated as shown in Figure 6.6. The properties were consistent with the previous studies done on the bare mesoporous CFO and the BFO did not

greatly influence amount to the magnetic properties. The saturation magnetization was found to be 151.1 emu/cm<sup>3</sup> out-of-plane and 89.4 emu/cm<sup>3</sup> in-plane while the magnetic coercivity was about 2.0 kOe for both in-plane and out-of-plane orientations.

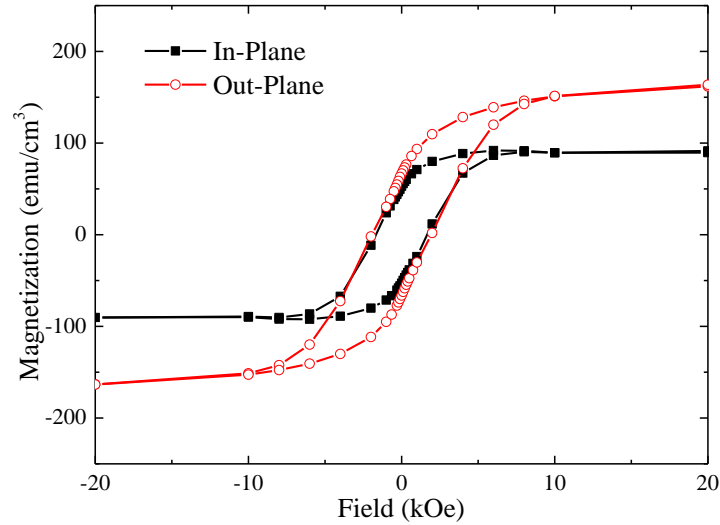


Figure 6.6. Magnetic hysteresis of ~7nm BFO/~100 nm CFO 0-3 configuration composite.

### 6.3 CoFe<sub>2</sub>O<sub>4</sub> and Pb(Zr,Ti)O<sub>3</sub> 0-3 configuration composite thin films by RE-ALD

In addition to CFO/BFO, the deposition of ALD CFO onto porous PZT was also studied. In order to confirm the initial growth, XPS was used as shown in Figure 6.7. The Co 2p and Fe 2p peaks were detected and the compositions were close to stoichiometric. In order to induce crystallization of the CFO, the films were annealed for 1 minute at 650 °C under oxygen atmosphere.

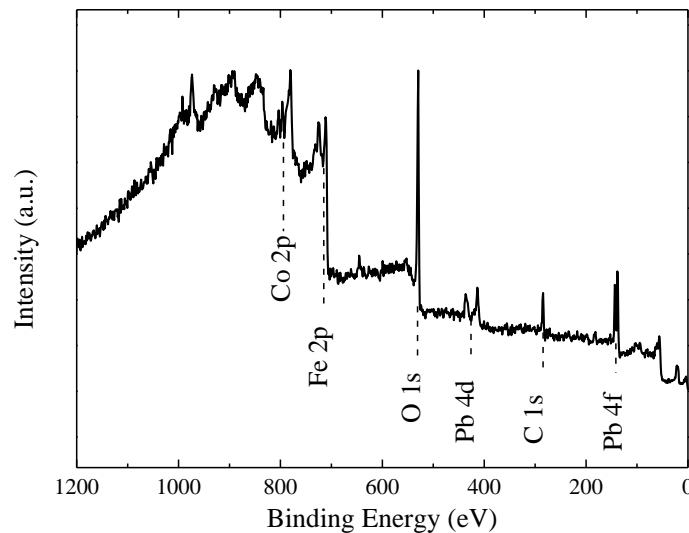


Figure 6.7. XPS survey scan of porous PZT/ALD CFO 0-3 multiferroic composite

The conformality of the CFO films was also studied using SEM as shown in Figure 6.8. By increasing the number of ALD cycles, the nanostructure of the coatings could be controlled as indicated by the decreasing pore sizes. The coating thickness was limited by the size of the necks of the interconnected pores after which the precursors could not penetrate the film any longer.

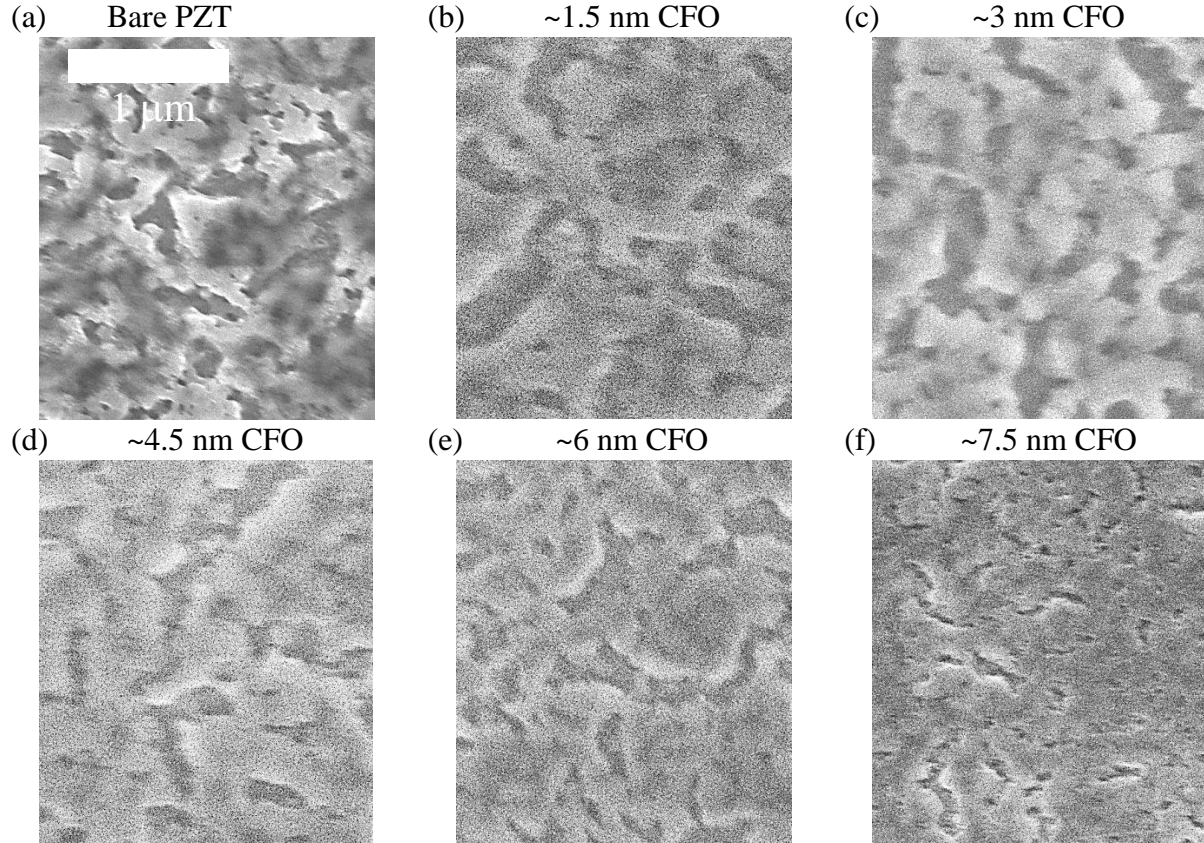


Figure 6.8. Top-down SEM images for (a) bare mesoporous PZT, (b) 1.5, (c) 3, (d) 4.5, (e) 6, and (f) 7.5 nm thick ALD CFO films deposited on mesoporous PZT.

The magnetic hysteresis of the films were also studied as a function of the CFO coating thicknesses as shown in Figure 6.9 (a). Because the pores of the PZT allow for a greater surface area for the coating to deposit onto, it was expected that the magnetization should be greater than that of a planar ALD film using the same number of cycles. Initially, it was found that as the film thickness increased, the magnetization also increased, which was expected due to the higher content of magnetic material. However, once the thickness of CFO exceeded approximately 4.0 nm, the saturation magnetization did not substantially increase significantly as a function of thickness as shown in Figure 6.9 (b). It is suggested that the pore-necks in the PZT matrix were filled, thus preventing the additional incorporation of CFO. The film magnetization was normalized by the total volume of the film, estimating that the PZT was approximately 100 nm

thick although the PZT film thickness was not completely homogenous. It was found that the  $M_s$  and  $H_C$  for the specimen with a 2.4 nm thick CFO film was 3.75 emu/cm<sup>3</sup> and 0.046 kOe, for a 3.6 nm thick film was 37.53 emu/cm<sup>3</sup> and 0.032 kOe, a 6.0 nm thick film was 39.87 emu/cm<sup>3</sup> and 0.25 kOe, and a 9.5 nm thick film was 44.88 emu/cm<sup>3</sup> and 0.87 kOe. In the work of Wan, et al., who synthesized 1  $\mu$ m thick films consisting of 140 nm CFO nanoparticles suspended in a PZT matrix using a sol gel solution synthetic method, the reported saturation magnetization was approximately 28.4 emu/cm<sup>3</sup> and the magnetic coercivity was 0.33 kOe (Wan, Zhang et al. 2006). Therefore, the hybrid ALD with sol-gel solution synthesis yielded a similar performance. It is predicted that if the incorporation of CFO can be improved by engineering the PZT matrix pore diameters, the magnetic response can be further increased. Further work to characterize the ferroelectric and magnetoelectric response is planned for the future.

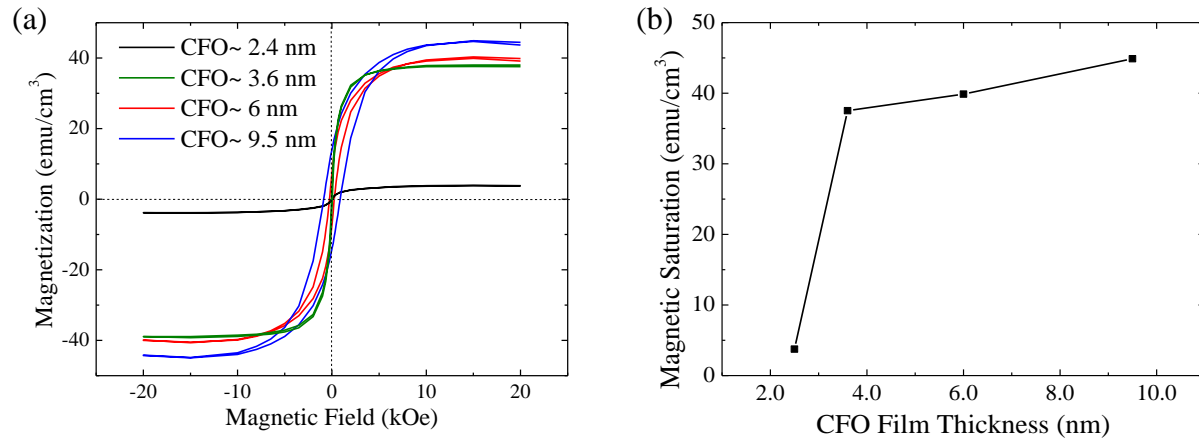


Figure 6.9. (a) Magnetic hysteresis for CFO/PZT 0-3 composite multiferroics with different CFO thicknesses. (b) Saturation magnetization for 0-3 composites with different CFO thicknesses.

## 6.4 Conclusions

Atomic layer deposition enabled the synthesis of nanoscale multiferroic composites. The growth and magnetic properties of BFO/CFO composites with a 2-2 configuration were studied and it was shown that the magnetic anisotropy could be changed from in-plane to out-of-plane by adjusting the nanostructure of the films. Conformal ALD coatings enabled the synthesis of 0-3 composites for both BFO/CFO and CFO/PZT thin films by coating mesoporous thin films that were synthesized using an evaporation induced self assembly technique. The magnetic properties were studied for the 0-3 composites and it was found that the magnetization of CFO/PZT films could be demonstrated for CFO coatings as low as 1.5 nm.



## CHAPTER 7: SUMMARY

The synthesis of multiferroic thin films was demonstrated using radical enhanced ALD. Specifically the processing, structure, and properties were assessed and cross-correlated. It was found that ALD was a viable technique for the synthesis of high-quality multiferroic thin films and that it could enable the integration of these materials into commercial applications.

$\text{YMnO}_3$  (YMO) was synthesized using radical enhanced atomic layer deposition (RE-ALD) on Si (111) and YSZ (111) between 6-80 nm thick. The film composition was controlled by adjusting the precursor pulsing sequence between  $\text{Mn}(\text{tmhd})_3$  and  $\text{Y}(\text{tmhd})_3$  precursors and was confirmed using XPS. The structure of the film was assessed as a function of the substrate choice, annealing conditions, as well as the composition and was shown to have primarily orthorhombic (o-YMO) phase when grown on Si (111), whereas on YSZ (111) had a mixture of hexagonal (h-YMO) and o-YMO, with the fraction of h-YMO increasing as the ratio between Mn/Y approached unity.

$\text{BiFeO}_3$  (BFO) thin films were synthesized using radical enhanced atomic layer deposition (RE-ALD), and the stoichiometry Bi/Fe could be controlled towards unity by adjusting the precursor cycle sequence as confirmed using XPS. Crystallization of the samples was obtained by rapid thermal processing of the samples between 550-650 °C and epitaxial BFO was formed on  $\text{SrTiO}_3$  (001) substrates as confirmed by XRD and TEM. However, the surface roughness substantially increased after the annealing process. Ferroelectric switching was demonstrated using piezoresponse force microscopy and weak ferromagnetic coupling was shown using the SQUID magnetometer, possibly due to the Dzyaloshinskii-Moriya interaction. Thus, the RE-ALD of high quality BFO thin films was achieved and the potential for large scale integration of BFO in microelectronics was demonstrated.

Stoichiometric  $\text{CoFe}_2\text{O}_4$  thin films were synthesized by RE-ALD which was confirmed using XPS. The crystal structure was determined using XRD and TEM to be c-axis textured consisting of both polycrystalline phases and an epitaxial interfacial transition. The magnetic properties were studied as a function of the annealing temperature and film thickness and the  $M_s$  ranged from 260 to 550  $\text{emu}/\text{cm}^3$  and the  $H_c$  ranged from 200 to 2180 Oe.

Atomic layer deposition enabled the synthesis of nanoscale multiferroic composites. The growth and magnetic properties of BFO/CFO composites with a 2-2 configuration were studied and it was shown that the magnetic anisotropy could be changed from in-plane to out-of-plane by adjusting the nanostructure of the films. Conformal ALD coatings enabled the synthesis of 0-3 composites for both BFO/CFO and CFO/PZT thin films by coating mesoporous thin films that were synthesized using an evaporation induced self assembly technique. The magnetic properties were studied for the 0-3 composites and it was found that the magnetization of CFO/PZT films could be demonstrated for CFO coatings as low as 1.5 nm.

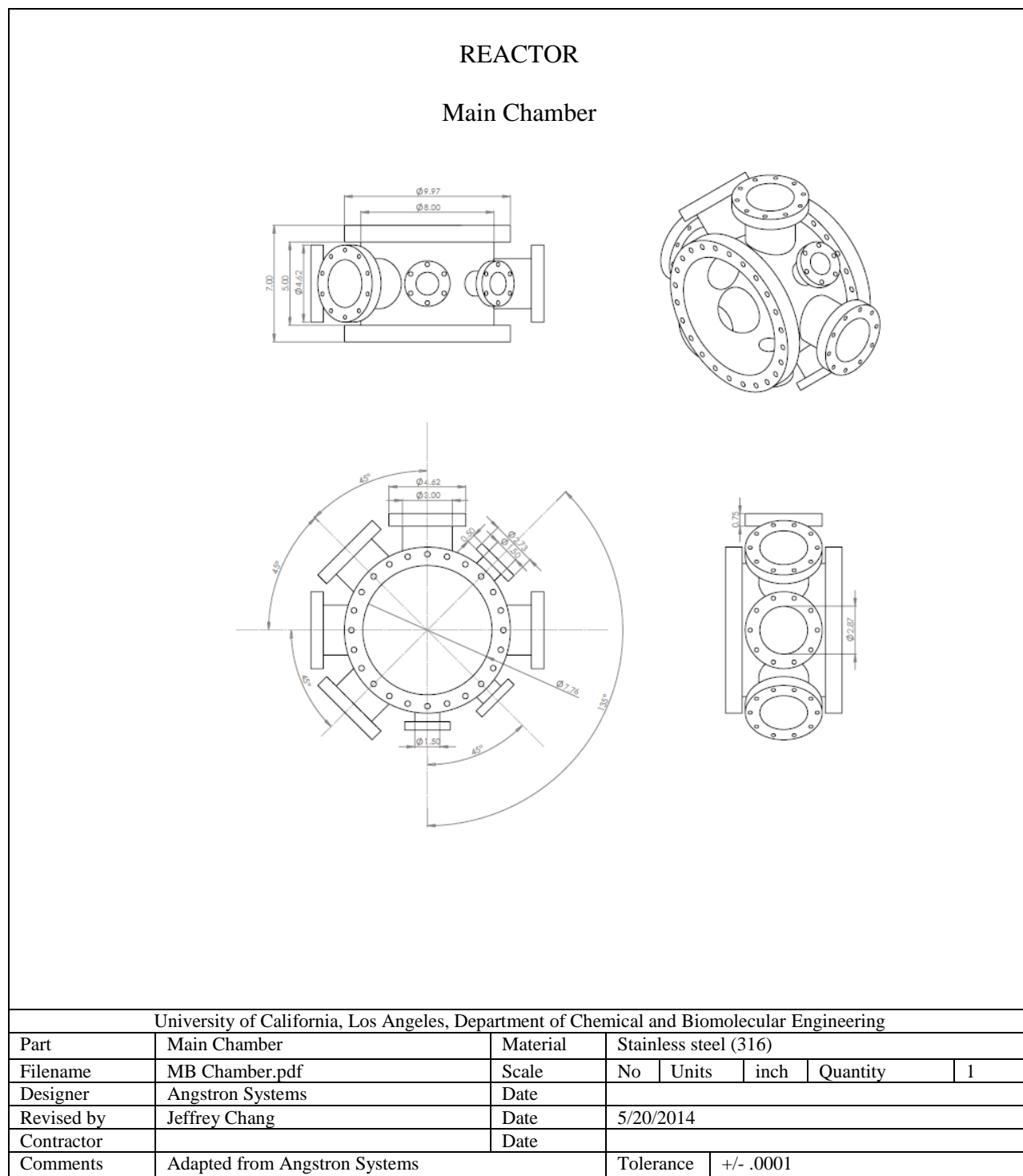
Future directions for this work would emphasize the synthesis and characterization of composite multiferroics. Most significantly, studying the effect of the nanostructure upon the magnetoelectric coupling coefficient, controlled using ALD, would provide the most impact to this field. Initially the measurement procedure for the coupling is a challenge that needs to be solved, but has been demonstrated in literature indicating that it should not be an insurmountable task. Specifically, using the SQUID magnetometer with an *in-situ* electric field can be accomplished using electrical feed-throughs applying a voltage across a sample. Since the framework for the synthesis of single phase ferroics has been demonstrated in this work, the progression towards different composite configurations can be realized. Particularly, conformal deposition of multiple phases upon three-dimensional surfaces could provide a route to unique

structures and, as a consequence, new or interesting material properties. In addition, the study of the exchange coupling effect for nanostructured systems consisting of an antiferromagnet and a ferromagnet is another potential route that could yield interesting results. Particularly, the coupling of antiferromagnetic and ferroelectric  $\text{BiFeO}_3$  with a ferromagnetic material such as  $\text{CoFe}_2\text{O}_4$  may allow electric-field control of the exchange bias, which would be a control parameter used for magnetoelectric memory.

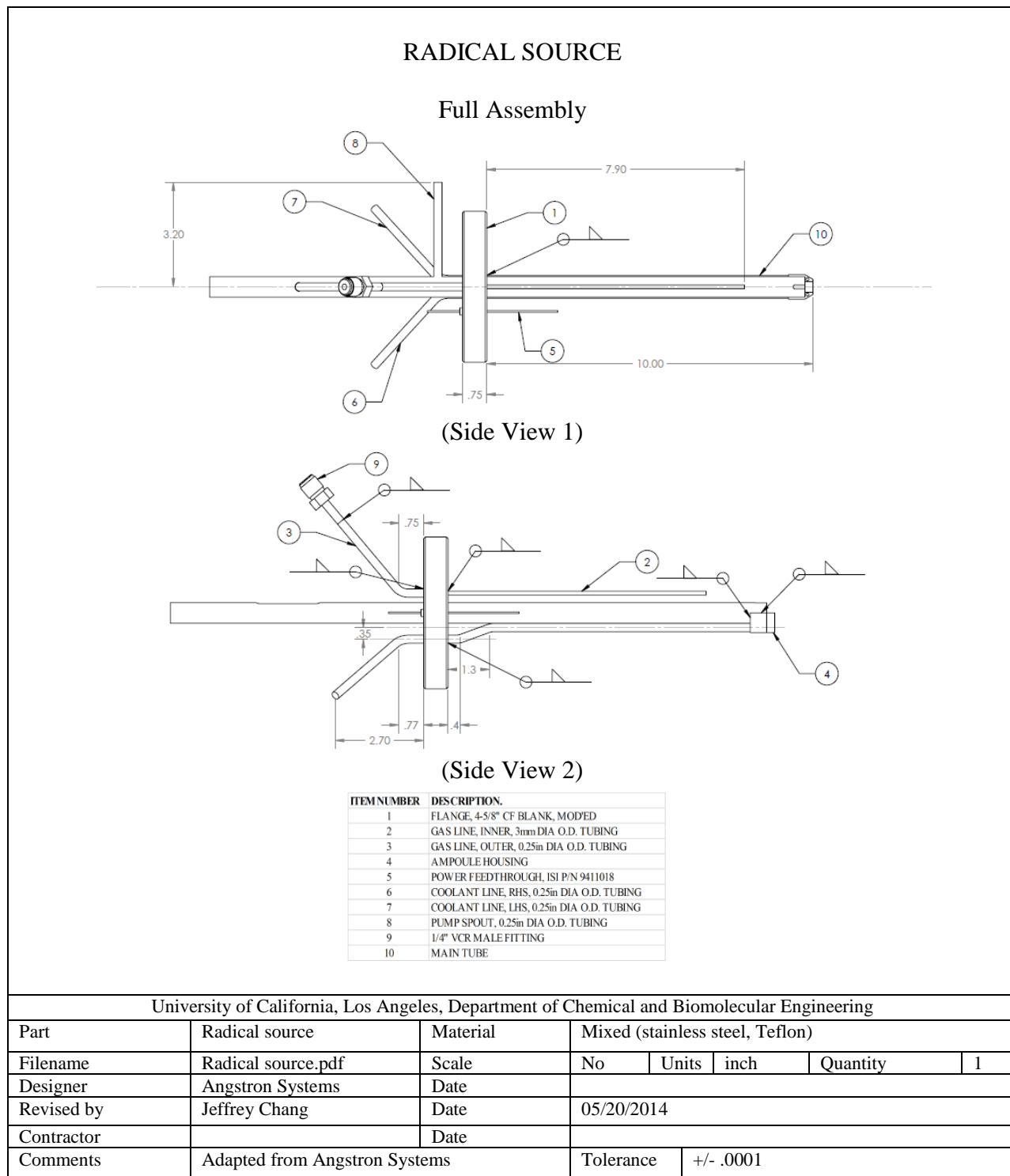
## APPENDICES

### APPENDIX A. SCHEMATICS OF THE HIGH VACUUM MULTI-BEAM CHAMBER

#### A.1. Main Chamber

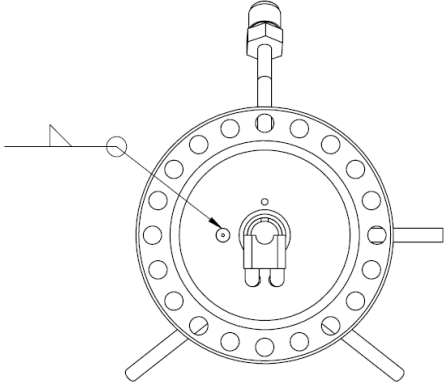


## A.2. Radical Source

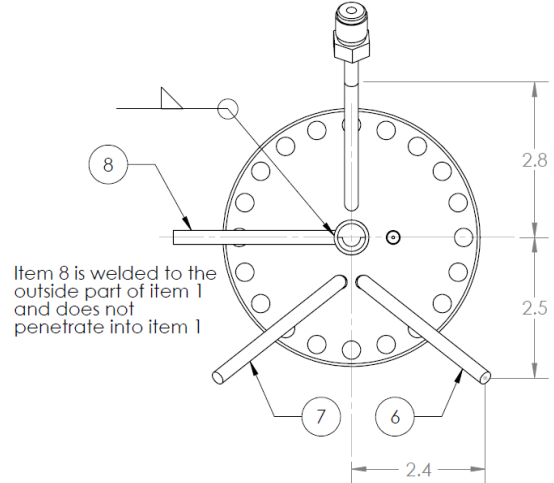


## RADICAL SOURCE (Continued)

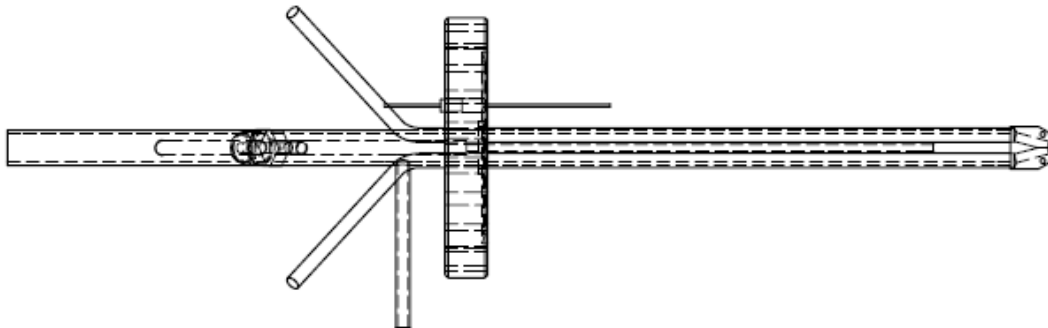
## Full Assembly



View from vacuum side



View from ambient side

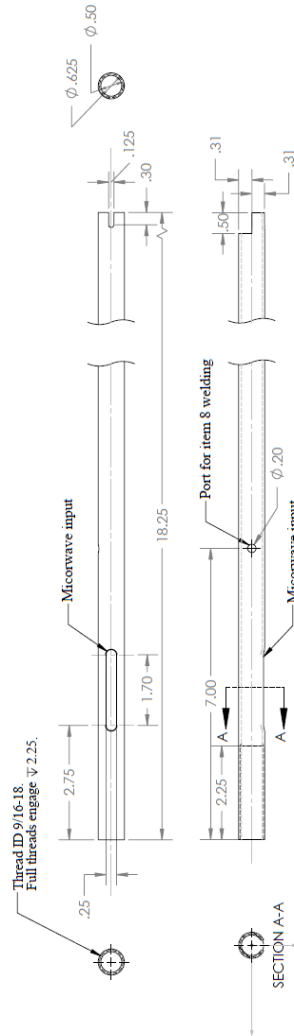


Full view

University of California, Los Angeles, Department of Chemical and Biomolecular Engineering							
Part	Radical source	Material	Aluminum Alloy (6082)				
Filename		Scale	No	Units	inch	Quantity	1
Designer	Angstrom Systems	Date					
Revised by		Date					
Contractor		Date					
Comments	Adapted from Angstrom Systems		Tolerance	+/- .0001			

## RADICAL SOURCE (Continued)

### Coaxial Waveguide

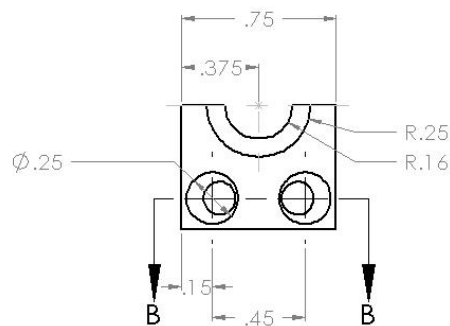
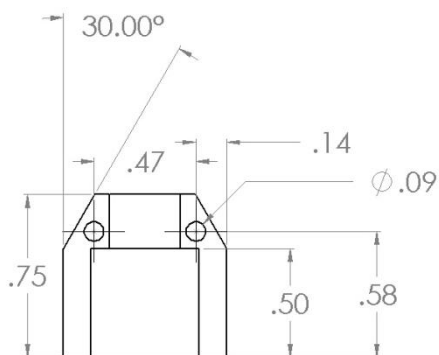
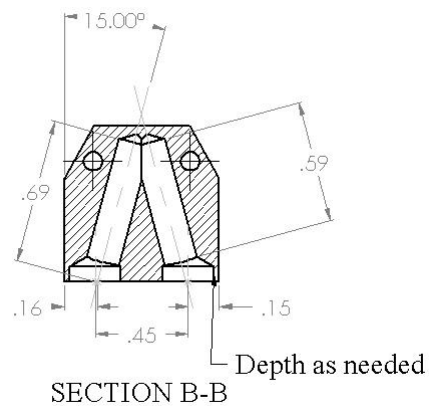
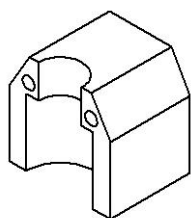


University of California, Los Angeles, Department of Chemical and Biomolecular Engineering

Part	Radical source	Material	Stainless steel, OD 0.625, Wall 0.0625				
Filename	Radical source.pdf	Scale	No	Units	inch	Quantity	1
Designer	Angstrom Systems	Date					
Revised by	Jeffrey Chang	Date	5/21/2014				
Contractor		Date					
Comments	Adapted from Angstrom Systems		Tolerance	+/- .0001			

# RADICAL SOURCE (Continued)

## Top Clamp for Quartz Ampoule



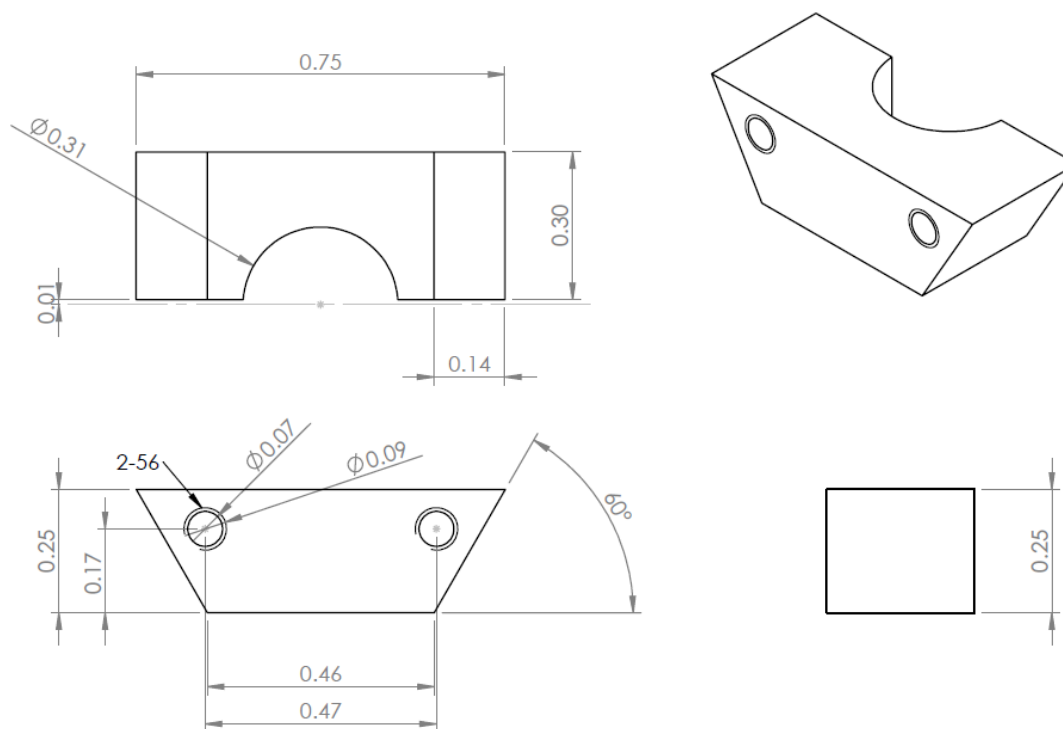
University of California, Los Angeles, Department of Chemical and Biomolecular Engineering

Part	Radical source	Material	Stainless steel (316)				
Filename		Scale	No	Units	inch	Quantity	1
Designer	Angstrom Systems	Date					
Revised by	Jeffrey Chang	Date	5/21/2014				
Contractor		Date					
Comments	Adapted from Angstrom Systems		Tolerance	+/- .0001			



## RADICAL SOURCE (Continued)

### Bottom Clamp for Quartz Ampoule

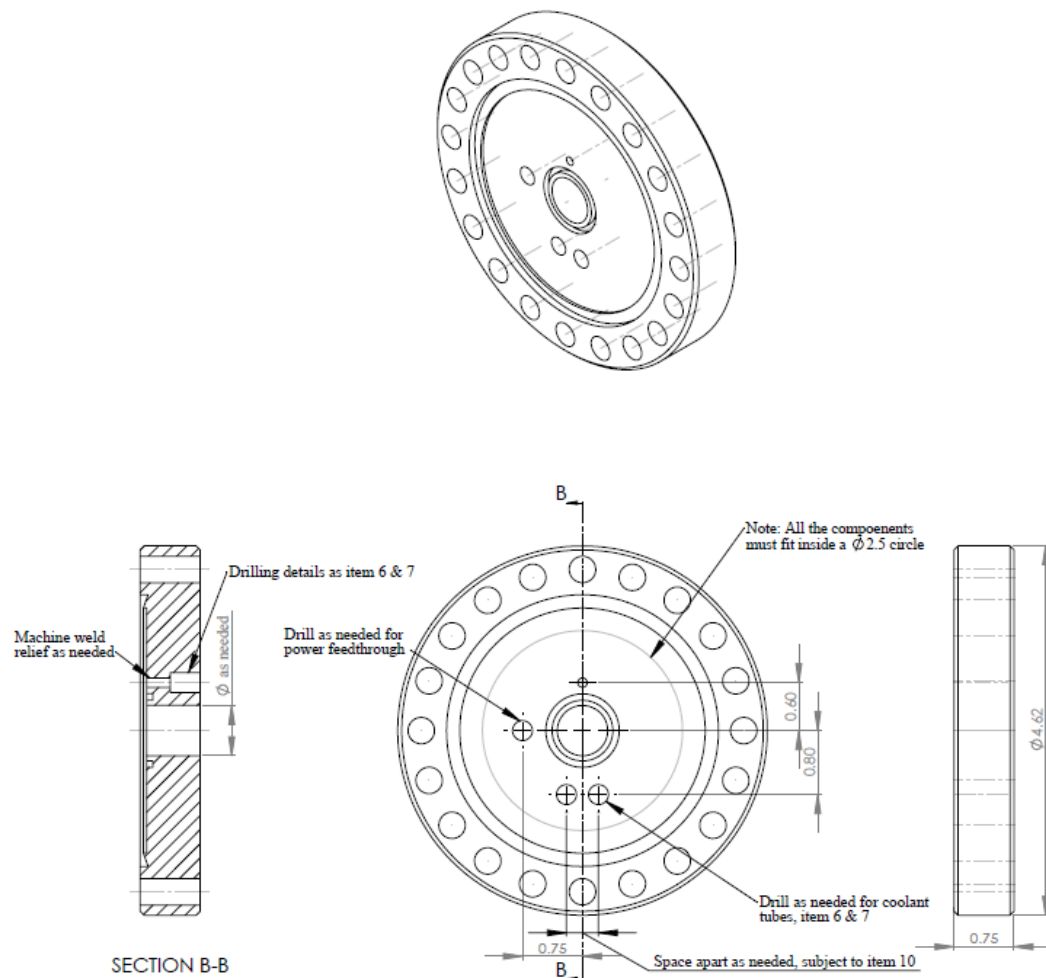


University of California, Los Angeles, Department of Chemical and Biomolecular Engineering

Part	Radical source	Material	Stainless steel (516)				
Filename	quartz bottom	Scale	No	Units	inc	Quantity	1
Designer	Angstrom Systems	Date					
Revised by	Jeffrey Chang	Date	05/21/2014				
Contractor		Date					
Comments	Adapted from Angstrom Systems		Tolerance	+/- .0001			

## RADICAL SOURCE (Continued)

### Modified 4-5/8" Conflat Flange

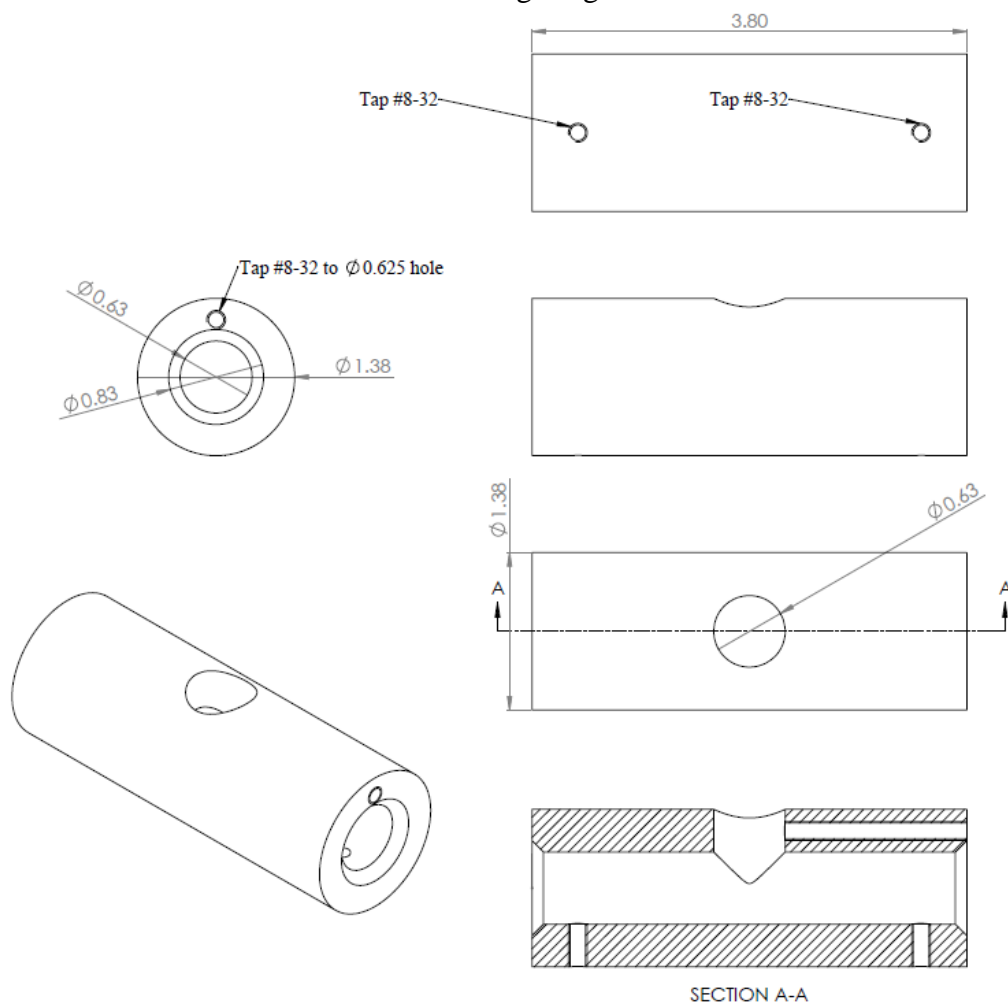


University of California, Los Angeles, Department of Chemical and Biomolecular Engineering

Part	Radical source	Material	4-5/8" Conflat flange (stainless steel)				
Filename		Scale	No	Units	inch	Quantity	1
Designer	Angstrom Systems	Date					
Revised by		Date					
Contractor		Date					
Comments	Adapted from Angstrom Systems		Tolerance	+/- .0001			

## RADICAL SOURCE (Continued)

### Tuning Slug

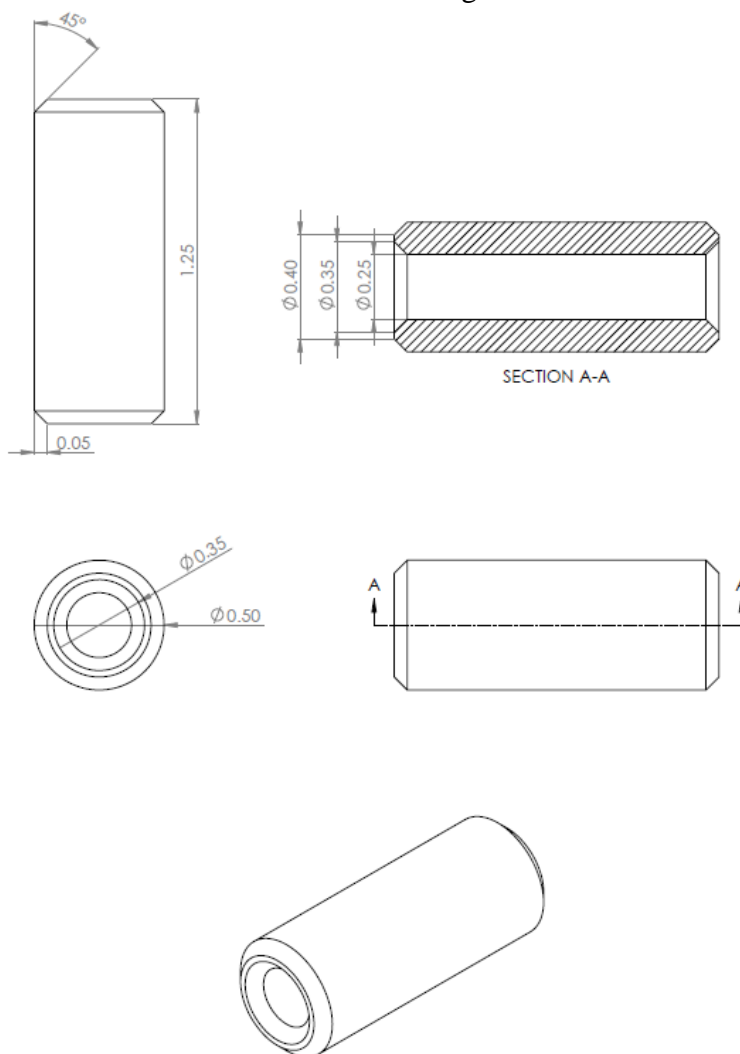


University of California, Los Angeles, Department of Chemical and Biomolecular Engineering

Part	Radical source	Material	Stainless steel (516)				
Filename	TuningSlug.pdf	Scale	No	Units	inch	Quantity	1
Designer	Angstrom Systems	Date					
Revised by	Jeffrey Chang	Date	5/22/2014				
Contractor		Date					
Comments	Adapted from Angstrom Systems		Tolerance	+/- .0001			

## RADICAL SOURCE (Continued)

### Teflon Bushing

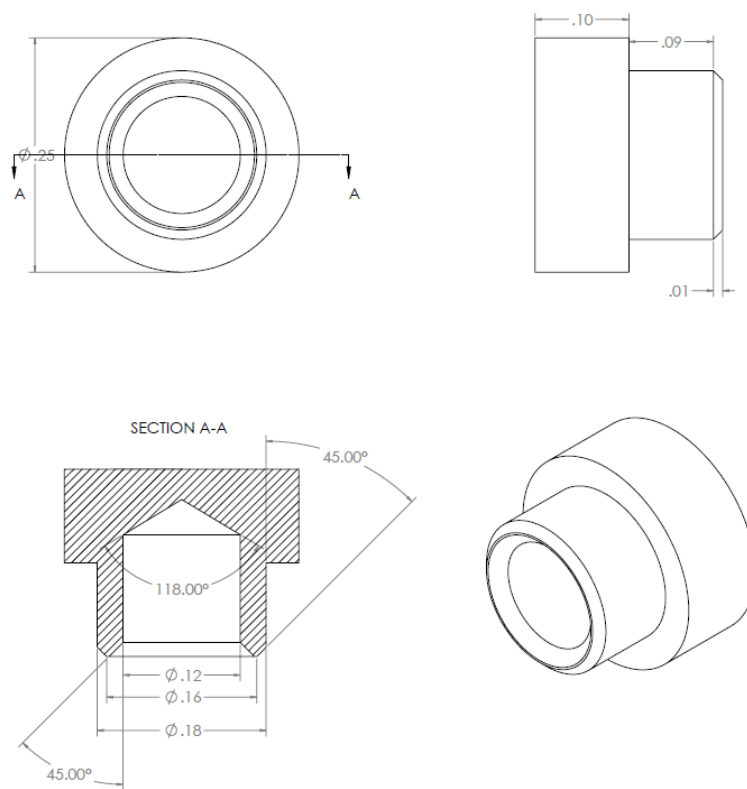


University of California, Los Angeles, Department of Chemical and Biomolecular Engineering

Part	Radical source	Material	Teflon				
Filename	Teflon.pdf	Scale	No	Units	inch	Quantity	1
Designer	Angstrom Systems	Date					
Revised by	Jeffrey Chang	Date	05/22/2014				
Contractor		Date					
Comments	Adapted from Angstrom Systems		Tolerance	+/- .0001			

## RADICAL SOURCE (Continued)

### Central Conductor

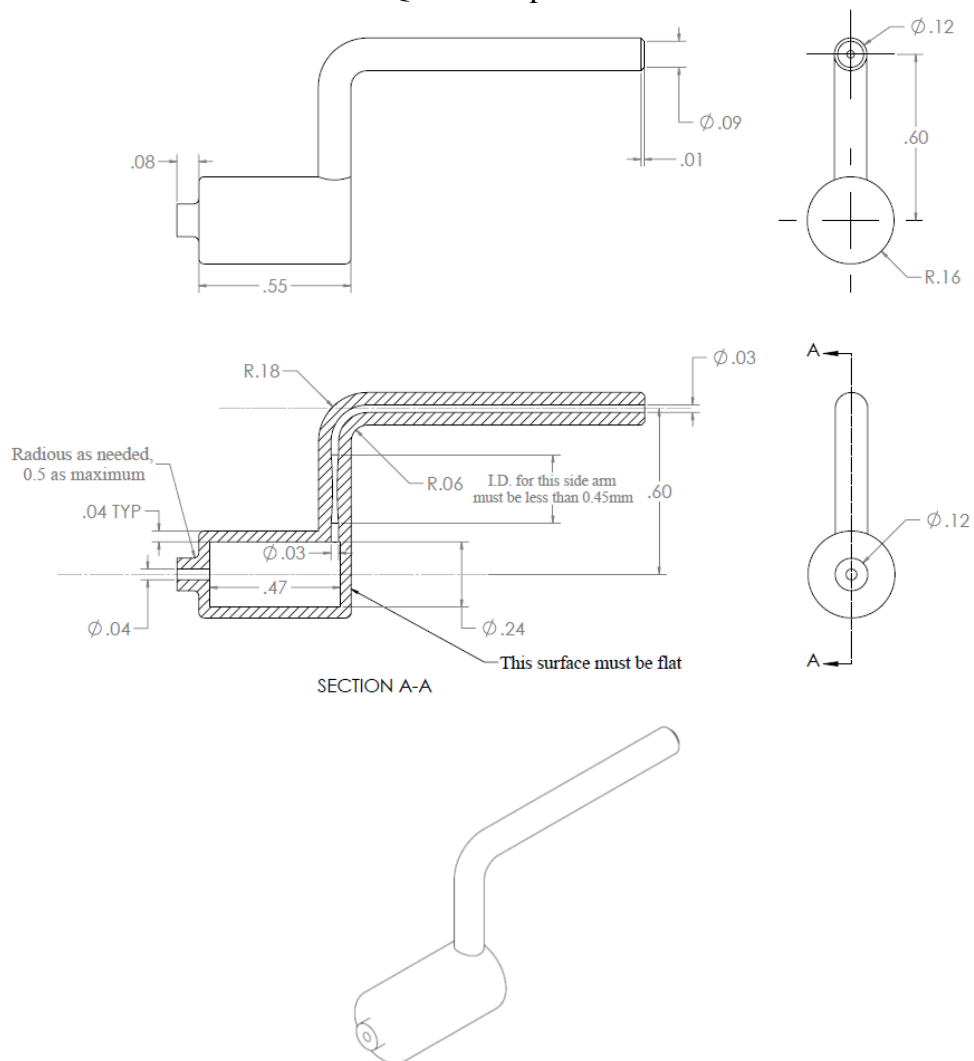


(Tip and Tube)

University of California, Los Angeles, Department of Chemical and Biomolecular Engineering							
Part	Radical source	Material	Stainless steel				
Filename	Central conductor.pdf	Scale	No	Units	inch	Quantity	1
Designer	Angstrom Systems	Date					
Revised by	Jeffrey Chang	Date	05/22/2014				
Contractor		Date					
Comments	Adapted from Angstrom Systems		Tolerance	+/- .0001			

## RADICAL SOURCE (Continued)

### Quartz Ampoule



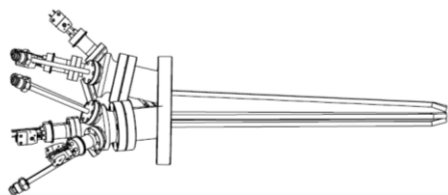
University of California, Los Angeles, Department of Chemical and Biomolecular Engineering

Part	Radical source	Material	Quartz				
Filename	Quartz Ampoule	Scale	No	Units	inch	Quantity	1
Designer	Angstrom Systems	Date					
Revised by	Jeffrey Chang	Date	05/22/2014				
Contractor		Date					
Comments	Adapted from Angstrom Systems		Tolerance	+/- .0001			

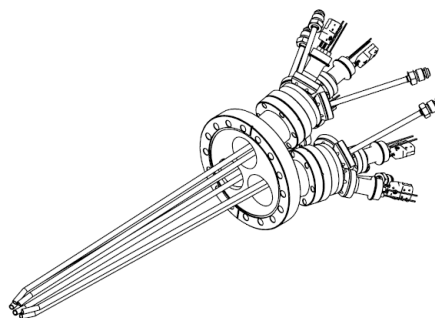
### A.3. Six-Array Precursor Doser

#### SIX-ARRAY DOSER

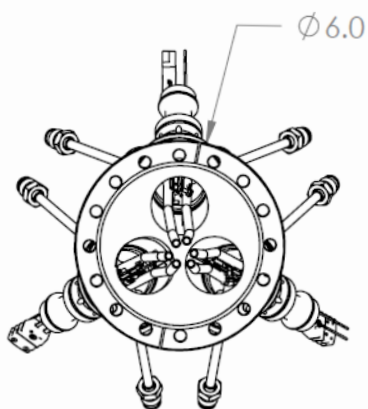
##### Full Assembly



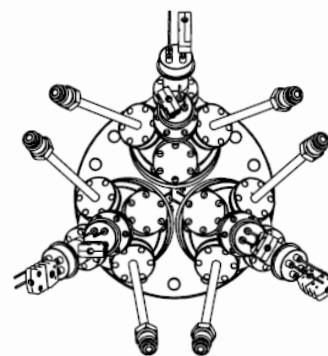
Side View



Trimetric View



Front View (from vacuum)



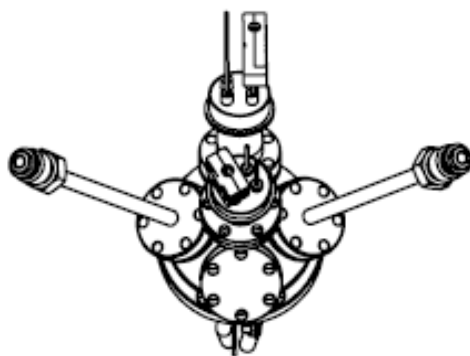
Back View (from ambient)

University of California, Los Angeles, Department of Chemical and Biomolecular Engineering

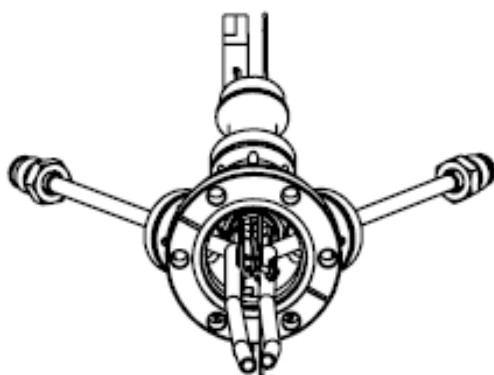
Part	Six Array Doser	Material	Stainless steel				
Filename		Scale	No	Units		Quantity	1
Designer	John Hoang	Date					
Revised by		Date					
Contractor		Date					
Comments	Three 2-array dosers on 3-way multi-flange		Tolerance	+/- .0001			

## SIX-ARRAY DOSER (Continued)

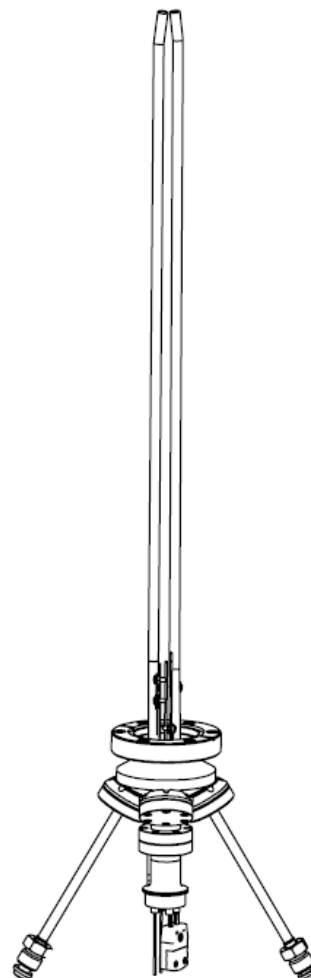
### Two-Array Precursor Doser Assembly



Back view (From ambient)



Front view (From vacuum)



Side view

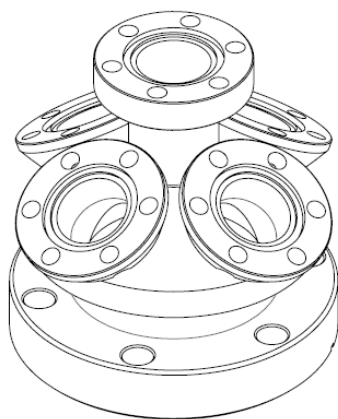
University of California, Los Angeles, Department of Chemical and Biomolecular Engineering

Part	2 Array Doser	Material	Stainless steel				
Filename	2_array_doser.pdf	Scale	No	Units		Quantity	3
Designer	John Hoang	Date					
Revised by	Jeffrey Chang	Date	05/28/2014				
Contractor		Date					
Comments	5-way multiport connects to 2-3/4" Conflat		Tolerance	+/- .0001			

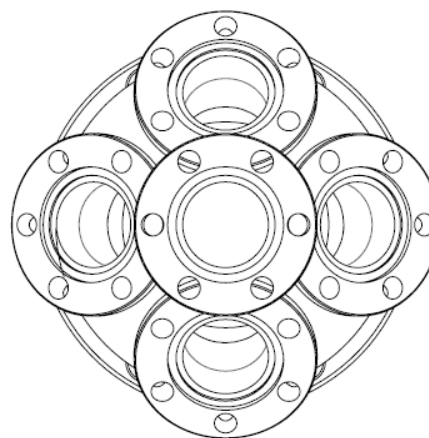


## SIX-ARRAY DOSER (Continued)

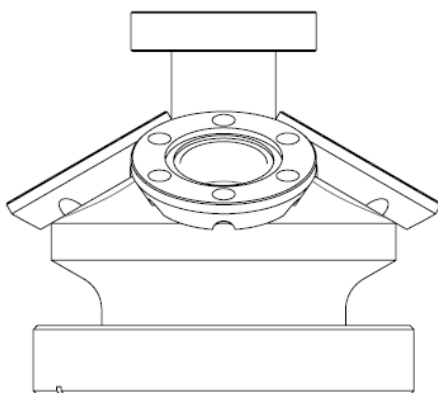
### 5-Way Multicomponent Conflat Flange, 2.74"CF to 1.33" CF Mini



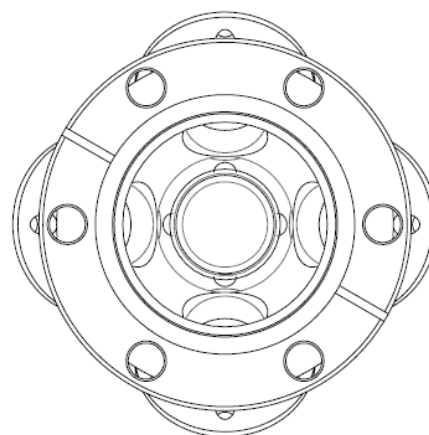
Trimetric view



Top view



Side view

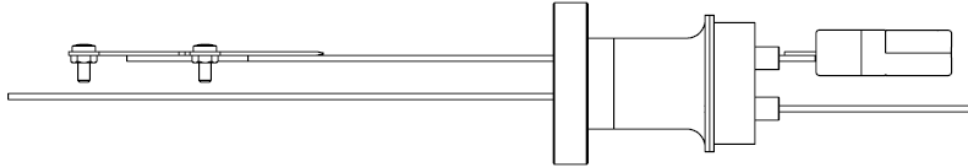


Bottom view

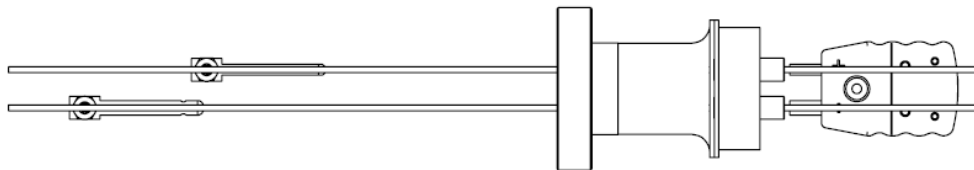
University of California, Los Angeles, Department of Chemical and Biomolecular Engineering							
Part	5-way Multiport 2.75"x5-1.33"Mini	Material	Stainless steel				
Filename	5way.pdf	Scale	No	Units		Quantity	3
Designer	MDC Vacuum	Date					
Revised by	Jeffrey Chang	Date	05/28/2014				
Contractor		Date					
Comments			Tolerance	+/- .0001			

## SIX-ARRAY DOSER (Continued)

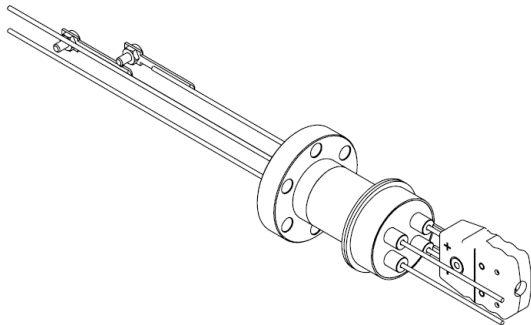
### Thermocouple/ Power Feedthrough, 1.33" CF Mini



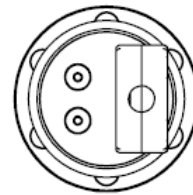
Top view



Side view



Trimetric view



Front view (from ambient)

University of California, Los Angeles, Department of Chemical and Biomolecular Engineering							
Part	Thermocouple/Power Feedthrough	Material	Stainless steel				
Filename	TC.pdf	Scale	No	Units		Quantity	6
Designer	Insulator Seal	Date					
Revised by	Jeffrey Chang	Date	05/28/2014				
Contractor		Date					
Comments			Tolerance	+/- .0001			

## APPENDIX B. OPERATING PROCEDURES

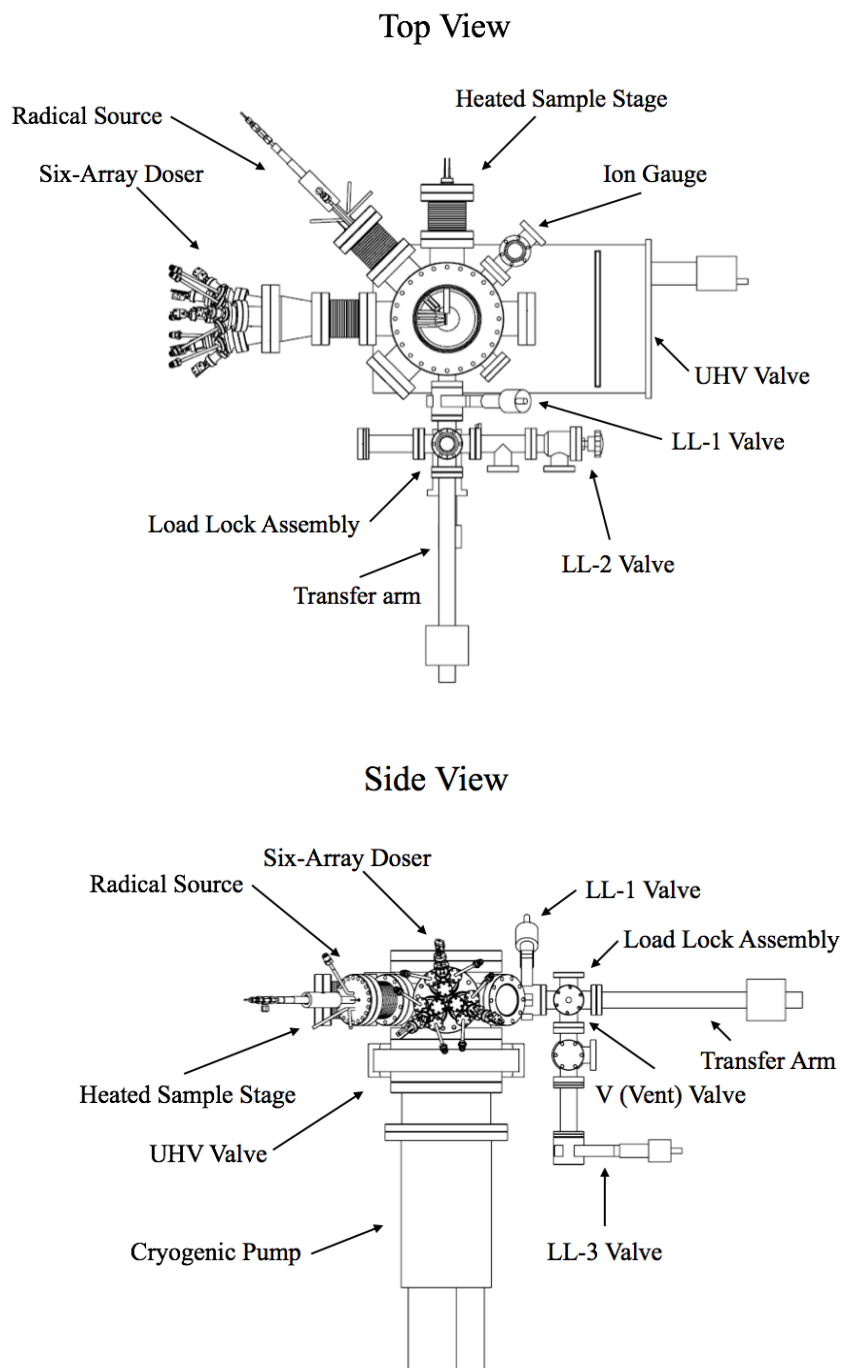


Figure B.1.1 Schematic of the main chamber (top and side views)

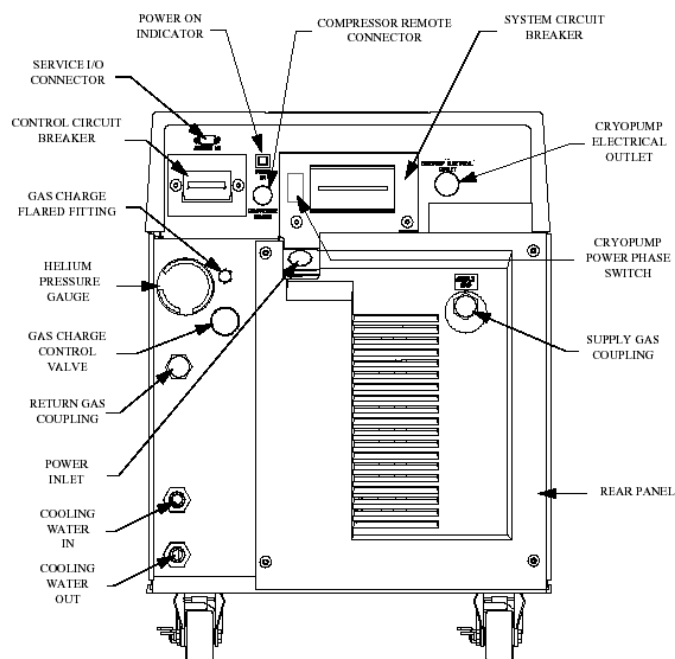


Figure B.1.2 Cryogenic pump compressor

## B.1. Loadlock Chamber

*For this part of appendix, please refer to Figures B.1.1, B.1.2 and B.8.2 for valve locations*

### B.1.1. Venting the Loadlock Chamber:

1. Close LL-1 gate valve first to isolate the main MB chamber from the loadlock chamber (this valve should normally be closed)
2. Close LL-3 gate valve to isolate the loadlock chamber from the turbomolecular pump
3. Half-open the V valve to slowly vent the chamber while observing the Pirani gauge to allow for controlled venting
4. After the loadlock is completely vented, a sample can now be removed from/loaded into the load lock chamber

### B.1.2. Pumping down the Loadlock Chamber

1. Close the V valve
2. Close the 5-L (turbomolecular pump to mechanical pump) pneumatic valve (green light) to isolate the turbomolecular pump from the mechanical pump
3. Close the 5-U (differential pumping atom source) pneumatic valve (red) for the differential pumping of the radical source
4. Slowly open the LL-2 valve (loadlock to mechanical pump) completely, then open the 5-L pneumatic valve, watch and wait until the TC gauge reaches the base pressure (30-60 mTorr)

5. Once system reaches base pressure, open the 5-U pneumatic valve
6. Close the LL-2 valve
7. Open the LL-3 gate valve, pump down loadlock chamber with turbomolecular pump until the base pressure  $< 9 \times 10^{-5}$  Torr is shown on the Pirani gauge (*note: this usually takes 25 minutes*)

## B.2. MB Radical Source

### *B.2.1. Turning on the Plasma Radical Source:*

1. Before using H<sub>2</sub> gas, notify the lab and post the sign first
2. Ensure that the cooling water is on; cooling water temperature should be about 18-20 °C
3. Turn on the microwave power supply unit (*note: let the electronics warm up for at least 20 minutes before engaging microwave power*)
4. Check the pressures of the gas cylinder and the gas line; if H<sub>2</sub> is used, open the H<sub>2</sub> gas cylinder and the gas line (*note: all three valves on the regulator should be open and the pressure of the gas line should be ~20-30 psi*)
5. Turn off the 5-L pneumatic valve (closing the differential pumping line for radical system)
6. Turn off the 5-U pneumatic valve (closing the back-pumping line for the turbomolecular pump)
7. Evacuate the gas line through the mechanical pump by opening valve A-3 while watching the pressure on the TC vacuum gauge
8. Wait until the pressure on the TC returns to base (the pressure should not fluctuate much)
9. Set the gas MFC flow rate to 0%
10. Open the valve before MFC controller:
  - a. 1-U if O<sub>2</sub> is used or
  - b. 2-U if Ar is used
11. Open the valve after the MFC controller:
  - a. 1-L if O<sub>2</sub> is used or
  - b. 2-L if Ar is used
12. To make sure that the O<sub>2</sub> gas line is completely pumped, wait for the TC gauge (indicating MB chamber) to be pumped down to base pressure, then close the purging valve A-3
13. Turn on the 5-U pneumatic valve (opening the differential pumping line for radical system)
14. Turn on the 5-L pneumatic valve (opening the back-pumping line for the turbomolecular pump)
15. Set the desired gas flow rate (~3%) on the MFC to achieve a pressure  $\sim 5 \times 10^{-6}$  -  $6 \times 10^{-6}$  Torr (*note: the main chamber pressure should not exceed  $3 \times 10^{-5}$  Torr*)
16. Press "ON" (green button) on the microwave power supply unit
17. Increase the power to 25 watts
18. If necessary, to attain the minimized reflected power to 0-1 watts, tune the tuning slug between the outer and inner conductor of the radical source

### B.2.2. Turning off the Plasma Radical Source

1. Decrease the microwave forward power to zero
2. Press “OFF” (red button) on the microwave power supply unit
3. Decrease the MFC gas flow rate to 0%
4. Close the valve before the MFC (valve 3-U or 4-U or A-2-U)
5. Close the valve after the MFC (valve 3-L or 4-L or A-2-L)
6. Close the injection valve A-1
7. Close the gas cylinder and the gas regulator if H<sub>2</sub> is used
8. Fill in the log sheet for H<sub>2</sub> run time
9. Turn off the microwave power supply unit

### B.2.3. Precursor Doser

### B.2.4. Flowing the Precursors

1. Make sure that all the valves are open to prevent the gas lines from clogging
2. Make sure that all the temperature controller are turned on, except during system maintenance
3. Each precursor doser has three different heaters corresponding to different doser location. The corresponding heater switch numbers of the temperature controller for different precursors are listed as following

Precursor	Temperature controller			Pneumatic valve
	Housing	Gas line/valve	In-vacuum	
Fe(TMHD) <sub>3</sub>	Controller 3, channel 1	Controller 3, channel 2	Controller 3, channel 3	#5
Bi(TMHD) <sub>3</sub>	Controller 3, channel 5	Controller 3, channel 6	Controller 3, channel 7	#6
Co(TMHD) <sub>3</sub>	Controller 1, channel 1	Controller 1, channel 2	Controller 1, channel 3	#7

4. Heat the precursors to operating temperatures by temperature controllers. The operating temperature of different precursors are listed below (*note: the operation temperatures should not exceed individual precursor's decompose temperature*):

Precursor	Operating temperature		
	Housing	Gas line/valve	In-vacuum
Fe(TMHD) <sub>3</sub>	130	190	185
Bi(TMHD) <sub>3</sub>	150-160	210	185
Co(TMHD) <sub>3</sub>	120	190	185

#### *B.2.5. Stopping the Precursor Flow (when loading samples/pumping down)*

1. The pneumatic valves should be open at all times (prevent doser system clogging)
2. Turn off the heaters that was turned on during deposition
3. Check the MB chamber pressure by IG while the heaters are cooling down, make sure that the pressure dose not rise significantly

#### *B.3. MB Chamber Compressor – Cryogenic Pump*

##### *B.3.1. Starting the Cryogenic Pump*

1. Close UHV and CM valve to isolate the cryogenic pump from main chamber and mechanical pump
2. Ensure the pressure of cryogenic pump is high enough (higher than the base pressure of mechanical pump) before pumping down the cryogenic pump
3. Air molecule condensation will occur if the cryogenic pump is turned on
4. Open the CM valve slowly to pump down the cryogenic pump by mechanical pump
5. Wait until mechanical pump base pressure is reached (~60-100 mTorr), close the CM valve
6. Quickly set the system circuit breaker to the ON (up) position (see Figure B.2)
7. Then set the control circuit breaker to the ON (up) position (see Figure B.2)

##### *B.3.2. Turning off the Cryogenic Pump (usually for Maintenance and Regenerating Purpose)*

1. Isolate the cryogenic pump by closing UHV valve
2. Set the System Circuit Breaker to the OFF (down) position
3. Set the Control Circuit Breaker to the OFF (down) position

#### *B.4. Main Chamber*

##### *B.4.1. Venting Main Chamber (usually for Maintenance and Cleansing Purpose)*

1. Close the 5-L (PV-9) valve to end the differential pumping for radical source
2. Close the A-1 valve to stop gas injection to radical source
3. Turn off the ion gauge by selecting the controller (Multi-gauge channel 1) and pressing “Emis” (*note: the ion gauge will can be seriously damaged if it remains on while venting*)
4. If the load lock chamber is at its base pressure, close the LL-3 gate valve. But if the load lock chamber pressure is higher than its base, pump it with the turbomolecular pump first (*note: for the pump down process of the load lock chamber, please see the previous section*)
5. Open valve LL-1 to connect the load lock chamber and main chamber
6. Close the UHV gate valve to isolate the cryogenic pump
7. Close the LL-3 valve to isolate the chamber from the turbomolecular pump
8. Slowly open the V venting valve, observe the pressure increase on Pirani gauge (*note: the Thermocouple gauge should stay at base pressure since mechanical pump is isolated*)

9. Eventually, the Pirani gauge should be displaying  $\sim 5.5 \times 10^{-2}$  Torr, depending on the ambient condition

#### B.4.2. Pumping down the Main Chamber

1. Make sure that the load lock chamber is connected to the main chamber and both of them are completely vented (Pirani gauge displaying  $\sim 5.5 \times 10^{-2}$  Torr)
2. Close the V venting valve and the load lock door
3. Close the 5-U pneumatic valve (green) to protect the turbomolecular pump and close the 5-L pneumatic valve (red) for the radical source differential pumping and isolating them from the mechanical pump (*note: prevent back flow*)
4. Open LL-1 roughing valve to pump down the system by mechanical pump, the Pirani gauge readings should decrease while the Thermocouple gauge will first have a drastic increase but decrease to its base pressure afterwards. (*note: the base pressures for Pirani gauge and Thermocouple gauge are low  $10^{-2}$  Torr and  $\sim 60$ -100 mTorr, respectively*)
5. Remember not to isolate the Turbomolecular pump too long otherwise the Turbomolecular pump seriously can suffer serious damage. Therefore, it is normally recommended to turn off the turbomolecular pump if it is to be isolated for longer than 10 minutes. However, for occasions when turning off the turbomolecular pump is not feasible, it should be pumped by mechanical pump every 10-15 minute interval, by closing the LL-2 valve and then open the 5-U valve for a few minutes. Close 5-U valve and open LL-2 valve to pump down the system again after pumping down the Turbomolecular pump
6. Once the base pressure of the mechanical pump is reached, start pumping down the system with Turbomolecular pump by closing the LL-2 valve (*note: to isolate the mechanical pump*) and then open the 5-L valve (*note: to connect the Turbomolecular pump with the mechanical pump*), and then open the LL-3 valve. The Pirani gauge reading should be lower than  $10^{-4}$  Torr
7. When the base pressure is reached, close LL-1 gate valve to isolate the load lock chamber from the main chamber
8. Open the UHV gate valve to pump down the main chamber by cryogenic pump. Turn the ion gauge by selecting Multi-gauge channel 1 and pressing “Emis”. The base pressure should be lower than  $10^{-6}$  Torr

#### B.5. Deposition Procedures

1. Load the sample into load lock chamber after venting, pump down the chamber following the guidelines provided in the load lock chamber section to base pressure (*note: it takes 25 minutes to pump down the load lock chamber from ambient to base pressure,  $\sim 9 \times 10^{-5}$  Torr*)
2. Make sure that the system is at its base pressure, and that the pneumatic valves are open so that the gas lines won't clog during operation
3. Open LL-1 gate valve, half close the UHV gate valve (*note: to prevent the sample from falling into the cryogenic pump*). Attach the sample onto sample heater using transfer arm. Close LL-1 gate valve and reopen the UHV gate valve completely, start to pump down the main chamber again. Turn on the heaters to its operating temperature (*note: it*



*takes 45 minutes to for the system to be pumped down and heated up to the operating condition)*

4. Before the next step, check whether if the pressure and temperatures are at the correct range
5. Close the pneumatic valves of the dosers in order to prevent the reaction when the radical source is on
6. Close the 5-U and 5-L pneumatic valve
7. Pump down the radical course gas supply lines by opening A-2 manual valve, and open the lower and upper pneumatic valves depending intended gas (1-U and 1-L for O<sub>2</sub>, 2-U and 2-L for Ar) for several seconds
8. Close the A-2 manual valve; reopen the 5-U and 5-L pneumatic valve. Double-check the pressure gauge for leaking. If no, open the A-1 manual valve, then open the MFC for intended gas to 3.0%
9. Turn on the radical source following guidelines in turning on the plasma section, with microwave power supply unit running under 25 watts, reflected power 0-1 watts
10. Check if the plasma strikes by seeing the white-colored glow of the radical source. If it's striking leave it on for several seconds to terminate the substrate surface with radical atoms
11. Turn off radical source power supply before clicking run
12. Details of automation, please see section F

## B.6. Emergency Shutdown Procedure

1. Turn off the ion gauge for the chamber. On the Varian Multi-Gauge display press CHAN to switch to the chamber pressure, then press EMIS to turn off.
2. Close the UHV and LL-1 gate valves, both are manual valves (see Figure B.1)
3. Turn off the Control Circuit Breaker on the compressor (see Figure B.2)
4. Turn off the System Circuit Breaker on the compressor (see Figure B.2)
5. Turn off the TMP by depressing the power button on the controller.

## B.7. Utilities for MB System

### B.7.1. Schematics for Electrical, Water, and Gases Systems

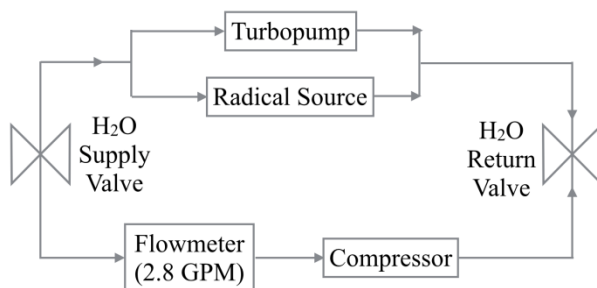


Figure B.7.1 Schematic of the cooling water system

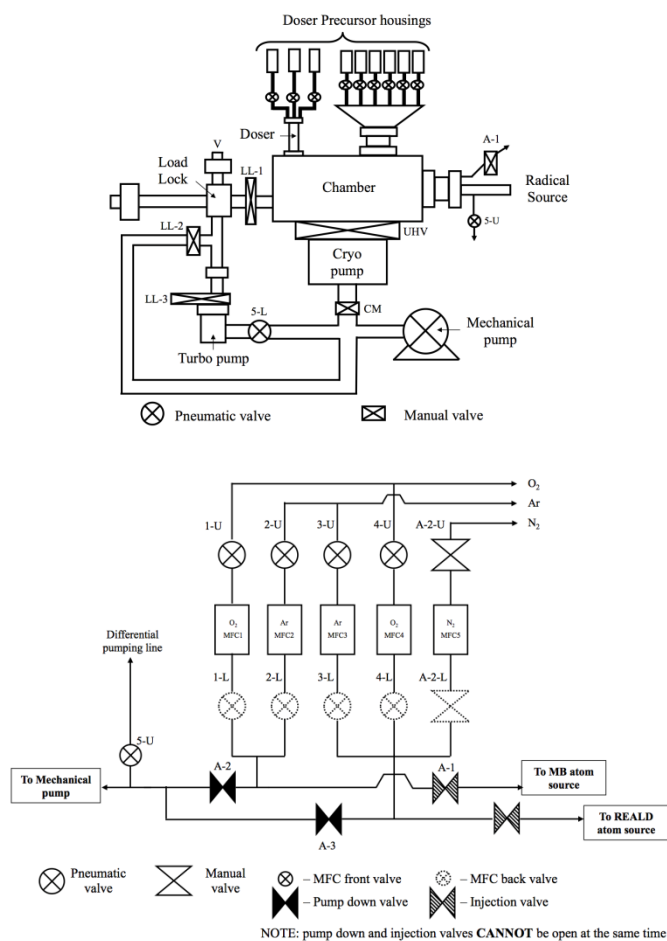


Figure B.7.2 Schematic of valves and gas lines for MB system

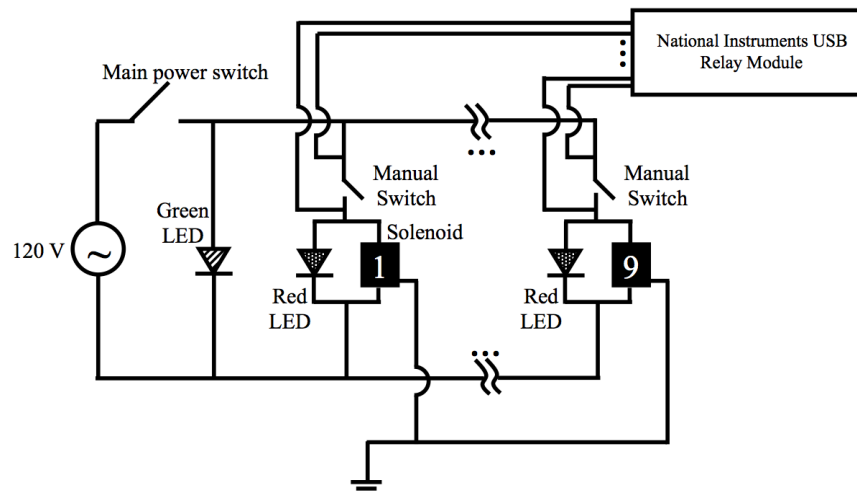


Figure B.7.3 Schematic of electrical wiring for pneumatic valve control

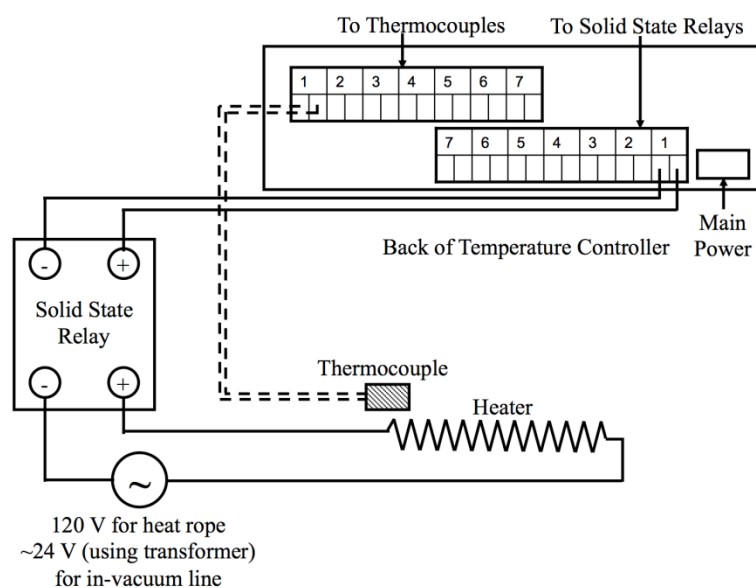


Figure B.7.4 Schematic of electrical wiring for controlled heaters

## APPENDIX C. LIST OF EQUIPMENT USED

### *C.1.1. List of Electrical Equipment Parameters*

Electrical equipment	Parameters
Mechanical pump	115 VAC, single phase
Cryogenic pump compressor	208 VAC, 3 phase, 30 A min
Turbomolecular pump	115 VAC, single phase
Microwave radical source power supply	110 VAC, single phase
Ion source power supply	115 VAC, single phase
Temperature controller	120 VAC, single phase
Sample heater	Variable 0-30 VAC using transformer
Radical source mass flow controller	120 VAC, single phase
Multi-gauge controller	115 VAC, single phase
Heating wires	120 VAC
Kapton heaters	120 VAC

### *C.1.2. List of Water and Gas Equipment Parameters*

Equipment	Parameters
Water compressor	Flow rate = 2.8 GPM
H <sub>2</sub> Cylinder to MFC5 to Radical Source	Flowing H <sub>2</sub>
O <sub>2</sub> Cylinder to MFC4 to Radical Source	Flowing O <sub>2</sub>
N <sub>2</sub> Cylinder to MFC3 to Radical Source	Flowing N <sub>2</sub>
Ar Cylinder to MFC2 to Ion Source	Flowing Ar
Ar Cylinder to MFC1	Flowing Ar

### *C.1.3. List of the Equipment/Parts Used for MB System Setup*

Vendor	Catalog No.	Description
Alfa Aesar	11386	Indium foil, 0.1mm (0.004in) thick Puratronic, 99.9975%, 100mm x 100mm
Alfa Aesar	41359	Bis(2,2,6,6-tetramethyl-3,5-heptanedionato)Cobalt (II) 99.9% - Co
Bid Service	40144	Ion Beam Drive, Commonwealth Scientific ID-2500-C
C.W. Swift	23N-50-0-30	Microwave connector, N type, article number 22642835
Cerac Inc.	1314-36-9	Yttrium Oxide, 99.9999 (REO basis)
Controlled Motion Solutions	PSFTN0N10NP	10 Station manifold
Controlled Motion Solutions	PS2982B53P	120/60 Coil Sol Kit
Duniway	FIL-7A	Replacement Filament for T-NUDE-F Ion Gauge
G. Finkenbeiner, Inc.		Quartz ampoule (custom-made)
Momentive Performance Materials	HTR1001	Boralectric™ heater on PBN plate substrate
Helix	7021002P001	Charging Line, 10' (For Compressor)
Helix	8140000K001	Installation Tool Kit (For Compressor)
Helix	8031403	Two Stage Regulator (For Compressor)
Helix	8080250K003	Maintenance Manifold (For Compressor)
ISI	9392000	1 TC pair/1 Power Pair / with TC connectors, C type
ISI	5TC-GG-K-30-36	Glass Insulated Thermocouples
ISI	9412008	Power feedthrough, 8 pins, 10 Amps, 500 V, 1-1/3" flange,

		conductor material Moly
ISI	9924001	Power-Push-On, 150 deg. C Air, 400 deg C Vacuum Service, Gold Plated
Kapton tape	KPTD-1/2	Double-sided Kapton tape
Kapton tape	KPT5-1/2	Single-sided Kapton tape
Long beach valves & fitting	SS-4-UT-6-400	Ultra-Torr Swagelok Tube Fitting Union
Maxtek	BSH-151	Bakeable QCM sensor head/feedthrough (vacuum)
Maxtek	103200-3	QCM Sensor Crystal, 6 MHz, SCV-14A-6N-Sil-S-B (Si over Au solid side)
MDC	409007	Cluster Flange 6"x3-2.75"
MDC	402039	Conical Reducer 6"x4.58"
MDC	110000	Flange, 1.33", Blank
MDC	409004	Multiport Flange 2.75"x5-1.33" Mini, T
MDC	402000	Nipple, 1.33"
MDC	41010	O-ring, Viton 2-010
National Instruments	779453-01	USB-9481 4-ch SPST Relay Module
Nor-Cal	133-1/4-MVCR	1 1/3" CF to Male VCR
Nor-Cal	LFT-075-1-025	Single Liquid Feedthrough
Omega	5TC-GG-K-30-36	Kapton insulated Thermocouples, 5 each, type K calibration 1m (40") long, 30 gauge, stripped lead termination
Omega	CN1507TC	7 Channel Controller
Omega	NI80-012-200	80%Ni/20%Cr, 200' pool of 28 gauge bare resistance heating wire, diameter 0.0126"
Omega	CO1-K-72 INCH	Cement on T/C
Omega	SSR330DC25	Solid State Relay DC 25 Amp
Omega	TT-K-20-SLE-100	Special Limits of Error wire
Pfeiffer Vacuum	PM041264X	Power cable for TPC 121 (PMC01475A M-02095)
Strem	93-3943	Yttrium foil, 99.9% REO, 25x25 mm, 0.127mm thick
Strem Chemicals	83-1000	Tris(2,2,6,6-tetramethyl-3,5-heptanedionato)Bismuth (III) 99.9%-Bi
Strem Chemicals	26-3610	Tris(2,2,6,6-tetramethyl-3,5-heptanedionato)Iron (III) 99.9%-Fe
Swagelok	SS-4-VCR-1	VCR Fitting, 1/4 in. Female Nut
Swagelok	SS-4MG-VCR-MH	SS Metering valve, 1/4 in. Male Swagelok VCR Metal Gasket Face Seal Fitting, Venire Handle
Swagelok	SS-HBVV51-C	Stainless Steel High-Pressure Bellows-Sealed Valve, 1/4 in. Female Swagelok VCR Face Seal Fitting, NC Actuator, Polyimide Stem Tip
Swagelok	SS-4-VCR-4	VCR Fitting, 1/4 in. Male Nut
Swagelok	316L-4-VCR-3AS	VCR Fitting, Short Automatic Tube Butt Weld Gland, 1/4 in. VCR
Transfer Engineering		Custom-made sample transfer, sample station, and heating system
Varian	L8321301	UHV Board (pressure controller)
Varian	L64403010	UHV Cable (pressure controller)

## APPENDIX D. MAINTENANCE

### D.1. Heated Sample Stage

#### D.1.1. Removing the Heated Sample Stage

1. Vent the chamber (see section B.5)
2. Remove the heated sample holder from the main chamber carefully, and be cautious not to damage the radical source and doser (*note: avoid to touch the chamber wall while removing the sample stage*)
3. After reattaching the sample stage, double check the alignment with transfer arm and adjust bellow as necessary

#### D.1.2. Replacing the Boroelectric Sample Heater

1. Remove the heated sample heater (see previous section)
2. Remove the sample holder clip, the sample thermocouple is attached to one of the screws
3. Remove the electrical connections to hold heater before removing the screws securing the heater to the sample stage
4. On the studs that secure electric connections, remove the nuts and washers to disassembly the old heater from the heated sample stage
5. Insert the stud into the new heater at one of the exposed electrodes with a nut fastened to the top of the stud along with the PG and Grafoil washers; the Grafoil washers should sandwich the heater on both sides. Fasten the stud to the heater with another nut on the other side. The sequence of washers should be as following:

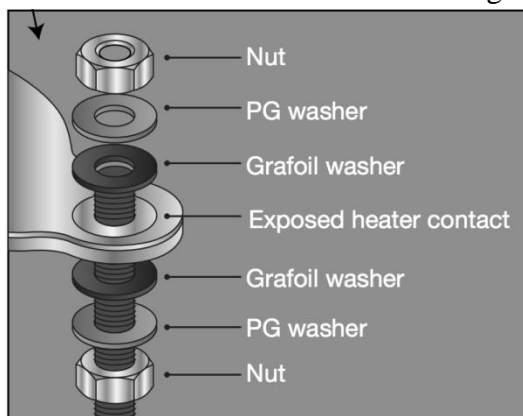


Figure C.1 Schematic of installation for Boroelectric sample heaters

6. Do the previous step again for the another exposed electrode
7. Use ceramic spacers/washers on the electrodes to prevent undesired electrical grounding to the sample stage
8. Reattach the heater to the sample stage with the screws and fasten tightly but not an excessive amount to avoid cracking the ceramic heater
9. Reattach the heater onto the sample stage with the screws and fasten it fairly tight to avoid the cracking of ceramic heater

10. Reattach the electrical contacts and secure tightly with nuts, it is optional using PG and Grafoil washers for the electrical connectors
11. Check the electrical connection with multimeter
12. Reattach the sample holder clips along with the sample thermocouple, make sure the thermocouple has sufficient thermal contact to the sample heater

## D.2. Radical Source

### *D.2.1. Replacing Quartz Ampoule*

1. Vent the main chamber and then remove all fittings and connections, remove the radical source as well
2. Remove the top clamp to reveal quartz ampoule
3. Remove Teflon heat-shrink tubing extending from gas-line feedthrough that is attached to the quartz ampoule
4. When installing a new quartz ampoule, Indium foil must be wrapped around the cylindrical section to ensure enough heat conduction. Failure to do so might result in unstable plasma due to overheating and poor heat removal
5. Replace Teflon heat-shrink tubing to connect gas line to quartz ampoule
6. Place quartz ampoule in the housing again making sure that proper thermal contact is achieved. Also make sure end of quartz ampoule is contacting the microwave waveguide
7. Secure quartz ampoule to radical source by screwing down the top clamp
8. Wrap wire extending from electrical feed through to allow Tesla coil induced plasma generation if necessary

### *D.2.2. Tuning the Radical Source*

1. The distance from the attached N-1 cable to the end of the waveguide must be tuned since the plasma generation highly depends on the waveguide resonance condition
2. Turn off the microwave power supply first, then remove the N-1 cable and move the tuning slug to desired location
3. For large adjustments, the set screws can be loosened allowing more free movement, otherwise, the corkscrew section of the tuning slug can be rotated to allow for fine adjustments
4. Adjust the tuning until the reflected power is at its minimum value (usually  $\sim 0-0.1$  watt), make sure that the plasma can strike spontaneously upon the application of microwave power

### D.3. Precursor Doser Arrays

#### D.3.1. *Replacing In-Vacuum Heaters*

1. Vent the chamber, and then remove the precursor doser carefully
2. Remove the Teflon gape, then the old Kapton heater (two, each in 12" × 1") from doser gas lines
3. Prepare a new Kapton heater, in the size of 12" × 1", which is sufficient for covering the entire gas line
4. Wrap the gas lines with the Kapton heater spirally (note: the heater should be evenly spaced with no overlapping to give a uniform heating throughout the entire gas line)
5. Tightly wrap the Kapton heater with the Teflon tape to fix the heater onto the gas lines
6. Make sure that the heaters are attached onto the gas lines properly, and remember to secure the corresponding thermocouple to the gas line (note: if the thermocouples are not well attached, the heater might be heated up uncontrollably and burn out)
7. Attach the heaters to correct power feed-through which corresponds to the correct thermocouple for that gas line
8. Heat up the in-vacuum gas lines for several hours to remove the moisture on it before using it

#### D.3.2. *Replacing Air-Side Vacuum Heaters for Gas Lines and Precursor Housing*

1. For air-side vacuum gas lines and precursor housing heaters, spirally wrap the parts with heating wires and make sure it is wrapped with even spacing, proper contact, and no overlapping
2. Secure the correct thermocouple to the gas line or precursor housing (*note: if the thermocouples are not well attached, the heater might be heated up uncontrollably and burn out*)
3. **MAKE SURE TO TURN OFF THE POWER STRIP BEFORE PUGGING IN HEAT ROPE.** In order to prevent clogging, wrap the heating wire more closely and tight at the cold spots (valves and connections such as VCR and Swagelok connections). Furthermore, setting a higher temperature can also prevent clogging

#### D.3.3. *Unclogging Gas Lines and Valves*

1. Vent the chamber, and then remove the clogged parts
2. Remove the clogging precursor by using acetone and by plugging another gas line with a smaller diameter into the clogged gas line
3. After removing clogging precursors, rinse the gas line with copious amount of acetone in order to remove all the remaining chemicals on the gas line wall
4. Dry out all the chemical solvents before placing the parts back onto the chamber
5. Dispose the chemical waste with proper procedures

#### D.3.4. *Replace Valve Bellows Assembly*



1. Vent the chamber, and then remove the valve from it
2. MUST actuate the valve with compressed air before disassembling the valve bellow assembly
3. Unscrew the top of the valve while its actuated to the OPEN position, be careful not to damage the gas line fittings (note: unscrewing while the valve is in CLOSE position will damage the valve)
4. Unscrew the bellows assembly from the valve and replace gaskets as needed

#### D.4. Cryogenic Pump and Compressor

*Note: for complete documentation, refer to HELIX 9600 Compressor operation manual*

##### D.4.1. Regenerating the Cryogenic Pump

1. Isolate the cryogenic valve by closing UHV gate valve from the main chamber
2. Turn off the compressor:
  - a. Set the System Circuit Breaker on the compressor to the “OFF” position
  - b. Set the Control Circuit Breaker on the compressor to the “OFF” position
3. Wait around 30 minutes for the manifold inside the cryogenic pump to approach room temperature
4. Heat up the cryogenic pump with heating sleeves to  $\sim 100^{\circ}\text{C}$  (100% using transformer) for at least an hour to prevent backflow from mechanical pump into cryogenic pump due to pressure difference
5. Close the LL-3 gate valve and 5-L pneumatic valve, isolating the Turbomolecular pump from the mechanical pump
6. Also make sure LL-2 valve is closed to isolate the load lock chamber to the mechanical pump
7. Open CM cryogenic evacuation valve and pump down the cryogenic pump to base pressure ( $\sim 30\text{m Torr}$ ) by mechanical pump
8. Occasionally (*note: each 5~10 mins*) pump down the Turbomolecular pump by mechanical pump by closing CM valve and opening the 5-L pneumatic valve in order to prevent it from winding down
9. After the base pressure of the cryogenic pump is reached, close CM valve and then pump down the load lock chamber by mechanical and Turbomolecular pump (*note: following the pump down procedure from section B.1.5*)
10. Turn on the compressor:
  - a. Set the System Circuit Breaker on the compressor to the “ON” position
  - b. Set the Control Circuit Breaker on the compressor to the “ON” position
11. Initiate the compressor and wait  $\sim 2$  hours to cooling down the cryogenic pump to the temperature of liquid He ( $\sim 17\text{K}$  on the cryogenic pump temperature reader)

12. After the load lock and main chamber are pumped down to Turbomolecular base pressure, open the UHV valve and start to pump down the main chamber by cryogenic pump (*note: for details, please see section B.1.5*)

#### D.4.2. Recharging Helium

1. Obtain UHP (99.9999%) He gas cylinder and secure the regulator to its top (*note: the regulator should be only used for He cylinder to prevent contamination*)
2. Open the LL-1 gate valve to unify the pressure between load lock chamber and main chamber (*note: to prevent potential pressure back shoot that could damage Turbomolecular pump*)
3. Isolate the cryogenic pump by closing UHV gate valve
4. Turn off the compressor:
  - a. Set the System Circuit Breaker on the compressor to the “OFF” position
  - b. Set the Control Circuit Breaker on the compressor to the “OFF” position
5. Open the valves on the regulator (*note: to purge the gas in the regulator gas line by He flow*)
6. Open the brass cap labeled as “Helium Gas Charge”
7. Attach the regulator gas line to the “Helium Gas Charge” port but do not tighten it completely (*note: continuing the purge process*)
8. Purge the gas line continue for ~1 minute
9. Fully tighten the gas line onto the “Helium Gas Charge” connection and adjust the regulator valve to proper extent
10. Crack open the gas charge control valve (black) under the “Helium Gas Charge” to recharge Helium into the compressor until the pressure gauge reaches “SYSTEM PRESSURE OFF POSITION” (the white region)
11. Immediately close the gas charge control valve (black) on the compressor
12. Remove the gas line and close the regulator valve
13. If the pressure gauge is reading higher than the “SYSTEM PRESSURE OFF POSITION” crack open the gas charge control valve (black) when there’ s nothing attached on the “Helium Gas Charge” to release the pressure inside compressor till acceptable region
14. Return the cap to “Helium Gas Charge” port
15. Turn on the compressor
  - a. Set the System Circuit Breaker on the compressor to the “ON” position
  - b. Set the Control Circuit Breaker on the compressor to the “ON” position
16. Initiate the compressor and wait ~2 hours to cooling down the cryogenic pump to the temperature of liquid He (~17K on the cryogenic pump temperature reader)
17. After the load lock and main chamber are pumped down to Turbomolecular base pressure, open the UHV valve and start to pump down the main chamber by cryogenic pump (*note: for details, please see section B.1.5*)

#### D.4.3. Discharging the Helium

1. Open the LL-1 gate valve to unify the pressure between load lock chamber and main chamber (*note: to prevent potential pressure back shoot that could damage Turbomolecular pump*)
2. Isolate the cryogenic pump by closing UHV gate valve
3. Remove the flare cap from “Helium Gas Charge” fitting
4. Open the gas charge control valve (black) very slowly to allow a slight amount of He to escape
5. Leave the valve open until the He pressure gauge is within the range of “SYSTEM PRESSURE OFF POSITION” and then immediately close the gas charge control valve (black)
6. Turn On the compressor
  - a. Set the System Circuit Breaker on the compressor to the “ON” position
  - b. Set the Control Circuit Breaker on the compressor to the “ON” position
7. Initiate the compressor and wait ~2 hours to cooling down the cryogenic pump to the temperature of liquid He (~17K on the cryogenic pump temperature reader)
8. After the load lock and main chamber are pumped down to Turbomolecular base pressure, open the UHV valve and start to pump down the main chamber by cryogenic pump (*note: for details, please see section B.1.5*)

#### D.4.4. Replacing the absorber

1. Open the LL-1 gate valve to unify the pressure between load lock chamber and main chamber (*note: to prevent potential pressure back shoot that could damage Turbomolecular pump*)
2. Isolate the cryogenic pump by closing UHV gate valve
3. Turn off the compressor:
  - a. Set the System Circuit Breaker on the compressor to the “OFF” position
  - b. Set the Control Circuit Breaker on the compressor to the “OFF” position
4. Remove the 4 screws which secure the rear panel and remove the rear panel
5. Use wrenches included with system (1-3/16” and 1-1/8”) and disconnect the Helium connectors quickly to reduce leakage
6. Using a 7/16” wrench, remove the absorber mounting bolt
7. Move the absorber from under the mounting tabs in the base and remove the absorber from the compressor
8. Install the replacement absorber under the mounting tabs and secure it into place with the bolt removed during step 6
9. Using the two wrenches as in step 5, connect the two self sealing Helium couplings quickly to minimize Helium leakage
10. Install the compressor rear panel

## APPENDIX E. TROUBLESHOOTING

### E.1. Heated Sample Stage

*Problem:* The temperature controller does not register an increase in sample heater temperature after being turned on

*Solutions:*

- It might be because of the heaters:
  - Check the power connections of the heater, the power strip and transformers, to make sure that the heaters are being fed with power
  - Check the electrical connections of the heater, whether if it has a correct resistance and electrical continuity (note: the heater resistance should be ranging between  $9\Omega$  to  $13\Omega$ ). If the resistance is not in the range of  $9\Omega$  to  $13\Omega$ , remove the sample stage as section C.1 and trouble shoot it
  - Outside vacuum, check with multimeter to see if the heater is having correct resistance between  $9\Omega$  to  $13\Omega$ , if no, replace the heater according to section C.1

*Problem:* The sample holder arms are wobbling or not secure enough

*Solutions:*

- Vent the chamber, and remove the sample holder according to section C.1
- Remove the sample holder and the heater assembly to remove the bellow
- Remove the bellow
- Check the tightness of the screws securing the arm to the flange, according to the screw condition, either tighten the screw or replace it
- Reassemble the sample holder unit (sample holder, heater, bellow, etc.) and reattach the entire unit back to the chamber

### E.2. Radical source

*Problem:* Plasma cannot be generated during operation

*Solutions:* There are several factors that can lead to the situation

- Oxygen flow
  - To check the oxygen flow, make sure that main chamber base pressure is somewhat elevated from its original base pressure since there is oxygen flowing in
  - If the pressure is not elevated, check the Oxygen connections and gas lines to see whether there is a leakage or not (for example, check the compressed air gas lines to see any possible leakage that prevent pneumatic valve to work normally, the mass flow controller flow reading, low pressure in Oxygen gas cylinder, etc.)
- Cooling water flow

- Make sure that the cooling water is working normally, the center conductor should be around 10-15°C (feeling cool by touching)
- The cooling water line might be clogged with algae
- If the quartz ampoule is not properly contacted to cooling block by Indium foil, the temperature of the ampoule could be too high (note: this problem is not likely to happen if the quartz ampoule is not being removed recently)
- Electrical connection
  - Tesla coil could be used to test the radical source; when the plasma gas is being glowed and when microwave power source is on and set to intended input power, contact the tip of the Tesla coil to the electrical feed through and quickly turn on and off Tesla coil (***note: take extreme caution when using Tesla coil, it generates a voltage ~10,000-50,000V, make sure the tip is contacted to electrical feedthrough***) This is not a permanent solution as the Tesla oil cannot be automated
  - It maybe also because of the bad contact between the N-1 cable and the inner conductor, check whether if there is greenish-blue oxidation of the inner conductor, which might influence the electric conduction. It can be fixed by using sand paper to scrub the inner conductor surface and by tuning the location of contact

*Problem:* Plasma is unstable or with high reflected power

*Solutions:*

- Make sure the 5-U differential pumping valve is open for the radical source tube
- Check the tip of Huber N-type microwave cable and the surface of the inner conductor, if greenish-blue oxidation has grown, remove it by sanding the surface to give proper contact between the N-1 cable and inner conductor
- Clean the inner conductor with isopropyl alcohol and with can of compressed air, metal fragments could potentially provide grounding and shortage to the conductors

### E.3. Precursor Doser Arrays

*Problem:* Temperature controller channel does not register an increase in temperature for in-vacuum heater, has line heater, or housing heater after being turned on

*Solutions:*

- Make sure that all the power strips and connections for the heaters are well connected and functioning
- Check the system with the thermometer probe to see if the heaters are actually heated up, in order to find out the problem is because of the heaters or the thermocouples (note: this may not be possible for the in-vacuum heaters)
- If the heaters are heated up, it means that the thermocouple is not functioning, check whether if the thermocouple is properly attached to temperature controller and the heaters

- Replace the thermocouples if the readings of thermocouples are not correct even with correct connection
- If the heaters are not heated up, check the resistance of the heater by multimeter, see whether the resistance is normal or the heaters has been grounded to gas lines (note: a resistance in the M $\Omega$  scale indicates that the heater is broken)
- Replace the heater if needed

*Problem:* Low precursor flux to substrate sample surface

*Solutions:*

- Alignment
  - Double check the alignment of the precursor doser to the sample surface, tune it if necessary
- Precursor
  - Precursor may not be sufficiently heated to give enough air flux, further heat up the parts to a higher temperature if necessary (*note: check the precursor MSDS in obtain the information of sublimation and decomposition temperature*)
  - Check precursor housing to see whether there is sufficient amount of precursor remaining
- Clogging
  - Clogging may happen inside the valves, precursor gas will frequently adsorb on gas lines and valves if they're not clean enough and or existing local cold spots
  - Detach the precursor gas line, clean it with acetone and then sonicate it to clean up the precursor clogging
  - Precursor gas lines must be baked (to remove the moisture) properly before being installed to the chamber (***note: acetone is extremely flammable, therefore make sure acetone has been totally removed before baking***)

#### E.4. Cryogenic pump and Compressor

*Problem:* Chamber is not pumping down to base pressure or pumping speed is reduced

*Solutions:*

- Pressure
  - Check and make sure that the compressor has enough He pressure by seeing the He pressure gauge
  - If the pressure is out of operational range, either recharge or discharge He gas (see section C.4)
- Temperature
  - Make sure that the cryogenic pump is working under proper temperature (~24K)
  - If the temperature is not under operating range, regenerate the cryogenic pump if necessary (see section C.4)

## APPENDIX F. MULTIFERROIC MEASUREMENTS

### F.1. Magneto-optic Kerr effect (MOKE) measurements

1. Before turning on the electromagnets, make sure that they are fastened as tight as possible to prevent the electromagnets to crush to each other due to strong attracting magnetic field
2. Fix the sample onto sample holder, and place the sample holder in between the two electromagnets (*note: be careful not to contact the holder and the electromagnet*)
3. Turn on the power of laser beam on the laser control box
4. Setup the MOKE measurement equipment on the laser table as shown in figure E.1, align the laser inducer, polarizer, spin polarizer, and laser detector properly
5. On the electromagnet power supply, turn on the primary power switch of the electromagnets first and then turn on the switch for the individual electromagnets
6. Adjust the location and angle for the detector to detect the reflected laser beam, if the detector is aligned properly, the intensity of the in-phase reflected light on the lock-in amplifier should be reasonably high (*note: the bar should be around 50%*) and at the same time, the out-of-phase reflected light intensity should be as low as possible
7. If the intensity of the in-plane reflected light is still low, tune the sensitivity of it by pressing the arrow bottoms in the SENSITIVITY box at the left until the reader becomes normal
8. If the lowest value of the out-of-plane reflected light intensity is not close to zero, press the AUTO bottom in the CALIBRATE box at the right to re-calibrate it
9. Start the MOKE measurement by setting different parameters in the MATLAB coding box and press start sweeping

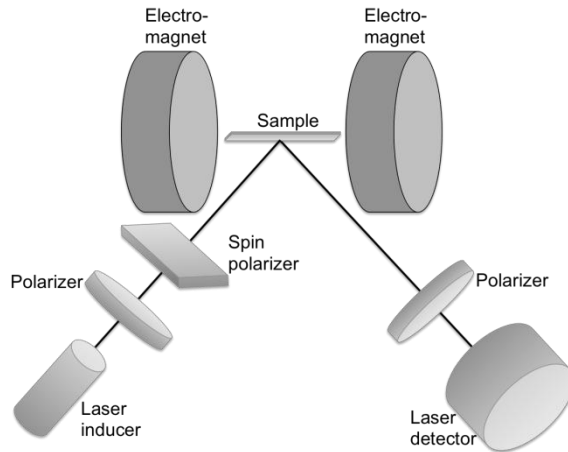


Figure E.1 Setup of the MOKE measurements

## F.2. Superconducting Quantum Interface Device (SQUID) Measurements

### F.2.1. Refilling Liquid Helium

1. Check the remaining percentage of liquid Helium, refill liquid Helium into SQUID system if the percentage is too low
2. To refill liquid Helium, firstly attach the pressured Helium gas cylinder to the liquid Helium tank, in order to provide back pressure to accelerate the refilling process
3. Vent the Helium gas in the tank (*note: due to the Helium liquid-gas equilibrium*)
4. Vent the Helium gas in SQUID and open the inlet (*note: due to the Helium liquid-gas equilibrium*)
5. Take off the cap on the liquid Helium tank, connect the tank and SQUID with the metal tube and secure the connections (*note: gloves needed to prevent frostbite*)
6. Close the venting valve and open the valve connected to gas Helium cylinder on the tank
7. After the connection is secured, the refilling process should begin simultaneously
8. The refilling rate should be around 2%/min, tune the flow controller of the cylinder to attain desired rate
9. Turn off the cylinder valve when the filling percentage reaches 91%, wait until the percentage slowly increases to 100%
10. Loosen the connections, pull out the metal tube, isolate the Helium cylinder from the tank
11. Cap the SQUID and the tank back, remember to open the venting valve of the tank

*Note:*

- *Liquid Helium doesn't have to be refilled when SQUID temperature is not increasing*
- *Liquid Helium is consumed faster when the experiment is under high magnetic field or high temperature*
- *Liquid Helium is needed for SQUID measurements to retain extremely low temperatures, which allows superconducting behaviors of the picking up coil*
- *Superconducting behavior of the picking up coil is needed to increase the sensitivity of the*

### E.2.2 Loading the sample

1. Click Sample -> Removal
2. Remove the sample holder, install the sample and make sure the sample is aligned properly before plugging back the sample holder
3. Press "Purge" to purge the airlock system in SQUID
4. Input sample description
5. Click Sequence, then depends on the sample being measured, click on the proper sequence
6. Center the sample position by clicking Center -> RSC
7. By trial and error, adjust the position and find the proper sample centering location
8. Input desired parameters for collecting data points
9. Click on Play to start SQUID measurement



## APPENDIX G. LABVIEW AND AUTOMATED DEPOSITION

### G.1. Programming an Automated Deposition

#### G.1.1. *To program a full deposition sequence*

We can express the deposition process into a pseudo-code format that consists several nested “For” loops and sequences as following:

```
for [number of overall deposition sequences, for analysis
purposes] (normally set to 1)
    wait [10 seconds]
    begin [remote microwave power interface]
    for [number of global cycles]
        for [number of local sequences for precursor]
            while [time for precursor exposure]
                Actuate channel to switch ON pneumatic valve
            end

            while [time for pump down]
                Actuate channel to switch OFF pneumatic valve
            end

            while [time for radical exposure]
                Actuate channel to switch ON radical source
            end

            while [time for pump down]
                Actuate channel to switch OFF radical source
            end

        end
    ... (repeat for each precursor )
    stop [remote microwave power interface]
end
```

#### G.1.2. *Programming One Single Local Deposition Cycle*

1. Inside the global cycle loop, create a “For” loop and insert a flat sequence
2. Connect a constant to the for loop, right click it, and left click on “change to control”
3. Create four blank frames in the flat sequence
4. In order to set a create waiting timer, create one control constant by creating a new constant and right clicking it, then left click on “change to control”. Create another constant and set it to 1000 (*note: the unit of time in the program is millisecond*).
5. Create a multiplication operation and connect the control constant and the “1000” constant into the input (left) side.
6. Create a “wait (ms)” and connect it to the output (right) side of the multiplication output.

7. Each frame is used to actuate the following process respectively:
  - a. Frame 1: Turn ON the pneumatic valve for a specific precursor, start precursor pulse
  - b. Frame 2: Turn OFF the pneumatic valve for a specific precursor, starting pump down process
  - c. Frame 3: Turn ON the microwave supply to start radical pulse
  - d. Frame 4: Turn OFF the microwave supply to start another pump down step
8. Depends on the process and precursor used, construct different local cycle loops if needed

## G.2. Programming for Data Acquisition Tool

### *G.2.1. Inserting Data Acquisition Module to Block Diagram Code for NI-USB 9481 Relay Module*

1. Inside the desired block inside block diagram, right click on empty space and click Express -> Output -> DAQ Assistant
2. Double click the DAQ Assistant block, expand General Signals -> Digital Signals -> Line Output to setup which switch the assistant is going to control
3. Find the corresponding device and add the first output, the device are named as following
  - a. Microwave Power (USB-9481): Radical source
  - b. PC1Thru4 (USB-9481): Pneumatic valves number 1-4
  - c. PC5Thru8 (USB-9481): Pneumatic valves number 5-8
  - d. Pneumatic Control (USB-9481): Pneumatic control panel
4. After choosing the desired control panel, click the first controller and press finish button
5. In the configuration tab, press the blue + button and add the rest of the controllers in (*note: the controllers will not follow its original sequence so please pay attention which corresponds to which*)
6. Click x to finish setting up DAQ Assistant

### *G.2.2. Actuating Relay Within Block Diagram Code*

1. Create a new numbered array by creating Array Constant
2. Create a new Boolean T/F module inside the Array Constant
3. Drag the connector from the numbered array in 1. To a data acquisition module in the block diagram code
4. For the desired channel, set T for turning it ON, or set F for turning it off. (*note: make sure to set the undesired channel F*)

### G.3. Running automated deposition

#### *G.3.1. Starting automated deposition*

1. After the instructions in B.1.6., input the desired experimental parameters onto automation control center. For example, number of total global cycles, number of local precursor cycles, exposure time for precursor or radical pulse, and pump down time (all in seconds).
2. Press start button (black triangle)

#### *G.3.2. Stopping an Automated Deposition*

1. If a deposition is still going on and has not reached the total number of global cycles, click the STOP button following the radical exposure step
2. Click on the top bar, Tools -> Measurement & Automation Explorer
3. Expand the Devices and Interfaces tab under My System
4. Find the NI-USB 9481 “Microwave Power” tab and right click -> left click on Test Panels
5. Click START and make sure all the switches are at the LOW configuration
6. Press STOP to resume the switches to its initial state
7. Close the Test Panels and close the Measurement & Automation Explorer
8. Press ON button of the microwave power source switch and ramp the power down to zero
9. Press OFF button of the microwave power source
10. Turn off the flow of oxygen gas by closing the upper valve, setting the mass-flow controller to zero, and then close the lower valve
11. Close A-1 manual valve to isolate the oxygen source and thus pump down the main chamber
12. Turn the pneumatic valves for all the precursors to the ON position in order prevent clogging of the precursor housing
13. Turn off all the temperature controllers

## BIBLIOGRAPHY

- (2000). "TEM: an introduction." III-Vs Review **13**(6): 36-40.
- Aimon, N. M., H. K. Choi, et al. (2014). "Templated Self-Assembly of Functional Oxide Nanocomposites." Advanced Materials: 3063–3067.
- Aimon, N. M., D. H. Kim, et al. (2012). "Deposition of epitaxial BiFeO<sub>3</sub>/CoFe<sub>2</sub>O<sub>4</sub> nanocomposites on (001) SrTiO<sub>3</sub> by combinatorial pulsed laser deposition." Applied Physics Letters **100**(9): 092901-092904.
- Aimon, N. M., D. H. Kim, et al. (2015). "Multiferroic behavior of templated BiFeO<sub>3</sub>-CoFe<sub>2</sub>O<sub>4</sub> self-assembled nanocomposites." ACS Applied Materials & Interfaces.
- Akbashev, A. R., G. Chen, et al. (2013). "A Facile Route for Producing Single-Crystalline Epitaxial Perovskite Oxide Thin Films." Nano Letters **14**(1): 44-49.
- Alekseevskii, N. E. (1992). "The Publications of L. V. Shubnikov." Soviet Physics Uspekhi **35**(10): 897.
- Alford, T. L., L. C. Feldman, et al. (2007). Fundamentals of nanoscale film analysis, Springer.
- Alzate, J. G., P. K. Amiri, et al. (2012). Voltage-induced switching of nanoscale magnetic tunnel junctions. Electron Devices Meeting (IEDM), 2012 IEEE International.
- Aoki, N., N. Fujimura, et al. (1997). "Formation of YMnO<sub>3</sub> films directly on Si substrate." Journal of Crystal Growth **174**(1-4): 796-800.
- Asokan, K., Y. S. Chen, et al. (2009). "Effect of Co, Ni, and Cu substitution on the electronic structure of hexagonal YMnO<sub>3</sub> studied by x-ray absorption spectroscopy." Applied Physics Letters **95**(13).
- Auth, C., C. Allen, et al. (2012). A 22nm high performance and low-power CMOS technology featuring fully-depleted tri-gate transistors, self-aligned contacts and high density MIM capacitors. VLSI Technology (VLSIT), 2012 Symposium on.
- Baibich, M. N., J. M. Broto, et al. (1988). "Giant Magnetoresistance of (001)Fe/(001)Cr Magnetic Superlattices." Physical Review Letters **61**(21): 2472.
- Baugh, C., J. Cullom, et al. (1982). "Fabrication and characterization of a crossbar random access memory." Magnetics, IEEE Transactions on **18**(6): 1782-1784.
- Bergum, K., H. Okamoto, et al. (2011). "Synthesis, structure and magnetic properties of nanocrystalline YMnO<sub>3</sub>." Dalton Transactions **40**(29): 7583-7589.

- Bez, R., E. Camerlenghi, et al. (2003). "Introduction to flash memory." Proceedings of the IEEE **91**(4): 489-502.
- Bibes, M. and A. Barthelemy (2008). "Multiferroics: Towards a magnetoelectric memory." Nat Mater **7**(6): 425-426.
- Binek, C., A. Hochstrat, et al. (2005). "Electrically controlled exchange bias for spintronic applications." Journal of Applied Physics **97**(10): 10C514-513.
- Borisov, P., A. Hochstrat, et al. (2005). "Magnetoelectric Switching of Exchange Bias." Physical Review Letters **94**(11): 117203.
- Bosak, A. A., A. A. Kamenev, et al. (2001). "Epitaxial phase stabilisation phenomena in rare earth manganites." Thin Solid Films **400**(1-2): 149-153.
- Bozorth, R. M., E. F. Tilden, et al. (1955). "Anisotropy and Magnetostriction of Some Ferrites." Physical Review **99**(6): 1788-1798.
- Burr, G. W., B. N. Kurdi, et al. (2008). "Overview of candidate device technologies for storage-class memory." IBM Journal of Research and Development **52**(4.5): 449-464.
- Cao, H., V. H. Schmidt, et al. (2004). "Elastic, piezoelectric, and dielectric properties of 0.58 Pb (Mg<sub>1/3</sub> Nb<sub>2/3</sub>) O<sub>3</sub>-0.42 PbTiO<sub>3</sub> single crystal." Journal of Applied Physics **96**(1): 549-554.
- Catalan, G. and J. F. Scott (2009). "Physics and Applications of Bismuth Ferrite." Advanced Materials **21**(24): 2463-2485.
- Cazayous, M., Y. Gallais, et al. (2008). "Possible observation of cycloidal electromagnons in BiFeO<sub>3</sub>." Physical Review Letters **101**(3): 037601.
- Chang, J. P., J. C. Arnold, et al. (1997). Kinetic study of low energy argon ion-enhanced plasma etching of polysilicon with atomic/molecular chlorine, AVS.
- Chen, W. R., F. C. Zhang, et al. (2005). "Re-entrant spin glass behavior in Mn-rich YMnO<sub>3</sub>." Applied Physics Letters **87**(4).
- Cheong, S.-W. and M. Mostovoy (2007). "Multiferroics: a magnetic twist for ferroelectricity." Nat Mater **6**(1): 13-20.
- Cheong, S. W. and M. Mostovoy (2007). "Multiferroics: a magnetic twist for ferroelectricity." Nature Materials **6**(1): 13-20.
- Cho, A. Y. and J. R. Arthur (1975). "Molecular beam epitaxy." Progress in Solid State Chemistry **10**(Part 3): 157-191.
- Cho, Y. J., Y.-S. Min, et al. (2003). "Atomic Layer Deposition (ALD) of Bismuth Titanium Oxide Thin Films Using Direct Liquid Injection (DLI) Method." Integrated Ferroelectrics: An International Journal **59**(1): 1483 - 1489.

- Choi, J. H., Y. Mao, et al. (2011). "Development of hafnium based high-k materials—A review." Materials Science and Engineering: R: Reports **72**(6): 97-136.
- Choi, J. H., F. Zhang, et al. (2013). "Tailoring the composition of lead zirconate titanate by atomic layer deposition." Journal of Vacuum Science & Technology B **31**(1): -.
- Chong, Y. T., E. M. Y. Yau, et al. (2010). "Direct Atomic Layer Deposition of Ternary Ferrites with Various Magnetic Properties." Chemistry of Materials **22**(24): 6506-6508.
- Chu, Y. H., L. W. Martin, et al. (2007). "Epitaxial Multiferroic BiFeO<sub>3</sub> Thin Films: Progress and Future Directions." Ferroelectrics **354**(1): 167-177.
- Chye, Y., T. Liu, et al. (2006). "Molecular beam epitaxy of YMnO<sub>3</sub> on c-plane GaN." Applied Physics Letters **88**(13).
- Clarke, J. S., C. George, et al. (2014). Process technology scaling in an increasingly interconnect dominated world. VLSI Technology (VLSI-Technology): Digest of Technical Papers, 2014 Symposium on.
- Cohen, R. E. (1992). "Origin of ferroelectricity in perovskite oxides." Nature **358**(6382): 136-138.
- Cohen, R. E. and H. Krakauer (1992). "Electronic structure studies of the differences in ferroelectric behavior of BaTiO<sub>3</sub> and PbTiO<sub>3</sub>." Ferroelectrics **136**(1): 65 - 83.
- Coll, M., J. M. Montero Moreno, et al. (2014). "Low Temperature Stabilization of Nanoscale Epitaxial Spinel Ferrite Thin Films by Atomic Layer Deposition." Advanced Functional Materials **24**(34): 5368-5374.
- Cross, E. (2004). "Materials science: Lead-free at last." Nature **432**(7013): 24-25.
- Curie, P. (1894). "Sur la symétrie dans les phénomènes physiques, symétrie d'un champ électrique et d'un champ magnétique." J. Phys. Theor. Appl. **3**(1).
- Daughton, J. M. (1992). "Magnetoresistive memory technology." Thin Solid Films **216**(1): 162-168.
- Debye, P. (1926). Z. Phys. **36**(300).
- Dho, J., C. W. Leung, et al. (2004). "Epitaxial and oriented YMnO<sub>3</sub> film growth by pulsed laser deposition." Journal of Crystal Growth **267**(3-4): 548-553.
- Dix, N., R. Muralidharan, et al. (2009). "Critical Limitations in the Fabrication of Biferroic BiFeO<sub>3</sub>–CoFe<sub>2</sub>O<sub>4</sub> Columnar Nanocomposites Due to Bismuth Loss." Chemistry of Materials **21**(7): 1375-1380.
- Dzyaloshinskii, I. E. (1957). "Thermodynamic theory of weak ferromagnetism in antiferromagnetic substances." Sov. Phys.—JETP **5**(1259).

- Dzyaloshinskii, I. E. (1960). "On the magnetoelectrical effects in antiferromagnetics." Sov. Phys.—JETP **10**(628).
- Dzyaloshinsky, I. (1958). "A THERMODYNAMIC THEORY OF WEAK FERROMAGNETISM OF ANTIFERROMAGNETICS." Journal of Physics and Chemistry of Solids **4**(4): 241-255.
- Eerenstein, W., N. D. Mathur, et al. (2006). "Multiferroic and magnetoelectric materials." Nature **442**(7104): 759-765.
- Eerenstein, W., M. Wiora, et al. (2007). "Giant sharp and persistent converse magnetoelectric effects in multiferroic epitaxial heterostructures." Nature Materials **6**(5): 348-351.
- Efremov, D. V., J. van den Brink, et al. (2004). "Bond- versus site-centred ordering and possible ferroelectricity in manganites." Nat Mater **3**(12): 853-856.
- Fennie, C. J. and K. M. Rabe (2005). "Ferroelectric transition in  $\text{YMnO}_3$  from first principles." Physical Review B **72**(10): 100103.
- Fiebig, M. (2005). "Revival of the magnetoelectric effect." Journal of Physics D: Applied Physics **38**(8): R123.
- Fiebig, M., D. Fröhlich, et al. (2002). "Probing of ferroelectric surface and bulk domains in  $\text{RMnO}_3$  ( $\text{R} = \text{Y}, \text{Ho}$ ) by second harmonic generation." Physical Review B **66**(14): 144102.
- Fiebig, M., T. Lottermoser, et al. (2002). "Observation of coupled magnetic and electric domains." Nature **419**(6909): 818-820.
- Fischer, P. and et al. (1980). "Temperature dependence of the crystal and magnetic structures of  $\text{BiFeO}_3$ ." Journal of Physics C: Solid State Physics **13**(10): 1931.
- Freitas, R. F. and W. W. Wilcke (2008). "Storage-class memory: the next storage system technology." IBM J. Res. Dev. **52**(4): 439-447.
- Fujimura, N., T. Ishida, et al. (1996). "Epitaxially grown  $\text{YMnO}_3$  film: New candidate for nonvolatile memory devices." Applied Physics Letters **69**(7): 1011-1013.
- Fujimura, N., N. Shigemitsu, et al. (2007). "Multiferroic behaviour of  $\text{YMnO}_3$  and  $\text{YbMnO}_3$  epitaxial films." Philosophical Magazine Letters **87**(3-4): 193-201.
- Gajek, M., M. Bibes, et al. (2007). "Tunnel junctions with multiferroic barriers." Nat Mater **6**(4): 296-302.
- Gao, F., X. Chen, et al. (2007). "Visible-Light Photocatalytic Properties of Weak Magnetic  $\text{BiFeO}_3$  Nanoparticles." Advanced Materials **19**(19): 2889-2892.
- Gao, X., B. J. Rodriguez, et al. (2010). "Microstructure and properties of well-ordered multiferroic  $\text{Pb}(\text{Zr}, \text{Ti})\text{O}_3/\text{CoFe}_2\text{O}_4$  nanocomposites." ACS Nano **4**(2): 1099-1107.

- Gibart, P., M. Robbins, et al. (1974). "Epitaxial growth of ferrite." Journal of Crystal Growth **24–25**(0): 166-171.
- Gilleo, M. A. (1957). "Crystallographic Studies Of Perovskite-Like Compounds. III. La ( $M_x$ ,  $M_{1-x}$ )O<sub>3</sub> With M= Co, Fe And Cr." Acta Crystallographica **10**(3): 161-166.
- Greer, J. (2007). Large-area commercial pulsed laser deposition. Pulsed Laser Deposition of Thin Films: Applications-Led Growth of Functional Materials. R. Eason, Wiley-Interscience: 281–304.
- Greer, J. A. and M. D. Tabat (1995). Large-area pulsed laser deposition: Techniques and applications, Denver, Colorado (USA), AVS.
- Han, T.-C., W.-L. Hsu, et al. (2011). "Grain size-dependent magnetic and electric properties in nanosized YMnO<sub>3</sub> multiferroic ceramics." Nanoscale research letters **6**(1): 1-8.
- Harjuoja, J., S. Väyrynen, et al. (2006). "Crystallization of bismuth titanate and bismuth silicate grown as thin films by atomic layer deposition." Journal of Crystal Growth **286**(2): 376-383.
- Hatanpaa, T., M. Vehkamäki, et al. (2010). "Study of bismuth alkoxides as possible precursors for ALD." Dalton Transactions **39**(13): 3219-3226.
- He, H., J. Ma, et al. (2009). "Enhanced magnetoelectric properties in Pb (Zr, Ti) O<sub>3</sub>-CoFe<sub>2</sub>O<sub>4</sub> layered thin films with LaNiO<sub>3</sub> as a buffer layer." Journal of Physics D: Applied Physics **42**(9): 095008.
- Heron, J. T., M. Trassin, et al. (2011). "Electric-Field-Induced Magnetization Reversal in a Ferromagnet-Multiferroic Heterostructure." Physical Review Letters **107**(21): 217202.
- Hidaka, H. (2009). Embedded Flash Memory. Embedded Memories for Nano-Scale VLSIs. K. Zhang, Springer US: 177-240.
- Hill, N. A. (2000). "Why Are There so Few Magnetic Ferroelectrics?" The Journal of Physical Chemistry B **104**(29): 6694-6709.
- Hoang, J. (2011). Sequential Radical Enhanced Atomic Layer Deposition of Nanostructured Yttrium Oxide Thin Films with Spatially Controlled Yttrium (III) and Erbium (III) Co-doping for Optical Applications. Ann Arbor, University of California, Los Angeles. **3515126**: 336.
- Hoang, J., R. N. Schwartz, et al. (2012). "The effects of energy transfer on the Er<sup>3+</sup> 1.54  $\mu$ m luminescence in nanostructured Y<sub>2</sub>O<sub>3</sub> thin films with heterogeneously distributed Yb<sup>3+</sup> and Er<sup>3+</sup> codopants." Journal of Applied Physics **112**(6): -.
- Hoang, J., R. N. Schwartz, et al. (2012). "Er<sup>3+</sup> interlayer energy migration as the limiting photoluminescence quenching factor in nanostructured Er<sup>3+</sup>:Y<sub>2</sub>O<sub>3</sub> thin films." Journal of Applied Physics **112**(2): -.



- Hoang, J., T. T. Van, et al. (2007). "Optical properties of  $\text{Y}_2\text{O}_3$  thin films doped with spatially controlled  $\text{Er}^{3+}$  by atomic layer deposition." Journal of Applied Physics **101**(12): 123116-123118.
- Hoffman, J., X. Pan, et al. (2010). "Ferroelectric Field Effect Transistors for Memory Applications." Advanced Materials **22**(26-27): 2957-2961.
- Horng, L., G. Chern, et al. (2004). "Magnetic anisotropic properties in  $\text{Fe}_3\text{O}_4$  and  $\text{CoFe}_2\text{O}_4$  ferrite epitaxy thin films." Journal of Magnetism and Magnetic Materials **270**(3): 389-396.
- Hsieh, C. C., T. H. Lin, et al. (2008). "Magnetic ordering anisotropy in epitaxial orthorhombic multiferroic  $\text{YMnO}_3$  films." Journal of Applied Physics **104**(10).
- Huang, Y. H., H. Fjellvag, et al. (2006). "Crystal and magnetic structure of the orthorhombic perovskite  $\text{YbMnO}_3$ ." Chemistry of Materials **18**(8): 2130-2134.
- Iliev, M. N., M. V. Abrashev, et al. (1998). "Raman spectroscopy of orthorhombic perovskitelike  $\text{YMnO}_3$  and  $\text{LaMnO}_3$ ." Physical Review B **57**(5): 2872-2877.
- Iliev, M. N., M. V. Abrashev, et al. (1998). "Raman spectroscopy of orthorhombic perovskitelike  $\text{YMnO}_3$  and  $\text{LaMnO}_3$ ." Physical Review B **57**(5): 2872-2877.
- Iliev, M. N., B. Lorenz, et al. (2005). "Structural, transport, magnetic properties and Raman spectroscopy of orthorhombic  $\text{Y}_{1-x}\text{Ca}_x\text{MnO}_3$  ( $0 \leq x \leq 0.5$ )." Journal of Physics-Condensed Matter **17**(21): 3333-3341.
- Imada, S., T. Kuraoka, et al. (2001). "Ferroelectricity of  $\text{YMnO}_3$  thin films on  $\text{Pt}(111)/\text{Al}_2\text{O}_3(0001)$  and  $\text{Pt}(111)/\text{Y}_2\text{O}_3(111)/\text{Si}(111)$  structures grown by molecular beam epitaxy." Japanese Journal Of Applied Physics Part 1-Regular Papers Short Notes & Review Papers **40**(2A): 666-671.
- Imada, S., S. Shouriki, et al. (1998). "Epitaxial growth of ferroelectric  $\text{YMnO}_3$  thin films on Si (111) substrates by molecular beam epitaxy." Japanese Journal of Applied Physics Part 1-Regular Papers Short Notes & Review Papers **37**(12A): 6497-6501.
- ITRS (2011). "Emerging Research Devices (ERD) " International Technology Roadmap for Semiconductors.
- Jalkanen, P., V. Tuboltsev, et al. (2014). "Magnetic Properties of Polycrystalline Bismuth Ferrite Thin Films Grown by Atomic Layer Deposition." The Journal of Physical Chemistry Letters: 4319-4323.
- Jang, H., S. Baek, et al. (2008). "Strain-induced polarization rotation in epitaxial (001)  $\text{BiFeO}_3$  thin films." Physical Review Letters **101**(10): 107602.
- Kadomtseva, A., Y. F. Popov, et al. (2006). "Phase transitions in multiferroic  $\text{BiFeO}_3$  crystals, thin-layers, and ceramics: enduring potential for a single phase, room-temperature magnetoelectric 'holy grail'." Phase Transitions **79**(12): 1019-1042.

- Kang, J.-S., S. Han, et al. (2005). "Photoemission and x-ray absorption of the electronic structure of multiferroic  $\text{RMnO}_3$  ( $R = \text{Y, Er}$ )." Physical Review B **71**(9): 092405.
- Kato, Y. and T. Takei (1933). "Permanent oxide magnet and its characteristics." Journal of the Institution of Electrical Engineers, Japan **53**(538): 408-412.
- Katsufuji, T., M. Masaki, et al. (2002). "Crystal structure and magnetic properties of hexagonal  $\text{RMnO}_3$  ( $R = \text{Y, Lu, and Sc}$ ) and the effect of doping." Physical Review B **66**(13): 134434.
- Katsufuji, T., M. Masaki, et al. (2002). "Crystal structure and magnetic properties of hexagonal  $\text{RMnO}_3$  ( $R = \text{Y, Lu, and Sc}$ ) and the effect of doping." Physical Review B **66**(13): 134434.
- Kelly, P. J. and R. D. Arnell (2000). "Magnetron sputtering: a review of recent developments and applications." Vacuum **56**(3): 159-172.
- Khalili, P. and K. L. Wang (2014). Electric Field-Induced Switching for Magnetic Memory Devices. Metallic Spintronic Devices, CRC Press: 197-234.
- Khomskii, D. (2001). Magnetism and ferroelectricity; why do they so seldom coexist? APS Meeting Abstracts.
- Khomskii, D. (2006). "Multiferroics: Different ways to combine magnetism and ferroelectricity." Journal of Magnetism and Magnetic Materials **306**(1): 1-8.
- Khomskii, D. (2009). "Classifying multiferroics: Mechanisms and effects." Physics **2**(20).
- Kim, D., D. Killingsworth, et al. (2006). "Ferroelectric properties of  $\text{YMnO}_3$  films deposited by metalorganic chemical vapor deposition on  $\text{Pt/Ti/SiO}_2/\text{Si}$  substrates." Materials Letters **60**(3): 295-297.
- Kim, D. H., N. M. Aimon, et al. (2014). "Integration of Self-Assembled Epitaxial  $\text{BiFeO}_3$ - $\text{CoFe}_2\text{O}_4$  Multiferroic Nanocomposites on Silicon Substrates." Advanced Functional Materials: n/a-n/a.
- Kim, H. and S. M. Rossnagel (2002). "Growth kinetics and initial stage growth during plasma-enhanced Ti atomic layer deposition." Journal of Vacuum Science & Technology A: Vacuum, Surfaces, and Films **20**(3): 802-808.
- Kim, J.-H., S. Khartsev, et al. (2003). "Epitaxial colossal magnetoresistive  $\text{La}_{0.67}(\text{Sr, Ca})_{0.33}\text{MnO}_3$  films on Si." Applied Physics Letters **82**(24): 4295-4297.
- Kimura, T., S. Kawamoto, et al. (2003). "Magnetocapacitance effect in multiferroic  $\text{BiMnO}_3$ ." Physical Review B **67**(18): 180401.
- Kiselev, S., R. Ozerov, et al. (1963). Detection of magnetic order in ferroelectric  $\text{BiFeO}_3$  by neutron diffraction. Soviet Physics Doklady.

- Kitahata, H., K. Tadanaga, et al. (2000). "Preparation and ferroelectric properties of  $\text{YMnO}_3$  thin films with c-axis preferred orientation by the sol-gel method." Journal Of Sol-Gel Science And Technology **19**(1-3): 589-593.
- Klepper, K. B., O. Nilsen, et al. (2007). "Growth of thin films of  $\text{Co}_3\text{O}_4$  by atomic layer deposition." Thin Solid Films **515**(20–21): 7772-7781.
- Kohlstedt, H., Y. Mustafa, et al. (2005). "Current status and challenges of ferroelectric memory devices." Microelectronic Engineering **80**: 296-304.
- Kryder, M. H. and K. Chang Soo (2009). "After Hard Drives-What Comes Next?" Magnetics, IEEE Transactions on **45**(10): 3406-3413.
- Kubel, F. and H. Schmid (1990). "Structure of a ferroelectric and ferroelastic monodomain crystal of the perovskite  $\text{BiFeO}_3$ ." Acta Crystallographica Section B **46**(6): 698-702.
- Lai, S. K. (2008). "Flash memories: Successes and challenges." IBM Journal of Research and Development **52**(4.5): 529-535.
- Laitner, J. A. (2010). "Semiconductors and Information Technologies." Journal of Industrial Ecology **14**(5): 692-695.
- Landau, L. D. L., E.M. (1960). "Electrodynamics of Continuous Media." (Oxford: Pergamon) (Translation of Russian Edition 1958).
- Lao, S. X., R. M. Martin, et al. (2005). "Plasma enhanced atomic layer deposition of  $\text{HfO}_2$  and  $\text{ZrO}_2$  high-k thin films." Journal of Vacuum Science & Technology A: Vacuum, Surfaces, and Films **23**(3): 488-496.
- Laukhin, V., V. Skumryev, et al. (2006). "Electric-Field Control of Exchange Bias in Multiferroic Epitaxial Heterostructures." Physical Review Letters **97**(22): 227201.
- Lawes, G. and G. Srinivasan (2011). "Introduction to magnetoelectric coupling and multiferroic films." Journal of Physics D: Applied Physics **44**(24): 243001.
- Lebeugle, D., D. Colson, et al. (2008). "Electric-Field-Induced Spin Flop in  $\text{BiFeO}_3$  Single Crystals at Room Temperature." Physical Review Letters **100**(22): 227602.
- Lee, J. H., Y. J. Cho, et al. (2002). "Plasma enhanced atomic layer deposition of  $\text{SrTiO}_3$  thin films with  $\text{Sr}(\text{tmhd})_2$  and  $\text{Ti}(\text{i-OPr})_4$ ." Journal of Vacuum Science & Technology A: Vacuum, Surfaces, and Films **20**(5): 1828-1830.
- Lee, J. H., P. Murugavel, et al. (2006). "Epitaxial Stabilization of a New Multiferroic Hexagonal Phase of  $\text{TbMnO}_3$  Thin Films." Advanced Materials **18**(23): 3125-3129.
- Lee, Y. M., J. Hayakawa, et al. (2007). "Effect of electrode composition on the tunnel magnetoresistance of pseudo-spin-valve magnetic tunnel junction with a  $\text{MgO}$  tunnel barrier." Applied Physics Letters **90**(21): 212507-212503.

- Leskelä, M. and et al. (1993). "Chemical vapour deposition of high-T<sub>c</sub> superconducting thin films." Superconductor Science and Technology **6**(9): 627.
- Leskelä, M. and M. Ritala (2002). "Atomic layer deposition (ALD): from precursors to thin film structures." Thin Solid Films **409**(1): 138-146.
- Leskelä, M. and M. Ritala (2003). "Atomic Layer Deposition Chemistry: Recent Developments and Future Challenges." Angewandte Chemie International Edition **42**(45): 5548-5554.
- Levanyuk, A. and D. G. e. Sannikov (1974). "Improper ferroelectrics." Physics-Uspekhi **17**(2): 199-214.
- Li, S. Z., Z. B. Yan, et al. (2009). "Preparation of epitaxial orthorhombic YMnO<sub>3</sub> thin films and the current-voltage rectifying effect." Applied Physics A-Materials Science & Processing **94**(4): 975-980.
- Li, Z., Y. Wang, et al. (2009). "Evidence for stress-mediated magnetoelectric coupling in multiferroic bilayer films from magnetic-field-dependent Raman scattering." Physical Review B **79**(18): 180406.
- Lide, D. R. (2010). CRC handbook of chemistry and physics, Taylor & Francis Group.
- Lie, M., K. Barnholt Klepper, et al. (2008). "Growth of iron cobalt oxides by atomic layer deposition." Dalton Transactions **0**(2): 253-259.
- Lie, M., H. Fjellvåg, et al. (2005). "Growth of Fe<sub>2</sub>O<sub>3</sub> thin films by atomic layer deposition." Thin Solid Films **488**(1-2): 74-81.
- Liu, M., O. Obi, et al. (2009). "Giant Electric Field Tuning of Magnetic Properties in Multiferroic Ferrite/Ferroelectric Heterostructures." Advanced Functional Materials **19**(11): 1826-1831.
- Liu, X.-M., S.-Y. Fu, et al. (2005). "Synthesis and magnetic characterization of novel CoFe<sub>2</sub>O<sub>4</sub>-BiFeO<sub>3</sub> nanocomposites." Materials Science and Engineering: B **121**(3): 255-260.
- Liu, Y.-T., C.-S. Ku, et al. (2013). "Ultrathin Oriented BiFeO<sub>3</sub> Films from Deposition of Atomic Layers with Greatly Improved Leakage and Ferroelectric Properties." ACS Applied Materials & Interfaces **6**(1): 443-449.
- Lorenz, B., Y. Q. Wang, et al. (2004). "Large magnetodielectric effects in orthorhombic HoMnO<sub>3</sub> and YMnO<sub>3</sub>." Physical Review B **70**(21).
- Lou, J., R. Insignares, et al. (2007). "Soft magnetism, magnetostriction, and microwave properties of FeGaB thin films." Applied Physics Letters **91**(18): 182504-182504-182503.
- Maeda, K., T. Yshimura, et al. (2006). Magnetic and Ferroelectric Properties of YMnO<sub>3</sub> Epitaxial Thin Films. MRS Proceedings, Cambridge Univ Press.

- Marchack, N. and J. P. Chang (2012). "Chemical Processing of Materials on Silicon: More Functionality, Smaller Features, and Larger Wafers." Annual Review of Chemical and Biomolecular Engineering **3**(1): 235-262.
- Marti, X., V. Skumryev, et al. (2009). "Ferromagnetism in epitaxial orthorhombic YMnO<sub>3</sub> thin films." Journal Of Magnetism And Magnetic Materials **321**(11): 1719-1722.
- Martin, L. W., Y. H. Chu, et al. (2010). "Advances in the growth and characterization of magnetic, ferroelectric, and multiferroic oxide thin films." Materials Science and Engineering: R: Reports **68**(4-6): 89-133.
- Masuoka, F., M. Asano, et al. (1984). A new flash E<sup>2</sup> PROM cell using triple polysilicon technology. Electron Devices Meeting, 1984 International.
- Mazumder, R., P. S. Devi, et al. (2007). "Ferromagnetism in nanoscale BiFeO<sub>3</sub>." Applied Physics Letters **91**(6): 062510-062510-062513.
- McKee, R. A., F. J. Walker, et al. (1998). "Crystalline Oxides on Silicon: The First Five Monolayers." Physical Review Letters **81**(14): 3014-3017.
- Meiklejohn, W. H. (1962). "Exchange Anisotropy---A Review." Journal of Applied Physics **33**(3): 1328-1335.
- Meiklejohn, W. H. and C. P. Bean (1956). "New Magnetic Anisotropy." Physical Review **102**(5): 1413-1414.
- Meiklejohn, W. H. and C. P. Bean (1957). "New Magnetic Anisotropy." Physical Review **105**(3): 904-913.
- Mills, P. and J. L. Sullivan (1983). "A study of the core level electrons in iron and its three oxides by means of X-ray photoelectron spectroscopy." Journal of Physics D: Applied Physics **16**(5): 723.
- Mistry, K., C. Allen, et al. (2007). A 45nm Logic Technology with High-k+Metal Gate Transistors, Strained Silicon, 9 Cu Interconnect Layers, 193nm Dry Patterning, and 100% Pb-free Packaging. Electron Devices Meeting, 2007. IEDM 2007. IEEE International.
- Miura, K., T. Kawahara, et al. (2007). A novel SPRAM (SPin-transfer torque RAM) with a synthetic ferrimagnetic free layer for higher immunity to read disturbance and reducing write-current dispersion. VLSI Technology, 2007 IEEE Symposium.
- Molegraaf, H. J. A., J. Hoffman, et al. (2009). "Magnetoelectric Effects in Complex Oxides with Competing Ground States." Advanced Materials **21**(34): 3470-3474.
- Moodera, J. S., L. R. Kinder, et al. (1995). "Large Magnetoresistance at Room Temperature in Ferromagnetic Thin Film Tunnel Junctions." Physical Review Letters **74**(16): 3273.

- Moore, G. E. (1965). "Cramming More Components Onto Integrated Circuits." Electronics **38**(8): 114-117.
- Moriya, T. (1960). "ANISOTROPIC SUPEREXCHANGE INTERACTION AND WEAK FERROMAGNETISM." Physical Review **120**(1): 91-98.
- Mostovoy, M. (2006). "Ferroelectricity in Spiral Magnets." Physical Review Letters **96**(6): 067601.
- Munoz, A., J. A. Alonso, et al. (2002). "The magnetic structure of  $\text{YMnO}_3$  perovskite revisited." Journal of Physics-Condensed Matter **14**(12): 3285-3294.
- Munoz, A., J. A. Alonso, et al. (2000). "Magnetic structure of hexagonal  $\text{RMnO}_3$  ( $\text{R} = \text{Y}, \text{Sc}$ ): Thermal evolution from neutron powder diffraction data." Physical Review B **62**(14): 9498-9510.
- Murugavel, P., P. Padhan, et al. (2004). "Enhanced magnetoresistance in ferromagnetic  $\text{Pr}_{0.85}\text{Ca}_{0.15}\text{MnO}_3$ /ferroelectric  $\text{Ba}_{0.6}\text{Sr}_{0.4}\text{TiO}_3$  superlattice films." Applied Physics Letters **85**(21): 4992-4994.
- Nakamura, M., Y. Tokunaga, et al. (2011). "Multiferroicity in an orthorhombic  $\text{YMnO}_3$  single-crystal film." Applied Physics Letters **98**(8): -.
- Nakamura, M., Y. Tokunaga, et al. (2011). "Multiferroicity in an orthorhombic  $\text{YMnO}_3$  single-crystal film." Applied Physics Letters **98**(8).
- Nan, C.-W. (1994). "Magnetoelectric effect in composites of piezoelectric and piezomagnetic phases." Physical Review B **50**(9): 6082.
- Nan, C.-W., M. I. Bichurin, et al. (2008). "Multiferroic magnetoelectric composites: Historical perspective, status, and future directions." Journal of Applied Physics **103**(3): 031101-031135.
- Nan, C.-W., G. Liu, et al. (2005). "Magnetic-field-induced electric polarization in multiferroic nanostructures." Physical Review Letters **94**(19): 197203.
- Nan, C. W., M. I. Bichurin, et al. (2008). "Multiferroic magnetoelectric composites: Historical perspective, status, and future directions." Journal Of Applied Physics **103**(3).
- Nan, C. W., M. Li, et al. (2001). "Possible giant magnetoelectric effect of ferromagnetic rare-earth-iron-alloys-filled ferroelectric polymers." Applied Physics Letters **78**(17): 2527-2529.
- Nan, C. W., M. Li, et al. (2001). "Calculations of giant magnetoelectric effects in ferroic composites of rare-earth-iron alloys and ferroelectric polymers." Physical Review B **63**(14): 144415.

- Newnham, R. E. (2004). Properties of Materials: Anisotropy, Symmetry, Structure: Anisotropy, Symmetry, Structure, OUP Oxford.
- Newville, M. (2004). Fundamentals of XAFS. Chicago.
- Nguyen, M. D., H. Nazeer, et al. (2010). "Characterization of epitaxial Pb (Zr, Ti) O<sub>3</sub> thin films deposited by pulsed laser deposition on silicon cantilevers." Journal of Micromechanics and Microengineering **20**(8): 085022.
- Nikonov, D. E. and I. A. Young (2012). Uniform methodology for benchmarking beyond-CMOS logic devices. Electron Devices Meeting (IEDM), 2012 IEEE International, IEEE.
- Nogués, J., J. Sort, et al. (2005). "Exchange bias in nanostructures." Physics Reports **422**(3): 65-117.
- O'Hanlon, J. F. (2003). A user's guide to vacuum technology, Wiley-Interscience.
- Oh, Y. S., S. Crane, et al. (2010). "Quantitative determination of anisotropic magnetoelectric coupling in BiFeO<sub>3</sub>-CoFe<sub>2</sub>O<sub>4</sub> nanostructures." Applied Physics Letters **97**(5): 052902.
- Ortega, N., A. Kumar, et al. (2008). "Impedance spectroscopy of multiferroic PbZr<sub>x</sub>Ti<sub>1-x</sub>O<sub>3</sub>/CoFe<sub>2</sub>O<sub>4</sub> layered thin films." Physical Review B **77**(1): 014111.
- Park, J., S. Lee, et al. (2010). "Doping dependence of spin-lattice coupling and two-dimensional ordering in multiferroic hexagonal Y<sub>1-x</sub>Lu<sub>x</sub>MnO<sub>3</sub> (0 ≤ x ≤ 1)." Physical Review B **82**(5).
- Park, J., J. G. Park, et al. (2003). "Magnetic ordering and spin-liquid state of YMnO<sub>3</sub>." Physical Review B **68**(10): 104426.
- Park, K.-I., S. Xu, et al. (2010). "Piezoelectric BaTiO<sub>3</sub> thin film nanogenerator on plastic substrates." Nano Letters **10**(12): 4939-4943.
- Parkin, S. S. P., M. Hayashi, et al. (2008). "Magnetic Domain-Wall Racetrack Memory." Science **320**(5873): 190-194.
- Petrov, V., G. Srinivasan, et al. (2007). "Theory of magnetoelectric effects in ferrite piezoelectric nanocomposites." Physical Review B **75**(22): 224407.
- Pockels, F. (1894). "On the effect of an electrostatic field on the optical behaviour of piezoelectric crystals." Abh. Gott. **39**(1).
- Pohm, A. V., J. S. T. Huang, et al. (1988). "The design of a one megabit non-volatile M-R memory chip using 1.5 × 5 μm cells." Magnetics, IEEE Transactions on **24**(6): 3117-3119.
- Posadas, A., J.-B. Yau, et al. (2005). "Epitaxial growth of multiferroic YMnO<sub>3</sub> on GaN." Applied Physics Letters **87**(17): 171915-171915-171913.

- Powell, C. J. and A. Jablonski (2000). "Evaluation of electron inelastic mean free paths for selected elements and compounds†." Surface and Interface Analysis **29**(2): 108-114.
- Prejbeanu, I. L., W. Kula, et al. (2004). "Thermally assisted switching in exchange-biased storage layer magnetic tunnel junctions." Magnetics, IEEE Transactions on **40**(4): 2625-2627.
- Profijt, H. B., S. E. Potts, et al. (2011). "Plasma-Assisted Atomic Layer Deposition: Basics, Opportunities, and Challenges." Journal of Vacuum Science & Technology A: Vacuum, Surfaces, and Films **29**(5): 050801-050826.
- Quickel, T. E., V. H. Le, et al. (2010). "On the Correlation between Nanoscale Structure and Magnetic Properties in Ordered Mesoporous Cobalt Ferrite ( $\text{CoFe}_2\text{O}_4$ ) Thin Films." Nano Letters **10**(8): 2982-2988.
- Ramesh, R. and N. A. Spaldin (2007). "Multiferroics: progress and prospects in thin films." Nat Mater **6**(1): 21-29.
- Richter, H. J. (2009). "Density limits imposed by the microstructure of magnetic recording media." Journal of Magnetism and Magnetic Materials **321**(6): 467-476.
- Rigato, F., J. Geshev, et al. (2009). "The magnetization of epitaxial nanometric  $\text{CoFe}_2\text{O}_4$  (001) layers." Journal of Applied Physics **106**(11): 113924.
- Rondinelli, J. M., M. Stengel, et al. (2007). "Carrier-mediated magnetoelectricity in complex oxide heterostructures." Nature Nanotechnology **3**(1): 46-50.
- Rooth, M., A. Johansson, et al. (2008). "Atomic layer deposition of iron oxide thin films and nanotubes using ferrocene and oxygen as precursors." Chemical Vapor Deposition **14**(3-4): 67-70.
- Ryu, H., P. Murugavel, et al. (2006). "Magnetoelectric effects of nanoparticulate  $\text{Pb}(\text{Zr}_{0.52}\text{Ti}_{0.48})\text{O}_3$ -- $\text{NiFe}_2\text{O}_4$  composite films." Applied Physics Letters **89**(10): 102907-102903.
- Ryu, M., H. Kim, et al. (2011). Impact of flash memory on video-on-demand storage: analysis of tradeoffs. Proceedings of the second annual ACM conference on Multimedia systems. San Jose, CA, USA, ACM: 175-186.
- Ryu, S., J. H. Park, et al. (2007). "Magnetoelectric coupling of [001]-oriented  $\text{Pb}(\text{Zr}_{0.4}\text{Ti}_{0.6})\text{O}_3$ -- $\text{Ni}_{0.8}\text{Zn}_{0.2}\text{Fe}_2\text{O}_4$  multilayered thin films." Applied Physics Letters **91**(14): 142910-142913.
- Sanchez, M. C., G. Subias, et al. (2003). "Cooperative Jahn-Teller phase transition in  $\text{LaMnO}_3$  studied by x-ray absorption spectroscopy." Physical Review Letters **90**(4).
- Sato, T., S.-H. Lee, et al. (2003). "Unconventional spin fluctuations in the hexagonal antiferromagnet  $\text{YMnO}_3$ ." Physical Review B **68**(1): 014432.



- Schlom, D. G. and J. H. Haeni (2002). "A Thermodynamic Approach to Selecting Alternative Gate Dielectrics." MRS Bulletin **27**(03): 198-204.
- Schmid, H. (1994). "Multi-ferroic magnetoelectrics." Ferroelectrics **162**(1): 317 - 338.
- Schwarzkopf, J. and R. Fornari (2006). "Epitaxial growth of ferroelectric oxide films." Progress in Crystal Growth and Characterization of Materials **52**(3): 159-212.
- Schwee, L. J., P. E. Hunter, et al. (1982). "The concept and initial studies of a crossbar random access memory (CRAM)." Journal of Applied Physics **53**(3): 2762-2764.
- Scintag, I. (1999).
- Sergienko, I. A., C. Scedilen, et al. (2006). "Ferroelectricity in the Magnetic E-Phase of Orthorhombic Perovskites." Physical Review Letters **97**(22): 227204.
- Seshadri, R. and N. A. Hill (2001). "Visualizing the role of Bi 6s "lone pairs" in the off-center distortion in ferromagnetic BiMnO<sub>3</sub>." Chemistry of Materials **13**(9): 2892-2899.
- Setter, N., D. Damjanovic, et al. (2006). "Ferroelectric thin films: Review of materials, properties, and applications." Journal of Applied Physics **100**(5): 051606-051646.
- Sheikholeslami, A. and P. G. Gulak (2000). "A survey of circuit innovations in ferroelectric random-access memories." Proceedings of the IEEE **88**(5): 667-689.
- Shen, Y. D., Y. W. Li, et al. (2012). "Growth of Bi<sub>2</sub>O<sub>3</sub> Ultrathin Films by Atomic Layer Deposition." The Journal of Physical Chemistry C **116**(5): 3449-3456.
- Sim, C. H., A. Z. Z. Pan, et al. (2008). "Thickness and coupling effects in bilayered multiferroic CoFe<sub>2</sub>O<sub>4</sub>/Pb(Zr<sub>0.52</sub>Ti<sub>0.48</sub>)O<sub>3</sub> thin films." Journal of Applied Physics **103**(12): 124109-124107.
- Singh, A. K., S. Patnaik, et al. (2010). "Dominance of magnetoelastic coupling in multiferroic hexagonal YMnO<sub>3</sub>." Physical Review B **81**(18).
- Singh, A. K., M. Snure, et al. (2009). "Effect of epitaxial strain on the magneto-electric coupling of YMnO<sub>3</sub> thin films." Journal Of Applied Physics **106**(1).
- Slaughter, J. M. (2009). "Materials for Magnetoresistive Random Access Memory." Annual Review of Materials Research **39**(1): 277-296.
- Smolenskii, G., V. Isupov, et al. (1961). "New Ferroelectrics of Complex Composition." Soviet Physics-Solid State **2**(11): 2651-2654.
- Spaldin, N. A. (2003). Magnetic materials: fundamentals and device applications, Cambridge University Press.
- Spaldin, N. A. and M. Fiebig (2005). "The Renaissance of Magnetoelectric Multiferroics." Science **309**(5733): 391-392.

- Srinivasan, G., E. T. Rasmussen, et al. (2002). "Magnetoelectric effects in bilayers and multilayers of magnetostrictive and piezoelectric perovskite oxides." Physical Review B **65**(13): 134402.
- Stern, E. A. (1988). Theory of EXAFS. X-ray Absorption: Principles, Applications, and Techniques of EXAFS, SEXAFS, and XANES. D. C. Koningsberger and R. Prins, Wiley.
- Stoner, E. C. (1933). "Atomic moments in ferromagnetic metals and alloys with nonferromagnetic elements." Philos. Mag. **15**(1080).
- Strem Chemicals, I. (2005). Material Safety Data Sheet (MSDS).
- Suzuki, Y., G. Hu, et al. (1999). "Magnetic anisotropy of epitaxial cobalt ferrite thin films." Journal of Magnetism and Magnetic Materials **191**(1–2): 1-8.
- T. Van, T., J. Hoang, et al. (2006). "Nanostructure and temperature-dependent photoluminescence of Er-doped  $\text{Y}_2\text{O}_3$  thin films for micro-optoelectronic integrated circuits." Journal of Applied Physics **100**(7): 073512-073517.
- Tachibana, M., J. Yamazaki, et al. (2005). "Heat capacity and critical behavior of hexagonal  $\text{YMnO}_3$ ." Physical Review B **72**(6): 064434.
- Takashima, D. (2010). Overview and Scaling Prospect of Ferroelectric Memories. CMOS Processors and Memories. K. Iniewski, Springer Netherlands. **0**: 361-380.
- Tan, B. J., K. J. Klabunde, et al. (1990). "X-ray photoelectron spectroscopy studies of solvated metal atom dispersed catalysts. Monometallic iron and bimetallic iron-cobalt particles on alumina." Chemistry of Materials **2**(2): 186-191.
- Tehrani, S. (2010). "Status and Prospect for MRAM Technology." Everspin Technologies.
- Tehrani, S., E. Chen, et al. (1999). "High density submicron magnetoresistive random access memory (invited)." Journal of Applied Physics **85**(8): 5822-5827.
- Tehrani, S., E. Chen, et al. (1996). High density nonvolatile magnetoresistive RAM. Electron Devices Meeting, 1996. IEDM '96., International.
- Terzzoli, M., S. Duhalde, et al. (2004). "High perpendicular coercive field of  $\text{CoFe}_2\text{O}_4$  thin films deposited by PLD." Journal of alloys and compounds **369**(1): 209-212.
- Thiele, C., K. Dörr, et al. (2007). "Influence of strain on the magnetization and magnetoelectric effect in  $\text{La}_{0.7}\text{A}_{0.3}\text{MnO}_3/\text{PMN-PT}(001)$  ( $\text{A}=\text{Sr}, \text{Ca}$ )." Physical Review B **75**(5): 054408.
- Thomas, G. and M. J. Goringe (1979). "Transmission electron microscopy of materials."
- Thomas, R., et al., (2010). "Multiferroic thin-film integration onto semiconductor devices." Journal of Physics: Condensed Matter **22**(42): 423201.

- Thompson, D. A. and J. S. Best (2000). "The future of magnetic data storage technology." IBM Journal of Research and Development **44**(3): 311-322.
- Tokura, Y. (2006). "Multiferroics as Quantum Electromagnets." Science **312**(5779): 1481-1482.
- Tomuta, D. G., S. Ramakrishnan, et al. (2001). "The magnetic susceptibility, specific heat and dielectric constant of hexagonal  $\text{YMnO}_3$ ,  $\text{LuMnO}_3$  and  $\text{ScMnO}_3$ ." Journal of Physics-Condensed Matter **13**(20): 4543-4552.
- Trinquier, G. and R. Hoffmann (1984). "Lead monoxide. Electronic structure and bonding." The Journal of Physical Chemistry **88**(26): 6696-6711.
- Uchida, K. and A. Ayame (1996). "Dynamic XPS measurements on bismuth molybdate surfaces." Surface Science **357–358**(0): 170-175.
- Uusi-Esko, K. and M. Karppinen (2011). "Extensive Series of Hexagonal and Orthorhombic  $\text{RMnO}_3$  (R = Y, La, Sm, Tb, Yb, Lu) Thin Films by Atomic Layer Deposition." Chemistry Of Materials **23**(7): 1835-1840.
- Uusi-Esko, K., J. Malm, et al. (2009). "Atomic Layer Deposition of Hexagonal and Orthorhombic  $\text{YMnO}_3$  Thin Films." Chemistry of Materials **21**(23): 5691-5694.
- Van Aken, B. B., T. T. M. Palstra, et al. (2004). "The origin of ferroelectricity in magnetoelectric  $\text{YMnO}_3$ ." Nature Materials **3**(3): 164-170.
- Van, T. T. and J. P. Chang (2005). "Radical-enhanced atomic layer deposition of  $\text{Y}_2\text{O}_3$  via a  $\beta$ -diketonate precursor and O radicals." Surface Science **596**(1-3): 1-11.
- Van, T. T. and J. P. Chang (2005). "Surface reaction kinetics of metal  $\beta$ -diketonate precursors with O radicals in radical-enhanced atomic layer deposition of metal oxides." Applied Surface Science **246**(1-3): 250-261.
- Van, T. T. and G. Peterson (1998). Guide to XAFS measurements at SSRL. Stanford, Stanford Synchrotron Radiation Laboratory.
- Vaz, C., Y. Segal, et al. (2010). "Temperature dependence of the magnetoelectric effect in  $\text{Pb}(\text{Zr}_{0.2}\text{Ti}_{0.8})\text{O}_3/\text{La}_{0.8}\text{Sr}_{0.2}\text{MnO}_3$  multiferroic heterostructures." Applied Physics Letters **97**(4): 042506-042506-042503.
- Vaz, C. A. F., J. Hoffman, et al. (2010). "Magnetoelectric Coupling Effects in Multiferroic Complex Oxide Composite Structures." Advanced Materials **22**(26-27): 2900-2918.
- Vehkamäki, M., T. Hatanpää, et al. (1999). "Growth of  $\text{SrTiO}_3$  and  $\text{BaTiO}_3$  Thin Films by Atomic Layer Deposition." Electrochemical and Solid-State Letters **2**(10): 504-506.
- Vehkamäki, M., T. Hatanpää, et al. (2006). "Atomic Layer Deposition of Ferroelectric Bismuth Titanate  $\text{Bi}_4\text{Ti}_3\text{O}_{12}$  Thin Films." Chemistry of Materials **18**(16): 3883-3888.

- Vernon-Parry, K. D. (2000). "Scanning electron microscopy: an introduction." III-Vs Review **13**(4): 40-44.
- Wagner, C. D. and G. E. Muilenberg (1979). Handbook of x-ray photoelectron spectroscopy: a reference book of standard data for use in x-ray photoelectron spectroscopy, Perkin-Elmer Corp., Physical Electronics Division.
- Wan, J.-g., H. Zhang, et al. (2006). "Magnetoelectric  $\text{CoFe}_2\text{O}_4$ -lead zirconate titanate thick films prepared by a polyvinylpyrrolidone-assisted sol-gel method." Applied Physics Letters **89**(12): 122914-122914-122913.
- Wan, J. G., X. W. Wang, et al. (2005). "Magnetoelectric  $\text{CoFe}_2\text{O}_4$ - $\text{Pb}(\text{Zr,Ti})\text{O}_3$  composite thin films derived by a sol-gel process." Applied Physics Letters **86**(12): 122501-122503.
- Wang, J., J. B. Neaton, et al. (2003). "Epitaxial  $\text{BiFeO}_3$  Multiferroic Thin Film Heterostructures." Science **299**(5613): 1719-1722.
- Wang, K. F., J. M. Liu, et al. (2009). "Multiferroicity: the coupling between magnetic and polarization orders." Advances in Physics **58**(4): 321-448.
- Wang, K. L., J. G. Alzate, et al. (2013). "Low-power non-volatile spintronic memory: STT-RAM and beyond." Journal of Physics D: Applied Physics **46**(7): 074003.
- Wang, Y., J. Hu, et al. (2010). "Multiferroic magnetoelectric composite nanostructures." NPG Asia Materials **2**(2): 61-68.
- Wang, Z., Y. Zhang, et al. (2014). "Magnetoelectric Assisted  $180^\circ$  Magnetization Switching for Electric Field Addressable Writing in Magnetoresistive Random-Access Memory." ACS Nano **8**(8): 7793-7800.
- Watson, G., S. Parker, et al. (1999). "Ab initio calculation of the origin of the distortion of  $\alpha$ - $\text{PbO}$ ." Physical Review B **59**(13): 8481.
- Webb, C., S. Weng, et al. (1987). "Growth of high  $T_c$  superconducting thin films using molecular beam epitaxy techniques." Applied Physics Letters **51**(15): 1191-1193.
- Weiss, P. (1907). J. Phys. **6**(661).
- Wilk, G. D., M. Verghese, et al. (2013). "(Invited) Current Status of High-k and Metal Gates in CMOS." ECS Transactions **50**(4): 207-210.
- Willmott, P. R. and J. R. Huber (2000). "Pulsed laser vaporization and deposition." Reviews of Modern Physics **72**(1): 315.
- Wood, R. (2000). "The feasibility of magnetic recording at 1 Terabit per square inch." Magnetics, IEEE Transactions on **36**(1): 36-42.

- Wood, R. (2009). "Future hard disk drive systems." Journal of Magnetism and Magnetic Materials **321**(6): 555-561.
- Wu, H., T. Burnus, et al. (2009). "Ising Magnetism and Ferroelectricity in  $\text{Ca}_3\text{CoMnO}_6$ ." Physical Review Letters **102**(2): 026404.
- Wu, J. and J. Wang (2009). "Multiferroic behavior and impedance spectroscopy of bilayered  $\text{BiFeO}_3/\text{CoFe}_2\text{O}_4$  thin films." Journal of Applied Physics **105**(12): 124107.
- Wu, S. M., S. A. Cybart, et al. (2010). "Reversible electric control of exchange bias in a multiferroic field-effect device." Nat Mater **9**(9): 756-761.
- Wu, T., M. A. Zurbuchen, et al. (2006). "Observation of magnetoelectric effect in epitaxial ferroelectric film/manganite crystal heterostructures." Physical Review B **73**(13): 134416.
- Yakel, H. L., Jr., W. C. Koehler, et al. (1963). "On the crystal structure of the manganese(III) trioxides of the heavy lanthanides and yttrium." Acta Crystallographica **16**(10): 957-962.
- Yamauchi, K., F. Freimuth, et al. (2008). "Magnetically induced ferroelectricity in orthorhombic manganites: Microscopic origin and chemical trends." Physical Review B **78**(1).
- Yan, L., Z. Wang, et al. (2010). "Magnetoelectric and multiferroic properties of variously oriented epitaxial  $\text{BiFeO}_3$ -- $\text{CoFe}_2\text{O}_4$  nanostructured thin films." Journal of Applied Physics **107**(6): 064106.
- Yan, L., Z. Xing, et al. (2009). "Direct measurement of magnetoelectric exchange in self-assembled epitaxial  $\text{BiFeO}_3$ -- $\text{CoFe}_2\text{O}_4$  nanocomposite thin films." Applied Physics Letters **94**(19): 192902.
- Yang, F., M. H. Tang, et al. (2007). "Eight logic states of tunneling magnetoelectroresistance in multiferroic tunnel junctions." Journal of Applied Physics **102**(4): 044504-044505.
- Zapata, J., J. Narvaez, et al. (2008). "Electric and Magnetic Properties of Multiferroic  $\text{BiFeO}_3$  and  $\text{YMnO}_3$  Thin Films." Ieee Transactions On Magnetics **44**(11): 2895-2898.
- Zavaliche, F., H. Zheng, et al. (2005). "Electric Field-Induced Magnetization Switching in Epitaxial Columnar Nanostructures." Nano Letters **5**(9): 1793.
- Zeng, M., J. Wan, et al. (2004). "Resonance magnetoelectric effect in bulk composites of lead zirconate titanate and nickel ferrite." Journal of Applied Physics **95**(12): 8069-8073.
- Zhai, J., N. Cai, et al. (2004). "Magnetic-dielectric properties of  $\text{NiFe}_2\text{O}_4$  /PZT particulate composites." Journal of Physics D: Applied Physics **37**(6): 823.
- Zhang, F., Y.-C. Perng, et al. (2011). "Atomic layer deposition of  $\text{Pb}(\text{Zr,Ti})\text{O}_x$  on 4H-SiC for metal-ferroelectric-insulator-semiconductor diodes." Journal of Applied Physics **109**(12): 124109-124104.

- Zhang, F., G. Sun, et al. (2013). "Atomic Layer Deposition of BiFeO<sub>3</sub> Thin Films Using  $\beta$ -Diketonates and H<sub>2</sub>O." The Journal of Physical Chemistry C **117**(46): 24579-24585.
- Zhang, Y., C. Deng, et al. (2008). "Enhancement in magnetoelectric response in CoFe<sub>2</sub>O<sub>4</sub>-BaTiO<sub>3</sub> heterostructure." Applied Physics Letters **92**(6): 062911-062911-062913.
- Zheng, H., J. Kreisel, et al. (2007). "Heteroepitaxially enhanced magnetic anisotropy in BaTiO<sub>3</sub>-CoFe<sub>2</sub>O<sub>4</sub> nanostructures." Applied Physics Letters **90**(11): -.
- Zheng, H., J. Wang, et al. (2004). "Multiferroic BaTiO<sub>3</sub>-CoFe<sub>2</sub>O<sub>4</sub> Nanostructures." Science **303**(5658): 661-663.
- Zheng, H. M., F. Straub, et al. (2006). "Self-assembled growth of BiFeO<sub>3</sub>-CoFe<sub>2</sub>O<sub>4</sub> nanostructures." Advanced Materials **18**(20): 2747-+.
- Zheng, R. Y., J. Wang, et al. (2008). "Electrical and magnetic properties of multiferroic BiFeO<sub>3</sub>/CoFe<sub>2</sub>O<sub>4</sub> heterostructure." Journal of Applied Physics **104**(3): 034106.
- Zhong, X., J. Wang, et al. (2007). "Multiferroic nanoparticulate Bi<sub>3.15</sub>Nd<sub>0.85</sub>Ti<sub>3</sub>O<sub>12</sub>-CoFe<sub>2</sub>O<sub>4</sub> composite thin films prepared by a chemical solution deposition technique." Applied Physics Letters **90**(15): 152903-152903-152903.
- Zhu, X. and S. Kang, H. (2014). Spin-Transfer-Torque MRAM: Device Architecture and Modeling. Metallic Spintronic Devices, CRC Press: 21-70.
- Ziese, M., A. Bollero, et al. (2006). "Magnetoresistance switch effect in a multiferroic Fe<sub>3</sub>O<sub>4</sub>/BaTiO<sub>3</sub> bilayer." Applied Physics Letters **88**(21): 212502.